PETROLOGIC EVOLUTION OF NEMRUT STRATOVOLCANO (TURKIYE): PERALKALINE MAGMATISM IN A COLLISIONAL DOMAIN

NEMRUT STRATOVOLKANININ PETROLOJİK EVRİMİ: ÇARPIŞMA BÖLGESİNDE PERALKALİ MAGMATİZMA

H. EVREN ÇUBUKÇU

Submitted to
HACETTEPE UNIVERSITY
THE INSTITUTE FOR GRADUATE STUDIES
IN SCIENCE AND ENGINEERING
in partial fulfillment of the requirements for the degree of
DOCTOR OF PHILOSOPHY
in
GEOLOGICAL ENGINEERING

2008

To the Directory of the Institute for Graduate Studies in Science and Engineering,

This study has been accepted as a thesis for the degree of DOCTOR OF PHILOSOPHY in GEOLOGICAL ENGINEERING by our Examining Committee.

Head:	Professeur, Attila ÇİNER
Advisor:	Professeur, Erkan AYDAR
Co-Advisor:	Professeur, Alain GOURGAUD
Member:	Professeur, Hasan BAYHAN
Member:	Chargé de Recherche, Hervé GUILLOU
Member:	Chargé de Recherche, Catherine DENIEL
Member:	Professeur, Niyazi GÜNDOĞDU

This is to certify that the Board of Directors of the Institute for Graduate Studies in Science and Engineering has approved this thesis on .../.../.....

Prof. Dr. Erdem YAZGAN
Director
The Institute for Graduate Studies in
Science and Engineering

NEMRUT STRATOVOLKANININ PETROLOJİK EVRİMİ:
ÇARPIŞMA BÖLGESİNDE PERALKALİ MAGMATİZMA

H.Evren ÇUBUKÇU

Öz

Aktif Nemrut startovolkanı, Anadolu ve Arap plakaları arasındaki kıtasal çarpışmanın güney sınırını temsil eden Bitlis-Zagros Kenet Kuşağı'nın 12 km kuzeyinde bulunur. Volkanın faaliyeti 1 my önce başlamış ve tarihsel zamanlarda da (~500 BP) devam etmiştir. Volkan 89 bin yıldan daha yaşlı omayan ignimbiritik patlamalarla ilişkilendirilen eliptik bir kalderaya sahiptir. Nemrut peralkali bir volkan olup, tipik ürünleri hafif alkali geçiş bazaltlarından silisçe aşırı doygun peralkali riyolitlere kadar değişiklik gösterir. Ortaç bileşimlerde ise belirgin bir boşluk gözlenir (Daly Gap). Gözlemlenen mineral toplulukları, enigmatit, arfvedsonit-ribekit, egirin, fayalit ve REE-Ti silikat şevkinit ile tipik peralkali mineraloji sergilemektedir. Mineral türleri arasındaki faz dengeleri, kristallenmenin sığ magmatik rezervuar (≤ 1 kbar) ve düşük oksijen kaçıcılığında meydana geldiğini önermektedir. Kristallenme ve magmatik rezervuar için hesaplanan yoğun hal parametreleri, sığ magma odasının kimyasal/fiziksel olarak zonlandığını ve muhtemelen kristalce zengin bir yoğunluk filtresi ile ayrıldığını işaret etmektedir. Mafik ve felsik eriyikler arasında kristalin bir filtre görevi gören bu tabaka, plajiyoklaz (labradorit-andezin) + klinopiroksence baskın mineral topluluğunun hızlı ve yoğun kristalleşmesi ve süspansiyonu nedeniyle oluşmuş olup volkanik ürünlerde ortaç bileşenlerin bulunmayışını açıklamaktadır (Daly Gap). Jeokimyasal evrim eğilimleri ve önerilen matematiksel modeller, başlıca feldispat ve klinopiroksen + olivin + Fe-Ti oksitlerini içeren mineral topluluğunun sürekli ayrımlanması ve eşlik eden değişken ancak belirgin derecelerde kabuksal kirlenmenin mevcut mafik bileşenlerden peralkali riyolitler oluşturabileceğini ortaya koymaktadır. İz element içerikleri ve Sr-Nd izotop oranları, Nemrut magmalarının değişik derecelerde kabuksal kirlenmeye sahip, dalma-batma süreçlerinden az miktarda etkilenmiş bir astenosferik mantodan türediğini belirtmektedir. Volkanın yerleştiği Muş baseninin, önceden varolan makaslamalarının doğrultu atım kazanması ile yerel genleşmelerin gelişmesi, astenosferik kısmi eriyiklerin sokulumu ve yükselimini dolayısıyla peralkali magmatizmaya yol açan sığ magma odalarının oluşmasını kolaylaştırmıştır.

Anahtar kelimeler: *Türkiye, Doğu Anadolu, Nemrut, kıtasal çarpışma, peralkali, bazalt, riyolit, Daly Gap, fraksiyonel kristallenme, kabuksal kirlenme, zonlanmış sığ magma odası, genleşme*

Danışmanlar: Prof.Dr. Erkan AYDAR – Hacettepe Üniversitesi Jeoloji Mühendisliği Bölümü
Prof. Dr. Alain GOURGAUD – Université Blaise Pascal, Laboratoire Magmas et Volcans, FRANSA

PETROLOGIC EVOLUTION OF NEMRUT STRATOVOLCANO (TURKIYE): PERALKALINE MAGMATISM IN A COLLISIONAL DOMAIN

H. Evren ÇUBUKÇU

Abstract

Active Quaternary Nemrut stratovolcano is situated 12 km north of the Bitlis-Zagros suture zone, southern margin of continental collision between Arabian and Anatolian plates. Volcanic activity of the volcano began 1 Ma ago and continued in historic times (~ 500 BP). It has an elliptical caldera related to paroxysmal ignimbritic eruptions not older than 89 ka. Nemrut is a peralkaline volcano with characteristic bimodal products varying from mildly alkali transitional basalts to silica oversaturated peralkaline rhyolites, with an evident gap in intermediate compositions (Daly Gap). Observed mineral assemblages represent typical peralkaline mineralogy with aenigmatite, arfvedsonite – riebeckite, aegirine, fayalite and REE-Ti silicate chevkinite. Phase equilibria among mineral species suggest that crystallization takes place in a shallow magmatic reservoir (≤ 1 kbar) and low oxygen fugacity. Intensive crystallization and reservoir parameters indicate that shallow chamber is stratified compositionally and physically, and probably separated by a crystal rich density filter. This filtering layer is formed because of rapid and intense crystallization and suspension of plagioclase (labradorite – andesine) + clinopyroxene dominant assemblage. Such “crystalline” filter between mafic and felsic melts explains the absence of erupted intermediate compositions (Daly Gap). Geochemical evolution trends and suggested mathematical modelling depict that protracted crystal fractionation dominated by feldspar, clinopyroxene, olivine and Fe-Ti oxides with varying but significant degrees of crustal assimilation would produce peralkaline rhyolites from the actual mafic compositions taken as parents. Trace element contents and Sr-Nd isotopic ratios indicate that Nemrut magmas have been derived from a slightly subduction modified asthenospheric mantle with varying degrees of crustal assimilation. The genesis of Nemrut peralkaline magmatism in this collisional context has been ascribed to the penetration and ascension of asthenospheric partial melts into upper crustal high level reservoirs under Mus ramp basin, whose pre-existing shears have gained strike slip component thus leading localized extensions where Nemrut volcano has been located.

Keywords: *Turkiye, East Anatolia, Nemrut, Continental Collision, Peralkaline, Basalt, Rhyolite, Daly Gap, Fractional Crystallization, Contamination, Shallow Zoned Magma Chamber, Extension*

Advisors: Prof.Dr. Erkan AYDAR – Hacettepe Üniversitesi Jeoloji Mühendisliği Bölümü

Prof. Dr. Alain GOURGAUD – Université Blaise Pascal, Laboratoire Magmas et Volcans, FRANCE

EVOLUTION PETROLOGIQUE DU STRATO-VOLCAN NEMRUT DAGI (TURQUIE) : MAGMATISME HYPERALCALIN EN DOMAINE DE COLLISION

H. Evren ÇUBUKÇU

Résumé

Le strato-volcan actif Nemrut Dagi (Est-Turquie) est situé à 12 km au nord de la zone de suture Bitlis-Zagros, au sud de la marge continentale de la collision entre les plaques Arabique et Anatolienne. L'activité volcanique du volcan a commencé il ya 1 Ma et s'est poursuivie jusqu'à la période historique (~ 500 BP). Le volcan présente une caldeira elliptique formée à la suite d'éruptions paroxystiques ignimbritiques, âgées de moins de 89 ka . Les magmas émis par le Nemrut sont globalement hyperalcalins, variant des basaltes légèrement alcalins à rhyolites hyperalcalines, avec une absence évidente de compositions intermédiaires (Daly Gap). Les paragenèses minérales observées sont typiques des magmas hyperalcalins avec en particulier aenigmatite, arfvedsonite - riebeckite, aegirine, fayalite et chevkinite. Les équilibres minéralogiques suggèrent que la cristallisation s'est développée dans un réservoir magmatique peu profond (≤ 1 kbar), zoné et sous basse fugacité d'oxygène.

Les corrélations inter-éléments et les modélisations mathématiques montrent que la cristallisation fractionnée est dominée par la séparation de feldspath, clinopyroxene, olivine et oxydes Fe-Ti avec différents degrés de contamination crustale, ce qui permet la genèse des rhyolites hyperalcalines depuis des magmas parents mafiques. Les éléments en traces et isotopes (Sr et Nd) montrent que les magmas du Nemrut dérivent d'un manteau asthénosphérique modifié légèrement par une subduction antérieure avec assimilation de la croûte.

La présence problématique d'un magmatisme hyperalcalin dans un contexte de collision continentale, est attribuée à la pénétration et l'ascension des liquides asthénosphériques dans la croûte supérieure, par un processus de « slab breakoff ». Par ailleurs, le Nemrut est situé dans un bassin d'effondrement récent, une phase d'extension étant associée à la collision.

Mots Clés : *Turquie, Anatolie de l'Est, Nemrut Dagi, Collision Continentale, Hyperalcalin, Basalte, Rhyolite, Daly Gap, Cristallisation Fractionnée, Contamination, Chambre Superficielle Zonée, Extension.*

Directeurs: Prof.Dr. Erkan AYDAR – Hacettepe Üniversitesi Jeoloji Mühendisliği Bölümü
Prof. Dr. Alain GOURGAUD – Université Blaise Pascal, Laboratoire Magmas et Volcans, FRANCE

Acknowledgements

This PhD thesis should be regarded as a testimony to my passion and endless curiosity for magma, the molten earth. En route to surface, for a couple of difficulties, numerous wonderful people were there to facilitate the ascent.

I would like to express my deepest gratitude to my advisor Prof. Dr. Erkan Aydar, whom I felt his support and faith at all times whatever I intended to do. Throughout the years, I have always been delighted to feel his guidance and encourage.

I am grateful to my co-advisor Prof. Dr. Alain Gourgaud, for his highly appreciated understanding, support and supervision. It was a great pleasure to work with him.

Many thanks go to İnan Ulusoy, Orkun Ersoy and Erdal Şen, whom I always enjoyed and benefited to work with, especially in Nemrut field.

I most feel indebted to Prof. Dr. Hasan Bayhan for his trust in me for various projects over the years. I would like to thank Catherine Deniel for her never-ending informative help on maintaining different perspectives and precision. Hervé Guillou must be thanked for his valuable support during radiometric dating in Gif-sur-Yvette and unique comprehension while preparing the report. I thank Prof. Dr. Attila Çiner for the report and leading the jury. Prof. Dr. Niyazi Gündoğdu is thanked for honoring me by accepting to be a member of the jury. I warmly thank Philippe Labazuy for being so sincere and helpful.

In the name of easing the roadblocks I have confronted, I would like to express my appreciation to technical staff in Hacettepe University (Ethem and Vahdet for urgent thinsectioning) and in LMV (Jean-Luc for microprobe séances and Mhammed for instructive major element analyses).

I would like to thank to all my friends, for their everlasting support, tolerance and devotion during my painful days. I owe them for keeping smiling every time I say, "*After the thesis...*" (Well, here we are).

I believe any expression in any language cannot voice my eternal gratitude for my Mum and Dad. They raised me with their infinite love, patience and confidence, leading the way in my pursuit of reaching anywhere I have determined to go. Without them, you would not be reading this. Also, I would like to convey my gratefulness to my brother Kıvanç and Müjgan for being there and their fidelity. My greatest luck is to have such a magnificent family.

And to my loving Zeynep, who was (and hopefully will be) incredibly patient and tactful, even when I was more than unbearable. She always managed to enlighten me whenever I got dim, because her vividness always rejuvenates.

Numéro d'Ordre:**1820**

UNIVERSITE BLAISE PASCAL

(U.F.R. de Recherche Scientifique et Technique)

ECOLE DOCTORALE DES SCIENCES FONDAMENTALES

N°: 561

THESE

Présentée pour obtenir le grade de

DOCTEUR D'UNIVERSITE

(Specialite : Petrologie - Volcanologie)

Par

ÇUBUKÇU H. Evren

Master

Evolution pétrologique du strato-volcan Nemrut Dagi (Turquie): Magmatisme hyperalcalin en domaine de collision

President (Rapporteur)	:	Attila Çiner	Université d'Orléans
Rapporteur	:	Hervé Guillou	LSCE CEA – CNRS – Gif-sur-Yvette
Examinateur	:	Catherine Deniel	Université Blaise Pascal Clermont-Ferrand
Examinateur	:	Hasan Bayhan	Université Hacettepe – Ankara
Directeur de thèse	:	Erkan Aydar	Université Hacettepe – Ankara
Co-directeur de thèse	:	Alain Gourgaud	Université Blaise Pascal Clermont-Ferrand
Invité	:	Niyazi Gündoğdu	

TABLE OF CONTENTS

CHAPTER 01

GEOLOGICAL BACKGROUND AND PURPOSES

Great things are done when men and mountains meet

William Blake

1 GEOLOGICAL BACKGROUND AND PURPOSES

Upon the acceptation of plate tectonics theory in the mid-20th century, significant acceleration has been attained in understanding the interactions between neighboring lithospheric plates and related magma genesis. During the last few decades, the results of enormous amount of research on this promising topic introduced the striking connection between tectonic settings and the nature of the generated magmas. Similar magmas with similar geochemical characteristics are generated in similar tectonic environments and such a relationship has become an essential comparison tool for petrologic researches. Hence, a better knowledge of the geodynamic context of the focused area would provide important constraints for magmatic processes: from their genesis to their solidification via differentiation.

1.1 Geodynamic Framework

1.1.1 Tectonic History

Anatolian peninsula, being an important component of the Alpine - Himalayan orogenic system, has been an attractive region of interest as it offers a broad spectrum of research areas owing to complex kinematics throughout its geodynamic evolution. Turkiye was situated at the collisional boundary between Gondwana in the south and Laurasia in the north and its geological history records the suturing of a succession of continental fragments (Figure 1.1, Bozkurt et al., 2000).

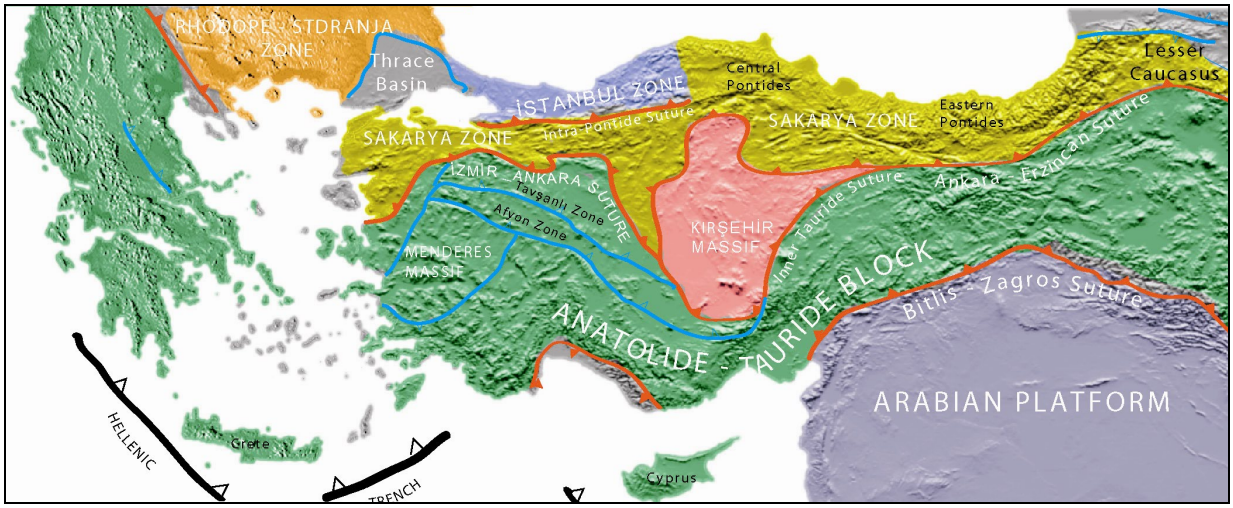

Figure 1.1: Tectonic map of Anatolian Region showing major sutures and continental blocks (modified from Okay and Tüysüz, 1999)

The Tethyan Ocean that existed between Laurasia and Gondwana as a westward narrowing embayment since the Carboniferous was not a single continuous oceanic plate during its long evolution (Şengör, 1987; Ricou 1994; Stampfli, 1996, Okay and Tüysüz, 1999). Throughout its evolution, small continental fragments were rifted off from either side of the Tethyan Ocean and moved towards the other side, creating new oceanic lithosphere in their wakes, and eventually colliding with the opposite continental margin (Figure 1.2, Okay and Tüysüz, 1999). Hence, in Anatolian region the boundary between Laurasia and Gondwana is represented by several sutures, which isolate distinct continental fragments. These continental blocks, with each have diverse marginal suture zones, are formed by the closure of Neo-Tethyan Ocean during the late Cretaceous - Eocene (Şengör and Yılmaz, 1981). These fragments, which exhibit various geological records, have been accreted to Eurasia throughout the Mesozoic and Cenozoic times. The final amalgamation of these fragments into a single continental mass occurred in Turkey at Late Tertiary, when the Arabian plate collided with the Anatolian plate (Okay and Tüysüz, 1999).

Figure 1.2: Tethyan oceans and their respective Palaeo-movements (modified from Şengör et al., 1985 and references therein)

After the closure of Palaeo-Tethys during the middle Jurassic, two oceans, northern and southern branches of Neo-Tethys, were remained in Anatolian region (Figure 1.2, Şengör and Yılmaz, 1981). The northern branch of Neo-Tethys (north Anatolian - Lesser Caucasian ocean) was demised diachronically (Late Paleocene in the west, late Burdigalian in the east) by final collision and suturing of Eurasia in the north and the Anatolian - Iranian platform in the south (Koçyiğit et al., 2001 and the references therein). A segment of the southern oceanic branch of the Neo-Tethys attached to the Arabian Plate continued its northward subduction beneath eastern Anatolia through the Middle Miocene, (Serravalian) (Yılmaz, 1993; Angus et al., 2006). Then it was also closed and demised entirely by the continent - continent collision and suturing of the Arabian Plate with the Eurasian Plate (Şengör and Yılmaz, 1981; Dewey et al., 1986; Koçyiğit et al., 2001) along Bitlis - Zagros suture. Following this collision, a major episode of widespread volcanism with varied and complex composition affected most of the eastern Anatolian region starting at about 11 Ma (Keskin, 2003; Angus et al., 2006). Post-collisional intracontinental convergence along Lesser Caucasian and Bitlis - Zagros sutures, the intervening area was compressed and ~2 km high plateau, east Anatolian - Iranian plateau has been formed (Figure 1.1, Şengör and Kidd, 1979).

1.1.2 Neotectonics of Eastern Anatolia

The neotectonic setting of Turkiye and surrounding regions is accepted to begin at the Middle Miocene (Serravalian), the time when Anatolian and Arabian continental plates began to collide along Bitlis - Zagros suture (Şengör and Yılmaz, 1981).

The intracontinental convergence and N - S directed compressional - contractional tectonic regime remained at the end of late Miocene and late Early Pliocene, in places along the Bitlis suture zone in eastern Turkey (Koçyiğit et al., 2001). In late Early Pliocene, three major neotectonic structures; the dextral North Anatolian (NAF), the sinistral East Anatolian Transform Faults (EAF) and the Anatolian Platelet formed (Figure 1.3, Koçyiğit et al., 2001). Because of its relative motion planes along North and East Anatolian Transform Faults, Anatolian Platelet began to “escape” towards African plate. The formation of NAF, thus the lateral escape of Anatolia has been recently ascribed to the break-off of subducting slab beneath the Bitlis - Hellenic subduction zone (Faccenna et al., 2006). Nevertheless, whatsoever the triggering mechanism is, starting from late Early Pliocene onward, earlier compressional - contractional tectonic regime was replaced by the compressional - extensional tectonic regime in Eastern Anatolia (Figure 1.4, Koçyigit et al., 2001).

Along the eastern portion of NAF, the present day state of deformation is dominantly right-lateral strike slip (Faccenna et al., 2006) Moreover, evidence has been reported for an early Quaternary change from regional transpressional to transtensional regime, preserving a NNW-trending orientation of the maximum horizontal stress axis (Over et al., 1997).

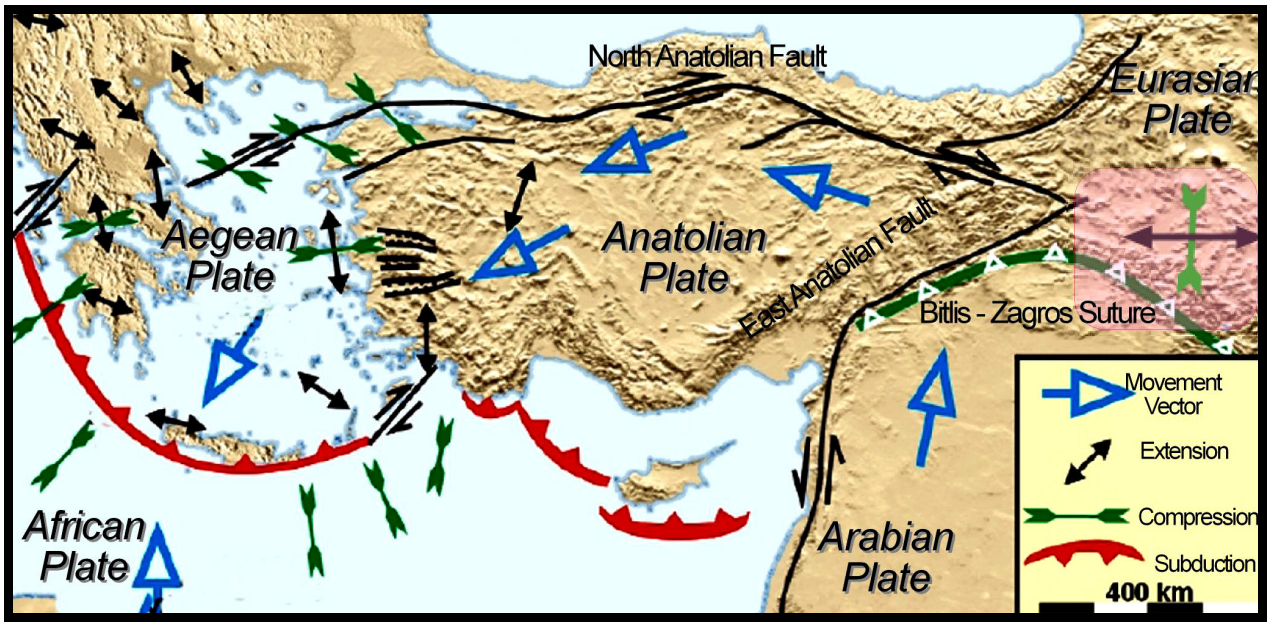

Figure 1.3: Neotectonic features and actual plate movements in Anatolian Region

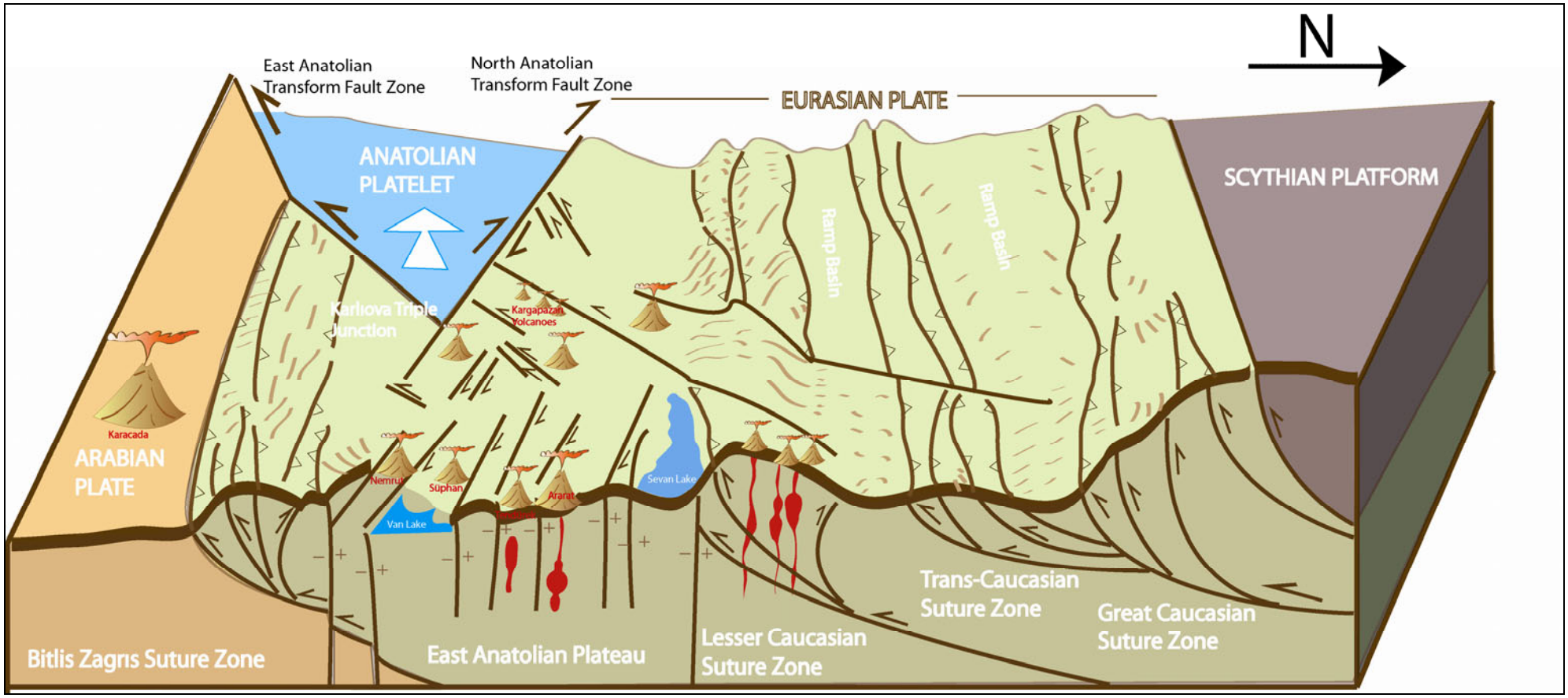

Figure 1.4: Block diagram depicting simplified compressional and tensional neotectonic structures resulting from N-S convergence between Arabian and Eurasian Plates in the East Anatolian Plateau and adjacent areas (modified from Koçyiğit et al., 2001)

1.2 Structural Context of East Anatolia

Neotectonics of Turkiye has been described as the convergence and relative motions of Anatolian, Arabian and Eurasian continental plates, which are separated by diverse tectonic boundaries. Aforementioned tectonic framework reveals that East Anatolian Plateau represents early stages of continental collision. Although its formation is analogous to Tibetan Plateau, the only well studied example of continental collision, East Anatolia deserves special importance because of the extensive volcanism observed.

In order to improve our understanding of the Bitlis - Zagros thrust zones, as well as the nature of continental escape along the EAF and NAF through the imaging of upper mantle and crustal structure, Eastern Turkey Seismic Experiment (ETSE[1]) was conducted across the East Anatolian plateau and the northernmost Arabian plate (Sandvol et al., 2003). The results of this experiment were surprising and brought pioneering perspectives to the ongoing debate both on the northward motion of the Arabian plate and lithospheric structure of the region.

Hypocentral distribution of local earthquakes during the operation of the network showed that there were no subcrustal earthquakes beneath the Arabian - Eurasian collision zone or beneath the Anatolian plateau suggesting no or very little underthrusting / subduction of the Arabian plate beneath Eurasia (Al-Lazki et al., 2003, Turkelli et al., 2003). Source properties of small - to - moderate magnitude seismic events suggest that in eastern Turkey, most of the collision is taken up by strike slip faults indicating the northward convergence of Arabia is being accommodated by escape tectonics, where compressive features (e.g. thrust faulting) are still active but are of lesser importance (Örgülü et al., 2003). Furthermore, seismic evidence indicates an average crustal thickness of 45 km for East Anatolian plateau (Zor et al., 2003), which was hitherto presumed to be ~ 55 km (e.g. Şengör, 1980). Moreover, Şengör et al. (2003) believe; crustal thickness, combined with tomographic models of regional seismic velocity and attenuation (Sandvol et al., 2003), shows that most of the East Anatolian plateau is devoid of mantle lithosphere. The absence of mantle lithosphere is ascribed to break-off of northward-subducted slab beneath East Anatolian Accretionary prism and the widespread volcanism to melting its lower levels because of direct contact with hot asthenosphere (Sandvol et al., 2003;

[1] ETSE was a 29 broadband station PASSCAL (*Program for the Array Seismic Studies of the Continental Lithosphere*) network which was operated from late October 1999 to August 2001 in eastern Turkey (Turkelli et al., 2003).

Şengör et al., 2003). Additionally, according to their Curie Depth Point and Pn velocity data, Elitok and Dolmaz (2007) propose that mantle lithosphere also gets thinner in the Arabian Foreland towards Bitlis suture zone probably due to its mechanical removal/erosion at the southernmost Anatolian side of the suture. Based on recent geophysical studies mentioned above and on the geochemical data on volcanics observed in the region, Keskin (2003) suggests the invalidity of the previous models concerning magma generation in Eastern Anatolia. According to his model, the northward subducting oceanic lithosphere beneath East Anatolian Accretionary prism is steepened and eventually detached from the continental lithosphere of Bitlis – Pötürge Massif. Following the continent - accretionary complex collision, astenospheric mantle contacts with the accretionary complex at shallow depths (~ 50 km) resulting in rapid regional uplift and extensive melting which leads to collisional volcanism (Keskin, 2003). S-wave receiver functions, however, presume the lithosphere - asthenosphere boundary (LAB) of the Arabian shield does not appear to underthrust eastern Anatolia and the existence of clear LAB below EAAC within the depth range of 60 - 80 km, where late Miocene to recent volcanism is significant (Figure 1.5.a and Figure 1.5.b, Angus et al., 2006). Thus it can be deduced that mantle lithosphere beneath EAAC is probably extremely thin (10-30km?) or even absent. Further studies on mantle shear wave velocity structure, which provide insight into the rheology and dynamic processes of the upper mantle, signifies a warm (above solidus, molten), low-density upper mantle beneath the Turkish - Iranian plateau (Maggi and Priestley, 2005) just under eastern Quaternary volcanic centers, especially Nemrut volcano (Figure 1.5.a and Figure 1.5.b).

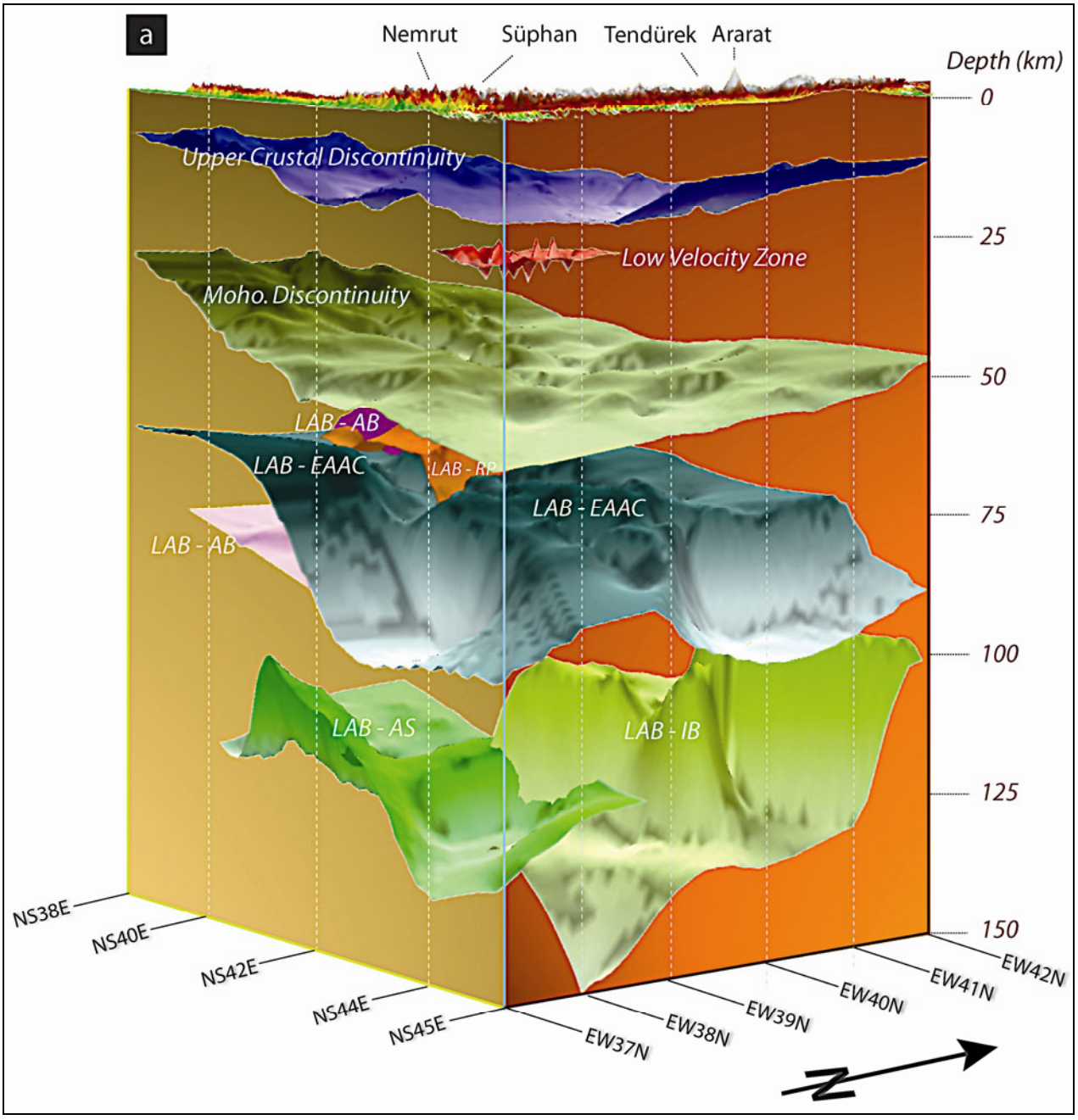

Figure 1.5.a: Three-dimensional reconstruction of S-wave receiver functions in Eastern Turkey viewed from two different angle of views (a and b). Data compiled and implemented from Angus et al. (2006). Abbreviations used are LAB (Lithosphere - Asthenosphere Boundary), Moho (Mohorovicic discontinuity), RP (Rodope-Pontide), AB (Anatolian Block), EAAC (East Anatolian Accretionary Complex), IB (Iranian Block), AS (Arabian Shield). Low Velocity Zone indicating molten (above solidus) material is depicted to be emplaced beneath Quaternary volcanic centers, especially Nemrut volcano. Geographical coordinates and depths have been projected (curvature of the earth is neglected).

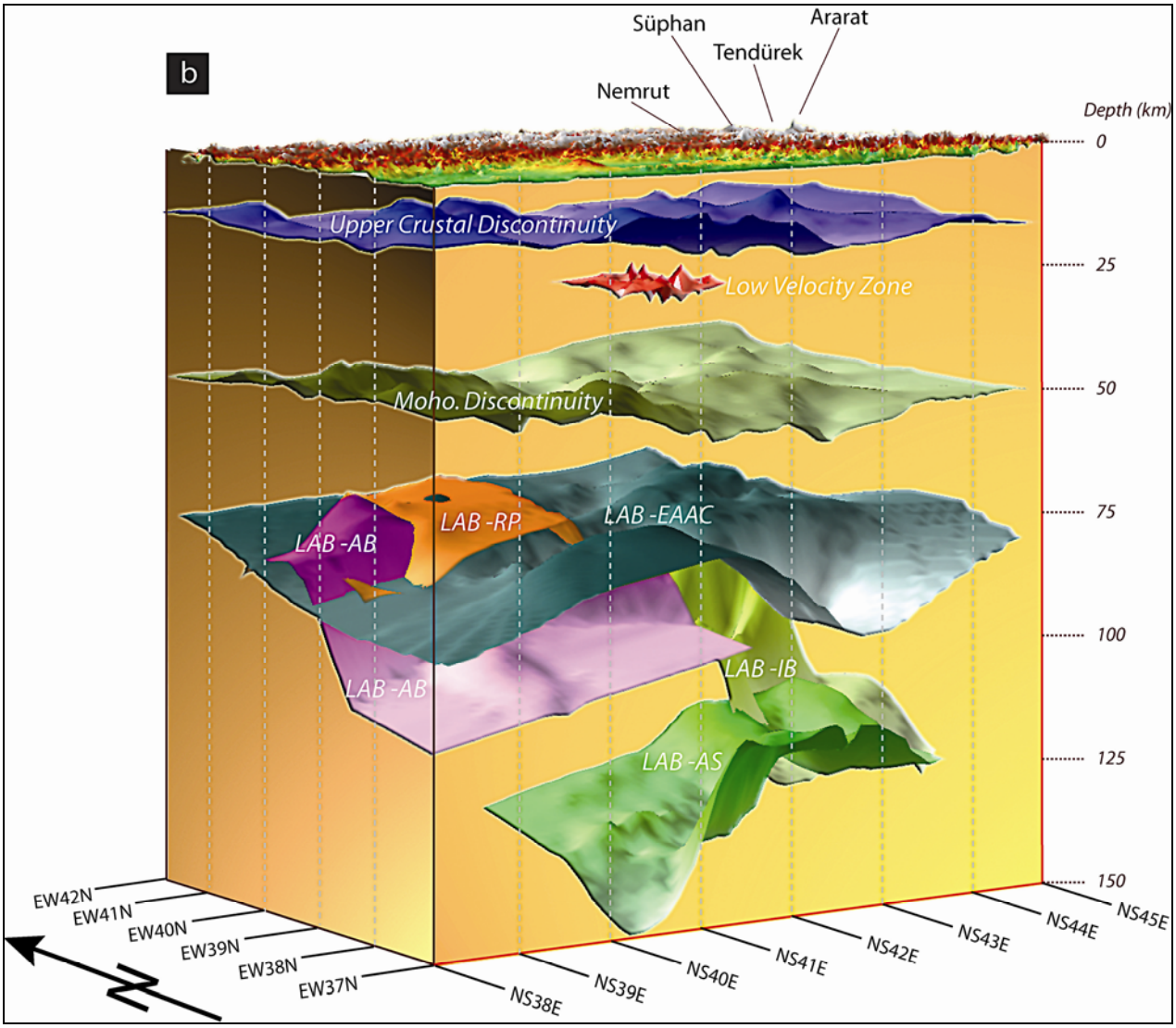

Figure 1.5.b: Three-dimensional reconstruction of S-wave receiver Functions in Eastern Turkey viewed from two different angle of views (a and b). Data compiled and implemented from Angus et al. (2006). Abbreviations used are LAB (Lithosphere - Asthenosphere Boundary), Moho (Mohorovicic discontinuity), RP (Rodope-Pontide), AB (Anatolian Block), EAAC (East Anatolian Accretionary Complex), IB (Iranian Block), AS (Arabian Shield). Low Velocity Zone indicating molten (above solidus) material is depicted to be emplaced beneath Quaternary volcanic centers, especially Nemrut volcano. Geographical coordinates and depths have been projected (curvature of the earth is neglected).

1.3 Volcanism in Eastern Anatolia

Eastern Anatolia represents an incomparable site to investigate the early stages of continental collision and related volcanism from the viewpoint of its tectonic and structural context discussed above. Over the years, the region has become the subject of gradually increasing number of studies, which aim to shed light on the generation and evolution of magmatism within these special settings. Although significant progress has been attained and accelerated during the last decade by the help of multidisciplinary collaborations, it is fair to say that all these valuable efforts are still insufficient for East Anatolia; where over the half of the region is covered with Neogene volcanic units. Regarding such a voluminous volcanic outcrop, one might presume a greater proportion of melt has remained emplaced in the crust indicating extensive magma generation. This brings out the problem of the validity of proposed magmatologic models due to the fact of sparse sampling and/or ill definition of the volcanic units. Nemrut stratovolcano, which is the primary focus of this study, suffers from such a lack of descriptive studies (c.f. Çubukçu et al., 2007).

Volcanism in eastern Anatolia was initiated following the rapid uplift of Eastern Anatolia and developed pervasively all over the region, producing subaerial lava flows and pyroclastic products, which exhibit varying eruption styles and geochemical characteristics (Pearce et al., 1990; Keskin et al., 1998; Yılmaz et al., 1998; Keskin 2003). Keskin (2003) proposes the migration of volcanic activity from the north of Erzurum - Kars plateau, from where the activity commenced (with maximum radiometric age of 11 Ma: Pearce et al., 1990), towards south - southeast, producing a vast volume of volcanic material almost covering two thirds of the region and reaching over 1 km of thickness in some localities.

Volcanism is dominantly represented by fissure fed eruptions; however, there are over 20 central eruption sites in the region (Figure 1.6). The erupted volume of volcanic products emphasize an enormous amount of melt generation beneath the region as a greater proportion should presumably have been emplaced deeper in crust as plutonic intrusions indicating the “melting anomaly” resulted from the collision of Arabian and Eurasian plates (Keskin, 2003).

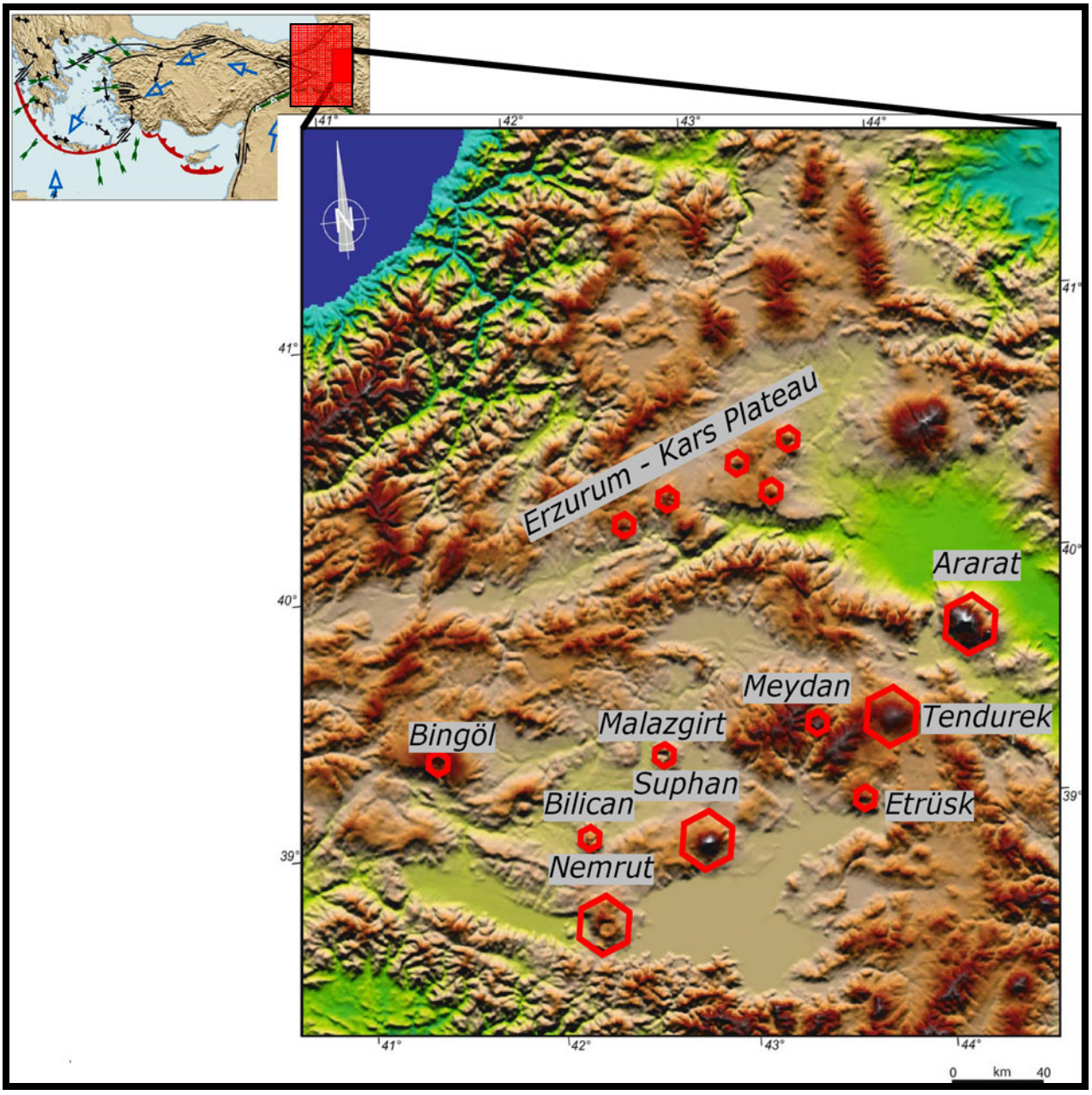

Figure 1.6: Distribution of Eastern Anatolian Volcanic Centers

Volcanism is still active in the region, represented by major Quaternary volcanic centers (Mt. Nemrut, Mt. Tendürek, Mt. Ararat, etc.) documented in historical records (c.f. Karakhanian et al., 2002; Aydar et al., 2003). Active Nemrut stratovolcano with observed fumerolic output, which is the primary concern for this study, is being monitored by Hacettepe University against a probable eruption risk.

1.4 Geochemistry of East Anatolian Volcanics

Neogene to Quaternary East Anatolian volcanic products, which cover over the half of the region, display significant compositional variability from basalt to phonolite and rhyolite reported in numerous studies (e.g. Innocenti et al., 1976, Gülen, 1984, Ercan et al., 1990, Pearce et al., 1990, Keskin et al., 1998, Yılmaz et al., 1998, Keskin 2003, Şen et al, 2004). Keskin (2003) proposes a considerable variation in lava chemistry in the N-S direction between the Erzurum-Kars Plateau (EKP) in the north and the Muş - Nemrut -Tendürek volcanoes in the south: Volcanic units of the EKP are calc-alkaline; Muş - Nemrut - Tendürek volcanoes are alkaline to mildly alkaline and lavas of the Bingol and Süphan volcanoes are transitional (Pearce et al., 1990). However, Süphan volcano, being transitional in character and located just between Tendürek and Nemrut volcanoes, seems somehow contradictory with the suggestion of a spatial discrimination between calc-alkaline and alkaline volcanism. Furthermore, mafic to peralkaline silicic magmatism is observed in Nemrut stratovolcano, on which this PhD study has solely been focused.

Pearce et al., (1990) suggest an enriched mantle source containing a distinct subduction signature for Erzurum - Kars Plateau and Mount Ararat volcanics, but on the other hand, for Muş - Nemrut -Tendürek alkaline volcanics they observe a gradual decrease in subduction signature displaying intra-plate characteristics. Calc-alkaline lavas of the Erzurum - Kars Plateau exhibit a contribution of a subduction component; however, alkaline basic lavas of Muş - Nemrut - Tendürek might have been derived from an enriched source with or without a slight subduction signature and then evolved through combined assimilation - fractional crystallization (Keskin, 2003).

Although these petrologic interpretations are useful to provide superficial comprehension of the nature, causes and the evolution of volcanism observed in the region, each major volcanic center should have been investigated thoroughly within their respective geological framework considering the volcanostratigraphy, petrography, mineralogy and magmatic reservoir properties as well as geochemistry. In this study, Mount Nemrut has been investigated in detail regarding those constraints, and the magmatic evolution, from genesis to solidification via differentiation, has been tried to be exposed considering state equilibria of related parameters.

1.5 On the Mount Nemrut

It is necessary to give brief descriptive information on the characteristics of Mount Nemrut in order to compare the existence of the volcano with the volcanic centers of similar petrologic nature in terms of geological settings, magma genesis, mineralogy and magmatic evolution.

Mount Nemrut is a Quaternary stratovolcano, located at the western shore of soda Lake Van, culminating at 2948 m. The volcano, with approximately 22 km of basal diameter, bears an elliptic spectacular summit caldera with 8.5 x 7 km diameters, of which the eastern half is filled by pyroclastic deposits related to maar-like explosion craters, lava domes and flows (Aydar et al., 2003). Whereas, the western half of the caldera is filled by a fresh water lake, covering a surface area of ~ 16 km^2 with a maximum depth of 176 m. Besides, there is a much smaller lake with hot springs with a maximum depth of 11 m. Fumarolic activity is present from a cave-like crack on a dome located at the northern part of the caldera. Nemrut volcano is active and its latest volcanic activity, although previously known to occur in 1441 (e.g. Oswalt, 1912), dates back to 1692 (Karakhanian et al., 2002). Besides, Aydar et al. (2003) report a live description of one of the latest eruptions based on an Arabic book.

Nemrut volcano, as the other important volcanic centers of Eastern Anatolia, suffers from the lack of detailed volcanological / petrological investigations. Although a number of studies have been realized and published about Nemrut volcanism in the last few decades, unfortunately none of them presented a meticulous examination especially on mineralogical - geochemical evolution in terms of volcanostratigraphy.

Previous Research

Özpeker (1973) realized the first petrochemical study on Nemrut volcanism, introducing the volcano and suggesting volcanological evolutionary stages. Moreover, he proposed a cratonic - simatic origin for the Quaternary volcanism of Mount Nemrut.

Innocenti et al. (1976) have shown the coexistence of both calc-alkaline and alkaline volcanism in the region. They further indicate two series of alkaline volcanism associated with central volcanoes, undersaturated series ranging from basalts to hawaiites to ne-normative trachytes (Tendürek) and oversaturated products up to peralkaline rhyolites (Nemrut). Despite the lack of detailed volcanological - mineralogical observations, this very study mentions the peralkalinity of

the products of Nemrut volcanism according to the geochemical properties for the first time. In their consequent paper, Innocenti et al (1982), although not focused on Nemrut, introduce the problematics of Quaternary calc-alkaline volcanism associated with Süphan volcano. They describe this activity as an episodic and isolated manifestation, explaining it because of renewed subduction of continental lithosphere very close to the suture.

Gülen (1984), in his PhD thesis presents extensive geochemical data (major/trace elements and Sr,Nd, Pb isotopes) for East Anatolian volcanics including Nemrut. He briefly states the peralkaline nature of the volcano and ascribes its (and other alkaline volcanoes') genesis to break-off of subducting slab and emplacement of asthenospheric partial melts.

In the late 80's, Nemrut has been investigated for its geothermal potential by Turkish Petroleum Corporation (TPAO) because of the evidences pointing out a recent shallow magma chamber. Despite the indications for an active magmatic heat source, drilling results in the caldera exhibit a lack of significant hydrothermal activity to depths of 5000 feet (~ 1520 m). Although this survey did not lead to any further economical attempt, it was fruitful in terms of petrological interest because of the broad range of analyses including geochemistry and related modeling, geochronology (K/Ar) and isotope geochemistry ($^{87}Sr/^{86}Sr$ and ^{18}O). The results have been compiled in unfortunately unpublished reports (e.g. Atasoy et al., 1988) maintaining a concrete background unluckily for a limited number of researchers. According to the preliminary detailed investigations, volcanic products of Nemrut are subdivided into three groups: 1) pre-caldera volcanics (1.01 ± 0.4 to 0.24 ± 0.15 Ma) consisting primarily of trachyandesite – trachyte and peralkaline rhyolite 2) Caldera-forming trachytic tuff (0.27 Ma) and 3) post-caldera bimodal basalt and rhyolite (Atasoy et al. 1988). This study, although was lack of detailed mineralogical inspections, was important not only for emphasizing the bimodal association for post-caldera products but also for extensive radiometric dating of eruptive products of Nemrut volcano.

Ercan et al. (1990), confirm the alkaline nature of the eruptive products of Nemrut volcanism and state radiometric ages of < 0.03 Ma for rhyolites, indicating the youngest volcanic products in Eastern Anatolia. Besides, they note a different fissural basaltic origin than Nemrut, as previously proposed (Özpeker, 1973, Güner, 1984) for the volcanics observed in Bitlis Valley. This, from our point of view, is the highlight of this study.

In their extensive review, Pearce et al. (1990) present geochemical, isotopic and radiometric age data for the Neogene Collision volcanics of Eastern Anatolia. They give brief petrography and volcanic facies for major volcanoes of the region including Nemrut. They point out that the alkaline series of the region, Nemrut and Muş volcanics lie on the silica-saturated side, whereas Tendürek contains strongly silica under-saturated samples. According to the evidences presented, Nemrut and Muş volcanics are characterized by alkaline compositions that follow basalt - trachyandesite - peralkaline rhyolite fractionation trends. The low ratios of CaO to alkalis and magnesium to iron and increase in Zr, Y and Nb indicate an anhydrous POAM (Plagioclase, Olivine, Augite, and Magnetite) crystallization assemblage (Pearce et al., 1990). Furthermore, isotopic data suggest that the combined assimilation and fractional crystallization (AFC) was an important process in the origin of Nemrut and the other forenamed volcanoes.

Türkecan (1991), although focused on the Pliocene Muş volcanics, stated that samples from Kirkor Domes of Nemrut volcanic system were peralkaline, and utilized the discrimination of Macdonald (1974) for the very first time in the literature suggesting that these samples were comendite / comenditic trachyte.

Notsu et al (1995), comparing the geochemical features of collision-related volcanic rocks in central and eastern Anatolia, present brief geochronological and isotopic data for Nemrut volcano. The ages of trachytic and rhyolitic eruptive products of Nemrut vary between 0.10 ± 0.05 Ma and < 0.01 Ma. Besides, they suggested that $^{87}Sr/^{86}Sr$ ratios for Nemrut and other East Anatolian volcanoes were higher than those of N-type MORB, but overlap arc volcanic rock values suggesting that the mantle source was possibly contaminated by fluids and melts during the pre-collisional events, even across the collision plate boundary.

Bigazzi et al. (1997) present age determination of obsidian bearing volcanics of Nemrut and the other eastern Anatolian volcanoes using fission track dating method. However, they have given neither any geochemical analysis nor the location of the sample taken. The only one sample was dated at 0.024 ± 0.014 Ma.

Yılmaz et al. (1998) aimed to provide comprehensive description of the major Quaternary volcanoes (Nemrut, Süphan, Tendürek and Ararat) of the East Anatolia, intending to describe these centers from a volcanological perspective, to review their petrogenetical nature and finally discuss their tectonic significance. Based on fieldwork and aerial imagery Yılmaz et al. (1998)

suggested pre-cone, cone building, climactic, post-caldera and late phases as the major volcanic episodes in the development of Nemrut volcano. They further proposed the same volcanic episodes for Süphan, Tendürek and Ararat volcanoes. However, their discrimination between these episodes was loosely based on solid discrepancies, rather mostly on the differences between volcanic facies of eruptive products. Concerning the geochemical characteristics, Yılmaz et al. (1998), mention about a slight gap between the silica contents of 56 - 52 %. Moreover, despite the oversaturated Nemrut volcanics fell in peralkaline fields in their discrimination diagrams, Yılmaz et al (1998) did not point out the peralkalinity of these units. They propose an enriched mantle source and significant POAM fractionation with slight crustal assimilation for the evolution of Nemrut volcanism.

Güleç et al. (2002), in their study in which they examine the distribution of helium ratios in the various tectonic provinces of Turkey, state that mantle contribution reaches a maximum at Nemrut volcano. In the intra-caldera lake of Mt. Nemrut, the highest R/R_A ratios in Turkey are recorded (where R = sample $^3He/^4He$ and R_A= air $^3He/^4He$) revealing an almost pure mantle-He being emitted (Güleç et al., 2002).

Aydar et al. (2003), for the very fist time in the literature, emphasize the potential risk of active Nemrut volcano. Moreover, they quote a live observation of the last eruption of Nemrut from an Arabic book (Şerefhan, 1597), suggesting that the volcano was very active about 400 years ago. They highlight that Mount Nemrut represents a real danger for 135 000 people living in the vicinity, proposing that a seismic survey combined with periodical water and gas sampling, and, establishing an alert code system and civil evacuation plans are imperative. From 2004 to present, the volcano has been monitored by Hacettepe University, led by E. Aydar, via a network of three dedicated seismometers transmitting real time data.

Karaoğlu et al. (2005) have documented the stratigraphy of the volcanic products around Nemrut caldera. They subdivided the volcanological development of the volcano into three stages: pre-caldera, post-caldera and late stages. However, stage discrimination between post-caldera and late stages was rather ambiguous with a lack of significant volcanological change.

In their study Özdemir et al. (2006) aimed at reconstructing the volcanostratigraphy and modelling the petrogenesis of the Nemrut stratovolcano through: i) detailed geological mapping, ii) mineralogical and petrographical investigations, iii) investigation of the chemical variations of

the volcanics and iv) determination of the petrogenetic significance of these variations in terms of mantle source characteristics, nature of mantle-crust interaction and relation to the active tectonics. However, their reconstruction of the volcanostratigraphy contains severe factual errors (c.f. Çubukçu et al., 2007 and further chapters). Mineralogical and petrographical descriptions are based only on optical observations and thus far from the actual modal associations. On the other hand, chemical variations of the volcanics are based on poorly identified volcanological stage definitions and therefore do not reflect the spatial and temporal evolution of Nemrut volcanism. This controversial study has been criticized by Çubukçu et al (2007), presenting a summary of the very first mineral chemistry analyses and a comparison of geochemical features of Nemrut volcano with the peralkaline suites observed worldwide, which have been realized within the context of this thesis.

Despite a number of previous geochemical and petrological studies on the Nemrut stratovolcano, only very early studies mention the peralkalinity of its oversaturated eruptive units (e.g. Innocenti et al., 1980; Pearce et al., 1990; Türkecan, 1991). The overall geochemical and mineralogical affinity of Nemrut volcanism exhibits strong similarities when compared to the well-known sites of continental intra-plate extension (Table 1.1). Nemrut peralkaline volcanism reflects such nature of continental extension. Considering this fact provides deeper insights into petrogenesis of Eastern Anatolian magmatism and regional geodynamics.

Table 1.1: Rock types and generalized mineral assemblage of peralkaline silicic rocks from various peralkaline suites (from Çubukçu et al., 2007)

	Rock Type	Agpaitic Index	Mineral Assemblage
Gedemsa, Central Ethiopian Rift *Peccerillo et al., 2003*	pantellerite	1< A.I. <1,8	Alkali Feldspar (anorthoclase, sanidine) + clinopyroxene + fayalite ± alkali amphibole ± aenigmatite ± biotite ± Fe-Ti Oxides
Transpecos, USA *White et al. (2006)*	comendite comenditic trachyte	1 < A.I. <1.2	anorthoclase, sanidine + hedenbergite + fayalite ± ilmenite ± magnetite ± ferrorichterite ± aenigmatite ± quartz ± annite ± monazite ± zircon
Olkaria, Kenya Rift *Scaillet and Macdonald (2001)*	comendite	1 < A.I. <1.4	Alkali feldspar + clinopyroxene + fayalite ± ilmenite ± magnetite ± quartz ± aenigmatite ± amphibole (ferrorichterite -ferroedenite - riebeckite arfvedsonite) ± chevkinite ± zircon ± biotite
Nemrut Stratovolcano *Our Study*	comendite comenditic trachyte rare pantellerite	1<A.I.<1,5	anorthoclase, sanidine + clinopyroxene (aug, hdn, ae) + fayalite ± ilmenite ± amp (ferrorichterite, arfvedsonite - riebeckite) ± ilmenite ± Ti-magnetite ± quartz ± aenigmatite ± chevkinite ± zircon ± apatite

1.6 Oversaturated Peralkaline Series

1.6.1 Definition

With the introduction of the term “alkali group” by Iddings (1892), much progress has been attained in recognition, classification and interpretation of the rocks with significant enrichment in alkali constituents. Shand (1922, 1923) pointed out that in igneous rocks alkalis are associated with alumina and silica to from (alkali) feldspar and mica, with the ‘molecular’ ratios $Na_2O + K_2O$: Al_2O_3: SiO_2 = 1:1:6 and 1:3:6 respectively. An alkaline[2] rock, according to the pioneering subdivision of Shand (1922), should be the one in which the alkalis are in the excess of 1:1:6, either alumina or silica or both being deficient.

Setting such solid limits for the definition of alkaline rocks has led them to be divided into three subgroups in consequent years, which can be summarized as in Sørensen (1974):

I. Both silica and alumina deficient: comprising feldspathoids, sodic pyroxene and/or amphibole, eudialyte, alkali feldspar and represented by i.e. agpaitic nepheline syenites,

II. Alumina adequate or excessive, silica deficient: comprising feldspar, feldspathoids, mica, hornblende, augite, corundum, etc. and represented by i.e. mica foyaite,

III. Silica adequate or excessive, alumina deficient: comprising alkali feldspar, pyroxene and/or amphibole, scarce quartz and represented by i.e. alkali granite, pantellerite.

Our studies (see further chapters) depict that Nemrut volcanism comprises of scarce olivine basalts with transitional nature towards abundant silica oversaturated trachytes and rhyolites. Silicic products of Nemrut volcanism, according to the aforementioned discrimination criteria, have a molecular excess of alkalis over alumina (Na + K > Al). The numerical value of this molecular ratio (Na + K / Al) is called Agpaitic Index (A.I.) or peralkalinity (Bowden, 1974), which therefore is greater than unity (A.I. >1) in silica oversaturated peralkaline rocks. Thus, it should be stressed that, Nemrut volcanics with excess silica are termed as peralkaline trachytes / rhyolites.

Pantellerites and comendites, type localities being Isle of Pantelleria and Comende - Sardinia respectively, are the peralkaline equivalents of rhyolites with lower Al and more Fe, Ti and Na

[2] Despite the recommendation of American Geological Institute (1962) that ‘alkalic’ be used instead of ‘alkaline’, the term ‘alkaline’, as stated by Sørensen (1974), regarding its preference by most authors in the literature, will be used throughout this study.

than their calc-alkaline or alkaline equivalents (Bowden, 1974). Although classification between comendites and pantellerites has been somewhat problematic in earlier studies, Macdonald (1974) has recognized significant differences in the distribution of Al and Fe as a function of normative quartz, and therefore, proposed a new, simple and still up-to-date, classificatory scheme based on iron (as FeO) and Al_2O_3 contents.

Peralkaline rocks have always puzzled and fascinated researchers for various reasons: their enormously variable and aesthetic mineralogy, their extreme enrichment of many rare elements, and their complexities of magma source and crystallization paths, which may lead to huge mineralogical diversity despite relatively small major element variations (Markl, 2006).

1.6.2 Occurrences

Salic magmas with peralkaline character are widely distributed in the regions of continental upwelling and/or rifting (Fitton and Upton, 1987) as well as within various geodynamical settings including oceanic islands (Caroff et al., 1993; Mungall and Martin, 1995) island arcs (Mahood, 1981; Civetta et al., 1984, Macdonald, 1987) and continental plate margins (Bowden, 1974). Silicic peralkaline volcanoes typically require moderate rates of extension (Mahood, 1984). Examples include centers associated with continental rifts (Pantelleria; East Africa), local extensional regimes in convergent margins (D'Entrecasteaux Island, Papua New Guinea; Mayor Island, New Zealand), and active or recently abandoned mid-ocean ridge segments (Socorro Island; Azores) (Bohrson and Reid, 1997).

Some brief information on the worldwide occurrences of peralkaline magmatism would help us compare Nemrut volcano and its geological background with the global peralkaline suites. However, given the quaternary geodynamic context, it is consequential to focus on continental settings in order to improve our understanding the possible causes and the development of Quaternary peralkaline volcanism in Nemrut volcano.

1.6.2.1 Peralkaline silicic magmatism in continental rifts

In non-orogenic continental settings, which have undergone crustal swelling and rifting, peralkaline silicic rocks are common (Le Bas, 1971). Peralkaline magmatism can occur during pre-rifting (epeirogenic doming), initial rifting (development of linear fractures and the beginning

of crustal attenuation) and continued rifting (extensive crustal attenuation leaving little or no sialic crust on the rift floor) (Bowden, 1974).

Comendites occur in subvolcanic ring complexes associated with non-peralkaline volcanics during pre-rifting, whereas in rift valleys they are more closely linked with peralkaline trachytes and pantellerites during initial rifting. However, abundance of comendites diminishes and they become virtually absent, and replaced by pantellerites, in well-developed, continued rifts where crustal attenuation is more extensive (c.f. Mohr, 1970; Bowden, 1974). Thus, it should be emphasized that pantelleritic volcanism is directly related to the extent of rifting. However, the more the rift evolves, the less the abundance of peralkaline rhyolites, which are replaced by intermediate basalts between alkaline and tholeiitic nature, and minor trachytes.

Undoubtedly, the largest and the most active intra-continental rift, with significantly greater volumes of volcanic products than other recent active rifts, is Afro-Arabian Rift system. It extends from Jordan in southwestern Asia southward through eastern Africa to Mozambique. The system is some 6,400 km long and averages 48–64 km wide including the Dead Sea (Levantine Rift), Red Sea, Gulf of Aden and East African rifts (Wilson, 1989). It is accepted as an excellent site for investigating all stages and related products of rifting. This huge system is represented by individual subsystems (Main Ethiopian Rift, Central Kenya Rift, etc.) and a wide spectrum of magmatic products from tholeiitic basalts to peralkaline rhyolites / phonolites and even carbonatites. Because of the extensive studies realized, East African rift system represents an indispensable comparison region.

There are several important intra-continental rifts worldwide, Precambrian Gardar province of Greenland, Permian Oslo Graben and Rio Grande Rift of North America being leading examples.

1.6.2.2 Peralkaline silicic volcanism on continental plate margins

Although alkaline rocks such as peralkaline trachytes and rhyolites are generally considered to be characteristic of intraplate magmatism (Bowden, 1974), such occurrences have been documented for convergent margin settings (White et al., 2006).

The best-known examples for this type peralkaline volcanism are located in mid-to-west USA. In the marginal parts of Great Basin, observed peralkaline silicic rocks are represented by lava

flows and ash-flow tuffs with comenditic affinity and with minor pantellerites (Noble et al., 1968). Peralkaline silicic volcanism in this region has been attributed to the overriding of the northeastern Pacific Rise by the North American plate during the Tertiary resulting in pervasive crustal extension and rifting (Bowden, 1974). On the other hand, the development of the Cenozoic peralkaline volcanism has been attributed to changes in plate behaviour after the collision of the East Pacific Rise with a mid-Tertiary continental margin trench causing direct contact of the American and Western Pacific plates along a right lateral transform fault system (Christiansen and Lipman, 1972; Bowden, 1974).

Another site of peralkaline silicic volcanism in North America is Trans-Pecos Magmatic Province. White et al. (2006) (and references therein) propose the tectonic history and associated magmatism: 1) Collision (flat subduction of Laramide plate resulting in lithospheric stacking and orogenic growth). 2) Post-collision or late orogenic relaxation, after the rollback or break-off of subducting slab resulted in astenospheric upwelling, partial melting of lithospheric mantle and crust. 3) Post-orogenic, early stage of continental rifting and astenospheric magmatism, represented by bimodal and peralkaline volcanism because of delamination and the sinking of the detached lithosphere. 4) Relaxation with a clear extensional intra-plate regime and magmatism with a greater influence from the asthenosphere.

1.6.3 Genesis and Evolution

Petrogenetic models proposed to explain the generation of peralkaline felsic magmas include the evolution from alkali basaltic or mugearitic magmas by fractional crystallization (Nelson and Hegre, 1990; Mungall and Martin, 1995; Bohrson and Reid, 1997; Civetta et al 1998), which is probably associated with moderate assimilation of crust (Peccerillo et al., 2003), partial melting of lower crustal gabbros (Lowenstern and Mahood, 1991) and partial melting of heterogeneous source regions, including metasomatized subcontinental mantle (Bailey and Macdonald, 1987) and upper crustal lithologies (Davies and Macdonald, 1987; Macdonald et al, 1987; Black et al 1997). However, no experimental study of crustal anatexis has yet produced peralkaline melts (Scaillet and Macdonald, 2003).

Peralkaline felsic rocks are generally associated with alkali basalts with a lack of intermediate compositions, as a widely observed feature of most peralkaline associations independent of geodynamic settings (Avanzinelli et al., 2004). Although fractional crystallization remains one of

the most satisfactory models for the magmatic evolution from basaltic to peralkaline magmas, the absence or scarcity of intermediate rocks (Daly Gap) and the predominance of silicic (daughter) with respect to mafic (parental) magmas are serious problems (Peccerillo et al., 2003). Despite the number of various processes thought to occur within, a significant consensus is established on ascribing magmatic evolution from mafic to peralkaline magmas and their bimodality to compositionally zoned magma chambers (e.g. Baker, 1987; Peccerillo et al, 2003; Macdonald and Scaillet, 2006).

1.7 Objectives of this Study

In order to investigate and interpret the significance of the causes for, and the development of Nemrut volcanism, the geological background is tried to be portrayed thoroughly in the previous sections. Given the geodynamical context and the geochemical features of Nemrut volcanism, two major points, with distinct particular problematics, need to be examined and discussed in an exhaustive manner. The problems and related studies, into which it is aimed to provide insights, will be discussed in the following subsections.

1.7.1 Problematics with Genesis

Located at East Anatolia, exceptionally active continental collisional site of the Alpine - Himalayan orogeny since the middle Miocene, existence of peralkaline silicic volcanism, just a few kilometers north to the Bitlis - Zagros suture, indicating extensional / rifting settings seems to be anomalous at the first glance. Moreover, Nemrut volcano, situated, represent a remarkable and unique site for studying the genesis and the development of peralkaline volcanism.

Recent multidisciplinary research, combined with neo-tectonic resolutions, revealed an absent or much-thinned lithospheric mantle and the existence of low velocity zones under compressional - extensional tectonic regime. This framework makes Nemrut volcano one of the rare examples of peralkaline volcanoes amongst well-known sites worldwide.

In order to shed light onto the genesis of peralkaline volcanism; magmatological studies including major and trace element geochemistry combined with Sr and Nd isotopic systematics have been performed. Furthermore, several approaches for determining source regions have been implemented. The results obtained have been discussed and have been compared with global occurrences of peralkaline suites.

1.7.2 Problematics Associated with Evolution of Peralkaline Magmas

After some 200 years of study, many particularities of peralkaline rocks are still enigmatic or, at least, lively debated such as: the processes responsible for the variations of melt composition and mineralogy, the influence of intensive variables such as oxygen fugacity on the development of peralkalinity, detailed evolution of peralkaline systems, and, the processes for characteristic textures, mineral assemblages and trace element enrichments (Markl, 2006).

For the purpose of revealing the temporal evolution from basaltic to peralkaline silicic melts, we have realized extensive sampling concerning the volcanostratigraphical relations of all eruptive units from Nemrut volcano. Besides, on eight samples radiometric data have been obtained by K/Ar method being the newest and unpublished ages for pre-caldera and post-caldera products revealing the possible time of caldera collapse. Detailed geochemical and mineralogical properties of each eruptive product regarding the volcanostratigraphy have been discussed.

Petrographical features are depicted thoroughly using both optical and electron microscopy techniques, cemented with elemental mapping using energy dispersive analytics.

In order to identify the importance of intensive variables during magmatic and mineralogical evolution, equations of thermodynamic equilibria, supported by over 1500 mineral microanalyses, have been set to determine the crystallization conditions. Furthermore, estimations crystal – liquid equilibria and elemental activities have been proposed to investigate aspects of crystallization in the magmatic reservoir.

Detailed geochemical modeling regarding the mineralogical, petrographical and thermodynamic data has been realized on both trace and isotopic data with the intention of determining magmatic evolution and petrogenesis of Nemrut volcanism.

1.8 Conclusions

Anatolian peninsula, an important component of the Alpine - Himalayan orogenic system, exhibits complex kinematics throughout its geodynamic evolution. Neotectonics of Turkiye has been described as the convergence and relative motions of Anatolian, Arabian and Eurasian continental plates. Eastern Anatolia represents an incomparable site to investigate the early stages of continental collision and related volcanism. Recent multi-disciplinary research point that most of the East Anatolian plateau is devoid of mantle lithosphere, which is ascribed to break-off of northward-subducted slab beneath East Anatolian Accretionary prism. Widespread volcanism is thought to be related with the direct contact with asthenosphere and melting. Besides, a warm (above solidus), low-density upper mantle beneath the Turkish - Iranian plateau is present. Neogene to Quaternary East Anatolian volcanic products, which cover over the half of the region, display significant compositional variability. Volcanic units of the EKP (Erzurum - Kars Plateau) are calc-alkaline; Bingol and Süphan volcanoes are transitional; Muş - Tendürek volcanoes are alkaline to mildly alkaline.

Nemrut volcano, as the other important volcanic centers of Eastern Anatolia, suffers from the lack of detailed volcanological / petrological investigations. Although there are a number of studies on Nemrut volcanism, unfortunately none of them presented a meticulous examination especially on mineralogical evolution in terms of volcanostratigraphy. Silicic products of Nemrut volcanism have molecular excess of alkalis over alumina (Na + K > Al; Agpaitic Index > 1) and comprised of typical peralkaline mineralogy (i.e. aenigmatite, aegirine, arfvedsonite - riebeckite, chevkinite) representing the peralkaline nature of the volcano.

This study aims to provide deeper insights into several problems of Nemrut volcano being an example for magmatic genesis and evolution of peralkaline magmas:

1) Occurrence of peralkaline magmatism typically requires moderate rates of extension. Regarding its location in a continental collision domain, Nemrut volcano is one of the rare examples of peralkaline volcanoes in convergent margins. Illustrating the possible genesis and the evolution of peralkaline magmatism in Nemrut volcano would contribute to the ongoing studies on regional tectonic regime and geodynamics of Eastern Anatolia.
2) We present petrographical, mineralogical and petrological data of all eruptive units concerning the volcanostratigraphy of Nemrut stratovolcano, in order to contribute to the efforts for revealing complex evolution of peralkaline magmatism. Detailed petrographical

and mineralogical properties of eruptive units have been investigated. Mineral chemistry studies have been realized in order to examine the mineralogical evolution of basic to peralkaline melts. The crystallization conditions of each eruptive unit during the course of magmatic evolution have been determined.

3) Fractional crystallization remains one of the most satisfactory models for the magmatic evolution from basaltic to peralkaline magmas. We present new geochemical data (major - trace elements and Sr-Nd isotopic ratios) of Nemrut volcanism. Several mathematical models have been applied using geochemical as well as mineralogical data, in order to test whether fractional crystallization (combined with crustal assimilation) is the dominant differentiation process.

4) Nemrut volcano, as most of the peralkaline associations worldwide, presents peralkaline felsic rocks associated with alkali basalts with a lack of intermediate compositions (Daly Gap). Besides, predominance of silicic with respect to mafic magmas, as is the case in Nemrut volcano, remains one of the important problems of bimodal peralkaline associations. In this study, we try to explain possible effects of magma chamber dynamics and its intensive state parameters to bimodality of the eruptive products.

5) We present eight new radiometric data for Nemrut volcano. Regarding the volcanostratigraphy, we constrain the age of the caldera collapse.

CHAPTER 02

METHODOLOGY

2 METHODOLOGY

This study has been carried out in two complementary stages, namely field and analytical studies.

2.1 Field Studies

Field studies started in September 2002 and continued for three consecutive summers. A total of 305 representative samples from Nemrut volcano and peripheral eruption centers have been collected. All eruptive products have been mapped, and comprehensive volcanostratigraphy has been established. In 2004, apart from these studies, bathymetric map of the Nemrut caldera lake has been completed using a radar-equipped zodiac boat, which also was used during sampling and mapping of the hardly-accessible western sector of the caldera wall. Several excursions on caldera walls have been carried out in order to observe and sample volcanic stratigraphy.

Sampling

The primary concern was to sample all volcanic units from Nemrut central cone and peripheral eruption centers, including pre-caldera intrusions in caldera walls. Pre-caldera mafic flows (mugearites) are only exposed in a narrow region on the south of the caldera. Felsic pre-caldera units are outcropped virtually on every direction from the caldera. Several expeditions to caldera walls are realized in order to sample pre-caldera lavas. Pyroclastic flows are relatively more abundant in E – W direction. Pyroclastic products have been tried to be sampled equidistantly to the caldera in order to minimize eolian fractionation. The post-caldera rhyolitic samples were collected from domes, lava flows and phreatomagmatic deposits inside the caldera, whereas basalts are sampled outside the north of caldera on the rift zone. Mafic - intermediate enclaves in post-caldera rhyolites are also sampled.

2.2 Analytical Studies

2.2.1 Petrography and Mineralogy

Polarized Microscopy

Covered and uncovered thin-sections of the samples have been prepared at Thin-sectioning and Polishing facility of Hacettepe University Dept. of Geological Engineering, Ankara. Preliminary petrographical studies have been carried out at Petrography Laboratories of Hacettepe University using Leica DM EP and DM 2500P model polarized microscopes. Polarized imagery has been obtained by Leica DFC 420 digital camera systems attached to aforementioned microscopes. Modal abundances of minerals have been obtained by regular point counting method realized using J. Swift semi-automatic point counter.

Electron Microscopy

Electron Microscopy observations have been realized in Electron Microscopy and Microanalysis Laboratories of Hacettepe University (Ankara) using hybrid Cameca SU-30 SemProbe and Zeiss EVO-50 EP scanning electron microscopes equipped with W filaments. Analytical conditions for Secondary Electron (SE) imaging are 10 - 15 kV accelerating voltage, 100 - 300 pA beam current, 1 - 5 μ beam diameter and 25 - 5 mm working distance (depending on the required magnification) on both instruments. Analytical conditions for Backscattered Electron Imaging (BSE) are 12 - 15 kV accelerating voltage, 10 - 15 nA beam current, 3 - 5 μ beam diameter and 16 - 9 mm working distance.

Electron Probe Micro Analyses (EPMA)

Upon the determination of petrographical types and modal mineralogical associations, representative samples of Nemrut volcanism have been selected for further mineralogical - geochemical analyses.

WDS (Wavelength Dispersive Spectrometry)

A total of 54 samples have been selected for Electron Probe Micro Analyses (EPMA). Microprobe analyses were performed on a Cameca SX-100 instrument in Blaise Pascal University, Laboratoire Magmas et Volcans and on a Cameca SU-3o SemProbe in Hacettepe University, Dept Geological Engineering Ankara. The analytical conditions for mineral analyses were set to 15 kV accelerating voltage, 15 nA beam current with 5 μm diameter. Counting times were 10 s for peaks (20 s for Cr and Ni) and 10 s for backgrounds. For glass analyses beam current decreased to 6 nA with the minimum diameter possible (~ 1 μm). In order to minimize the migration effect of alkalis, Na and K were analyzed first. Upon

the acquisition of raw data, ZAF correction procedure has been applied. Calibration standards, analyzing crystals and sinθ values for WDS analyses on each instrument are given in Table 2.1.

Table 2.1: WDS systems, their calibration standards and the diffracting crystals used in mineral analyses; peak positions for each element are also shown.

	Cameca SX-100	**Cameca SU-30**	**Crystal**	**sinθ**
Si	Albite ($NaAlSi_3O_8$)	Albite ($NaAlSi_3O_8$)	TAP	27737
Ti	$MnTiO_3$	TiO_2	LIF/PET	68261/31416
Al	Al_2O_3	Albite ($NaAlSi_3O_8$)	TAP	32463
Fe	Fe_2O_3	Andradite ($Ca_3Fe_2(SiO_4)_3$)	LIF	48083
Mg	MgO	MgO	TAP	38499
Mn	MnTiO3	MnO	LIF	52200
Ca	Wollastonite ($CaSiO_3$)	Andradite ($Ca_3Fe_2(SiO_4)_3$)	PET	38387
Na	Albite ($NaAlSi_3O_8$)	Albite ($NaAlSi_3O_8$)	TAP	46363
K	Orthoclase ($KAlSi_3O_8$)	Orthoclase ($KAlSi_3O_8$)	PET	42765

EDS (Energy Dispersive Spectrometry)

EDS analyses are utilized dominantly for compositional mapping and to a lesser degree for full quantitative mineral analyses (especially for the minerals which bear unanalyzed elements on WDS: i.e. chevkinite) on polished uncovered thin sections. The equipment is Bruker-Axs XFlash 3001 SDD (Silicon Drift Detector) EDS with peltier cooling. Analyses have been realized in full quantitative standardless mode. For a comparison between WDS and SDD-EDS microanalyses refer to Çubukçu et al (2006).

2.2.2 Geochemical Analyses

Sample Preparation

For the sake of precise geochemical analyses, dirt and weathering dust (if present) were removed by compressed air. Then they are crushed into rock chips by hammering. Gravels are further cleaned form dirt by compressed air before they are crushed and milled in agate mortar. Enclaves are separated from the host rock by chipping, trying to prevent any interference of the host rock.

ICP-AES (Inductively Coupled Plasma - Atomic Emission Spectrometry)

Major element (Si, Al, Fe, Mn, Mg, Ca, Na, K, P, and Ti) analyses have been performed at Blaise Pascal University, Laboratoire Magmas et Volcans using Jobin Yvon 70. 200 mg of powdered samples have been molten with $LiBO_2$, and dissolved by HNO_3. Prepared

solutions have been analyzed by the automatic procedure installed in the system. Detection limits and uncertainties at given intervals for major elements have been given in Table 2.2.

Table 2.2: Detection limits for major element analyses for ICP-AES

Major Element Content

Oxides	> 20%	> 10%	> 5%	> 1%	> 0.5%	> 0.2%	>0.1%	Limit %
SiO2	< 1%	-	-	< 10%	-	-	-	**0.20**
Al2O3	-	< 1%	< 3%	-	< 10%	-	-	**0.10**
Fe2O3	-	-	< 1%	-	< 5%	-	-	**0.10**
MnO	-	-	-	-	-	< 2%	< 5%	**0.03**
MgO	-	-	< 1%	-	-	< 10%	-	**0.10**
CaO	-	-	< 2%	< 10%	-	-	-	**0.01**
Na2O	-	-	-	< 2%	-	-	< 10%	**0.05**
K2O	-	-	-	-	< 2%	-	< 10%	**0.05**
TiO2	-	-	-	< 2%	-	-	< 20%	**0.05**
P2O5	-	-	-	< 5%	-	< 10%	-	**0.05**

ICP-MS (Inductively Coupled Plasma - Mass Spectrometry)

Trace element analyses have been conducted in Service d'Analyse des Roches et des Minéraux, CRPG - CNRS- Nancy, France using Perkin Elmer 500 Mass Spectrometer. Detection limits for trace elements have been given in Table 2.3.

Table 2.3: Detection limits for trace element analyses and uncertainties for a given concentration

Trace Element Content

	>100 µg/g	> 50 µg/g	>10 µg/g	> 1 µg/g	> 0.1 µg/g	Limit µg/g
As	-	-	< 7%	< 20%	-	**0.50**
Ba	-	< 5%	< 10%	-	-	**3.00**
Be	-	< 5%	< 10%	< 20%	-	**0.90**
Bi	-	-	< 5%	< 10%	-	**0.05**
Cd	-	-	< 6%	< 20%	-	**0.30**
Ce	-	-	< 5%	< 10%	< 15%	**0.05**
Co	-	< 5%	< 10%	< 15%	-	**0.30**
Cr	-	< 5%	< 15%	-	-	**5.00**
Cs	-	< 5%	< 10%	< 15%	-	**0.20**
Cu	< 5%	< 10%	< 15%	-	-	**5.00**
Dy	-	-	-	< 7%	< 20%	**0.05**
Er	-	-	-	< 5%	< 10%	**0.04**
Eu	-	-	-	< 5%	< 12%	**0.02**
Ga	-	-	< 5%	< 10%	-	**0.13**
Gd	-	-	-	< 6%	< 15%	**0.07**
Ge	-	-	< 5%	< 15%	< 20%	**0.08**
Hf	-	-	-	< 5%	< 10%	**0.04**
Ho	-	-	-	< 5%	< 10%	**0.01**
In	-	-	-	< 5%	< 20%	**0.10**
La	-	-	< 5%	< 10%	< 15%	**0.05**
Lu	-	-	-	< 5%	< 10%	**0.01**
Mo	-	-	< 5%	< 10%	< 15%	**0.15**

	>100 µg/g	> 50 µg/g	>10 µg/g	> 1 µg/g	> 0.1 µg/g	Limit µg/g
Nb	-	-	-	< 5%	-	**0.10**
Nd	-	-	< 5%	< 10%	< 15%	**0.15**
Ni	< 5%	< 10%	-	-	-	**5.00**
Pb	-	-	< 10%	< 20%	-	**0.60**
Pr	-	-	-	< 5%	< 15%	**0.04**
Rb	-	-	< 8%	-	-	**1.00**
Sb	-	-	-	< 5%	-	**0.10**
Sm	-	-	< 5%	< 10%	< 15%	**0.06**
Sn	-	-	< 5%	< 10%	-	**0.50**
Sr	< 5%	-	< 10%	-	-	**4.00**
Ta	-	-	-	< 5%	< 10%	**0.01**
Tb	-	-	-	< 5%	< 10%	**0.01**
Th	-	-	-	< 7%	-	**0.08**
Tm	-	-	-	< 5%	< 10%	**0.01**
U	-	-	< 5%	< 8%	-	**0.10**
V	-	< 5%	< 10%	-	-	**1.50**
W	-	-	< 10%	< 15%	-	**0.10**
Y	-	-	-	< 5%	-	**0.05**
Yb	-	-	-	< 5%	< 10%	**0.03**
Zn	-	< 5%	< 10%	-	-	**4.00**
Zr	-	< 5%	< 10%	< 15%	-	**0.50**

Isotope Analyses

Sr and Nd isotopic ratios have been determined at Laboratoire Magmas et Volcans in Clermont-Ferrand, France using VG Sector 54E multicollector and Triton mass spectrometers. For $^{143}Nd/^{144}Nd$ isotopic ratios of 5 samples have been analyzed by VG 54E. For these runs, Nd isotope ratios were normalized to AMES $^{143}Nd/^{144}Nd = 0.511953 \pm 0.000009$ (2σ). 5 samples have been analyzed by Triton. For these runs, Nd isotope ratios were normalized to AMES $^{143}Nd/^{144}Nd = 0.511959 \pm 0.000009$ (2σ). Sr isotope ratios of 5 samples have been analyzed by VG 54E and were normalized to NBS 987 $^{87}Sr/^{86}Sr = 0.710266$ and precision (2σ) is better than ± 0.000017.

2.2.3 K-Ar Dating

Radiometric analyses have been realized on eight samples representing the volcanological history using K-Ar methodology. Analyses have been performed at "Laboratoire des Sciences du Climat et de l'Environnement" - Unité Mixte de Recherche CEA - CNRS, in Gif-sur-Yvette, France.

Sample Preparation

Selected samples have been crushed, ground and sieved to 0.25 - 0.125 mm size fraction and washed by HC_2H3O_2 in ultrasonic cleaner. Groundmass of the rocks has been separated according to Guillou et al. (1998). Phenocrysts and xenocrysts were removed from the groundmass using density (with heavy liquids) and magnetic separation methods. K was analyzed by atomic emission spectrometry in Blaise Pascal University. For Ar extraction and analysis methods see Guillou et al. (1998). The isotopic composition of Ar and the total Ar content were determined using an unspiked K-Ar technique (Cassignol et al., 1978; Guillou et al., 1998). For calibration reference materials, analytical procedure and the settings of the mass spectrometers used refer to Guillou et al. (1998) and references therein.

2.3 Data Handling

Although the primary goal of this study is to introduce the previously unpublished petrologic features of Nemrut volcano and to propose possible magmatological evolutionary steps, this thesis greatly benefits from the fertile realms of modern digital era. Beginning from our first step onto the Nemrut volcanic field, a plethora of digitally acquired data supported by human judgment, have been the driving force for reaching our goals. However, the more digital we have chosen to be, the bigger the ocean of petrologic data we had to swim across. In the field, we record our locations on GPS, take loads of digital photographs, write down the observations on notebooks, taking samples, drawing sketches; in the laboratory, we again take heaps of pictures, acquire tremendous amount of mineralogical/geochemical data. And also we need to synthesize much more data from what we have previously obtained. Finally, we do spend much longer time for re-organizing them, in fact longer than for acquiring.

Although we believe that modern day computerized technology would ease our loads, it is somehow enigmatic not to be able to find a complete solution for integrated petrologic interest. There are, of course, lots of valuable specific tools we frequently utilize. MELTS family for modelling magmatic processes, Igpet or GCDkit for plotting diagrams and basic geochemical modelling, QUILF for mineral equilibria and intensive parameter calculations, a great number of available Excel spreadsheets for numerous purposes, and the list goes on and on. Although we do not feel desperate about plotting geochemical diagrams thanks to easy-to-handle digital graphics, it can not be deniable that we do not have as much resources for integrated mineralogical and geochemical calculations.

Problems arise when it is intended to compare a mineral analysis with another one which is in another rock. Maybe comparing that “specific mineral” with any other geochemical data in anywhere would be the breaking point of the study. Is plotting on special diagrams adequate? Consider a sample set of 50 rocks. Let’s imagine that each sample has all the major and trace element analysis, isotopic systematics, age data, CIPW norms, modal mineralogy, intensive crystallization parameters. That makes roughly 120 fields of data for each sample. Furthermore, the question is what if each rock has an average of 40 microprobe analyses? We would need to know every minute detail for each microanalysis: The mineral name, type of the crystal, location of the analysis, state of equilibrium, whether it is an inclusion, or it is in an enclave? Combined with the chemical results, that would make 25 data fields for each microprobe analysis. This each 40 mineral analysis should be governed by the nominal rock chemical data in order to

reveal mineral-liquid equilibria. A radical proposition could be to make a gigantic table to put each mineral analysis in a row with the nominal bulk rock data. Only this would make a ([40x50] x 120) sized table. What if we want to review the geographical distribution, stratigraphical position...? Could we enlarge our table? This is neither economic nor wise.

I, during my studies, have faced all these kinds of irritating problems. In order to overcome them, I have spent pretty much time establishing the database approach to handle and integrate the complete data for various applications.

Databases, or collections of related data, can provide a tool that aids geologists to extract information from datasets (Giles, 1995). As long as the collection of data is logically coherent with some inherent meaning, it is a database (Elmasri and Navathe, 1989). The function of a database is to organize a volume of data and to make it accessible so that it becomes information (Giles, 1995).

2.3.1 Nemrut Petrology Database (NPD)

Nemrut Petrology Database (NPD) has been built with the intention of providing a basis for digital data integration with various processing environments. In order to be convenient and flexible, Microsoft Access has been operated. Each data type has been stored in tables, as in Microsoft Excel. But, the leading goal of building a database is to associate specific relationships between these tables. Hence, identifying the relationships between data tables is particularly important, as an operational database principally depends on well-defined relationships. NPD is modeled using Entity-Relationship (ER) approach. The information types in the ER model are defined by three main concepts (Rasmussen, 1995):

- **Entities** (or tables of things) about which information is expressed
- **Attributes** (or properties) of entities which express information about entities
- **Relationships** which are meaningful association between entities

In fact these terms could be simply regarded as analogous components of a table. Attributes and records would represent the columns and rows of the entity, which is the table itself (Figure 2.1).

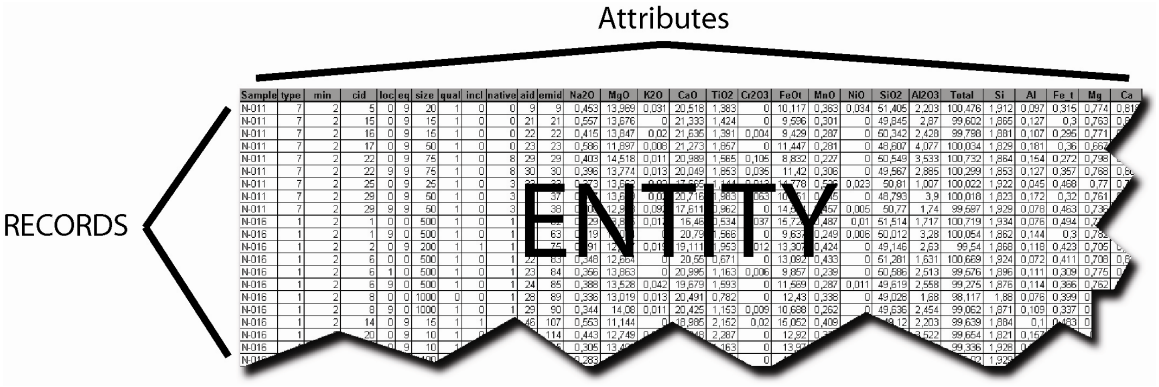

Figure 2.1: A sample entity and its components

An entity or a table of information is related to another by the help of “primary keys”. The power of a relational database system such as Microsoft Access comes from its ability to quickly find and bring together information stored in separate tables using queries, forms, and reports. In order to do this, each table should include an attribute or set of attributes that uniquely identifies each record stored in the table. This information is called the primary key of the table (for more information see: Microsoft Access Help).

Although it is clearly beyond the scope of this study to examine and define all the components and inter-entity relationship types contained in NPD, it is crucial to introduce some basic entities and attributes as they are frequently referred throughout the text and the appendices.

2.3.2 Primary Entities of NPD

There are over 30 entities used in NPD, however some particularly important ones and their attributes are listed below:

Sample List: This table contains the basic information on samples. It includes the “Sample No” field (attribute) as the primary key representing the bridge for the separate tables (entities) which contain information for respective samples. This table (entity) also comprises the lithological description, geographical coordinates and the analyses realized for each record (sample). To sum up; samples represent the records while all information listed above correspond to respective attributes.

Microprobe: This table contains raw data of realized microanalyses. It contains major oxide data of analyzed minerals. Besides all records have been defined by several attributes which are vital

to some extend. Emid stands for unique “Electron Microprobe ID” of each record and is used as the primary key for this table and the other mineralogical tables (Mineralogical Entity Suite, see below). Besides, mineral species, analyzed crystal, location of the analysis, state of equilibrium and size (ø) of the analyzed crystal are described in the contained attributes.

Mineralogical Entity Suite: It is composed of nine tables containing namely Feldspar, Pyroxene, Olivine, Amphibole, Magnetite, Ilmenite, Amphibole, Aenigmatite and Glass analyses. They contain cationic distribution and calculated end-member data of each record as well as descriptive fields for each record. Emid is used as the primary key.

ID: Stores the two basic types of attributes for mineralogical and/or chemically analyzed records. These attributes are SID (Stratigraphic ID) and PID (Petrologic ID).

SID represents the stratigraphical positions of each unit which are discussed thoroughly in the following chapters. It has been used only for representative indexing and subdividing the whole volcanic suite into comparable portions. It has no geological meaning at all.

PID, although not mentioned frequently in the subsequent chapters to prevent complexity, is used for discrimination between petrological types of the eruptive units. Table 2.4 depicts the PIDs and their correspondences. Sample No is used as the primary key.

Table 2.4: PIDs and their correspondences in NPD

TAS Classification	**McDonald Classification**	**PID**	
		Pre-Caldera	Post-Caldera
Basalt		4060	8060
Mugearite		4010	8010
Benmoreite		4080	8080
Trachyte	*Comenditic*	4031	8031
	Pantelleritic	4035	8035
	Metaluminous	4039	8039
Rhyolite	*Comendite*	4021	8071
	Pantellerite	4025	8075

Age: K/Ar ages of eight records. It contains measured ages and error intervals. Sample No is used as the primary key.

Modal: Stores information of point count analyses with the attributes of actual minerals, groundmass and/or glass percentages. Sample No is used as the primary key.

Norm: Stores calculated CIPW normative mineral contents.

Geochemistry: It is one of the most frequently used entity as it stores major and trace element contents as well as Sr and Nd isotopic ratios. Calculated Agpaitic Indices are also contained. Furthermore, this entity encompasses nearly all the published geochemical data for Nemrut volcanic rocks compiled from literature. Sample No is used as the primary key.

Thermo: It stores calculated intensive crystallization parameters obtained by thermodynamic calculations via MELTS, QUILF etc. Sample No is used as the primary key.

2.3.3 Relationships between Entities

As it has been stated before, the power and the usability of the database strongly depends on the defined relationships between these entities listed above. Figure 2.2 illustrates these tables and their relationships. Basically there are two types of relationships used in NPD: a) One-to-One and b) One-to-Many.

One-to-One relation is used when the primary keys of the separate entities are same and unique. For example, Sample No attribute is used as primary key in Geochemistry and ID tables. Thus, for a record in Geochemistry table, there is only one record in ID table. Hence, given the Sample No, we would acquire the ID of only that sample. For this reason, such relation between entities is used when there is only one record for any given sample in any table. Similarly Emid represents only one record both in microprobe table and mineralogical entity suite.

On the other hand, one-to-many relation is used when there are multiple records for a given key in separate tables. For instance, although Sample No attribute holds for only one record in geochemistry table, it corresponds to tens of records in microprobe entity, as there is more than one mineral analysis for that sample.

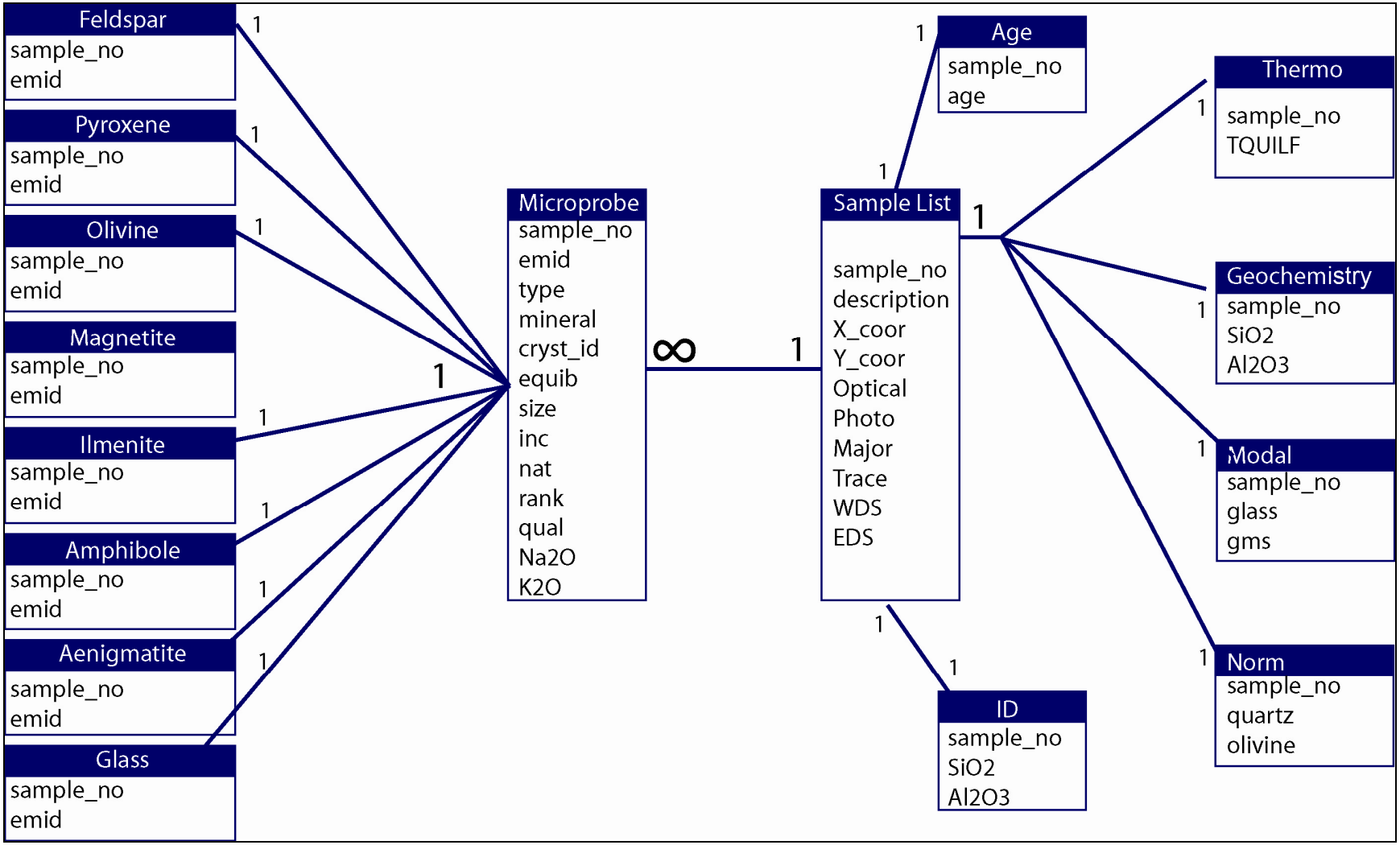

Figure 2.2: Relationships between entities in NPD. Lines with 1 in both ends represent one-to-one, while ∞ in one end represent one-to-many relationships

2.4 Data Integration

The mot significant advantage of using a database is to be able to create custom datasheets comprised of information stored in separate entities. For this purpose, queries are used. A select query is the most common type of query. It retrieves data from one or more tables and displays the results in a datasheet where it can be used to update the records (with some restrictions). Besides, using a select query to group records and calculate sums, counts, averages, and other types of totals is possible (for more information see: Microsoft Access Help).

Furthermore, SQL (Structured Query Language) is used in any software which supports accessing the relational Nemrut Petrology Database. Hence, within data processing software such as MATLAB or ARC family, it is possible to access NPD and retrieve purpose-specific datasheets.

MATLAB has been extensively used to process and synthesize obtained data in NPD thanks to its SQL capability. Custom tables such as for geochemical comparisons between mineral and whole rock data have been created relatively easily. Besides, geographical distribution of geochemical properties can be easily plotted on surface maps using ARC environment.

2.5 Conclusions

In order to overcome the problems while evaluating the extensive amount of digital data obtained, Nemrut Petrology Database has been created as a basis. It represents an easily accessed medium which is used thoroughly by the data processing platforms. Hence, a database approach in petrologic studies would shorten the time spent interpreting and minimize the efforts assessing and synthesizing the digital geological data.

CHAPTER 03

VOLCANIC EVOLUTION OF NEMRUT DAGI

History never looks like history when you are living through it

John W. Gardner

3 VOLCANIC EVOLUTION OF NEMRUT DAGI

The region of interest for this study encompasses the metamorphic basement rocks, overlain by Tertiary sedimentary units and Quaternary Nemrut volcanics (Figure 3.1). In order to provide deeper insights into the regional geology, pre-volcanic rocks will only be presented briefly. Quaternary volcanics of Mt. Nemrut and their stratigraphical relationships will be the focus of this section and will be investigated thoroughly.

3.1 Pre-Volcanic Basement

Although the stratigraphy of the basement rocks in the area is well known, predicting exactly what the basement rocks are beneath becomes difficult since they have been structurally disrupted since the Mesozoic (Gunderson, 1988). The oldest crustal rocks comprising the basement are the Palaeozoic - Mesozoic Bitlis Metamorphics. Bitlis Metamorphics are outcropped along the steep mountains of the southern margin of Muş basin (Atasoy et al, 1989). They are also observed at scarce outcrops at the south of Nemrut volcano, near Tatvan city and the surrounding area. Bitlis metamorphics, whose thickness is presumed to be more than a few kilometers, consist of amphibole - biotite gneiss, chlorite - schist, meta-quartzite, recrystallized carbonate rocks and marble (Atasoy et al, 1989). Commonly thrusts on top of the Bitlis Metamorphics are Cretaceous ophiolitic rocks (Çatak Ophiolite; Atasoy et al, 1989), which were emplaced during compressional events of the Eocene and Miocene (Gunderson, 1988). These ophiolitic rocks typically include serpentinites, greenschists, cherts, micrites, limestones and graywackes (Gunderson, 1988). Exposure of this unit is confined to ~ 20 km north of Nemrut and to the vicinity of Ahlat city. Cretaceous ophiolitic units are overlain unconformably by the Tertiary sedimentary sequence. These sedimentary rocks are thought to be deposited in small, usually E - W elongated basins that were opened between the Eocene and Miocene (Gunderson, 1988). They are comprised of sandstones, mudstones and carbonates with lacustrine and coarse-grained fluvial deposits. Moreover, outcrops of the unit, located east and north of Nemrut, include Eocene - and Oligocene conglomerates and sandstones, Miocene limestones and Pliocene lacustrine deposits (Gunderson, 1988).

3.2 Quaternary Volcanics

3.2.1 Regional Geology

Nemrut stratovolcano, which culminates at 2948 m, is located at the southwestern tip of Lake Van on the Rahva plains of eastern Muş Basin and bounded by mountainous units of Bitlis metamorphic massive in the south, and by Ahlat plains in the north (Figure 3.1). Nemrut volcano is formed close to the northern marginal thrust fault of the basin. Reverse fault systems is thought to extend into Lake Van (Atasoy et al., 1989). Besides, it has been proposed that the formation of the volcano on a palaeo-watercourse (Karasu River) valley as a natural dam has led the formation of Lake Van inhibiting water discharge (İlhan, 1968). According to the gravity studies realized during geothermal surveys, this valley represents an asymmetrical depression basin, which rotates towards north at the eastern flank of the volcano due to the prevailing N-S compressional tectonic regime (UNOCAL, 1988; Atasoy et al., 1989). Muş basin seems to still retain its earlier nature of ramp basin, although its northern margin-bounding reverse fault has a considerable dextral strike slip component since Pliocene (Koçyiğit et al., 2001).

Nemrut volcanic system is comprised of polygenetic Nemrut stratovolcano and concentric monogenetic dome systems (Figure 3.1). Nemrut volcano exhibits an elliptical summit caldera with 8.5 x 7 km diameters. The eastern half of the caldera is filled by post-caldera pyroclastic deposits related to maar-like explosion craters, lava domes and flows (Figure 3.2., Aydar et al., 2003). The western half of the caldera is filled with a fresh water lake (5 x 3 km), with a maximum depth of 176 m, revealed during our bathymetric surveys. Besides, there is a small shallow hot lake (Ilığ Göl) with hot springs located at the northern basal rim of the caldera with a maximum depth of 11 m (Figure 3.2.). Fumarolic activity is observed in the cracks of an intra-caldera lava dome. Helium isotope ($^{3}He/^{4}He$) ratios indicate an almost pure mantle He is being emitted in Nemrut caldera (Güleç et al., 2002).

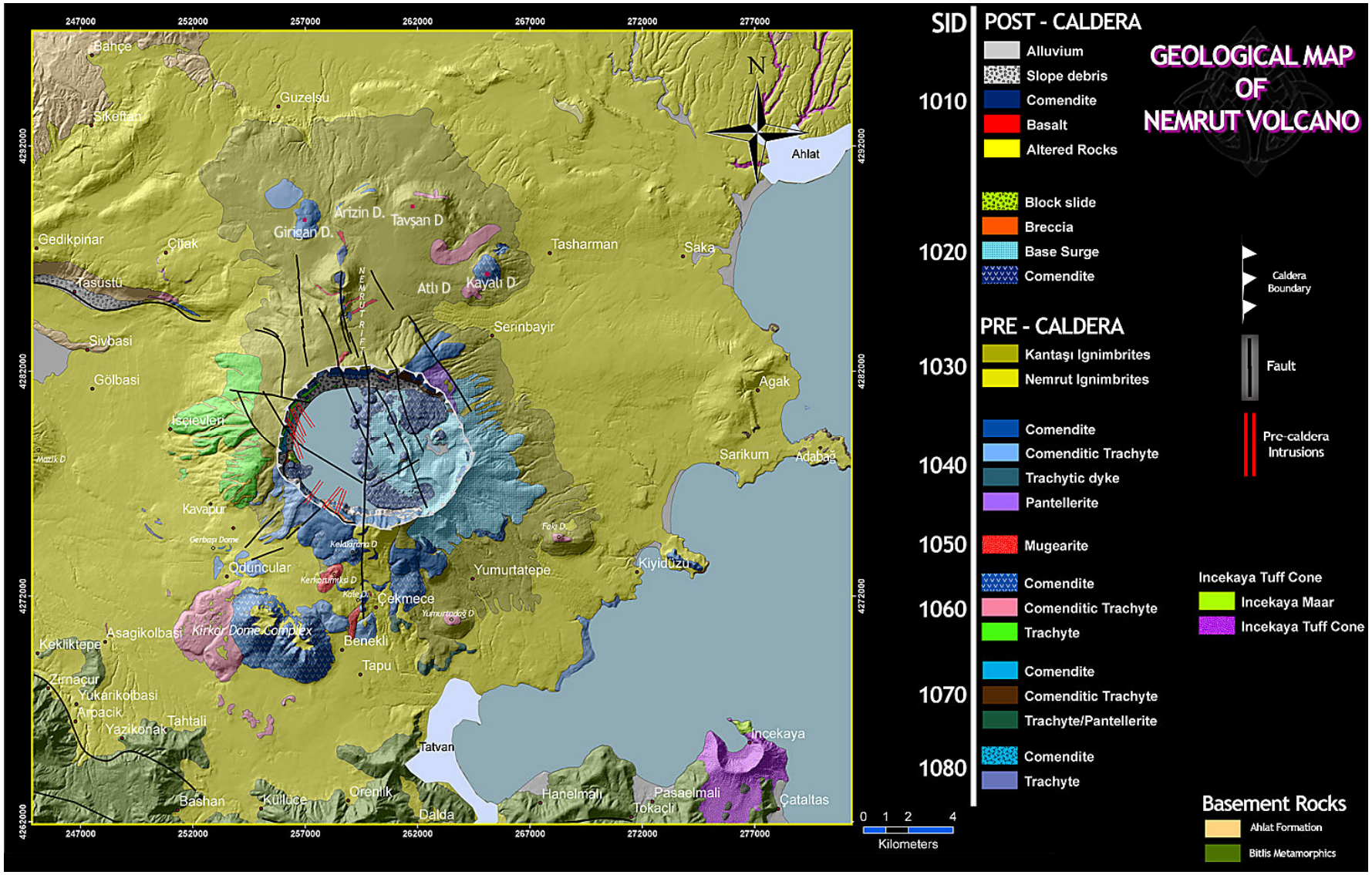

Figure 3.1: Geological Map of Nemrut Volcano

Figure 3.2: Overview of Nemrut Caldera from North

Extra-caldera peripheral eruption centers display a somewhat circular alignment around the Nemrut volcano. Such distribution reminds of a radial exposure of volcanism and / or prevailing ring fractures above the magma chamber. However, as all these extra-caldera domal eruption centers are formed before the caldera collapse and overlain by thick pyroclastic cover, no further structural evidence of such a relationship can be acquired by mere field observations. The structural relationships between these domes, which are highly likely to occur, will not be discussed in this study. However, such distribution could reflect the spatial extend of which magmatic reservoir could reach. To the north of the Nemrut volcano, Nemrutbaşı, Tavşan, Arizin and Girigan domes; to the northeast, Atlı, Mezarlık, Kayalı domes; and to the east, Meşelik, Fakı, Yumurta domes are somewhat located in a semi-circular pattern. Kalekirani and Kale domes are in the south of the volcano. Although these secondary eruption sites outnumber in the southern and eastern side of the volcano, there are larger scaled significant domes in the west. These are Kirkor dome complex in the southwest and Germav and Mazik domes in the east. Besides, İncekaya tuff cone, although located at the opposite shore of Lake Van, is regarded as a component of the Nemrut volcanic system (Figure 3.1).

3.3 Volcanic Stratigraphy of Nemrut

Volcanic evolution and interrelations of volcanic units of Nemrut volcano have been a subject of debate since the introductory study of Özpeker (1973). Detailed geothermal investigation of TPAO (Turkish Petroleum Corporation) and UNOCAL has led the researchers to divide volcanic evolution of the Nemrut Stratovolcano into four stages, namely pre-cone, cone building, caldera-forming and post-caldera stages (Atasoy et al., 1989). Some ten years later, despite a number of studies on the volcano (e.g. Ercan et al., 1990, Pearce et al., 1990, Notsu et al., 1995) volcanic stratigraphy of Nemrut volcanism was still unpublished. However, Yılmaz et al. (1998) proposed pre-cone, cone building, climactic, post-caldera and late

phases as the major volcanic episodes in the development of Nemrut volcano. On the other hand, Aydar et al. (2003) suggested two main evolutionary stages cut by the paroxysmal eruption leading to the caldera collapse: pre-caldera and post-caldera stages. Furthermore, they have subdivided the pre-caldera stage into construction and destruction phases. Conversely, Karaoğlu et al. (2005) and Özdemir et al (2006) proposed somehow ambiguous evolutionary stages: pre-caldera, post-caldera and late stages. Furthermore, the criteria for such discrimination were unclear and the solid volcanological perspective is lacking (c.f. Çubukçu et al., 2007).

In this study, the volcanological evolution of Nemrut volcanism will be investigated under two main stages: Pre-caldera and post-caldera stages. Pre-caldera stage is comprised of building of the volcano and peripheral eruption centers followed by the caldera collapse due to the paroxysmal caldera forming ignimbrite flows. Post-caldera stage includes the intra-caldera activity and the bimodal rift volcanism on the northern flank of the volcano. Modern volcanic activity of Nemrut has been defined in numerous historical records (c.f. Karakhanian et al., 2002; Aydar et al, 2003)

Volcanostratigraphic studies are supported by new geochronological (K/Ar) analyses realized on eight representative samples (Table 3.1). Related analytical procedures have already been given in Chapter 2.

Table 3.1: K/Ar ages of samples from Nemrut volcano. Age calculations are based on the decay and abundance constants from Steiger and Jäger (1977). (*) indicates the suspicious analysis of mugearite.

Sample	Weight molten (g)	K (wt. %)	$^{40}Ar^{*}$ (%)	$^{40}Ar^{*}$ (10^{-13} mol/g)	Age ± 2σ ka
N-238	1.26988	4.203 ± 0.042	14.477	19.007	
	1.57533	4.203 ± 0.042	12.734	19.379	264 ± 6
N-149	1.53223	3.868 ± 0.039	18.025	10.586	
	1.08822	3.868 ± 0.039	10.14	10.719	158 ± 4
N-98	1.01908	3.852 ± 0.039	7.72	7.081	
	1.49449	3.852 ± 0.039	7.555	6.341	99 ± 3
N-181	1.08036	4.059 ± 0.041	4.734	6.317	
	1.15475	4.059 ± 0.041	2.927	6.878	93 ± 3
N-80	1.17125	4.284 ± 0.043	11.159	6.719	
	2.35809	4.284 ± 0.043	7.915	6.561	89 ± 2
N-51	0.96572	3.873 ± 0.039	1.28	0.79	
	2.60063	3.873 ± 0.039	2.513	1.005	15 ± 1
N-305	0.94719	3.686 ± 0.037	0.145	0.611	
	1.08099	3.686 ± 0.037	0.072	0.404	8 ± 3
N-209*	1.22361	1.992 ± 0.020	0.126	0.277	
	1.08205	1.992 ± 0.020	0.056	0.162	7 ± 4

Throughout its evolution, Quaternary Nemrut volcanism produced volcanics with similar geochemical affinities (Table 3.2). A synthetic table (Table 3.2) depicting rock types, age intervals, respective SIDs (Stratigraphic ID) and representative samples has been given. Vast majority, by both volume and superficial distribution, of volcanics are acidic. In addition, glass-rich silicic lavas and domes represent the prevailing rock type, excluding the widespread ignimbritic flows. Silicic volcanism dominates both in pre- and post-caldera stages. However, there are minute basic lava flows observed both before and after the caldera collapse. Despite the abundant felsic and rare mafic rocks, there is a significant lack of intermediate compositions (Daly Gap). Bimodality of the consecutive eruptive units is perfectly exposed in post-caldera historical fissural activity where rhyolites overlie coeval basalts.

Since silicic Nemrut volcanics dominate the volcanic activity and represent similar geochemical / lithological properties, proportion of total alkali to alumina content, in other words degree of peralkalinity would be a better discriminating parameter for distinguishing the lava types and for the nomenclature. Hence, from hereafter, the nomenclature of the volcanic units will be based on nominal geochemical compositions. For all of the erupted products, Total Alkali versus Silica diagram (TAS, after Le Bas et al., 1986) will be utilized. Additionally, for peralkaline {*Agpaitic Index (molecular* $Na_2O + K_2O$*) >1*} silica rich (SiO_2 > 64 wt %) rocks, FeO* versus Al_2O_3 diagram will be used. Thus, it will be a better practice to refer to Table 6.1 and Figure 6.1 given in Chapter 6 for a better comprehension.

The evolution of volcanism, associated volcanic events, nature of eruptive products and the key features are depicted on a volcanostratigraphic timeline, a synthetic illustration of the Nemrut volcanism (Figure 3.3). In addition, our new radiometric data are presented with available former data as well.

Table 3.2: Synthetic table depicting rock types, age intervals, respective SIDs (Stratigraphic ID) and representative samples

Rock	Type	Age Interval	SID	Representative Samples
Comendite with Benmoreitic Enclaves		~ 500 BP		N-011, N-257
				N-256
Basalt	Lava/Dome Flow		1010	N-010
		8 ka		N-305
Comendite	Phreatom.		1020	N-051, N-065
		~15 ka		
Trachyte	Ejecta	< 30 ka		N-272, N-220
	Kantaşı Ignimbrite		1037	N-009, N-259, N-062
	Plinian Airfall		1036	N-036
Trachytic Pyroclastic Units	Nemrut Ignimbrite	90 - 30 ka	1035	N-233, N-248
			1034	N-023, N-179
			1033	
	Plinian Airfall		1032	N-247, N-268
			1031	N-046, N-020
Comenditic Trachyte	Lava/Dome Flow	100 - 90 ka	1040	N-080, N-181
Comendite / Pantellerite				N-227, N-194, N-098
Basalt ??		~ 100 ka	1050	
Mugearite	Lava Flow			N-016, N-209
Comenditic Trachyte / Comendite	Dome	300 -160 ka	1060	N-239, N-149
Trachyte	Lava Flow			N-136
Comenditic Trachyte / Comendite	Lava Flow	570 -300 ka	1070	N-186, N-281, N-135
Pantelleritic Trachyte				N-184, N-188
Rhyolite		1.0 Ma - 570 ka	1080	
Trachyte	Lava Flow			N-141, N-299

1030

1345

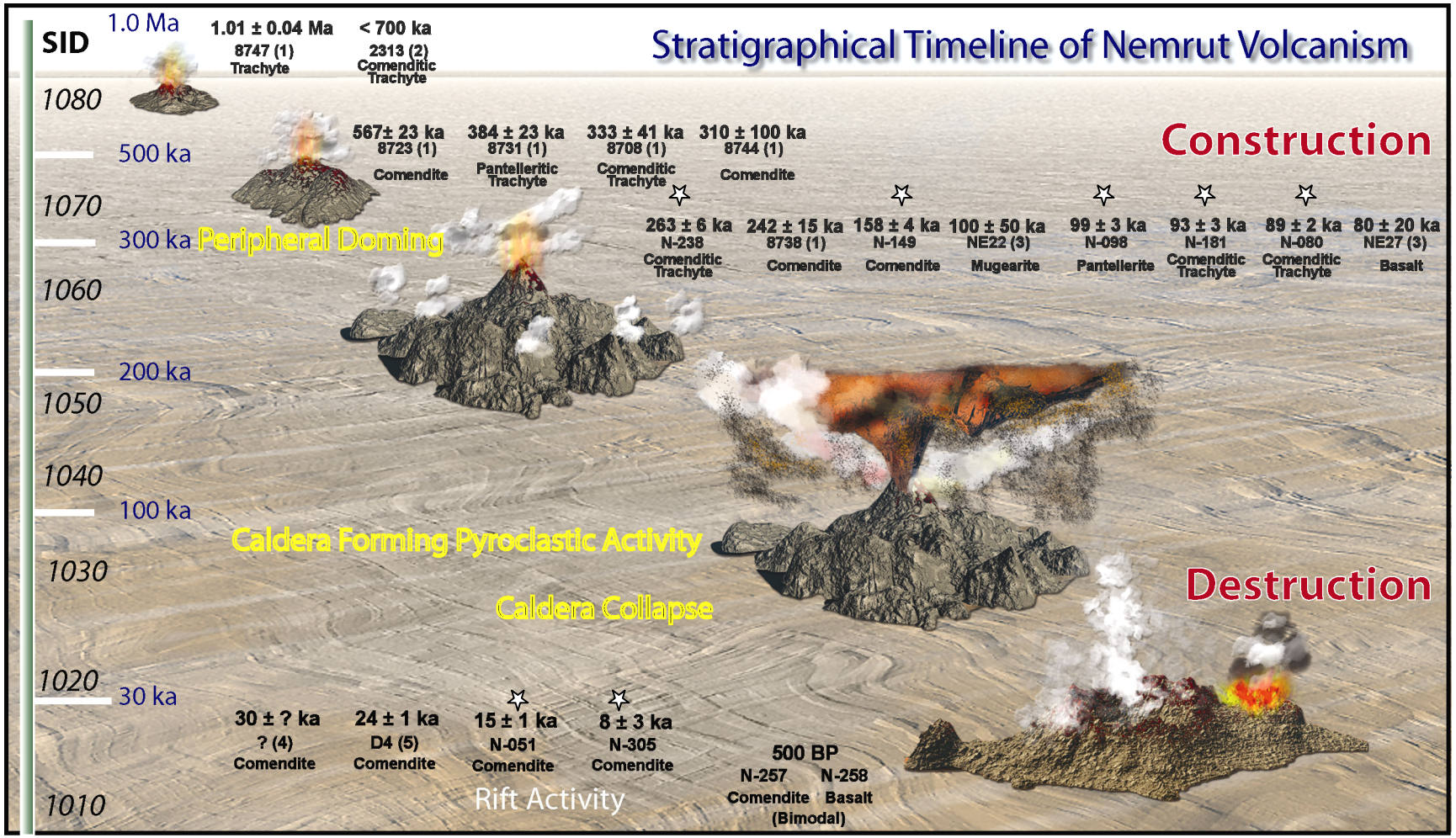

Figure 3.3: Stratigraphical timeline of Nemrut volcanism. Sources for K/Ar ages are (1) Atasoy et al., 1989 (2) Pearce et al, 1990 (3) Notsu et al, 1995) (4) Matsuda, 1988 (5) Ercan et al., 1990. Also given are the respective sample numbers and rock names. SID represents Stratigraphic ID. Analyses marked with stars have been obtained during this study.

3.3.1 Pre-caldera Stage

It has been suggested that the oldest volcanic products of Nemrut volcanism were fissure basalts (e.g. Özpeker, 1973, Güner, 1984, Atasoy et al., 1989, Karaoğlu et al., 2005, Özdemir et al., 2006) located in Bitlis Valley, some tens of kilometers south of the Nemrut volcano. However, during our field studies, we could not observe a solid relationship between these basaltic flows and the Nemrut volcanic system. Furthermore, Ercan et al. (1990) proposes a different fissural basaltic origin than Nemrut for these volcanics observed in Bitlis valley, which conforms to our observations. Hence, we suggest that these relatively older (<2.5 Ma; Ercan et al., 1990) Bitlis valley basalts should not be investigated under Nemrut volcanic system, although they present similar geochemical properties with the basaltic units of Nemrut (i.e. Ercan et al., 1990).

Pre-caldera products of Nemrut volcanism, prior to the caldera forming eruptions, are dominantly comprised of silica oversaturated trachytes and rhyolites. Nevertheless, there are scarce outcrops of basaltic trachyandesite (mugearite) and metaluminous trachytes. Caldera forming pyroclastic sequence comprised of silica oversaturated (quartz normative) metaluminous trachytes, although they indicate a chemically zoned magmatic reservoir significantly in terms of mineralogical compositions which will be discussed in the subsequent chapters.

~ 1.0 Ma – 500 ka

The oldest known volcanic units of Nemrut volcanism are metaluminous felsic rocks (*Stratigraphic ID*, *SID: 1080*) exposed on the southern and southwestern flanks of the volcano. They are exposed typically in the south of Kavapur village in the west and at the western escarpments of Gerbaşı dome (Figure 3.1). They yield K/Ar age of 1.01 ± 0.4 Ma on a sample (Atasoy et al., 1989) taken from the western flank of the volcano. Furthermore, this unit is exposed on the western wall of the caldera (Figure 3.3). However, lower lithological boundary of the unit could not be observed. Therefore, it would not be viable to state whether volcanism has initiated during this activity or not. Nevertheless, this age signifies the lowest limit of temporal space of Nemrut volcanic history, sampled and discussed throughout this study.

According to their K/Ar ages (< 0.79 Ma), Atasoy et al. (1989) suggest trachybasaltic (hawaiite) flows follow the oldest trachytes. Their sample, on which geochronological analysis has been realized, was taken from Bitlis valley, ~ 45 km away from the central volcano. Although they associate these distant basic lava flows with the ones exposed on the

southern flank of Nemrut (Figure 3.1), our field studies could not depict such solid relationship between these two lavas. As we have mentioned earlier, Ercan et al (1990) propose that the basaltic lava flows outcropped in Bitlis valley are unrelated with Nemrut volcanic system. Besides, in their recent paper, Özdemir et al (2006) advocate that these basalts are the first effusive products of pre-caldera stage of Nemrut volcanism, relying on their single sample (BD-3) taken ~ 40 km away from the central vent. Considering the fact that effusive products and peripheral eruption sites of Nemrut volcanic system are distributed within an area with ~ 20 km radius, associating these trachybasaltic units solely with Nemrut system is not practical.

Pearce et al. (1990) report a relatively younger age (< 700 ka,) for a trachytic sample and Atasoy et al. (1989) state a K-Ar age of 567± 23 ka for a rhyolite sample taken from western caldera wall (*SID: 1080*, Figure 3.4). These rocks are the oldest known peralkaline silicic units of Nemrut volcanism. They are exposed on the western caldera wall forming blocky rare outcrops on the basal rim (Figure 3.4). They are poorly porphyritic (feldspar-phyric) with microcrystalline groundmass. Imprints of alteration were observed along the centimeter - decimeter sized cracks on the blocks.

Figure 3.4: Western caldera wall. Pre-caldera felsic lava flows are depicted with their respective stratigraphic IDs (SID) as given in Table 3.2

Although it was hard to collect samples representing the activity between 1.0 Ma and 500 ka due to the lack of their extra-caldera outcrops and steepness of caldera walls, we claim that volcanism produced more alkaline lavas with time: From metaluminous to peralkaline trachytes and rhyolites. However, it should be noted that future meticulous sampling from the western and southern caldera walls, would provide a better understanding for the volcanic activity between ~ 1 Ma and ~ 400 ka.

500 – 100 ka

Volcanic activity seems to be intensified and central cone is believed to be formed during this period. Outcrops of cone-building lava flows (SID: 1070) are observed on southern and western walls of caldera and on the extra-caldera regions of respective directions. Moreover, they are observed up to 15 km to the east of central cone, forming topographically evident lava fronts and the Adabağ peninsula in the Lake Van (Figure 3.1).

Atasoy et al. (1989) report three K-Ar ages of samples collected from south (sample 8731), east (sample 8708) and southwest (sample 8744) of the central cone. They yield 384 ± 23 ka; 333 ± 41 ka and 310 ± 100 ka, respectively. These lava flows (*SID: 1070*) exhibit stratigraphical, thus temporal evolution from trachytic to rhyolitic compositions. They are moderately porphyritic (feldspar-phyric) with crystalline-microcrystalline groundmass. However, glassy bands and lenses are frequently observed as interbedded with lavas. These hypo-holohyaline bands could represent the “frozen skin” covering the lava flow. On the other hand, these lavas are also observed to form massive flows with blocky and columnar jointing. They are greenish dark gray in color and could attain reddish spots due to the alteration of ferromagnesian phases in the groundmass.

These lava flows are marginally-to-moderately peralkaline. The oldest known lavas (384 ± 23 ka) of 400 - 300 ka timespan are the more peralkaline trachytes being pantellerite in composition. Marginally peralkaline (comenditic) trachytic lava flows (333 ± 41 ka) are followed by peralkaline rhyolites (comendite) (310 ± 100 ka). However, it must be noted that possible error intervals for these three dates are getting larger towards more evolved compositions, implying that these flows might be coeval.

Nemrut volcanism continued to produce trachytic lavas (*SID: 1060*) after ~ 300 ka. On the western caldera wall and along the Gedikpınar rise, ~ 10 km northwest of the cone, slightly metaluminous to marginally peralkaline lavas are observed. One weakly peralkaline comenditic trachyte sample from Gedikpınar rise (N-238) yielded K-Ar age of 264 ± 6 ka.

Lavas observed especially on the Gedikpınar rise, contain slightly darker and vesicular cognate inclusions, without any evidence of reaction or significant mineralogical/geochemical discrepancy (see further chapters, Figure 3.5.). These trachytes are dark grey and poorly porphyritic with microcrystalline groundmass. On the caldera wall sections of the unit, glassy lenses are observed.

Figure 3.5: 264 ka comenditic trachyte (sample N-238, SID: 1060) and its co-magmatic inclusions

Periodic acidic volcanic activity has led Nemrut stratovolcano to be built. As the volcanism intensified, numerous concentric peripheral eruption centers were formed. Besides, Incekaya tuff cone located ~ 18 km to the southeast of Nemrut volcano, at the opposite coast of Lake Van, is believed to have been formed during this peripheral doming episode. Kirkor Dome complex, located at ~6 km southwest of volcano, represent the highest domes in the area (Figure 3.1). There are several peaks on both of the main twin domes. Lavas originating from Kirkor complex have flowed ~ 4 km to the west forming steep plateaus with ~ 50 m elevation. One rhyolitic sample from the southern flank of Kirkor Domes is 242 ± 15 ka (Atasoy et al., 1989). There are numerous lava domes located in the region between Kirkor Domes and Nemrut volcano. Kelakirana, Kerkorumıksi, Kale and Yumurtadağ domes at the southern and Fakı dome located at the eastern flanks of the volcano, acted as barriers against the flow of the younger southern pre-caldera lavas. One sample from the comendite (N-149) flow, which is observed to change direction after bumping onto Kelakirana and Kerkorumıksi domes, yielded K-Ar age of 158 ± 4 ka. We concluded that the timing of peripheral doming, in at least well-exposed southern area, could be confined to ages older than 160 ka.

Among these peripheral silicic domes, Mazik Dagi is one of the largest with 4 x 6 km basal diameter. There is a wide extensional crack (N30E) with a maximum width of 910 m on the dome.

100 – Circa 50 ka

Volcanic activity of Nemrut volcano produced basaltic trachyandesitic (mugearite) lava flows (*SID: 1050*) and one sample from western caldera wall, which clearly indicates a mugearitic activity during the construction of the volcano, yielded a K-Ar age of 100 ± 50 ka (sample NE-22 of Notsu et al, 1995). We have observed scarce outcrops of mugearites on the southern escarpments of the caldera, in the vicinity of Çekmece (Şıhmıran) village (Figure 3.6.a). They are observed to be overlain by ignimbritic flows. Hence, it was not possible for these outcrops to distinguish their lower boundary relationships with relatively older units. On the other hand, another outcrop of mugearite has been exposed after a highway construction, in the vicinity of Aşağı Kolbaşı village, 7 km west of Kirkor Dome complex. This flow was also observed to be overlain by the thick ignimbritic flow (Figure 3.6.b). However, a sample (N-209) from this outcrop yielded a K-Ar age of 7 ± 4 ka. Considering the fact that caldera forming eruptions have been thought to occur between 80 - 40 ka (see above), 7 ka would be an inconsistent age for mugearite. They are dark brown in color and moderate to highly porphyritic. Besides, feldspar phenocrysts, which sometimes reach up to 1 millimeter, display textures of disequilibrium, even in hand specimens.

Potassium / Argon dating is based on the determination of Ar^{40} and K abundances in a rock sample. Argon, which is highly sensitive to alteration and high temperature, tend to be released due to damaged rock/mineral lattice because of these external factors. This causes the calculated K/Ar age to be younger than the absolute age of the analyzed specimen (i.e. Le Pennec et al., 2005). In fact, textural evidence indicating possible heterogeneity combined with the possible heating of the rock because of the ignimbritic emplacement above, could explain our suspicious radiometric age of this unit. We aimed to date the unique pre-caldera basic activity exposed, but unfortunately we believe that its true age could not be determined due to the nature of the rock, although the measured age is analytically correct (H. Guillou, pers. comm.). Therefore, we do agree with Notsu et al. (1995) on this unit for being older than at least ~80 ka.

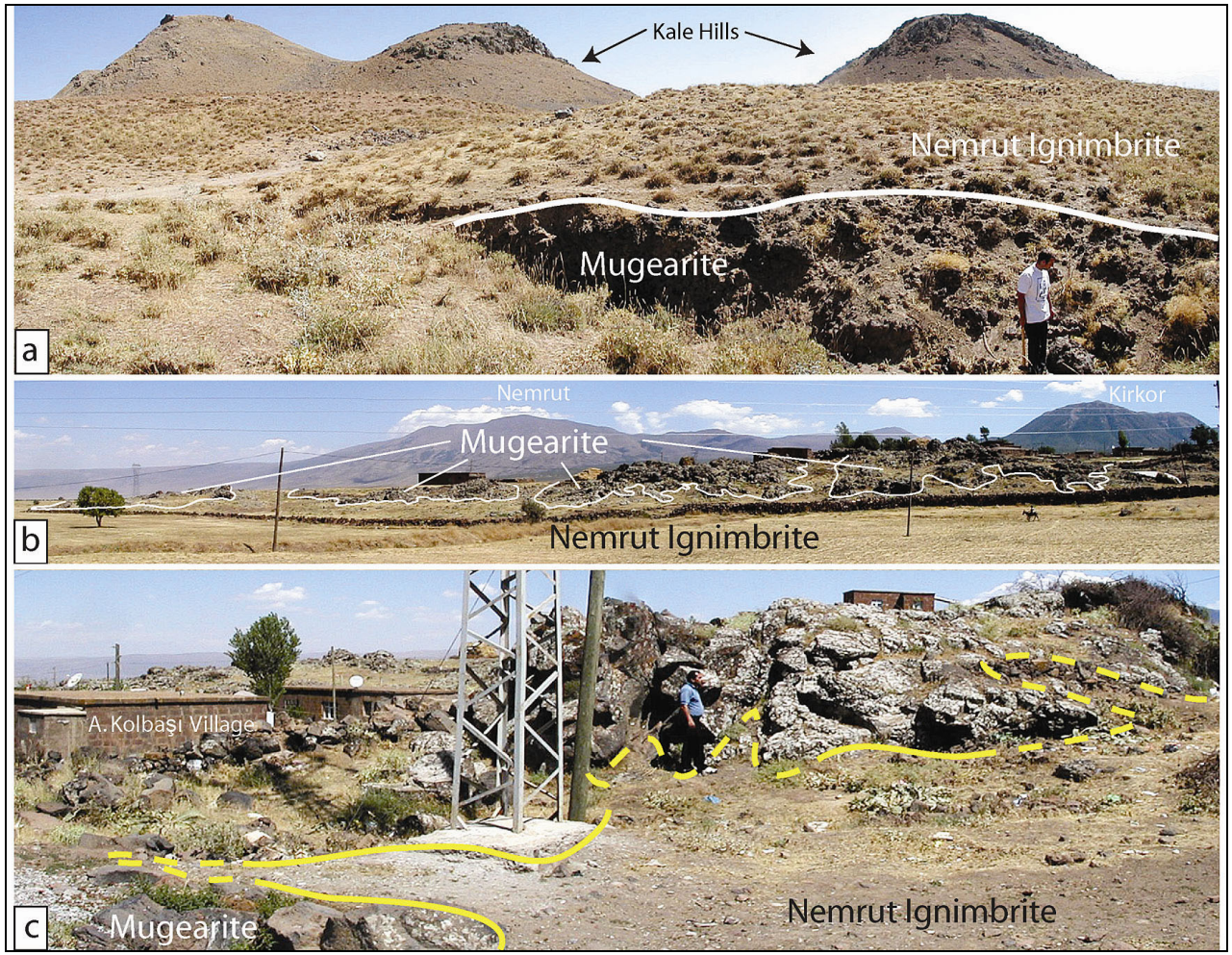

Figure 3.6: Stratigraphical relationships between mugearite and Nemrut ignimbrite (a) Mugearite is clearly overlain by ignimbrite in the west of Çekmece (Şıhmıran) village, (b) Packets of mugearite observed in overlying ignimbrite in Aşağı Kolbaşı village. Horizontal structure is the town wall made from bricks of ignimbrite, (c) Mugearite outcrops are covered with ignimbrite. Houses are built from ignimbrite.

During its construction, the volcano has been calculated to culminate about 4500 m (Aydar et al., 2003). Prior to caldera forming eruptions, rhyolitic, trachytic and basaltic effusive activities occurred. One vitreous rhyolite sample with pantelleritic affinity (N-098) collected from northeastern flank of the volcano was dated 99 ± 3 ka. Coeval lavas (*SID: 1040*) are located along the eastern rim of the caldera and mostly hypo-/ holohyaline, with rare occurrences of feldspar-phyric vitreous sections. Besides, there are abundant benmoreitic enclaves are observed. Viscous rhyolitic flows are observed to form cap shaped flows with some tens of meters thickness along the flanks. Microcrystalline planar flow bands and laminae are frequently observed (Figure 3.7). Although such banding represents physical discrepancy with the host rock, no significant geochemical variation has been noticed during their chemical mapping performed by EDS (see subsequent chapters).

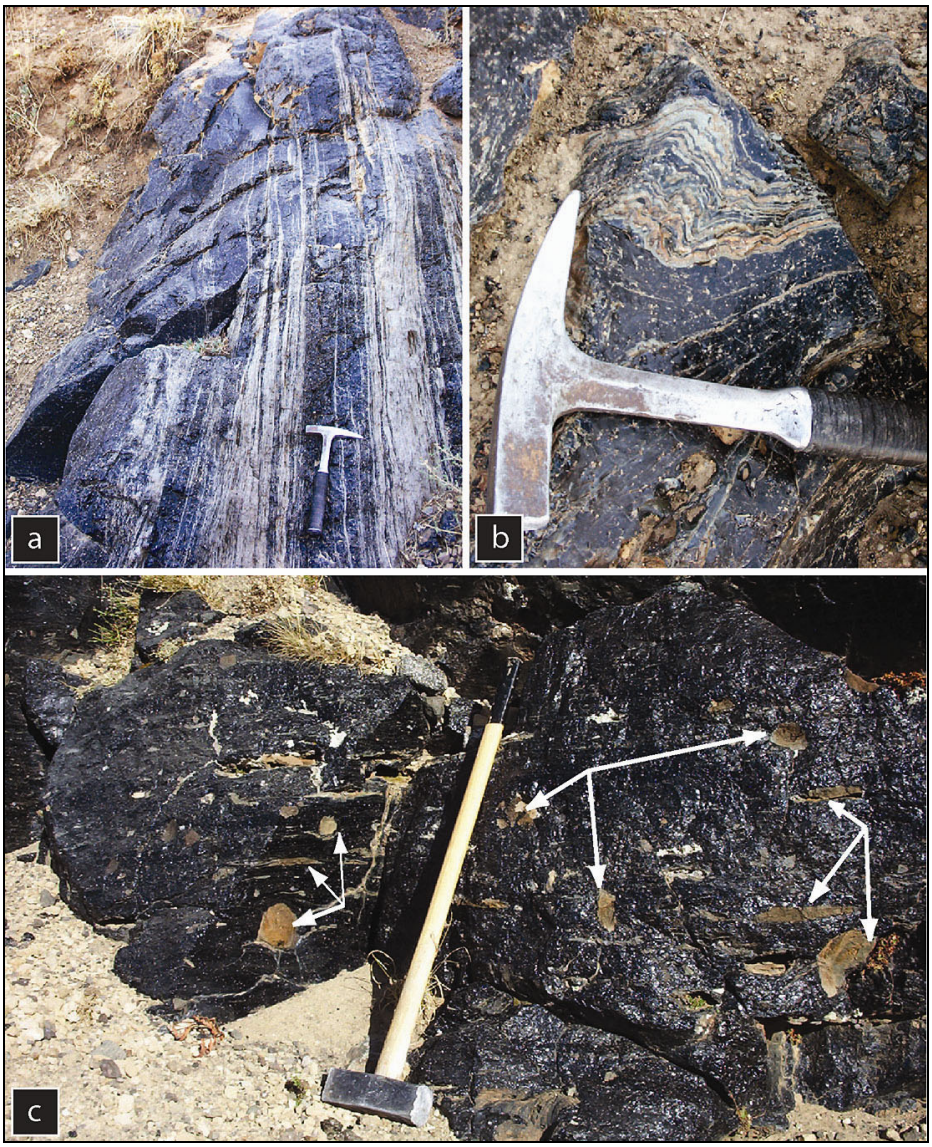

Figure 3.7: Flow banding in pre-caldera glassy peralkaline trachytes (a) planar and, (b) distorted laminae due to flow dynamics (c) mafic enclaves with irregular shapes in glassy comendite. (SID: 1040)

Less viscous trachytic lavas have reached the coast of Lake Van. One sample from the southeast of present caldera (N-181), collected from the coastal region of Lake Van, was dated at 93 ± 3 ka. Another sample (N-080) from southwestern flanks was dated at 89 ± 2 ka. These trachytes have peralkaline character (comenditic). They are highly porphyritic massive lavas with sporadic occurrences of columnar jointing.

Notsu et al. (1995) report basaltic lava flows (NE27) on the east of Tatvan city with K-Ar age of 80 ± 20 ka. As the exact location of their sample is unknown, our field observations failed to verify such an activity. Nonetheless, although we could not strictly confirm, we presume a possible basaltic activity, as Nemrut volcanism has produced bimodal episodes throughout its evolution.

Under the spotlight of radiometric data, supported by field observation, the youngest products prior to caldera forming pyroclastic events were circa 80 - 90 ka old. Therefore, we suggest a younger age for ignimbritic flows, at most 89 ka. It has previously been suggested a K-Ar age of 270 ka for a “brown tuff” sample from eastern flatlands (Atasoy et al., 1989). Yet, we propose that the timing of intense caldera forming eruptions, which has evacuated the magma chamber leading to the caldera collapse, was younger than ~90 ka.

Pre-Caldera Intrusions

Numerous magmatic intrusions are observed in the caldera walls (Figure 3.8), especially on the western half. With varying thicknesses and strikes, these dykes are in trachytic composition and are observed to cut all former lava flows. Their structures and relationships with the host rock bodies strongly imply that there must have been an overburden during their emplacement. Hence, these dykes should have been formed before the caldera collapse. If they had been formed after the caldera collapse, there must have been lava flows, which is not the case. Although some of these intrusions have been erroneously defined as post-caldera dykes by Özdemir et al (2006), we could not verify any existence of post-caldera intrusive emplacements on caldera walls.

Figure 3.8: Pre-caldera trachytic intrusions. (a) Feeder dyke on the northwestern caldera wall, (b) Feeder dyke on the southwestern wall, (c) Intrusion on the western wall, (d) Its bubbly contact with the host rock

3.3.2 Caldera Forming Eruptions

Following the construction of the volcano, explosive eruptions, which occurred in at least two rapid consecutive stages, produced plinian fallout and ignimbrite deposits observed extensively in the region. Thickness of the pyroclastic units varies on the location of their emplacement. The thickest deposits are observed on the basal plains of the volcano and in the valleys in the vicinity. In Bitlis valley, thickness reaches up to several meters. The volume of ignimbrites and associated products has been calculated as 40 km^3 over an area of 860 km^2 (Aydar et al., 2003).

Products of caldera forming eruptions begin with felsic fallout tephra due to initial plinian phase (SID: 1031). It is observed extensively in southern and eastern sectors; in the western sector, it becomes thinner. It is pale yellow to whitish in color, pumice rich with rare lithics and sometimes slightly intercalated with ash. Bedding is symmetrically graded progressively from normal to reverse in the co-set. Maximum pumice size decrease from bottom to middle set and then exhibits an increase towards the uppermost set (Figure 3.9).

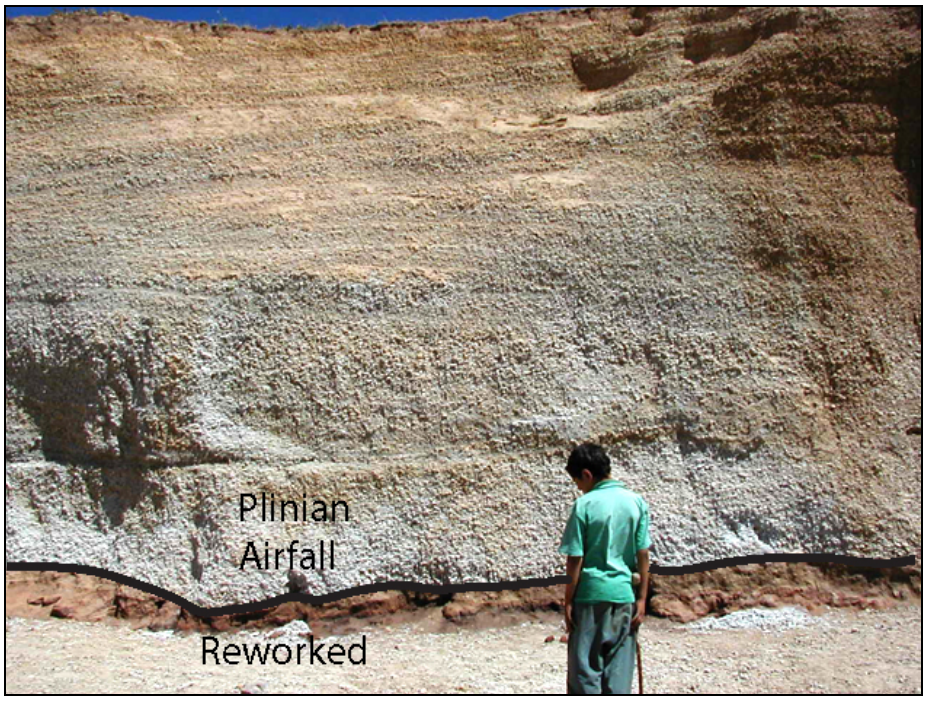

Figure 3.9: Upper sections of the initial plinian phase (SID: 1031). Reworked layers are also observed within the unit.

The pale colored initial plinian fallout is overlain by relatively thinner fallout tephra, which bears a dark colored fine ash matrix (SID: 1032). It is observed principally on the southeastern flatlands of the volcano. This set of plinian falls comprised of both dark and

pale colored pumice. In addition, some pumice fragments are streaky with both dark brown and whitish yellow colored laminates (Figure 3.10).

Figure 3.10: Nemrut ignimbrite overlying plinian air fall units in Şıhmıran village; pale (SID: 1031) and dark colored (SID: 1032)

These two plinian phases are sometimes overlain by a level of ground surge especially in eastern flanks. The surge would represent the lowermost section of the main ignimbrite flow deposit, observed extensively in the region. This pyroclastic flow unit is named as Nemrut Ignimbrite (Figure 3.11.a).

Nemrut ignimbrite emplaced broadly in the region. It is observed to cover nearly all former lava flows and domes. Particularly, during its flow, Kirkor Dome complex in the southwest; Mazik dome in the west, Yumurtatepe and Fakı domes in the southeast acted as obstacles, onto which Nemrut ignimbrite has bumped and changed its direction. Moreover, deposits of Nemrut ignimbrite have covered most parts of these domes diminishing their probable steepness. Its thickness reaches up to several tens of meters on the flatlands, while getting thicker in the valleys into which it canalized. Especially in the Bitlis valley, it reaches nearly 50 m thickness.

The basal section of Nemrut ignimbritic flow (SID: 1033) is significantly well exposed in Bitlis Valley, 25 km southwest of the volcano. It is strongly welded with significant fiammes exhibiting eutaxitic texture. These collapsed and deformed juvenile pumice fragments are dark brown in color set in brown to black matrix composed of (fine) ash. It comprises free juvenile crystals and lithic fragments. Lithic fragments belong to former volcanics and metamorphic basement. These metamorphic fragments reach up to 2 cm in size and interestingly look like euhedral alkali feldspar crystals at the first glance in hand specimens. In Bitlis valley, they exhibit columnar jointed cooling units (Figure 3.11.b).

Nemrut ignimbrite is occasionally observed to change color progressively: dark brown/black to pale yellow progressively from bottom towards the top (Figure 3.11.c). Pumice fragments, however, are various in colors between dark brown to whitish. Their sizes and distribution within the flow unit is varying. Besides, the degree of welding depends on the location with respect to palaeo-topography and distance from the volcano (Figure 3.11.d). Free crystals are omnipresent throughout the flow unit. However, the nature of lithic fragments depends on the relative levels in the unit. As we have mentioned above, basal sections bear readily metamorphic fragments whereas their abundance diminishes and these metamorphic fragments become absent towards the top, replaced by trachytic and rhyolitic fragments. Furthermore, abundant obsidian fragments are also observed in the upper sections of the unit.

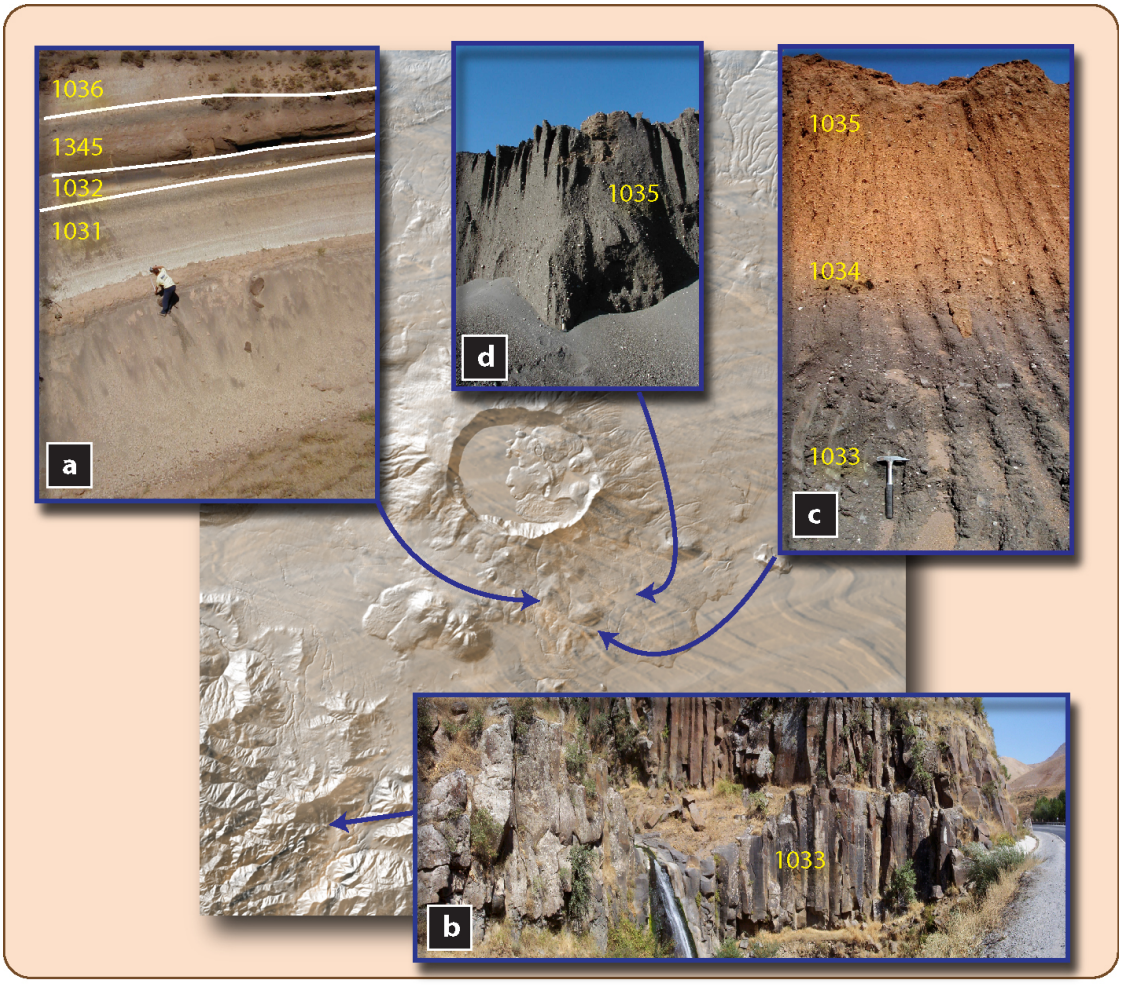

Figure 3.11: Nemrut ignimbrite (SID: 1345) (a) overlies plinian airfalls (1031, 1034) and overlain by another plinian phase (1036). (b) Basal sections of the ignimbrite in Bitlis valley exhibit columnar jointing (c) color of the ignimbrite often displays progressive change from black to brownish red (d) welding depends on the location as this upper part (1035) is weakly welded in the southwestern parts of the volcano

Nemrut ignimbrite is overlain by pumice air falls (SID: 1036) indicating a second plinian phase (Figure 3.11.a). Fallout is pumice rich in a gray fine ash matrix. Lithic fragments are rare and belong solely to trachytic - rhyolitic former volcanic rocks. Intercalations of ash rich levels are observed, probably indicating the energy fluctuations during the plinian eruption. Pumice is highly vesicular with pale gray to white in color. Moreover, pumices with streaky appearance due to the smear of mafic melt are rare but omnipresent. This unit is followed by light colored pumice rich plinian fallout set. Pumice is highly vesicular and pale gray to yellowish white in color set in a whitish fine ash matrix.

A second unit of ignimbritic flow is observed dominantly on the north of the caldera. It is observed to overlain former pyroclastic units especially on the northern caldera rim (Figure 3.12). This unit is termed as Kantaşı ignimbrite due to its best exposure in that locality. It is reddish to pale brown in color. Welding is moderate-to-strong. Free crystals and rare lithic fragments are omnipresent.

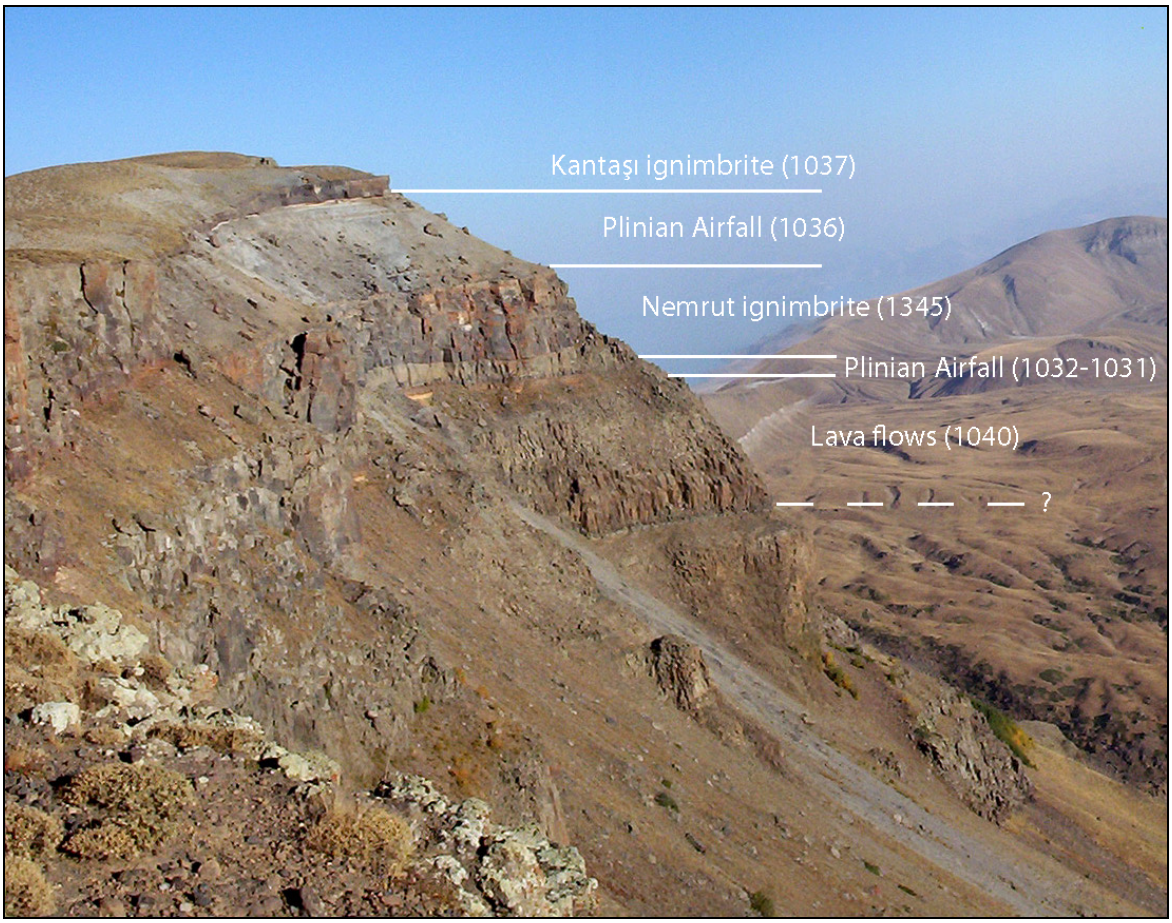

Figure 3.12: Kantaşı ignimbrite overlies preceding pyroclastics; Northern caldera rim. Numbers in parentheses are the respective SIDs (Stratigraphic ID)

Caldera Collapse

After the evacuation of magma chamber due to the caldera forming pyroclastic activity, excess lithostatic pressure on the reservoir leads to the collapse of the roof. Although the exact time of caldera collapse is unknown, we do assume that this major event has possibly taken place between 80 to 30 ka ago (Figure 3.3). Nemrut caldera was collapsed in a piecemeal manner and constituted of four main blocks. Boundaries limiting these blocks and the main structural caldera boundary seem to control the hydrothermal activity in the caldera. (Ulusoy et al, in rev.).

Peralkaline calderas are associated with areas of high extension and are common in the East African Rift, but also occur in areas of unusually high rates of localized extension in convergent margin (e.g., Mayor Island, New Zealand) or intra-plate oceanic islands (e.g., Canary Islands) (Cole et al., 2005; and references therein). Besides, rhyolitic calderas occur mostly in continental or continental margin areas where mild extension occurs, either associated with a convergent plate boundary (e.g., Taupo Volcanic Zone, New Zealand) or with rifting in continental crust (e.g., Rio Grande Rift, south central USA) (Cole et al., 2005; and references therein).

3.3.3 Post-Caldera Stage

Post-caldera activity at Nemrut is confined to intra-caldera region and to the northern flank where a “rift zone” has occurred in historic times (1441 AD). Lava domes, flows and phreatomagmatic activity are represented in the eastern half of the caldera. Only one notable post-caldera lava flow is observed on the southwestern caldera rim along a possible ring fracture (Figure 3.1).

Intra-caldera lavas and domes (*SID: 1020*) are peralkaline and rhyolitic in composition and the oldest post-caldera rhyolite dates back to 30 ka (Figure 3.3; Matsuda, 1988). Furthermore, one peralkaline rhyolite (comendite) sample (N-051) collected from the coast of the hot lake located in northern intra-caldera region yielded a K-Ar age of 15 ± 1 ka. Intra-caldera comendites are usually aphyric with rare occurrences of feldspar phenocrysts. They exhibit evident planar flow banding (Figure 3.13.a). Although, we frequently observe holohyaline, obsidian facies on these units, occurrence of vesicular pumiceous zones within aforementioned units is common. Most importantly, intracaldera lavas bear benmoreitic enclaves (Figure 3.13.b, c). Between the enclaves and the vitreous host comendite, a pumiceous interface is frequently observed (Figure 3.13.d). Relationships between enclaves and host comendites will be discussed thoroughly in the subsequent chapter.

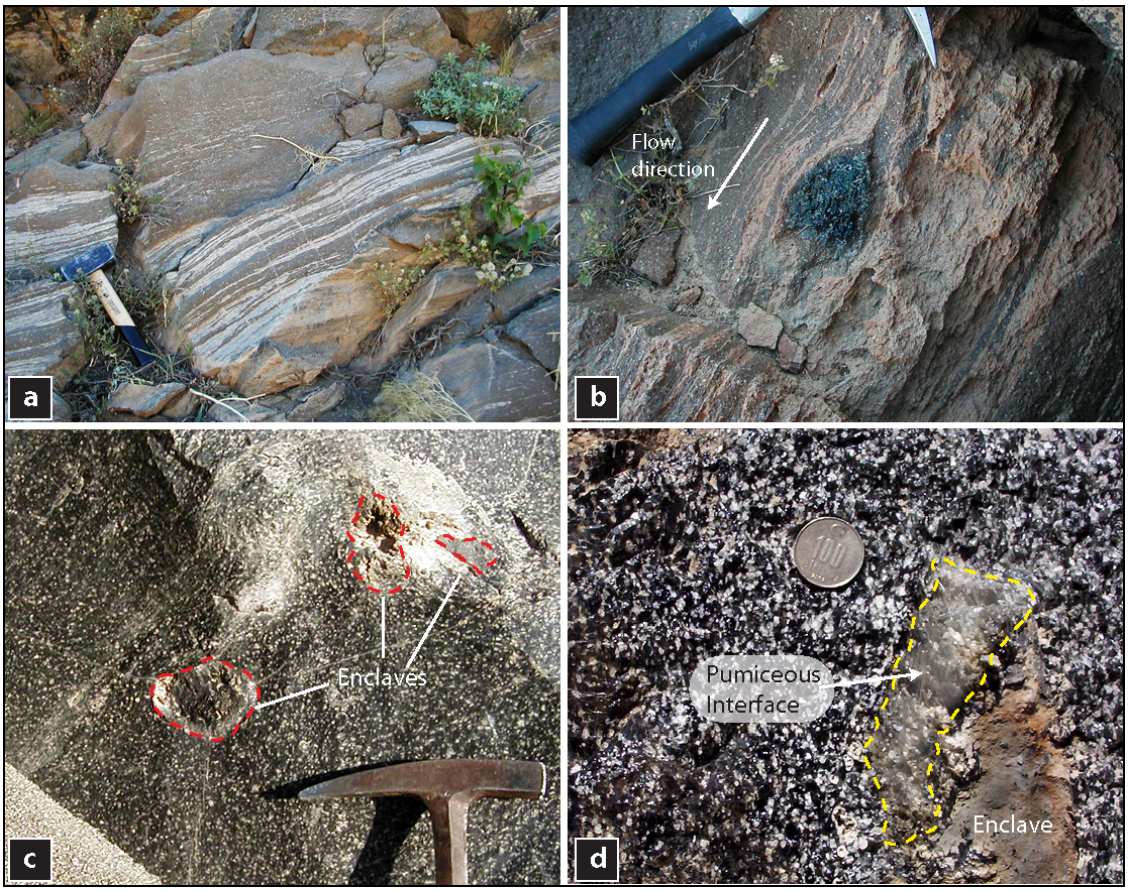

Figure 3.13: Post-caldera comendites within the caldera. (a) Planar flow banding, observed to be (b) deformed around the enclaves. (c) Irregularly shaped mafic-to-intermediate (benmoreitic) enclaves are abundant representing blobs or blebs of mafic-to-intermediate melt (d) interfacial pumiceous zones are frequently observed between enclave and the host comendite

Products of phreatomagmatic eruptions, formed by several explosion craters, are observed to overlay comendite lavas and domes (Figure 3.1). On the tuff rings of these craters, base surge deposits with dune and anti-dune structures, bomb sags and pool structures, bread-crust bombs and cross bedding are observed (Figure 3.14). These base surge deposits are also observed plastering on the western caldera wall. One pumice sample (N-305) from these phreatomagmatic units has yielded 8 ± 3 ka. Juvenile glass of phreatomagmatic activity displays identical mineralogical/geochemical properties with the former post-caldera comendites.

Furthermore, abundant lithic fragments have been observed in phreatomagmatic base surges. Two types of phreatomagmatic lithic ejecta have been discriminated. One type, being porphyritic, bears highly destabilized (xeno) crysts noticed even by naked eye, and another type exhibits holocrystalline (semi) equigranular texture, resembling to those of plutonic rocks (see below).

Özdemir et al. (2006) define monzonitic intrusions exposed in topographic lows within the caldera. They have neither given any petrographical / mineralogical description nor geochemical analysis of this unit. It should be noted that the exposure of a magma chamber which is the plutonic equivalent of the caldera volcanics require significant erosion (Cole et al. 2005). The Nemrut Stratovolcano is not eroded but it is still active (Aydar et al. 2003) and is very young compared to the calderas with plutonic outcrops (i.e. Bodrum Caldera, Ulusoy et al. 2004), which does not meet the criteria stated above. In addition, the locations which Özdemir et al. (2006) define as monzonitic outcrops are the regions of caldera fill with very young (< 10 kA, Notsu et al. (1995)) volcanic units. Furthermore, in their stratigraphic columnar section, Özdemir et al. (2006) suggest that the monzonite (Unit 18) is younger than intra-caldera vitrophyre rhyolite (Unit 16, Age: < 0.01 Ma). Such young volcanism inhibits the erosion which would lead any plutonic body to outcrop. In addition, the area mapped (~0.4 km^2) as monzonite by Özdemir et al. (2006) is within intra-caldera maars whose post-caldera products contain abundant holocrystalline fragments. These intra-caldera maars are among the centers of post-caldera phreatic - phreatomagmatic activities. Their basements are filled with post-eruption deposits while their walls are subjected to intense hydrothermal alteration.

Figure 3.14: Base surge deposits of post-caldera phreatomagmatic activity plastered onto southern caldera wall.

The fissure eruption in 1441 AD, mentioned in historical records, produced a spectacular outcrop of bimodal rhyolite and basalt (*SID: 1010*). During this event, a rift zone of 4 km length with approximately 250 m wide has been formed (Figure 3.1 and Figure 3.15). The average depth of the rift is about 50 m. There are several narrow cracks (< 2 m by width) with almost unknown depths.

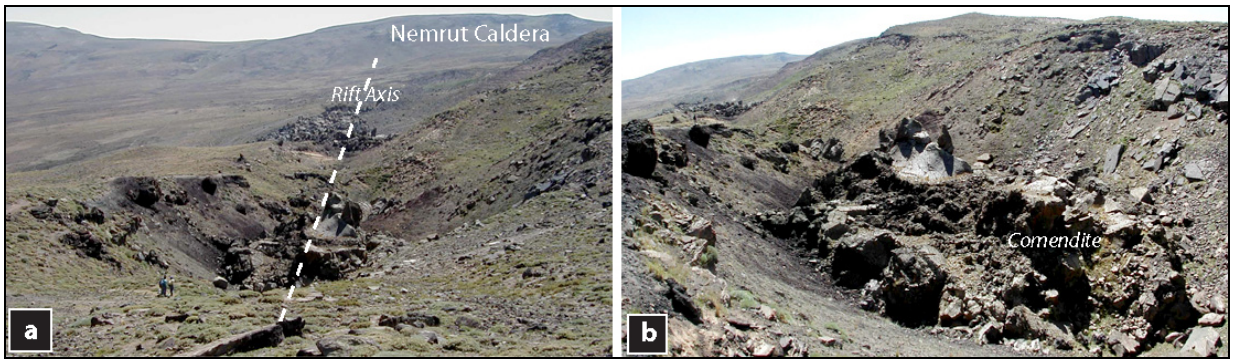

Figure 3.15: (a) Rift zone viewed from north (b) Comenditic spikes in the rift

Bimodal rift zone activity commences with basaltic lavas that flowed towards east, west and northern directions, and reached 1.5 km in lengths with ~ 100 m wide (Figure 3.16). Basalts are highly porphyritic (plagioclase and olivine phyric) and sometimes highly vesicular.

Along the rift zone, comendite emplacements exhibit spectacular morphological features such as spikes and superficial plugs reaching up to several meters of height. The basaltic lava flow, which has been defined as the latest product [unit #21 in volcanostratigraphy of Özdemir et al. (2006)], was clearly observed to be overlain by approximately 10 m thick vitreous rhyolitic flow along the N-S trending Nemrut extensional fissure (Figure 3.16.a). Although this observation has been suggested in a comment for their paper (Çubukçu et al., 2007), Özdemir et al insist basalts have injected (!) into rhyolites (Özdemir et al., 2007). Moreover this rhyolite flow has utilized the same crack system with the basalt to reach the surface (Figure 3.16.b).

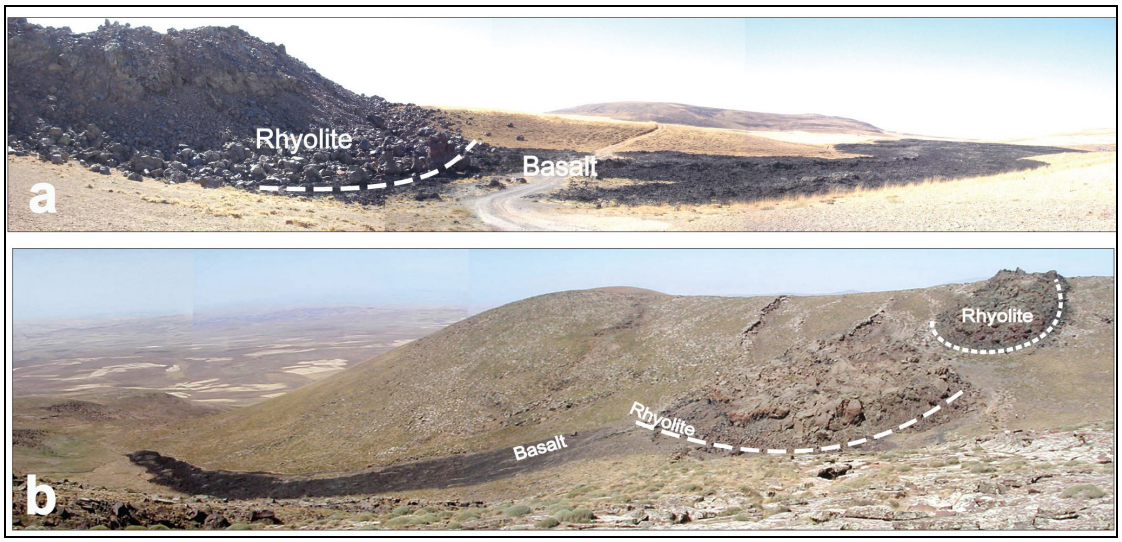

Figure 3.16: Post-caldera basalt and comendite (rhyolite) in the vicinity of the rift. (a) Rhyolite is observed to clearly overlie basalt (b) Rhyolite has utilized the same cracks with the basalt to reach surface

3.4 Conclusions

Quaternary Nemrut volcano is situated in E - W elongated Muş basin overlying Palaeozoic - Mesozoic Bitlis metamorphics and Jurassic to Cretaceous Çatak ophiolites. Nemrut volcanic system comprises polygenetic Nemrut stratovolcano and concentric monogenetic dome systems. The volcano has an elliptical summit caldera, which is partly filled by freshwater lakes with an almost pure mantle Helium contribution (Güleç et al., 2002).

Volcanic evolution of Nemrut volcano is investigated in two main stages, namely pre- and post-caldera, which are separated by paroxysmal caldera forming eruptions. According to the radiometric data available, oldest pre-caldera rocks, being metaluminous trachytes extend 1.01 ± 0.04 Ma (Atasoy et al., 1989). Volcanism produced dominantly peralkaline trachytes and rhyolites between ~700ka (Pearce et al., 1990) and ~ 100 ka (Notsu et al., 1995) whilst the construction of the volcano and peripheral eruption centers have been intensified. Latest pre-caldera peralkaline silicic lavas, dated during this study, concentrates between 99 - 89 ka, constraining the timing of caldera collapse being younger than hitherto believed.

Intense ignimbritic eruptions, separated in two distinct flow units (Nemrut and Kantaşı ignimbrites) have evacuated the magmatic reservoir leading the collapse of its roof in a piecemeal manner.

Volcanic activity continues after the caldera collapse, confined mostly to intra-caldera region. The oldest dated intra-caldera comendite (30 ka; Matsuda, 1988) represent the upper limit for the age of caldera collapse. Intra-caldera activity is represented by comenditic domes and associated lava flows. Phreatomagmatic activity, indicating the presence of water in the caldera is dated at ~8ka. During this period, extra-caldera rifting has been initiated along N-S direction and produced bimodal basalt - comendite flows, which are described in historic times (~500 BP).

The compositional spectrum of eruptive units, predominance of silica oversaturated peralkaline rocks to mafic rocks, representation of intermediate compositions merely by enclaves, and hence the bimodality, illustrate that Nemrut volcano exhibits spectacular resemblance with worldwide examples of peralkaline volcanoes in extensional settings.

CHAPTER 04

PETROGRAPHY

When observation is concerned, chance favors only the prepared mind

Louis Pasteur

4 PETROGRAPHY

Nemrut volcanism produced dominantly silicic rocks with minor occurrence of mafic units throughout its eruptive history. Petrographical features of Nemrut volcanism is presented concerning the volcanic stratigraphy.

Samples representing the eruptive history have been preliminarily examined in detail by techniques of polarized microscopy. The features, for which the optical microscopy was inadequate to determine, techniques of electron microscopy have been applied. For detailed analytical conditions for both optical and electron microscopy, comprehensive information is presented in Chapter 2 - Methodology.

Mineral abbreviations used in the text and figures are given in Table 4.1. A condensed summary of textural properties of Nemrut eruptive products have been depicted on synthetic Table 4.2.

Table 4.1: Abbreviations of mineral names and used in the text and in the figures

Abbreviations	Mineral	Abbreviations	Mineral
Ab	Albite	Fsp	Feldspar
Aeg	Aegirine	Ilm	Ilmenite
Aen	Aenigmatite	Kf	K-feldspar
Af	Alkali feldspar	Mgn	Magnetite
Amph	Amphibole	Ol	Olivine
Ap	Apatite	Qtz	Quartz
Arf	Arfvedsonite	Plg	Plagioclase
Chvk	Chevkinite	Py	Pyrite
Cpx	Clinopyroxene	Ti-mgn	Titanomagnetite
Fa	Fayalite	Zrn	Zircon
Frch	Ferrorichterite		

Table 4.2: Synthetic table depicting petrographical features of Nemrut eruptive units

SID	Rock Type	Porphyritic Index (%)	Rock Texture	Major Crystals and Size	~$\varnothing_{max}$ (μ)	Groundmass
500 BP	Comendite with	7 -15	Hypohyaline with minor devitirification Dispersed blebs of mafic inclusions	*AF* *Cpx* *Ol*	*3000* *1000* *500*	*Glassy with quench crystals. Mafic inclusions seperated by vesicular and microcrystalline interface*
1010	Benmoreitic Enc.	37 - 40				
	Basalt	49 -53	Variolitic to sub-ophitic. Vesicular Euhedral - subhedral Plg and Ol -phyric	*Plg* *Ol*	*1000* *750*	*Pilotaxitic with microlites of plg, ol and Fe-Ti oxides. Laths and clusters of nucleating cpx*
< 30 ka 1020	Comendite	7 -18	Euhedral Af -phyric with karlsbad twinning Blebs of mafic inclusions seperated by vesicular and microcrystalline interface. Vesicular and crystalline flow bands without chemical discrepancy	*Af* *Cpx* *Ol*	*2000* *1000* *300*	*Glassy with minor devitrification and microspherulites along cracks.*
1037	Kantaşı Ignimbrite		Unwelded to welded eutaxitic Euhedral - subhedral plg, af, cpx and ol			*Glassy with subordinate vapor phase crystallization*
1036	*Plinian Fallout*		Highly vesicular, sub-anhedral plg, cpx ol			*Minor devitrification, spherulitic -axiolitic*
1345	Nemrut Ignimbrite		Eutaxitic, welding depends location (An)subhedral spongy cellular ternary feldspar. Euhedral feldspar rare. Subhedral cpx slightly resorbed Anhedral ol moderately resorbed Glass shards exhibit fiamme depending on welding. Lithic fragments are of former volcanics and basement metamorphics	*Af* *Plg* *Cpx* *Ol*		*Crystal / Lithic rich fine ash matrix, sometimes glassy with axiolitic and/or spherulitic devitrification*
1032			Highly vesicular, sub-anhedral spongy af-phyric, subhedral cpx, anhedral ol			*Glassy with quench crystals.*
1031	*Plinian Fallout*		Highly vesicular, euhedral af-phyric rare cpx and olivine			*Glassy with quench crystals.*
1040	Comenditic Trachyte	36 -39	Holocrystalline seriate. Euhedral to subhedral Af-phyric, poikilitic with cpx and rounded ol.	*Af* *Cpx* *Ol*	*2500* *1000* *400*	*Pilotaxitic with microlites of Af, cpx, ol, Fe-Ti oxides*
89 -100 ka	Comendite / Pantellerite	9 -13	Hipohyaline. Euhedral Af-phyric. Eu-subhedral cpx and slightly rounded ol. Vesicular and crystalline flow bands without chemical discrepancy	*Af* *Cpx* *Ol*	*5000* *2000* *400*	*Glassy with quench crystals.*
1050	Basalt ?	?	Holocrystalline aphyric to seriate porphyritic. Porphyritic rocks are Plg, cpx and ol -phyric. Stable and destabilized anhedral spongy cellular plg. Glomeroporphyritic plg ol and cpx. Frequently poikilitic with cpx and Fe-Ti oxides.	*Plg* *Plg (s)* *Cpx* *Ol*	*3000* *4000* *1000* *1500*	*Pilotaxitic plg, cpx, ol and oxides.*
~ 100 ka	Mugearite	6 - 29				
1060	Comenditic Trachyte / Comendite	17	Hypo/Holocrystalline Seriate Porphyiritic. Euhedral Af with slight spongy rims. Moderately resorbed ol.	*Af* *Cpx* *Ol* *Amp*	*4000* *1000* *2000* *750*	*Pilotaxitic af, cpx, ol, (amp) and oxides.*
160 - 300 ka	Trachyte	25 -32				
1070	Comenditic Trachyte / Comendite	11	Hypo/Holocrystalline Seriate Porphyiritic. Euhedral Af, cpx. Moderately vesicular.	*Af* *Cpx* *Ol*	*4000* *1000* *1200*	*Pilotaxitic to trachytic af, cpx, ol, (amp) and oxides.*
300 - 570 ka	Pantelleritic Trachyte	25				
> 570 ka 1080	Comenditic Trachyte / Rhyolite		Hypo/Holocrystalline Seriate Porphyiritic. Subhedral Af with slight spongy rims Sub/Anhedral plg with frequent dieqilibrium.Subhedral cpx.Moderately resorbed ol.	*Af* *Plg* *Cpx* *Ol*	*3500* *2000* *1000* *800*	*Pilotaxitic to trachytic af, plg, cpx, ol and oxides.*
	Trachyte					

4.1 Pre-Caldera Silicic Rocks

Oldest known (> 700 ka; Pearce et al., 1990) volcanic rocks of Nemrut volcanism are marginally metaluminous to comenditic trachyte (SID: 1080). They consist of hypo/holocrystalline porphyritic lava flows. Metaluminous trachytes are moderately porphyritic with about 20% of the phenocrysts in the groundmass (Porphyritic Index, PI) is about 20%. Euhedral and subhedral phenocrysts of plagioclase and alkali feldspar display seriate texture. Metaluminous trachytes, being rarely observed, are the only rocks which bear both plagioclase and alkali feldspar. Clinopyroxene and olivine bear frequently opaque rims. Rare cumulates of plagioclase, clinopyroxene and olivine exhibit glomeroporphyritic texture. Groundmass is micro/cryptocrystalline with pilotaxitic feldspar, clinopyroxene and olivine microlites (Figure 4.1.a).

Younger silicic rocks (SID: 1070; 570 - 300 ka) are comprised of peralkaline (Agpaitic Index > 1) trachytes and rhyolites. Trachytes are holocrystalline whereas rhyolites are hypohyaline and moderately porphyritic (Porphyritic Index, PI: 11 - 25 %). They are moderately vesicular. Phenocrysts and microphenocrysts of alkali feldspar display seriate texture, exhibiting a wide range in crystal sizes. Euhedral alkali feldspar and clinopyroxene with scarce anhedral olivine represent the phenocryst assemblage. Groundmass is dominantly (micro) crystalline with microlites of alkali feldspar, clinopyroxene, olivine and rare aenigmatite and Fe-Ti oxides. Groundmass is dominantly pilotaxitic, however trachytic texture is observed due to the alignment of microlites (Figure 4.1.b). There is no textural or petrographical discrepancy due to the degree of peralkalinity: Pantelleritic rocks display similar petrographical features with comenditic counterparts.

Extensive silicic volcanism between 300 and 160 ka, produced slightly metaluminous to marginally peralkaline trachytic and rhyolitic rocks (SID: 1060). Stratigraphically lower metaluminous trachytes are hypohyaline and moderately seriate porphyritic (Porphyritic Index, PI: 25 - 32 %). Subhedral and anhedral alkali feldspars display Carlsbad twinning. Feldspars have spongy rims where aligned inclusions of ferromagnesian phases are observed. Clinopyroxene and destabilized olivine represent microphenocryst assemblage. Apatite inclusions are observed in clinopyroxene. Groundmass is pilotaxitic with microlites of alkali feldspar, clinopyroxene, olivine, Fe - Ti oxides and apatite (Figure 4.1.c). We note a decrease in phenocryst content towards stratigraphically younger seriate porphyritic peralkaline trachytes and rhyolites of the same period (PI: ~ 17 %). Glomeroporphyritic euhedral alkali feldspar, clinopyroxene and sometimes olivine represent the phenocryst assemblage. Olivine is moderately resorbed and sometimes exhibits a gnawed appearance.

Scarce amphibole phenocrysts with opaque reaction rims (with aenigmatite, see further sections) are observed only in rhyolites. Groundmass is pilotaxitic with microlites of alkali feldspar, clinopyroxene, olivine, amphibole and Fe - Ti oxides. Intersertal quartz is observed in silica rich samples (Figure 4.1.d).

Silicic volcanism produced extensive trachytic - rhyolitic lava flows between 90 - 100 ka (SID: 1040). They are peralkaline and dominantly comenditic in composition. However, there are minute pantelleritic counterparts especially observed northeast of the volcanic center. Comendites are hypohyaline and weakly porphyritic (PI: 9 - 13 %). They are euhedral alkali feldspar-phyric with microphenocrysts of clinopyroxene and minute fayalite. Trachytes are holocrystalline seriate porphyritic (PI: 36 - 39 %). Euhedral to subhedral alkali feldspar exhibits poikilitic texture with smaller clinopyroxene and fayalite (Figure 4.1.e). Hyaline rocks bear groundmass with evident quench crystals and scarce microlites of their nominal mineral assemblage. Crystalline counterparts have pilotaxitic groundmass with microlites of alkali feldspar, clinopyroxene, olivine and Fe - Ti oxides.

Above mentioned trachytes and rhyolites significantly possess flow banding. These flow bands are crystalline and exhibit pilotaxitic - to trachytic texture with microlites of alkali feldspar, clinopyroxene, olivine and aenigmatite. Besides, these bands are vesicular, aligned almost parallel to the direction of these bands. Furthermore, minor devitrification with spherulites is observed along cracks and vesicles. In addition, dispersed blebs of relatively mafic material have been observed (Figure 4.1.f). This mafic-to-intermediate material is comparable to the enclaves of post-caldera comendites. They bear fragments of (cellular) plagioclase, olivine and clinopyroxene. However, being scarce, these mafic materials remind that similar processes forming the post-caldera enclaves might be ongoing before the caldera collapse (see section 3.1.6 on enclaves).

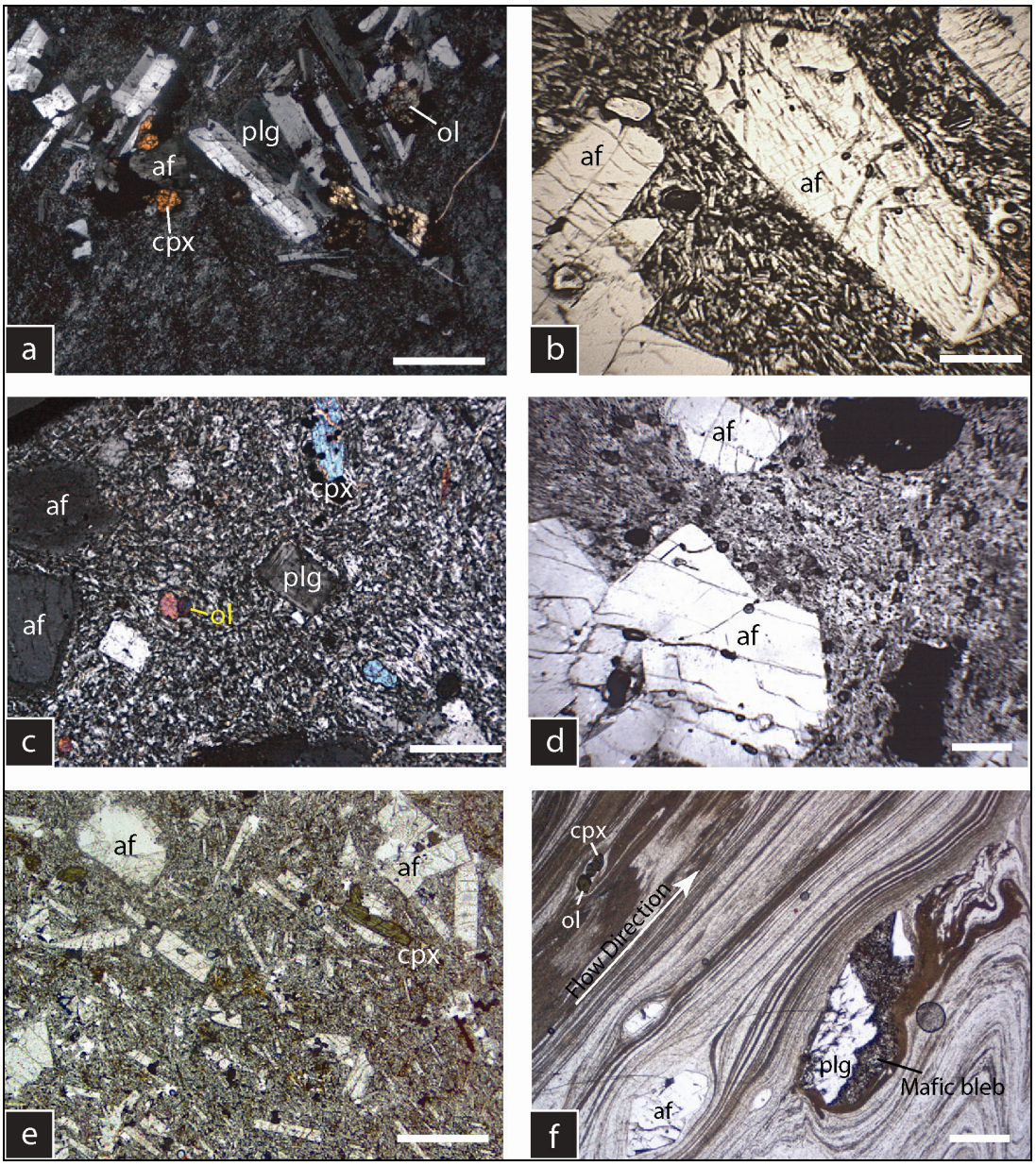

Figure 4.1: Petrographical features of pre-caldera silicic products of Nemrut volcanism. Scale bars are 1000 µm. Cross Polarized Light (CPL) and Plane Polarized Light (PPL).

a) Metaluminous trachyte (SID: 1080), glomeroporphyritic clusters of alkali feldspar and plagioclase with clinopyroxene and olivine set in a pilotaxitic groundmass (CPL).

b) Peralkaline trachyte (SID: 1070), euhedral alkali feldspar and microlites of af, olivine and clinopyroxene set in a groundmass with typical trachytic texture (PPL).

c) Metaluminous trachyte (SID: 1060), anhedral-to-subhedral af phenocrysts with spongy rims, euhedral plagioclase, slightly destabilized cpx and ol set in a pilotaxitic-to-trachytic groundmass of the same assemblage (CPL).

d) Peralkaline trachyte (SID: 1060), alkali feldspar is euhedral and is in equilibrium with the melt, with microphenocrysts of cpx and ol set in a pilotaxitic microcrystalline groundmass (PPL).

e) Peralkaline trachyte (SID: 1040), euhedral seriate af with euhedral cpx and ol in groundmass of the same assemblage (PPL).

f) Glassy comendite (SID: 1040) with euhedral af phenocrysts, euhedral microphenocrysts of ol and cpx. Blebs or droplets of mafic melt with cellular plg. Flow bands wrap crystals and mafic enclave (PPL).

4.2 Pre-Caldera Basic Rocks

As we have demonstrated in the previous chapter, Notsu et al. (1995) present two radiometric ages for pre-caldera basaltic activity associated with Nemrut volcanism. However, they did not describe the petrographical features of these two samples. Nonetheless, one of their samples is from the western caldera wall (NE 27), which reveals a basaltic activity during the construction of the volcano. We have observed mugearitic volcanics in the west of the volcano, but have failed to achieve a radiometric age consistent with Notsu et al. (1995). Our sample (N-209) yielded an age of 7 ± 4 ka. Despite such a younger age for this unit, which is clearly overlain by ignimbritic flows, we presume that this unit is pre-caldera and the cause of our dating error can be explained by its petrographical properties.

Mugearites consist of both aphyric (Figure 4.2.a) and porphyritic (P.I. 6 – 29 %) varieties. Phenocrysts exhibit seriate texture and consist of plagioclase, clinopyroxene, olivine and oxides.

Some plagioclase phenocrysts display evident disequilibrium textures. Instable plagioclases are spongy or boxy cellular and frequently anhedral and embayed (Figure 4.2.b). Besides, subordinate amphibole occurrences have been observed to be restricted to the instable inner zones of plagioclase phenocrysts (see Mineral Chemistry Section, Chapter 4). On the other hand, euhedral plagioclase without disequilibrium textures is present in the rocks (Figure 4.2.c). Polysynthetic twinning and oscillatory zoning is typical.

Clinopyroxene is sub-to-anhedral. Sector zoning is frequent. They bear abundant inclusions of oxides. Olivine phenocrysts are mostly embayed and are gnawed (Figure 4.2.d). However, euhedral microphenocrysts are also present in the groundmass.

Groundmass is pilotaxitic to trachytic and consists of feldspar, clinopyroxene, olivine and oxides. Besides, some samples bear significant bands with darker color than the nominal groundmass. Dominant mineralogy of these darker bands is virtually similar to that of the bulk rock, except the lower abundance of microlites (Figure 4.2.e).

Besides, mugearites bear somehow more stable phenocrysts of plagioclase, clinopyroxene, olivine and oxides displaying ophitic/subophitic glomeroles (Figure 4.2.f).

From their petrographical properties, it is clear that mugearites display evidence of heterogeneity. Although we have aimed to radiometrically date this pre-caldera basaltic event, we obtained an inconsistent age of 7± 4 ka. Such unexpected results can be explained by the significant textures of disequilibrium, as well as reheating of mugearite by the overlying ignimbrite.

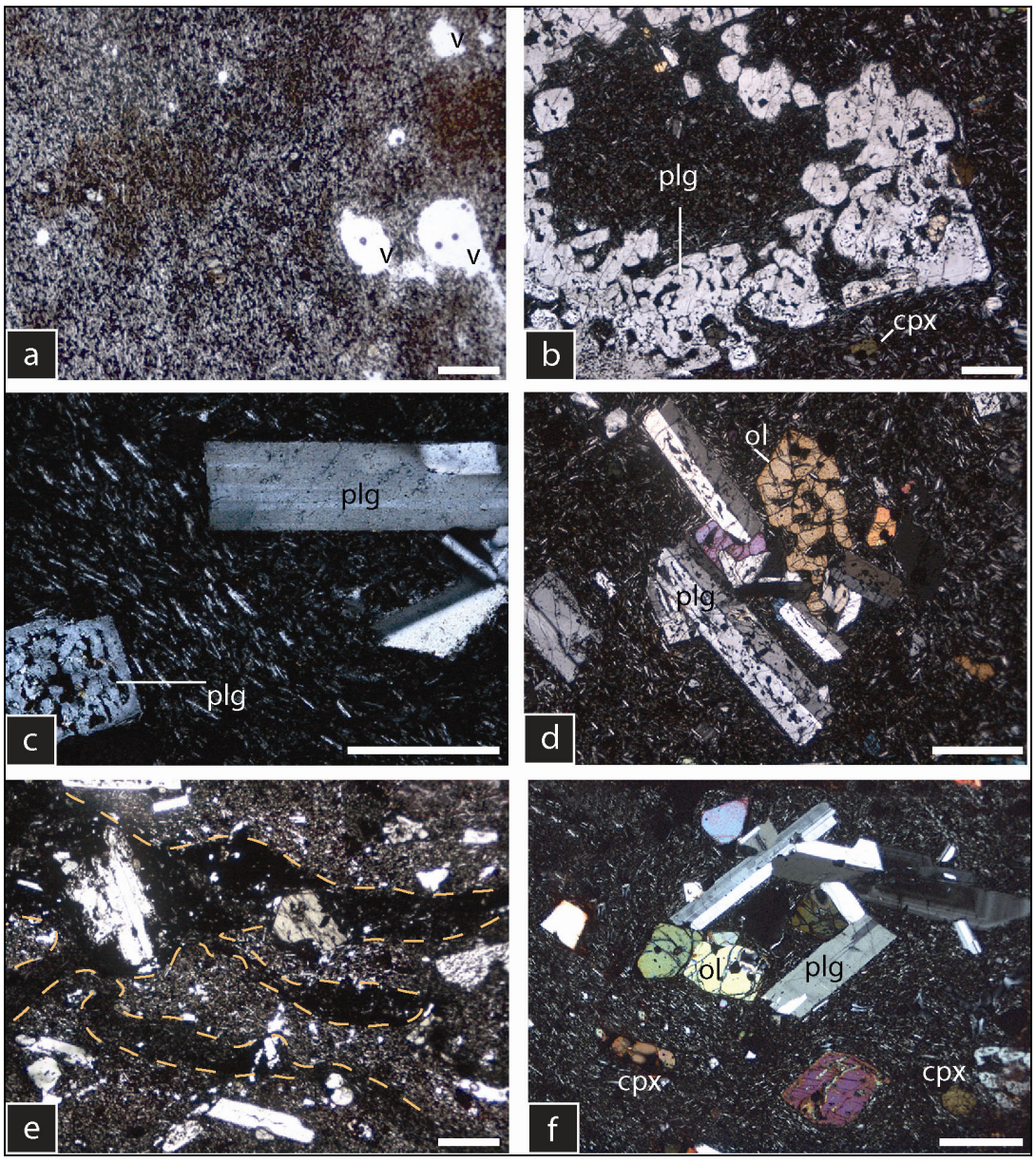

Figure 4.2: Petrographical features of mugearite. Scale bar is 1000 µm. (CPL: Cross Polarized Light, PPL: Plane Polarized Light).

a) Aphyric mugearite with scarce vesicles (v), CPL (sample N-240).
b) Spongy cellular gnawed plg, typical disequilibrium texture of mugearite (CPL, sample N-209).
c) Subhedral patchy cellular and euhedral stable plagioclase (CPL, sample N-209).
d) Glomeroporphyritic clusters of embayed ol, spongy (cellular) plg (CPL, sample N-016).
e) Dark colored bands in mugearite (PPL, sample N-191)
f) Glomeroporphyritic cluster of stable plg, ol and microphenocrysts of cpx (PPL, Sample N-209).

4.3 Caldera Related Rocks

Caldera forming pyroclastic products exhibit petrographical and mineralogical discrepancy towards the top of the sequence. Stratigraphically, pyroclastic sequence commences with plinian type fallouts. Lower section of this fallout (SID: 1031) is pale yellow to white in color and consists of white pumice, whereas upper sections (SID: 1032) are reddish to black in color and comprised of dark colored pumice. White pumices of the lower section bear euhedral to subhedral alkali feldspar phenocrysts in a highly vesicular glass. Microphenocrysts of clinopyroxene and olivine are very scarce (Figure 4.3.a). Opaque minerals are observed only as microlites. Moreover, dark plinian section, observed stratigraphically above the whitish fallout, is comprised of ternary feldspar, clinopyroxene and minute olivine. Clinopyroxene is subhedral, whereas olivine is anhedral and display slight resorption. Groundmass is highly vesicular aphyric glass (Figure 4.3.b).

In order to maintain an approach for the vertical variation of petrographical features in Nemrut ignimbrite (SID: 1345), it is investigated in three parts, namely lower (SID: 1033), middle (SID: 1034) and upper (SID: 1035) sections, where lower and upper sections represent the floor and roof of the ignimbrite respectively.

Lower sections of the ignimbrite (SID: 1033) bear euhedral to subhedral alkali feldspar phenocrysts in a densely welded crystal and lithic rich fine ash matrix. Aligned flattened pumice fragments define eutaxitic texture, characteristic of welded ignimbrite (McGhee et al., 1993). Moreover, abundant lithic fragments are comprised of presumably pre-volcanic basement, namely micaschists and former volcanics (Figure 4.3.c).

Samples representing middle section (SID: 1034) of the main ignimbrite show that it is moderately to slightly welded depending on the location. Pumice fragments display higher degrees of compaction and elongation in the more welded samples. In slightly welded samples, glass shards are observed to retain original bubble wall shapes. However, deformed and slightly compacted shards are also observed, especially adjacent to the crystal and lithic components. The middle ignimbrite section is dominantly crystal rich with anhedral spongy cellular phenocrysts of ternary feldspar (Figure 4.3.d). Subhedral clinopyroxene and anhedral moderately resorbed olivine represent the crystal components. Besides, lithic fragments of former volcanics are observed. Groundmass is composed of fine ash matrix.

Upper ignimbrite section (SID: 1035) is moderately welded with eutaxitic texture. Cognate glass shards are observed to be compacted, collapsed and elongated, chiefly along the

crystal fragments. This upper section is pumice rich with again anhedral spongy cellular ternary feldspars. Subhedral clinopyroxene and slightly resorbed anhedral olivine with opaque reaction rims represent the crystal assemblage. Groundmass is glassy with minor axiolitic devitrification.

The main ignimbrite is overlain by a pale-to-dark brown plinian fall unit (SID: 1036). Pumice samples are highly vesicular. Vesicles are round to oval in shape and sometimes exhibit foliation due to slight to moderately compaction and elongation of their walls. Subhedral to anhedral crystals and fragments of plagioclase, clinopyroxene and olivine represent the phenocryst assemblage set in a glassy matrix (Figure 4.3.e). Weak devitrification and scarce spherulitic subordinate mineralization is also observed on juvenile glass. Spherulitization is initiated via nanometer scaled chemically altered spherical nuclei (Figure 4.4).

A second ignimbrite, (from hereafter, Kantasi ignimbrite) is also confined to the northern escarpments and northern walls of the caldera. This second flow is observed to overlain former plinian falls mentioned above. It is moderately to densely weld. Eutaxitic texture is common in the welded sections. In unwelded or partially welded counterparts, subordinate feldspar mineralization with fan shape or axiolitic texture is observed in the vesicles of non-deformed pumice. Hence, vapor phase crystallization, which involves the growth of fine grained minerals in pore space within non-welded pyroclastic flow deposits (McPhie et al., 1993), is thought to occur after emplacement. Subhedral to anhedral cellular alkali feldspar with plagioclase, euhedral clinopyroxene and scarce olivine represent the phenocryst assemblage set in a glass rich fine grained matrix (Figure 4.3.f). Lithic fragments consist of either cognate or former volcanic activities.

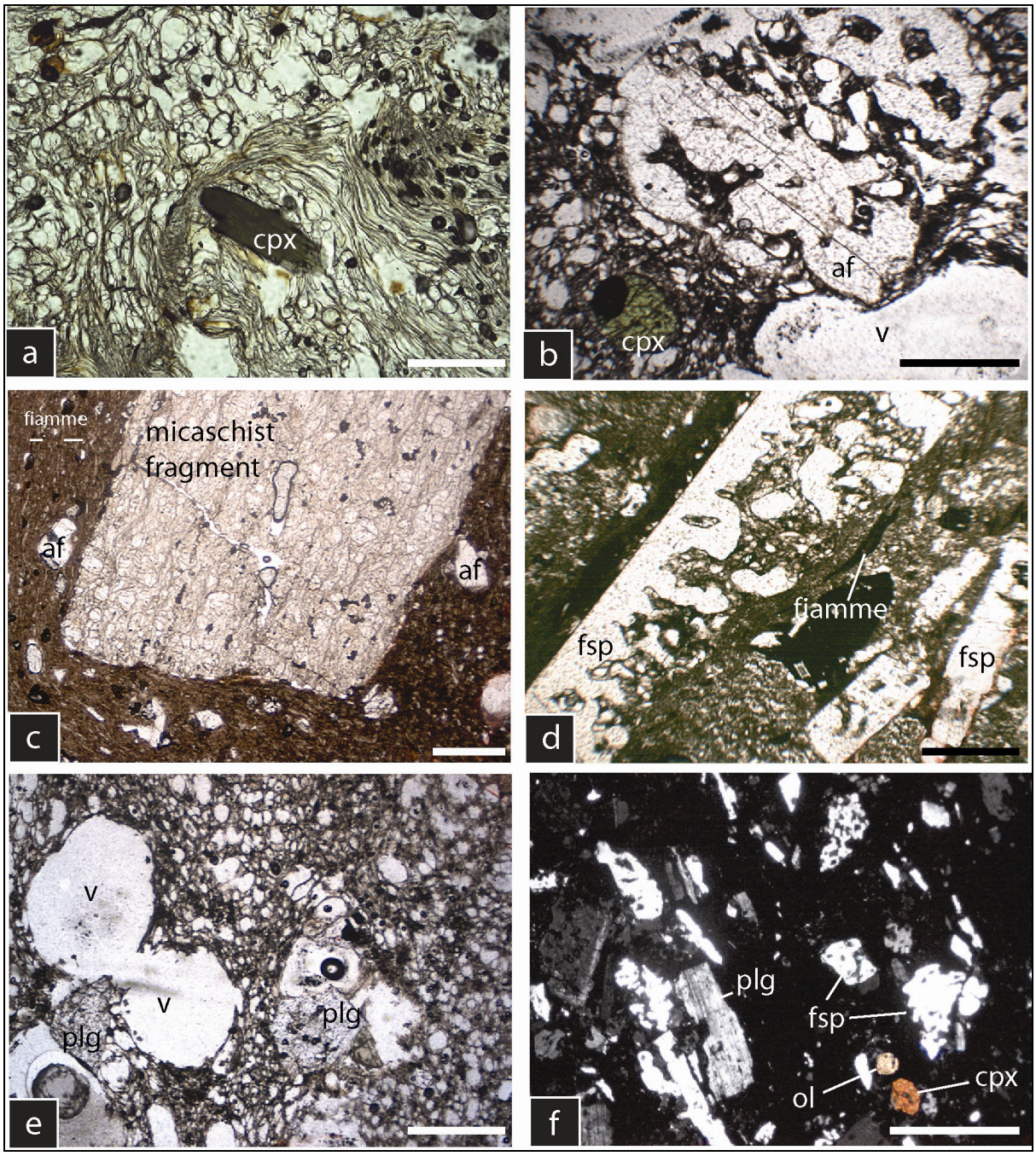

Figure 4.3: Petrographic features of caldera forming eruptions. Scale bar is 1000 µm. (v: vesicle, CPL: Cross Polarized Light, PPL: Plane Polarized Light)

a) Pale colored plinan fall underlying Nemrut ignimbrite (SID: 1031) PPL.
b) Dark colored plinian fall underlying Nemrut ignimbrite (SID: 1032), resorbed cellular af with euhedral cpx (PPL).
c) Welded lower sections of Nemrut ignimbrite (SID: 1033), metamorphic xenoliths are frequent (PPL). Fiamme are aligned along the micaschist fragment.
d) Upper sections of Nemrut ignimbrite (SID: 1034 and 1035), ternary feldspars are significantly resorbed and exhibit textures of disequilibrium. Welding is common (PPL).
e) Dark colored highly vesicular plinian fall overlying Nemrut ignimbrite (SID: 1036), plagioclase is subhedral (PPL).
f) Kantaşı ignimbrite (SID: 1037). Note the presence of both resorbed cellular ternary feldspar and relatively stable plagioclase.

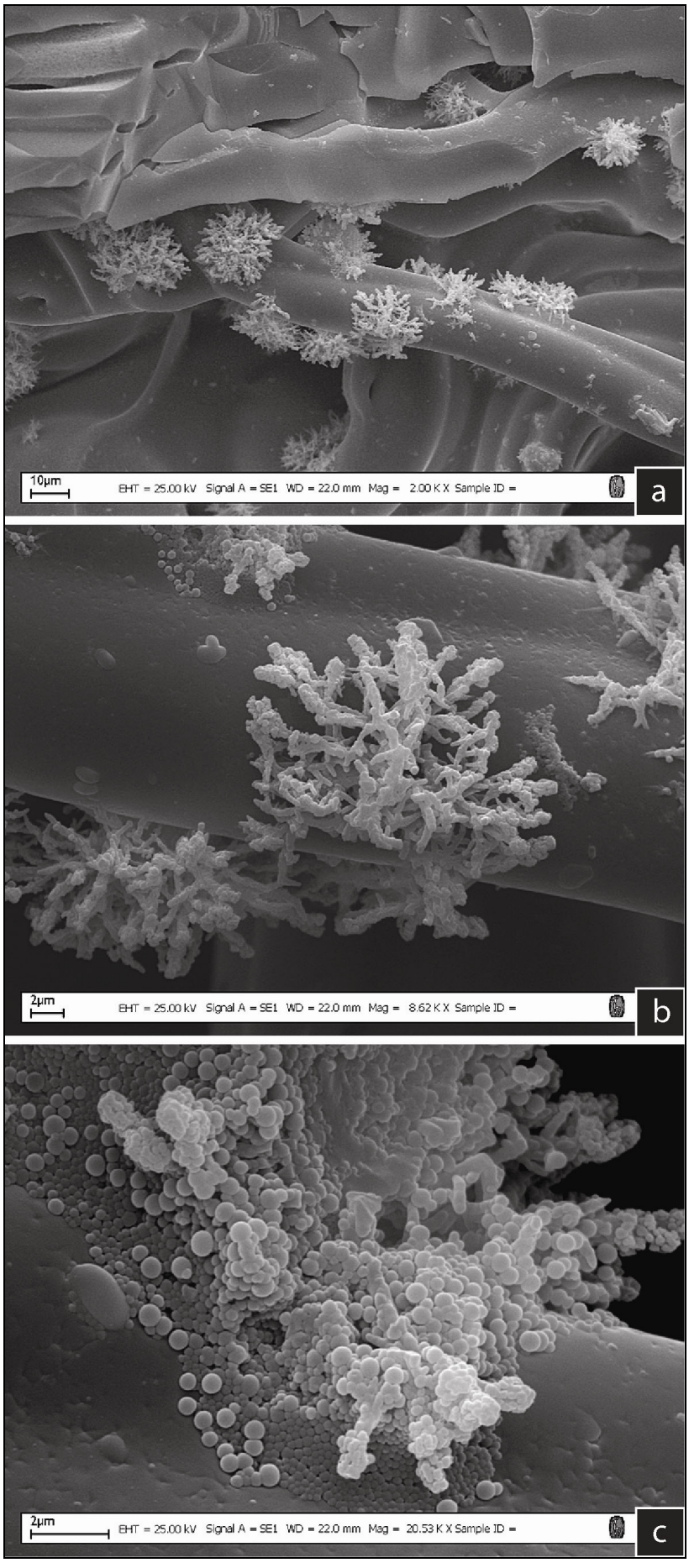

Figure 4.4: Spherulitic devitrification of pumice under Scanning Electron Microscope with various magnifications

a) Spherulite occurrences on glass shards.

b) Spherulites are formed due to the subsolidus alteration of the volcanic glass into radial crystallites.

c) Spherulitic devitrification initiates. Nanometer scaled spherical nuclei represent the beginning of devitrification.

4.4 Post-Caldera Silicic Rocks

Post-caldera stage of Nemrut volcanism is represented by bimodal rhyolitic and basaltic activity. Rhyolitic activity is peralkaline in character (comendite) and comprised of lava flows, dome emplacement and flows and associated phreatomagmatic products. On the other hand basaltic activity is represented by scoriaceous lava flows.

Post-caldera comendite lavas (SID: 1020 and 1010) are glass dominant lava flows, however pumiceous counterparts are also observed. Flow banding and micro-foliations are common (Figure 4.5.a). They are weakly porphyritic (Porphyritic Index: 15 -18 %). Euhedral to subhedral alkali feldspar with Carlsbad twinning represents the dominant phenocryst phase. Moreover, euhedral to subhedral clinopyroxene and olivine (fayalite) are either phenocrysts or microphenocrysts (Figure 4.5.b). Groundmass is glassy except vesicular and microcrystalline flow foliations. Quench crystals are also observed aligned sub-parallel to flow foliations.

Furthermore, there are enclaves with mafic-to-intermediate composition (benmoreite) detected in post-caldera comendite lavas. They occur as millimeter to decimeter-sized blobs or diffused droplets with irregular rounded margins (see section 3.1.6)

Phreatomagmatic eruptions from intra-caldera maars or explosion craters produced base surge deposits. Bread-crust bomb and juvenile pumice is common and reach up to several decimeters in size. These juvenile fragments are glass rich and dominantly alkali feldspar – phyric with smaller crystals and fragments of clinopyroxene and olivine.

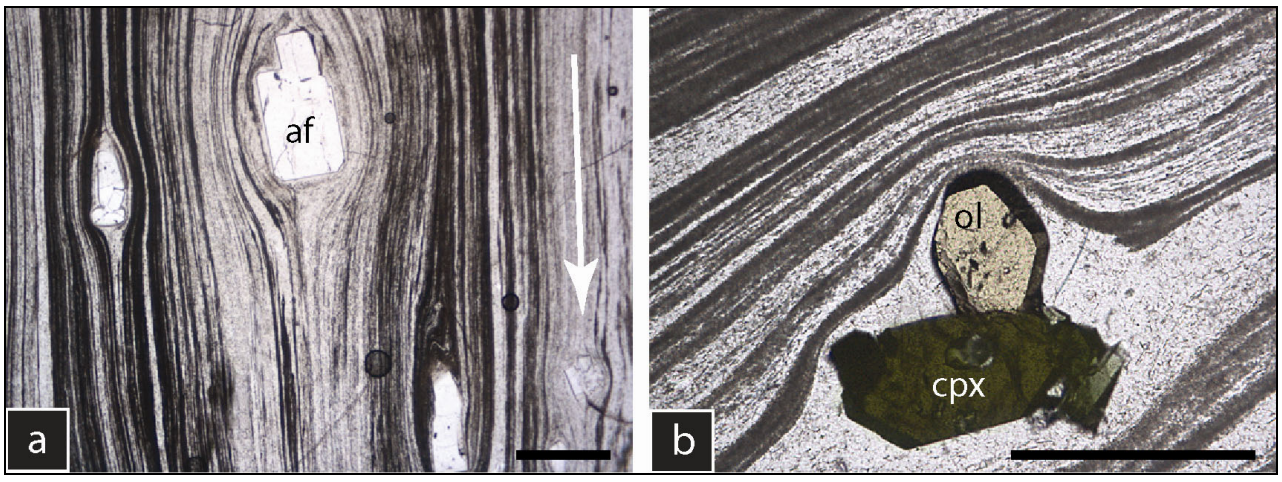

Figure 4.5: Post-caldera glassy comendite. Scale bar is 1000 µm. Plane polarized light. Arrow indicates the flow direction.
a) Euhedral alkali feldspar and b) clinopyroxene and fayalite in flow banded comendite glass.

4.5 Post-Caldera Basic Lavas

Post-caldera basic activity is confined to the northern rift zone on the northern escarpments of the caldera. Four distinct flows are observed in the region; however, they exhibit no chemical or physical discrepancy with each other. They are vesicular and strongly porphyritic (Porphyritic Index: 47 - 51%) with phenocrysts of plagioclase and olivine, whose sizes reach up to 1 mm (Figure 4.6.a). Polysynthetic twinning is omnipresent in plagioclase phenocrysts. Plagioclase and olivine display glomeroporphyritic texture due to synneusis (Figure 4.6.b). Clinopyroxene is not a significant phenocryst phase, stated erroneously in earlier studies (Atasoy et al., 1989; Özdemir et al., 2006). Rather, laths and clusters of nucleating interstitial clinopyroxene are observed with a maximum measured size of 50 µm. Groundmass is microcrystalline and display pilotaxitic texture with microlites of plagioclase, olivine and Fe- Ti oxides.

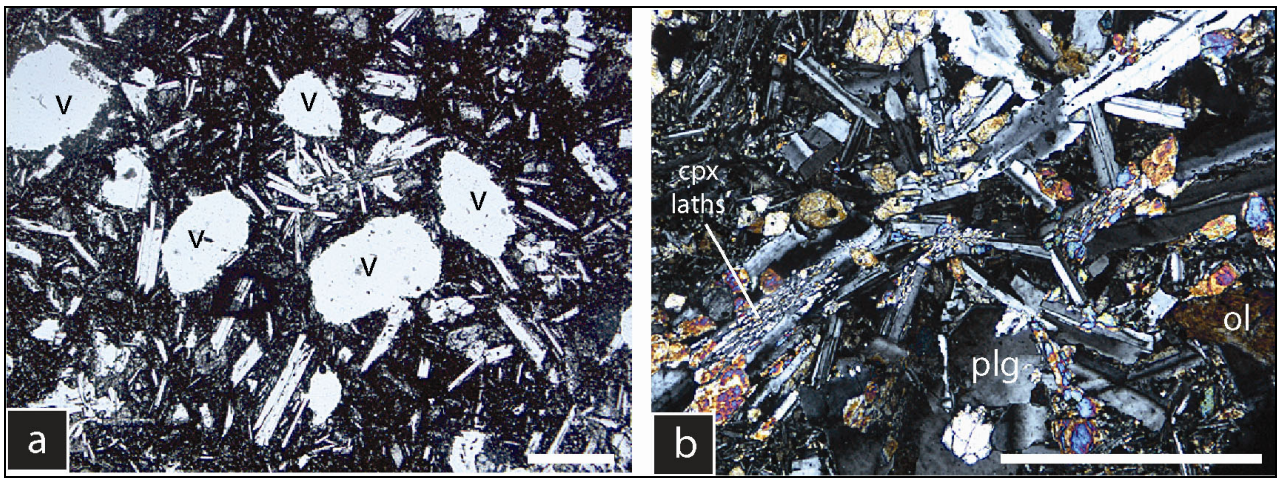

Figure 4.6: Post-caldera rift zone basalt. Scale bar is 1000 µ.

a) Highly vesicular (v) and strongly porphyritic. Plane polarized light.
b) Glomeroporphyritic clusters of plagioclase and olivine. Clinopyroxene is represented by radial laths. Cross polarized light.

4.6 Benmoreitic Enclaves in Comendites

Comendites of post-caldera stage (SID: 1010 -1020) and latest pre-caldera effusive stage (SID: 1040) bear significant enclaves with benmoreitic compositions (for rock geochemistry see Chapter 5). They occur as millimeter to decimeter-sized blobs or diffused droplets with irregular rounded margins (Figure 4.7.a). Dispersed phenocrysts and/or phenocrystic cumulates surrounded by mafic matrix are occasionally observed in rhyolitic glass (Figure 4.7.b). These enclaves display varying degrees of interminglement of mafic and rhyolitic magma, due to their varying textural properties.

In general, two main petrographical types of enclaves occur in post-caldera comendites: 1) Enclaves with similar textural properties with the historic basalt (Type I) and, 2) Enclaves with similar textural properties with the pre-caldera mugearite (Type II).

4.6.1 Type I Enclaves

These enclaves dominantly occur in post-caldera glassy comendites both in intra-caldera regions and the extra-caldera rift zone. Between enclave and comendite glass, significant interface zone is formed probably because of thermal discrepancy between inclusion and the host. The interface between host and the enclave is represented by two distinct sub-zones: 1) fine grained microcrystalline margin, composed of mafic minerals of those in the enclaves and, 2) highly vesicular pumiceous aphyric glass in contact with the felsic host. The boundary between pumiceous and microcrystal-rich zones is represented by elongated vesicles (Figure 4.7.b). Such textural relationships strongly testify to the concurrent presence of mafic and silicic melts and their liquidus interaction within the magma chamber, a common feature of well-known bimodal peralkaline associations (i.e. Peccerillo et al., 2003).

Type I enclaves are moderately porphyritic (P.I. 30 – 45%) with phenocrysts of plagioclase and olivine exhibiting scattered glomeroporphyritic clusters (Figure 4.7.c-d). Due to their porphyritic nature, these enclaves probably have relatively longer residence time in magma chamber. As in basalts, Type I enclaves does not bear clinopyroxene as a phenocrystic phase, but only as scarce microlites. Groundmass is microcrystalline-to-crystalline and exhibits pilotaxitic texture.

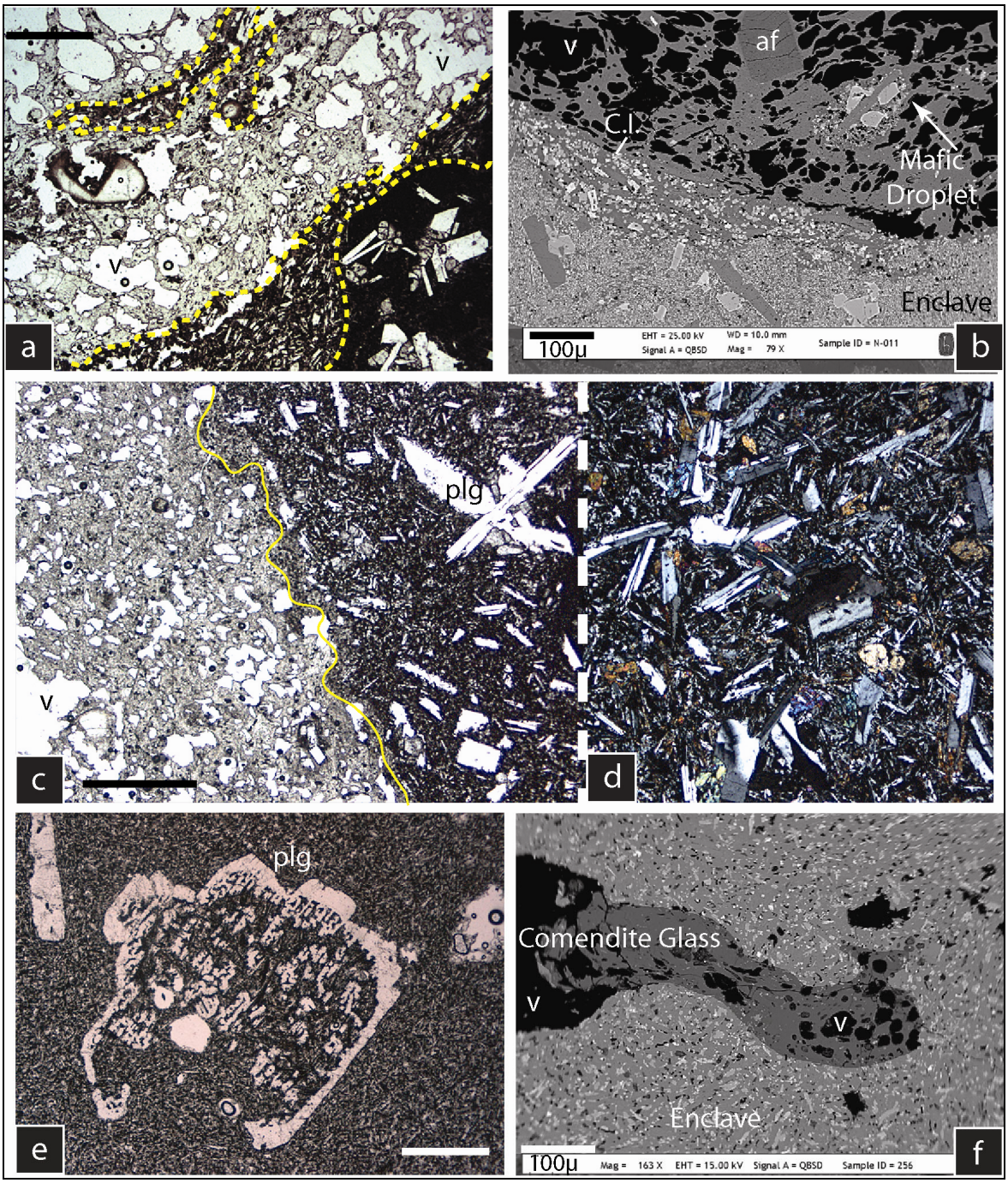

Figure 4.7: Petrographical properties of benmoreitic enclaves in peralkaline rhyolites. Scale bars are 1000 µm unless stated.

a) Enclave and diffused blebs in pumicified vesicular (v) comendite glass. Plane polarized light.
b) Backscattered view of enclave, crystalline interface (C.I) and highly vesicular interface between the comendite glass. Note the alignment of vesicles along the enclave rim. Droplets of mafic material are dispersed in comendite.
c) Characteristic Type I enclave with similar petrographic features with historic basalt (PPL).
d) Type I enclave under cross polars.
e) Highly resorbed ghost-like skeletal cellular plg in Type II enclaves. Note the textural similarity between mugearites (Fig. 4.2) and Type II enclaves. Plane polarized light.
f) Backscattered view of the boundary between comendite glass and Type II enclave. Comenditic melt intrudes into benmoreitic melt. Note the originating vesicles (v).

4.6.2 Type II Enclaves

These enclaves are observed in the hyaline comendites of the historic rift zone activity (SID: 1010) and the latest pre-caldera comendites (SID: 1040) on caldera rims. Transition from enclave to rhyolitic glass is dominantly represented by a vesicular pumiceous zone. Microcrystalline interface, contrary to Type I enclaves, is usually absent or characterized by very thin marginal films (Figure 4.7.f).

Disequilibrium textures and xenocrysts are often observed. These enclaves are moderately porphyritic (Porphyritic Index: 36 – 40 %) with phenocrysts of ternary feldspar, clinopyroxene and olivine. Feldspars exhibit extreme cellular skeletal texture (Figure 4.7.e). Alkali feldspar is observed to mantle plagioclase. Besides, subordinate microcrysts of amphibole are observed within the embayed inner portions of resorbed plagioclase core zones (see next chapter). Clinopyroxene is euhedral to subhedral, whereas olivine is often embayed and display opaque rims.

4.7 Phreatomagmatic Trachytic Ejecta

Intra-caldera phreatomagmatic activity (8 ± 3 ka) produced extensive base surge deposits (SID: 1020). These deposits bear significant lithic ejecta, which exhibit holocrystalline textural features. Generally, two types of holocrystalline ejecta have been discriminated according to proportion of the phenocrysts. The first type is holocrystalline semi-equigranular with P.I. ~75%. However, coarse feldspar phenocrysts exhibit seriate porphyritic texture. The second type is holocrystalline porphyritic with P.I. < 50%.

Ejecta are observed as centimeter-to-decimeter sized fragments within the marginal zones of the deposits. Their sizes naturally increase towards the intra-caldera explosion center (Göl Tepe maar). At the floor of the maar, fragments are block sized with significant hydrothermal alteration. In their recent paper, Özdemir et al (2006) misinterpret them as monzonite (Çubukçu et al, 2007).

Granular Ejecta (P.I. ~ 75%) G-Ejecta

These fragments are holocrystalline porphyritic with phenocrysts of alkali feldspar, plagioclase, clinopyroxene, olivine, amphibole, Fe-Ti oxides and quartz (Figure 4.8.a).

Feldspars represent the largest crystals in the rock. Alkali feldspars are perthitic with optically visible coherent lamellar intergrowths of Na and K rich phases. Alkali feldspars are dominantly subhedral and have dusty appearance. Plagioclases, on the other hand, are

anhedral and mantled by dusty alkali feldspar perthites (Figure 4.8.b). They exhibit complex twinning.

Olivine is anhedral and exhibit transformation to clinopyroxene and amphibole. Olivine is usually mantled concentrically by ferromagnesian aggregates of amphibole, clinopyroxene and aenigmatite (See Chapter 5 - Mineralogy).

Clinopyroxene is sub-to-anhedral and its typical green color is especially significant rimwards. They are often observed to be grown together with amphibole. Amphibole is anhedral and pale brownish in color. Although rare, euhedral microphenocrysts of amphibole have been observed. Fe-Ti oxides are frequently found in the aggregates of relict olivine, clinopyroxene and amphibole. Aenigmatite is also observed along the rims of relict olivine and amphibole. Quartz is anhedral and interstitial (See Chapter 5 - Mineralogy).

Textural properties of this type of ejecta testify to the relatively slower and subvolcanic conditions for its cooling history.

Porphyritic Ejecta (P.I. < 50%) P-Ejecta

These fragments are found as decimeter-to-meter sized blocks in the intra-caldera Göl Tepe maar crater. Trachytic in nature, these fragments are holocrystalline and dominantly feldspar-phyric. Alkali feldspar and plagioclase phenocrysts, sometimes-exceeding 8000 μ, and relatively smaller clinopyroxene set in a crystalline groundmass comprised of feldspar, clinopyroxene and Fe-Ti oxides.

Feldspars exhibit remarkable disequilibrium textures. Coarse phenocrysts (ø > 5000 μm) of alkali feldspar are dominantly anhedral and are spongy boxy-to-cellular (Figure 4.8.c). They are observed as embayed, gnawed instable crystals. Plagioclase is represented by relatively more stable phenocrysts (ø < 5000 μm) and microphenocrysts. Although they are not resorbed like alkali feldspars, their rims contain reaction belts (Figure 4.8.c). They exhibit fine lamellar polysynthetic and complex twinning. They are seldom poikilitic with concentrated inclusions of clinopyroxene.

Clinopyroxene rarely exceeds 1000 μm and generally exhibit evident resorption (Figure 4.8.d). They are frequently poikilitic with Fe-Ti oxides. Ghost-like crystals are common and are penetrated by microcrystalline groundmass. Fe-Ti oxides are microcrystals either in groundmass or inclusions in phenocrysts.

Groundmass is crystalline and composed of microcrystals of dominantly alkali feldspar with concentric zoning, polysynthetic plagioclase, clinopyroxene and Fe-Ti oxides.

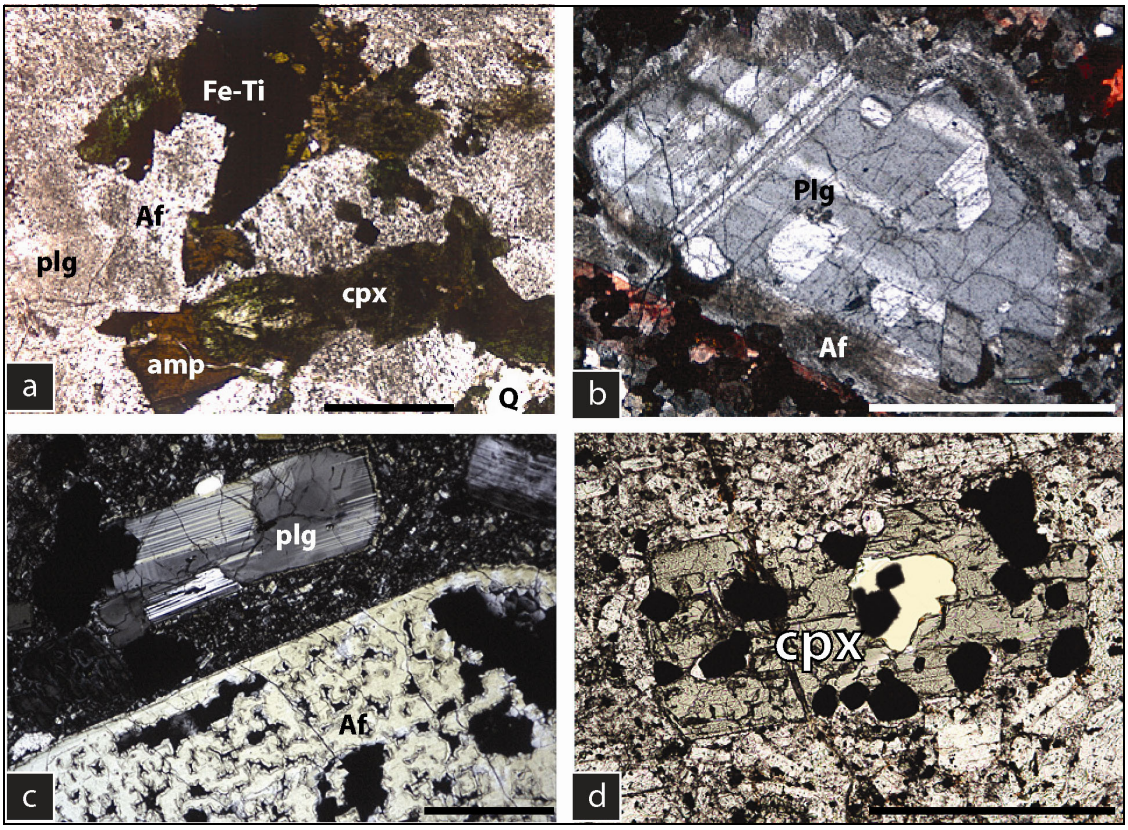

Figure 4.8: Post-caldera trachytic phreatomagmatic ejecta. PPL: Plane Polarized Light, CPL: Cross Polarized Light. Scale bars are 500 μm.

a) Type G granular ejecta consists of alkali feldspar, plagioclase, clinopyroxene, amphibole and Fe-Ti oxides, PPL.
b) Type G ejecta, plagioclase is anhedral and mantled by dusty alkali feldspar, CPL.
c) Type P porphyritic ejecta, alkali feldspar phenocrysts are anhedral with spongy-to-boxy cellular disequilibrium texture. On the other hand, plagioclase is subhedral with weak mantling of alkali feldspar, CPL.
d) Type P ejecta, resorbed clinopyroxene is subhedral with abundant opaque inclusions, poikilitic texture, PPL.

4.8 Conclusions

The vast majority of the volcanic rocks produced throughout the eruptive history of Nemrut stratovolcano are felsic (trachytes and rhyolites) with rare basalts. Intermediate rocks (benmoreites), however, are found as enclaves in glassy rhyolites. All rocks have various volcanic textures, with the exception of trachytic ejecta exhibiting holocrystalline granular texture.

Basalts are highly porphyritic with coarse plagioclase (plg) and olivine (ol) phenocrysts. Mugearites are dominantly porphyritic, with rare aphyric samples. They exhibit significant disequilibrium textures with resorbed anhedral and frequently spongy/boxy cellular plagioclase. Olivine and to a lesser degree, clinopyroxene (cpx) exhibit resorption. Mugearites sometimes bear glomeroporphyritic clusters with lack of disequilibrium. Benmoreitic enclaves are of two dominant types, petrographically resembling to basalt (Type I) and to mugearite (Type II). Type I bears microcrystalline and pumiceous interface with the host rhyolite, in which irregular blebs of mafic melt are observed, indicating interminglement. Type II, however, lacks of interface between its host rhyolite. Trachytes are of varying degrees of crystallization, being highly (plg)/af-phyric in metaluminous samples and af-phyric with glassy-to-crystalline groundmass in peralkaline counterparts. Cpx and ol are common phenocrysts. Trachytic flow texture is confined to hypocrystalline varieties. Rhyolites are dominantly hypohyaline with phenocrysts of af, cpx and fayalite (fa). Flow bands, comprised of minute crystallites, are common in rhyolites. One of the most notable characteristics of peralkaline rhyolites of pre-caldera (SID: 1040) and post-caldera (SID: 1020-1010) is the abundant benmoreitic enclaves displaying varying degrees of interminglement with mafic melt.

Caldera related rocks, especially Nemrut ignimbrite display stratigraphic, thus temporal, petrographical variation. Lowermost plinian underlying the main Nemrut ignimbrite unit (SID: 1031) is euhedral af-phyric with cpx and scarce ol. Nemrut ignimbrite, although scatter is observed within the unit, bears spongy cellular an/subhedral af. Unlike the feldspars of mugearites (and Type II benmoreitic enclaves), these feldspars do not exhibit significant chemical reaction with the melt. What could be inferred is that these crystals have undergone rapid decompression during eruption (c.f. Hibbard, 1994; Deer et al., 2001). Uppermost plinian fallout (SID: 1036) bears sub/euhedral plagioclase with cpx and ol. Kantaşı ignimbrite bears both spongy af and relatively stable plg.

Lithic ejecta of post-caldera phreatomagmatic eruptions are of dominantly two types. Type G is holocrystalline granular, whereas Type P is porphyritic with strong disequilibrium textures.

CHAPTER 05

MINERALOGY

5 MINERALOGY

Modal mineralogical assemblages for each rock type have been obtained by regular point counting method. Point counting has been performed on a minimum of three samples for each rock type concerning the volcanostratigraphy. 1,500 – 2,000 points have been counted for each thin section. Distribution of mineral assemblages as well as accessory phases has been given on Figure 5.1 and Table 5.1. Each microprobe analysis has been labeled with "Electron Microprobe ID (emid)" in the constructed Nemrut Petrology database (see Chapter 2.2 - Data Handling and Integration). Therefore, throughout the text, worth-to-mention analyses will be referenced by their respective emid.

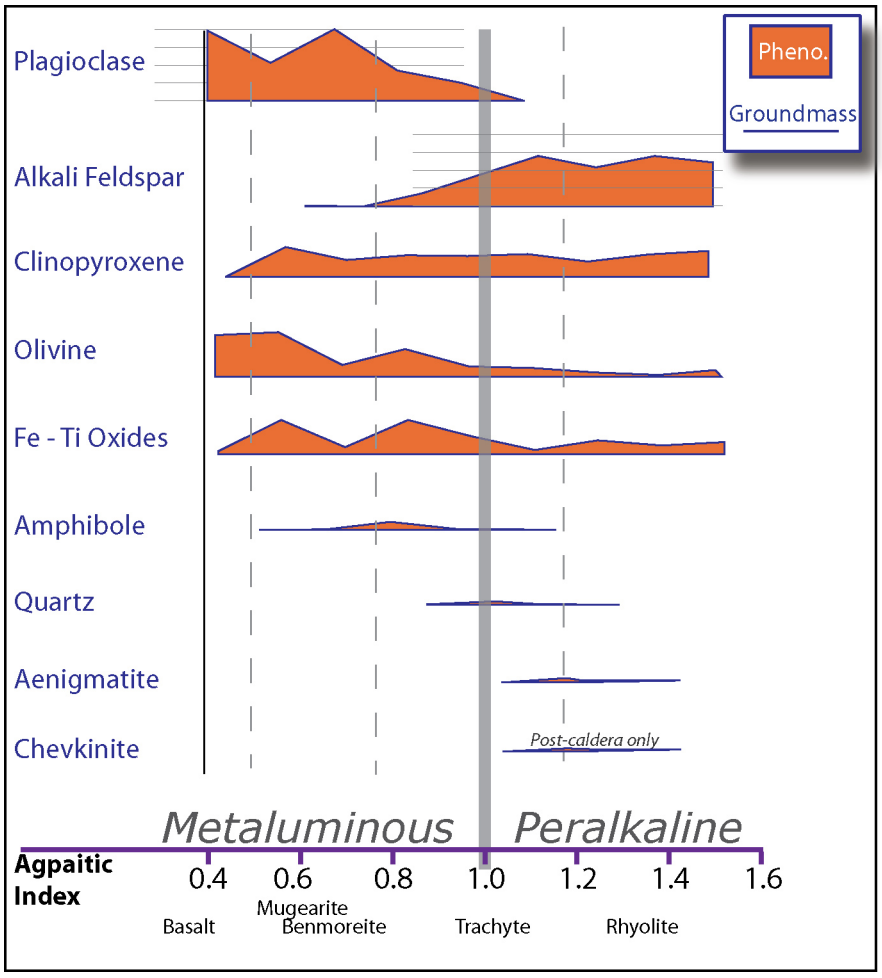

Figure 5.1: Distribution of mineral assemblages in Nemrut eruptive products.

In Nemrut volcanics, feldspar is by far the most abundant crystallized major phase, followed by clinopyroxene, olivine, Fe-Ti oxides and rarely amphibole. Accessory phases include apatite, aenigmatite, iron sulfides, zircon and chevkinite.

Basalts bear essentially plagioclase + olivine + magnetite ± clinopyroxene. Mugearites and benmoreitic enclaves exhibit slightly more evolved assemblage of plagioclase + clinopyroxene + olivine + magnetite ± ilmenite ± alkali feldspar ± apatite. Trachytes are represented by alkali feldspar + clinopyroxene + olivine + magnetite ± ilmenite ± amphibole ± aenigmatite ± aegirine ± apatite. Finally rhyolites contain alkali feldspar + clinopyroxene + olivine + ilmenite ± magnetite ± amphibole ± quartz ± aenigmatite ± apatite.

Table 5.1: Modal proportions of phenocrysts, groundmass and/or glass in Nemrut eruptive units. SID: Stratigraphic ID, PID: Petrologic ID, PI: Porphyritic Index. Abbreviations are as in Table 4.1.

								Percent Normalized Proportions of Phenocrystic Phases							
		Sample	**SID**	**PID**	**Groundmass(%)**	**Glass (%),**	**PI (%)**	**af**	**plg**	**cpx**	**ol**	**Fe-Ti**	**amp**	**aen**	**q**
Pre-caldera rocks	*Mugearite*	N-016	1050	4010	70,50		29,50	1,02	54,24	17,63	18,98	8,14			
		N-240	1050	4010	93,50		6,50		15,38	23,08	35,38	26,15			
		N-209	1050	4010	70,80		29,20	1,37	56,51	17,12	13,70	11,30			
	Comendite	N-149	1060	4021	82,60		17,40	60,92		9,77		4,60	13,22	4,02	7,47
		N-135	1070	4021	89,00		11,00	70,91		20,00		6,36		2,73	
		N-194	1040	4021	9,30	81,50	9,20	53,26		26,09	11,96	8,70			
		N-227	1040	4021		83,80	16,20	66,30		6,79	2,47	8,02	4,32	1,23	10,86
	Pantellerite	N-098	1040	4025	6,30	80,80	12,90	74,42		13,18	9,30	2,33		0,78	
	Comenditic trachyte	N-080	1040	4031	60,70		39,30	76,59		12,98	4,07	5,85	0,51		
		N-181	1040	4031	63,10		36,90	75,07		15,18	3,25	5,15		1,36	
		N-239	1060	4031	74,70		25,30	62,85		15,42	7,51	10,28	3,95		
		N-151	1070	4031	73,20		26,80	91,79		8,21					
	Pantelleritic trach.	N-188	1070	4035	73,70		26,30	79,47		11,03	4,56	4,94			
	Trachyte	N-268	1033	4039	70,90	10,40	18,70	89,84		5,35	0,53	4,28			
		N-136	1060	4039	67,50		32,50	74,15		13,23	4,00	8,62			
		N-064	1070	4039	75,20		24,80	73,39		11,29	4,03	4,84			6,45
Nemrut Ignimbrite	*Trachyte*	N-022	1031	4039		88,50	11,50	68,70		13,91	11,30	6,09			
		N-047	1032	4039		75,00	25,00	42,80	38,40	11,60	6,00	1,20			
		N-037	1034	4039	80,10		19,90	87,44		7,54	2,01	3,02			
		N-259	1037	4039	64,00		36,00	37,22	36,11	15,28	9,44	1,94			
		N-036	1036	4039	82,60		17,40	74,71		9,20	10,34	5,75			
Post-caldera rocks	*Basalt*	N-264	1010	8060	51,00		49,00		78,37		20,00	1,63			
		N-258	1010	8060	47,30		52,70		76,85		22,39	0,76			
	Comendite	N-254	1010	8071	5,10	80,00	14,90	74,50		14,77	8,05	2,68			
		N-305	1020	8071		93,00	7,00	81,43		15,71		2,86			
		N-065	1020	8071	6,80	74,80	18,40	81,52		13,04	5,43				
	Type II enclave	N-050	1010	8080	63,40		36,60		79,51	10,93	6,01	3,01	0,55		
	Type I enclave	N-256	1010	8080	54,50		50,90		77,20	2,30	18,30	2,20			

5.1 Mineral Chemistry

Chemical analyses of mineral species have been carried out on various wavelength and energy dispersive spectrometers. Analytical conditions and reference materials have been given in Chapter 2 - Methodology.

5.1.1 Feldspar

Feldspars are by far the dominant mineral species in all of the Nemrut volcanic rocks. Table 5.2 reports selected typical feldspar compositions and Figure 5.2.a depicts the distribution of feldspars in various rock types. Occurrence of plagioclase is confined to metaluminous products, whereas peralkaline (Agpaitic Index, AI > 1) products bear alkali feldspar. Plagioclase is observed in basalts (An_{66-36}), mugearites (An_{58-29}), benmoreitic enclaves (An_{69-61}), rare metaluminous trachytic lava flows and stratigraphically uppermost trachytic

pyroclastic units (SID: 1036 - 1034). This trend conforms to the experimental studies of Scaillet and Macdonald (2001), which states that the crystallization of plagioclase is suppressed as soon as the melt becomes peralkaline. Alkali feldspar, being either microlite or inclusion, virtually exists on all types of rocks except basalts. Feldspar compositions exhibit slight bimodality especially in lava and dome flows, being dominantly located on either plagioclase or Na-rich alkali feldspar fields. However, ternary feldspars of pyroclastic products, mafic enclaves and some metaluminous trachytes fill the compositional gap between plagioclase and alkali feldspar, exhibiting a gradual transition into alkali varieties.

Mafic Rocks

Primary feldspar in basalts is labradorite - andesine plagioclase (An_{66-36}) (Figure 5.2.b). Phenocrysts (1000 > ø > 200 μm) exhibit normal zoning with rimwards enrichment of Ab. Furthermore, as the crystals get smaller in size, An contents tend to decrease down to 15 % in microlites.

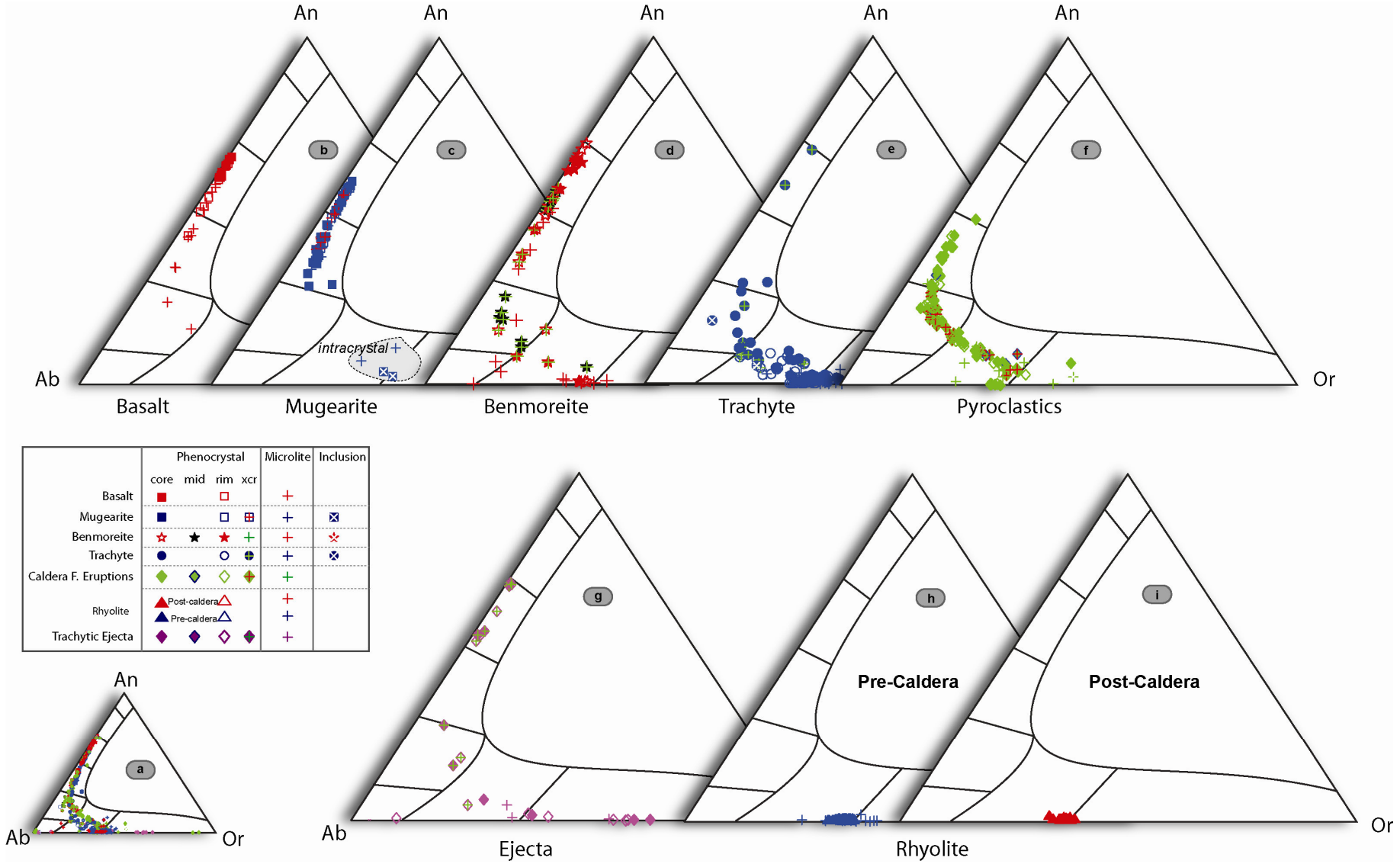

Figure 5.2: Feldspars of Nemrut eruptive units depicted on Ab-An-Or diagrams

Table 5.2: Selected feldspar analyses, calculated for 32 oxygens. SID: Stratigraphic ID, emid: Electron Microprobe ID, Location (0: center, 9: border), Stability (0: disequilibrium, 9: stable). B: Basalt, M: Mugearite, BM1/2 (Benmoreitic enclave Type 1 or 2), (C) T: (Comenditic) Trachyte, C: Comendite, P: Pantellerite

	PRE-CALDERA ROCKS										NEMRUT IGNIMBRITE										
Sample	**N-141**	**N-141**	**N-281**	**N-188**	**N-239**	**N-136**	**N-083**	**N-016**	**N-016**	**N-209**	**N-080**	**N-080**	**N-098**	**N-098**	**N-194**	**N-022**	**N-047**	**N-247**	**N-023**	**N-233**	**N-036**
SID	1080	1080	1070	1070	1060	1060	1060	1050	1050	1050	1040	1040	1040	1040	1040	1031	1032	1033	1034	1035	1036
subtip	T	T	CT	P	CT	T	CT	M	M	M	CT	CT	P	P	C	T	T	T	T	T	T
emid	1535	1539	763	1100	1352	1165	372	70	74	507	1049	1050	1017	1003	1304	136	285	1464	187	560	238
Location	0	0	9	0	0	0	0	0	9	0	0	9	9	0	0	0	0	0	9	9	0
Stability	9	9	9	9	9	9	0	0	0	9	9	9	9	9	9	9	0	9	9	0	9
Size (µ)	500	1650	6000	2000	2000	2000	500	3000	3000	35	1500	1500	500	30	2000	1000	1500	500	150	1500	1200
SiO_2	65,57	60,93	67,32	67,85	64,70	66,69	65,72	54,60	52,91	57,84	66,87	67,07	67,22	68,68	66,93	67,53	65,31	57,99	57,00	64,08	57,57
Al_2O_3	20,79	23,94	19,41	18,58	21,23	19,37	20,62	28,09	28,97	25,09	19,17	18,57	18,44	16,43	19,01	18,92	20,77	26,04	25,50	21,85	27,06
FeO	0,42	0,52	0,33	0,48	0,17	0,25	0,15	0,52	0,59	0,83	0,27	0,75	0,79	2,85	0,31	0,45	0,20	0,36	0,57	0,28	0,35
MgO	0,04	0,00	0,02	0,00	0,00	0,00	0,02	0,08	0,12	0,06	0,00	0,00	0,03	0,00	0,00	0,01	0,00	0,03	0,06	0,00	0,06
CaO	1,97	5,85	0,44	0,05	2,00	0,47	1,36	10,92	11,87	8,24	0,20	0,11	0,04	0,05	0,10	0,05	1,86	8,45	8,73	2,94	9,22
Na_2O	7,84	6,77	6,92	7,59	7,49	7,28	7,41	5,35	4,80	6,40	7,07	7,74	7,81	8,29	7,47	7,92	7,34	6,64	6,72	7,92	6,30
K_2O	2,49	1,12	6,95	6,14	4,76	6,48	5,57	0,41	0,29	0,79	6,88	6,19	5,68	4,34	6,19	5,95	5,00	0,56	0,85	3,02	0,59
Total	99,11	99,12	101,38	100,68	100,35	100,55	100,84	99,96	99,55	99,25	100,46	100,43	100,00	100,64	100,02	100,83	100,48	100,06	99,43	100,09	101,14
Si	11,64	10,94	11,90	12,04	11,52	11,88	11,66	9,89	9,65	10,48	11,93	11,98	12,02	12,22	11,96	11,98	11,61	10,41	10,35	11,40	10,24
Al	4,38	5,09	4,04	3,89	4,46	4,07	4,31	5,99	6,23	5,36	4,03	3,91	3,88	3,45	4,00	3,95	4,35	5,51	5,46	4,58	5,67
Fe	0,06	0,08	0,05	0,07	0,03	0,04	0,02	0,08	0,09	0,13	0,04	0,11	0,12	0,42	0,05	0,07	0,03	0,05	0,09	0,04	0,05
Mg	0,01	0,00	0,00	0,00	0,00	0,00	0,01	0,02	0,03	0,02	0,00	0,00	0,01	0,00	0,00	0,00	0,00	0,01	0,02	0,00	0,02
Ca	0,38	1,07	0,08	0,01	0,38	0,09	0,26	2,12	2,32	1,60	0,04	0,02	0,01	0,01	0,02	0,01	0,35	1,62	1,70	0,56	1,76
Na	2,71	2,37	2,37	2,61	2,59	2,52	2,55	1,88	1,70	2,25	2,44	2,68	2,71	2,86	2,59	2,72	2,53	2,31	2,36	2,73	2,17
K	0,57	0,26	1,57	1,39	1,08	1,47	1,26	0,09	0,07	0,18	1,56	1,41	1,29	0,98	1,41	1,35	1,13	0,13	0,20	0,69	0,13
Tot	19,78	19,82	20,03	20,01	20,07	20,07	20,08	20,08	20,10	20,03	20,05	20,11	20,03	19,96	20,04	20,08	20,03	20,05	20,18	20,01	20,06
An	10,30	29,00	2,07	0,25	9,44	2,20	6,35	51,80	56,78	39,69	0,93	0,52	0,18	0,26	0,50	0,24	8,83	39,97	39,86	14,10	43,26
Ab	74,19	64,05	58,95	65,10	63,85	61,68	62,67	45,91	41,57	55,77	60,40	65,18	67,52	74,18	64,39	66,77	62,95	56,88	55,50	68,67	53,43
Or	15,52	6,95	38,98	34,65	26,71	36,12	30,98	2,29	1,65	4,55	38,67	34,29	32,30	25,55	35,11	32,98	28,23	3,16	4,64	17,23	3,32

	POST-CALDERA ROCKS															
Sample	**N-146**	**N-220**	**N-220**	**N-220**	**N-220**	**N-272**	**N-272**	**N-272**	**N-272**	**N-011**	**N-011**	**N-050**	**N-050**	**N-258**	**N-258**	**N-254**	**N-254**
SID	1020	1020	1020	1020	1020	1020	1020	1020	1020	1010	1010	1010	1010	1010	1010	1010	1010
subtip	C	T	T	T	T	T	T	T	T	BM1	BM1	BM2	BM2	B	B	C	C
emid	912	508	509	547	548	872	873	887	888	3	4	1494	1495	819	820	632	633
Location	0	0	9	0	9	0	9	0	9	0	9	0	9	0	9	0	9
Stability	9	9	9	0	0	9	9	0	0	9	9	0	0	9	9	9	9
Size (µ)	1500	7000	7000	1000	1000	2500	2500	3500	3500	1200	1200	2500	2500	1000	1000	2000	2000
SiO_2	67,57	65,06	66,16	54,36	54,22	67,10	67,11	51,10	51,61	52,15	51,74	58,20	58,65	52,04	55,54	66,94	67,77
Al_2O_3	19,20	19,37	19,22	28,78	28,61	19,03	18,70	30,72	31,16	30,71	31,29	25,82	25,49	30,28	27,93	18,46	18,79
FeO	0,17	1,23	0,39	0,48	0,51	0,26	0,31	0,42	0,45	0,55	0,72	0,37	0,28	0,56	0,90	0,17	0,23
MgO	0,00	0,00	0,00	0,04	0,15	0,01	0,00	0,13	0,07	0,13	0,15	0,02	0,00	0,14	0,12	0,01	0,00
CaO	0,19	1,26	0,37	11,34	11,12	0,31	0,22	14,20	14,45	13,29	13,67	7,93	7,46	13,54	10,93	0,12	0,11
Na_2O	7,21	8,12	6,94	5,00	5,25	7,12	6,57	3,56	3,63	3,94	3,79	6,99	7,22	3,98	5,54	7,86	7,67
K_2O	6,47	4,72	6,59	0,31	0,27	7,02	7,56	0,12	0,17	0,13	0,11	0,44	0,51	0,09	0,33	5,99	6,37
Total	100,81	99,74	99,67	100,30	100,13	100,83	100,48	100,25	101,53	100,90	101,47	99,76	99,61	100,61	101,30	99,55	100,94
Si	11,98	11,67	11,89	9,81	9,80	11,94	11,99	9,30	9,28	9,40	9,29	10,47	10,54	9,41	9,92	12,01	12,00
Al	4,01	4,10	4,07	6,12	6,09	3,99	3,94	6,59	6,60	6,52	6,62	5,47	5,40	6,45	5,88	3,90	3,92
Fe	0,02	0,18	0,06	0,07	0,08	0,04	0,05	0,06	0,07	0,08	0,11	0,06	0,04	0,08	0,13	0,03	0,03
Mg	0,00	0,00	0,00	0,01	0,04	0,00	0,00	0,04	0,02	0,03	0,04	0,01	0,00	0,04	0,03	0,00	0,00
Ca	0,04	0,24	0,07	2,19	2,15	0,06	0,04	2,77	2,78	2,57	2,63	1,53	1,44	2,62	2,09	0,02	0,02
Na	2,48	2,83	2,42	1,75	1,84	2,46	2,27	1,25	1,27	1,38	1,32	2,44	2,52	1,39	1,92	2,74	2,63
K	1,46	1,08	1,51	0,07	0,06	1,59	1,72	0,03	0,04	0,03	0,03	0,10	0,12	0,02	0,07	1,37	1,44
Tot	19,99	20,16	20,03	20,03	20,09	20,08	20,02	20,04	20,06	20,03	20,05	20,07	20,07	20,05	20,10	20,08	20,05
An	0,89	5,83	1,79	54,61	53,09	1,42	1,06	68,33	68,09	64,56	66,13	37,57	35,29	64,97	51,22	0,57	0,51
Ab	62,33	68,13	60,44	43,61	45,37	59,80	56,30	30,98	30,96	34,68	33,21	59,98	61,82	34,53	46,96	66,23	64,36
Or	36,78	26,04	37,77	1,78	1,54	38,79	42,63	0,68	0,95	0,76	0,66	2,45	2,89	0,50	1,82	33,21	35,13

Mugearites bear slightly evolved plagioclase compared to the ones in basalts (Figure 5.2.b). Plagioclase in mugearites is mainly represented by two generations of phenocrysts: One type is with and the second type is without disequilibrium textures (Figure 5.2.c). Plagioclase in disequilibrium is dominantly richer in anorthite than the stable varieties (Figure 5.3).

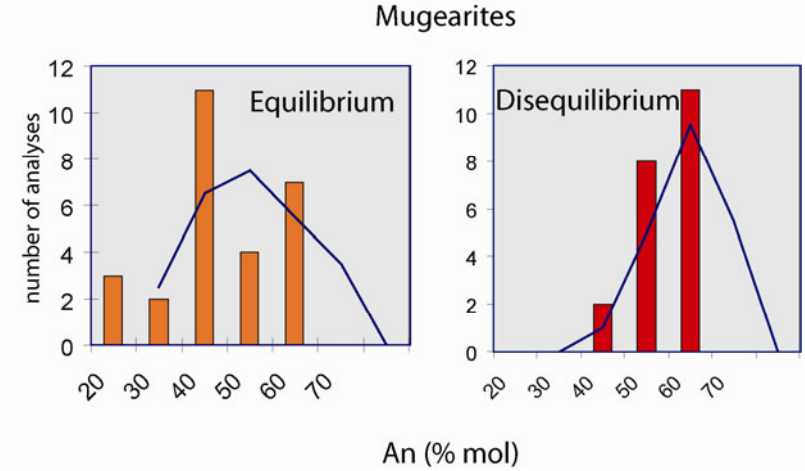

Figure 5.3: Frequencies of stable (equilibrium) and unstable (disequilibrium) plagioclase feldspars of the mugearites depict that most of the calcic plagioclase (An>50%) are unstable

Strongly resorbed destabilized plagioclase comprises of two basic contiguous morphologic portions: cellular inner portion and rimwards mantle with weak oscillatory zoning (Figure 5.4.a). Inner cellular zones exhibit typical honeycomb texture and embay intracrystal ponds / pools with different mineralogical assemblage than that of the rock groundmass. We observe anorthoclase (Figure 5.2.c; intracrystal. emid: 110 and 112), amphibole (ferrorichterite, emid: 479) and clinopyroxene (emid: 480). Textures of mafic minerals in the intracrystalline pools reflect the inwards dissolution of calcic plagioclase. Besides, crystal mantles are calcic plagioclase however; it is Ca-poor anorthoclase (emid 478) in the contact zones with the ponds (Figure 5.4.b). Dendritic laths and crystallites of mafic minerals originate from plagioclase and grow towards the intracrystal pond, similar to that of enclaves (Figure 5.6).

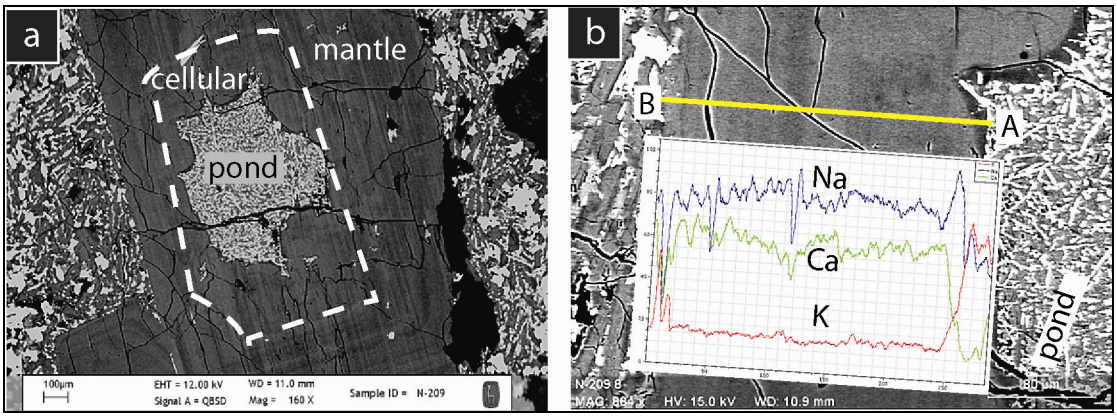

Figure 5.4: Resorbed plagioclase in mugearite. (a) Morphological portions of plagioclase in disequilibrium with the melt; cellular inner portion embaying confined ponds and mantling portion with weak oscillatory zoning, (b) EDS profile on an unstable plagioclase reveals that rims of inner cellular portion embaying inter-crystal ponds are Ca-poor anorthoclase.

Felsic Rocks

Figure 5.2.f and Table 5.2 depicts the feldspar compositions of caldera related eruptive products. Although Kantaşı ignimbrite (SID: 1037) contains dominantly anorthoclase ($Ab_{62-70}An_{2-32}Or_{5-35}$), underlying plinian fallout (SID: 1036) comprise essentially normally zoned andesine plagioclase (An_{31-43}). Ternary feldspars of metaluminous trachytic Nemrut ignimbrite (SID: 1345) scatter between oligoclase and anorthoclase. In Nemrut ignimbrite, feldspar phenocrysts occasionally exhibit cellular honeycomb texture (Figure 5.5). Stratigraphically upper and middle portions of Nemrut Ignimbrite (SID: 1035 and 1034 respectively) contain normally zoned ternary feldspar ($Ab_{46-74}An_{1-40}Or_{3-47}$). In comparison, feldspars of stratigraphically lower portions of Nemrut ignimbrite (SID: 1033) and underlying dark colored plinian fallout (SID: 1032) are again oligoclase and andesine. However, these normally zoned crystals are in compositional range of ($Ab_{54-71}An_{42-4}Or_{2-36}$). We note a slight enrichment of Ab component towards the bottom of Nemrut ignimbrite. Finally stratigraphically lowermost pale colored felsic plinian air fall (SID: 1031) bear euhedral anorthoclase with $Ab_{65-67}An_{0}Or_{33-35}$. As we have mentioned earlier, pyroclastic sequence, at least the Nemrut Ignimbrite, exhibits gradually evolving feldspar compositions towards its bottom sections.

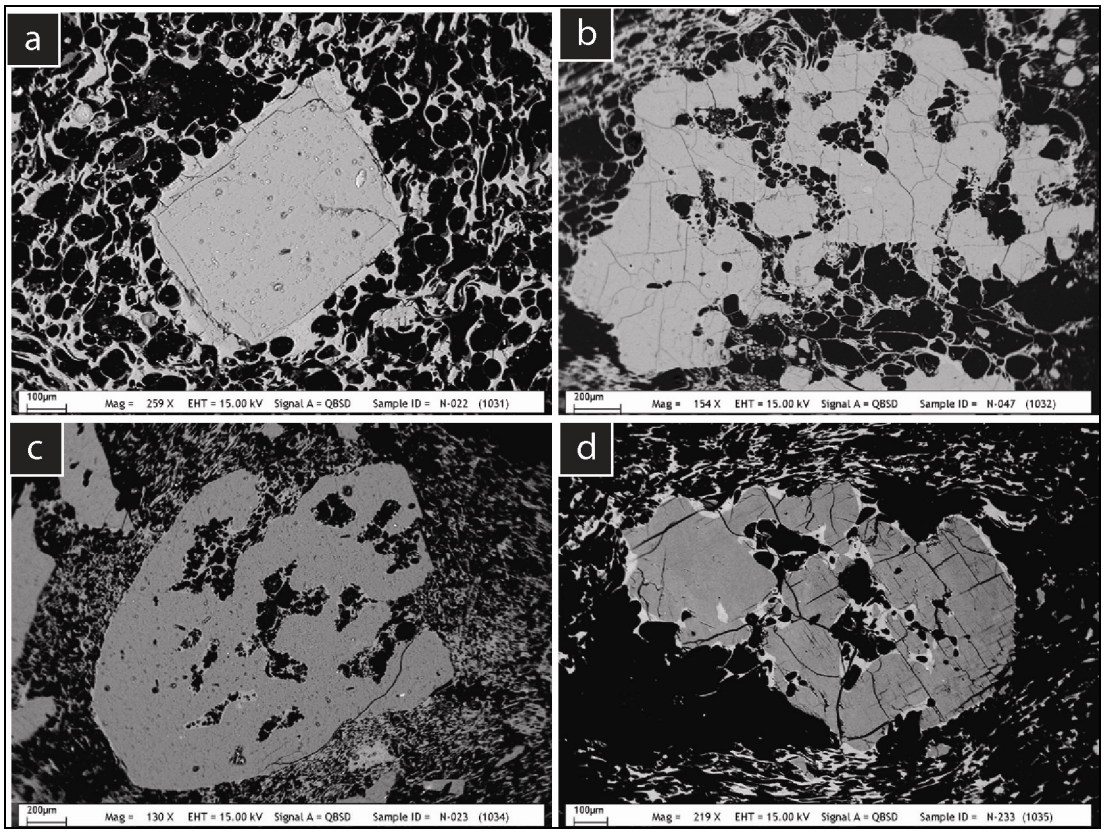

Figure 5.5: Feldspars of Nemrut ignimbrite sequence (SID: 1345). (a) Plinian fall underlying the main ignimbrite section (SID: 1031) comprise euhedral anorthoclase. (b) Dark colored lower plinian however contains cellular honeycomb plagioclase. Middle (c) and upper (d) sections of Nemrut ignimbrite contain cellular ternary feldspar.

Pre-caldera metaluminous trachytes contain dominantly oligoclase - anorthoclase with scarce unstable labradoritic plagioclase. Plagioclase in metaluminous trachytes displays disequilibrium with calcic and alkaline zones within euhedral to anhedral phenocrysts. Besides microphenocrysts of plagioclase (An_{67}, emid: 1505 and 1506) are observed together with anorthoclase ($Ab_{38}An_2Or_{60}$, emid: 1182). Peralkaline trachytic lavas (Figure 5.2.e) and domes are comprised of dominantly anorthoclase and rarely Na-rich sanidine. Compositional window is relatively narrow with $Ab_{53\text{-}72}An_{0\text{-}8}Or_{21\text{-}44}$. We observe slight enrichment in Or mole fraction in microlites.

Anorthoclase ($Ab_{57\text{-}69}An_{0\text{-}2}Or_{30\text{-}42}$) in pre-caldera comendites (Figure 5.2.h; SID: 1040, 1060, 1070) exhibits slight depletion of An and enrichment in Or compared to pre-caldera trachytes. On the other hand, anorthoclases of post-caldera comendites seem to be confined in $Ab_{61\text{-}67}An_{0\text{-}1}Or_{32\text{-}38}$ composition range (Figure 5.2.i). In these silica oversaturated peralkaline rocks alkali feldspar is normally zoned with slight enrichment in Or rimwards.

Enclaves

As mentioned earlier in Chapter 4 (Petrography), two petrographical types of enclaves occur in comendites. They are benmoreitic in composition (for whole rock geochemical data see Chapter 6). The interface, comprised of microcrystal-rich and vesicular zones, is omnipresent between Type I enclaves and the host rock. This indicates the concurrent presence of mafic and felsic magma (see Section 4.1.6).

Type I enclaves bear plagioclase which resemble compositionally to the historic basalts (An_{69-38}). Microcrystalline interface, between the pumiceous transition zone of comendite host and the enclave, bears microphenocrysts with An_{50-46} and microlites with An_{18}. Pumiceous zone bears fragments of both anorthoclase of the host and the plagioclase of the enclave. Both textural and compositional features strongly emphasize the mingling of mafic and silicic magmas. In fact; it is not viable not to think interminglement between coeval silicic and mafic magmas.

Type II enclaves in comendites comprise honeycomb cellular anhedral/subhedral plagioclase (An_{56-35}) with evident reverse zoning (Figure 5.6.a). Besides, highly resorbed xenocrystic ternary feldspar is observed. However, the contact zones of cellular plagioclase crystals with the melt are found to be mantled by ternary feldspar with very low An (<15) and relatively higher Or (6-34) content. However, microlites are plagioclase with An_{37-33}.

We have noted the similarity between mugearites and Type II benmoreitic enclaves (see section 4.1.6). Highly destabilized boxy cellular plagioclase contains intracrystal ponds with different mineralogical assemblage than the groundmass (Figure 5.6.b). Tschermakitic amphibole, clinopyroxene and anorthoclase represent the intracrystal assemblage. Especially the radial amphibole dendrites and spindles originate from plagioclase (Figure 5.6.c), similar to that of mugearites. Contact zone of plagioclase with these intracrystal ponds are Or rich. These ponds are usually observed penetrated by the groundmass due to the extreme resorption of plagioclase (Figure 5.6.d).

Post-caldera phreatomagmatic trachytic ejecta

Petrographically two distinct types of ejecta of post-caldera phreatomagmatic activity have been identified. Granular Type G ejecta (see section 3.1.7) contain plagioclase and alkali feldspar. Plagioclase (An_{52-55} emid: 447, 448, 557 and 558) is mantled by dusty cellular K-feldspar. Alkali feldspar is perthitic consisting of the exsolution of Na-rich (Ab_{90}) and K-rich (Or_{65}) lamellae (Figure 5.7.a).

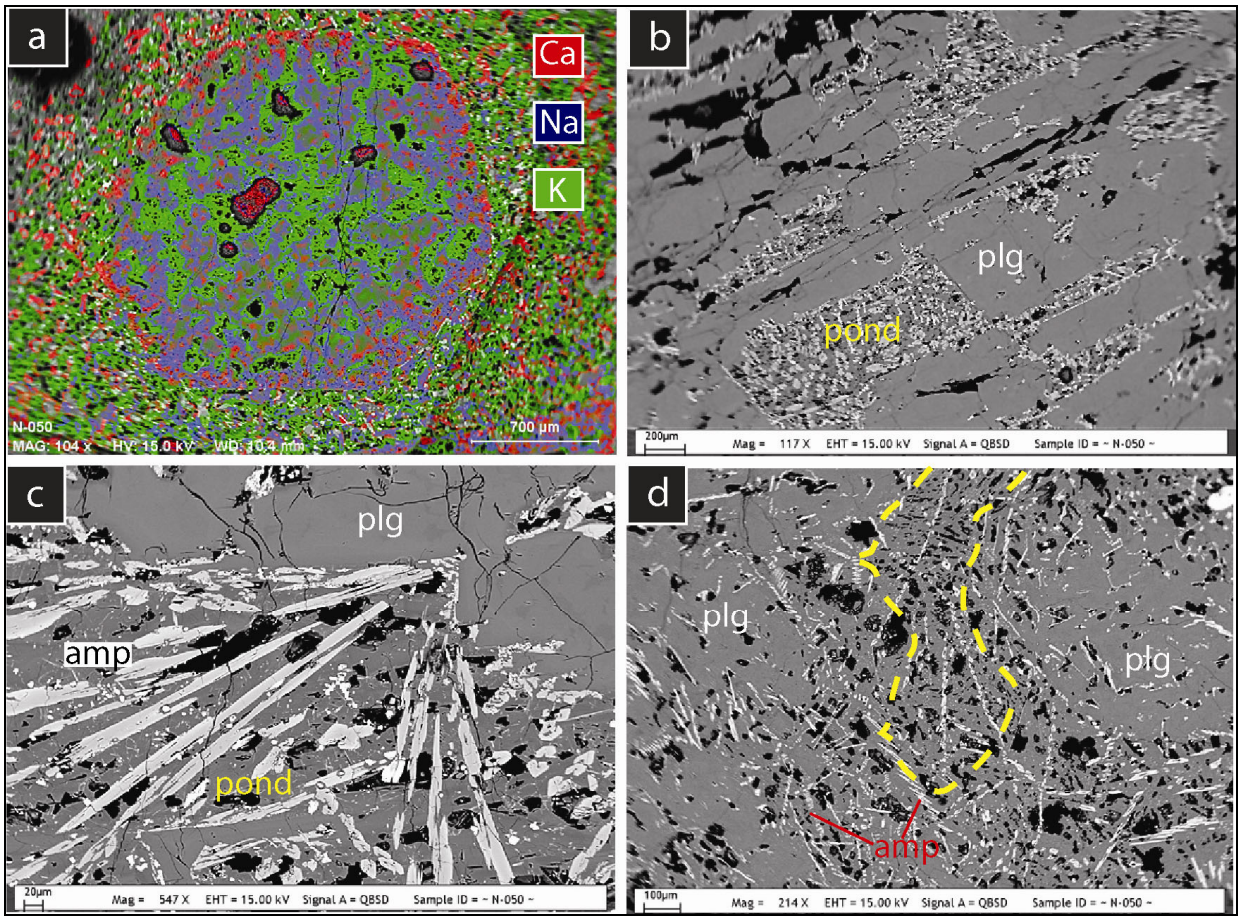

Figure 5.6: Plagioclase feldspars of Type II benmoreitic enclaves. (a) Chemical map of reversely zoned (semi)cellular honeycomb plagioclase. Or-rich inner cells are evident. (b) Intracrystal ponds of resorbed feldspar bear different mineral assemblage than the rock groundmass. (c) Radial amphibole in the ponds originates from plagioclase. (d) Groundmass is observed to penetrate into the ponds of extremely resorbed plagioclase.

Porphyritic trachytic ejecta (Type P) bears destabilized anorthoclase ($Ab_{56-42}An_{1-18}Or_{15-43}$) with relatively stable plagioclase ($Ab_{30-38}An_{60-68}Or_{1-2}$). The abundance of iron-titanium inclusions in destabilized cellular feldspars is noteworthy (Figure 5.7.b).

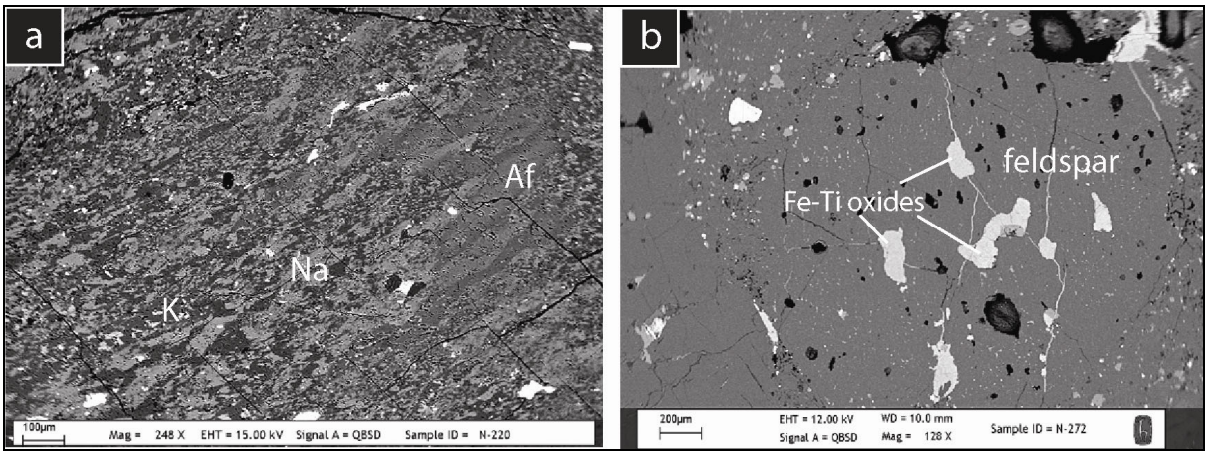

Figure 5.7: (a) Granular Type G ejecta bear perthitic alkali feldspar. (b) Cellular feldspars of porphyritic Type P ejecta contain abundant inclusions of Fe-Ti oxides.

5.1.2 Clinopyroxene

Clinopyroxene is observed in all rocks with varying cationic proportions of Ca, Mg, Fe and Na. Some typical clinopyroxene analyses are shown on Table 5.3. Phenocrysts are abundant throughout the whole suite except the basalts in which they are represented by scarce dendritic laths and microlites. The vast majority of clinopyroxenes belong to Ca - Mg - Fe (QUAD) chemical group (Figure 5.8.a; Morimoto et al., 1988). However, microlites of Ca - Na and Na chemical groups are also present in trachytes and comendites (1.2 < Agpaitic Index whole rock < 1.4) of pre-caldera period (Figure 5.8.b).

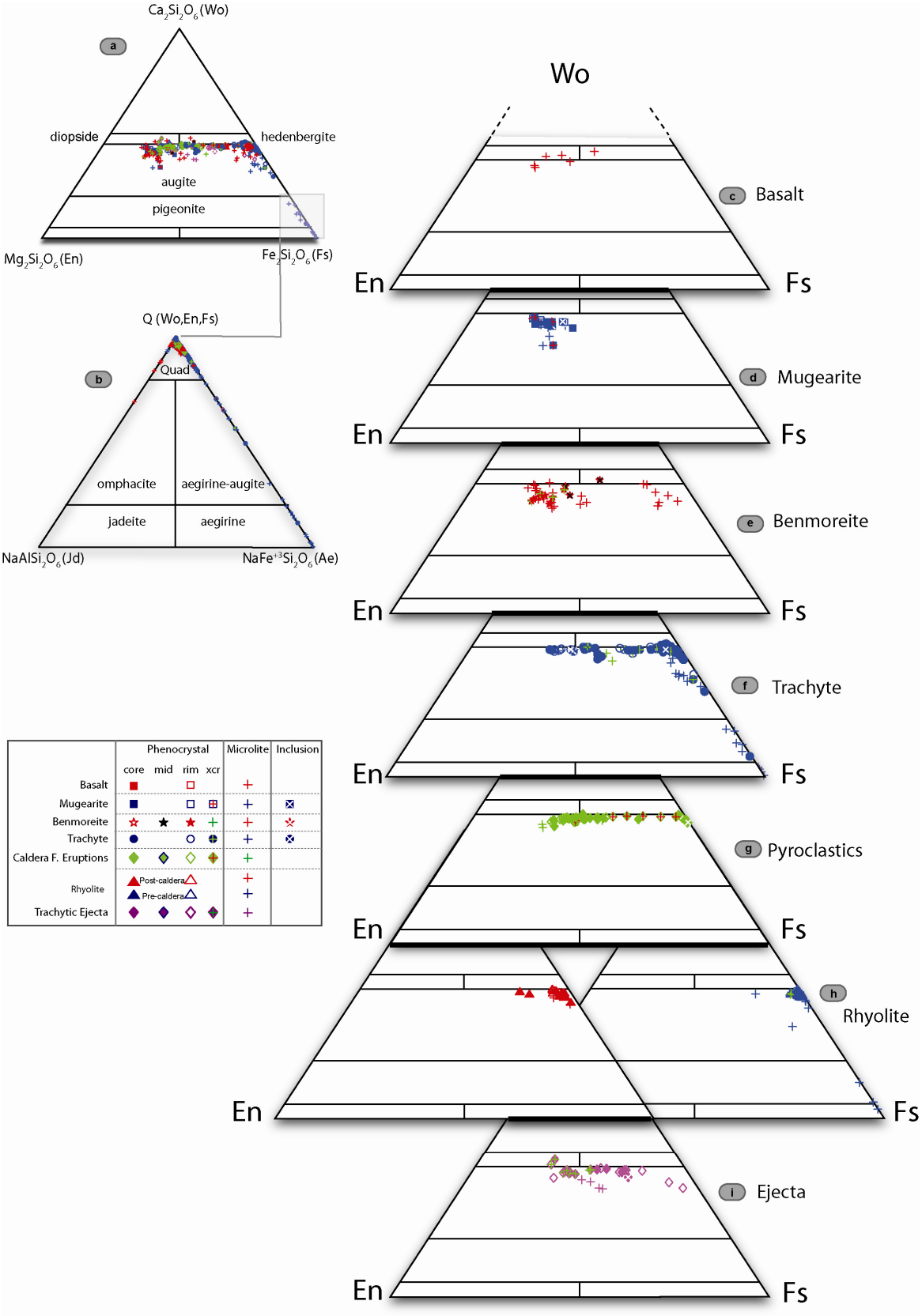

Figure 5.8: Distribution of QUAD clinopyroxenes of Nemrut eruptive units depicted on Wo-En-Fs diagrams. Ca-Na and Na-pyroxenes are shown on Q-Jd-Ae triangular diagram (after Morimoto et al., 1988)

Table 5.3: Selected clinopyroxene analyses. SID: Stratigraphic ID, emid: Electron Microprobe ID, Location (0: center, 9: border), Stability (0: disequilibrium, 9: stable). B: Basalt, M: Mugearite, BM1/2 (Benmoreitic enclave Type 1 or 2), (C) T: (Comenditic) Trachyte, C: Comendite, P: Pantellerite. End members, Ae: Aegirine, Aug: Augite, Wo: Wollastonite, En: Enstatite, Fs: Ferrosilite. Mg# = ($100*Mg^{+2}/Mg^{+2}+Fe^{+2}$)

	Pre-Caldera Rocks											Nemrut Ignimbrite				Post-caldera Rocks					
Sample	**N-141**	**N-184**	**N-188**	**N-151**	**N-136**	**N-239**	**N-016**	**N-209**	**N-080**	**N-098**	**N-228**	**N-022**	**N-047**	**N-023**	**N-036**	**N-225**	**N-256**	**N-220**	**N-272**	**N-254**	**N-255**
SID	1080	1070	1070	1070	1060	1060	1050	1050	1040	1040	1040	1031	1032	1034	1036	1040	1010	1020	1020	1010	1010
Rock	T	P	P	T	T	CT	M	M	T	P	C	T	T	T	T	BM2	BM1	CT	T	C	C
emid	1542	1145	1116	457	1159	1341	83	499	1060	1007	977	145	301	180	253	1509	685	523	891	629	1209
Location	0	0	0	0	0	0	0	0	9	9	0	9	9	0	9	9	0	9	9	9	0
Stability	9	9	9	9	9	0	0	9	9	9	9	9	9	9	0	0	9	9	0	9	9
Size (µ)	250	40	250	50	750	400	500	400	200	500	1700	500	1200	250	250	300	120	700	300	500	10
SiO_2	49,12	51,89	48,58	52,04	51,14	51,05	51,28	51,44	47,51	48,77	47,60	47,62	50,00	50,83	50,81	52,41	48,33	49,70	49,96	48,18	47,94
TiO_2	0,72	0,87	0,63	4,89	0,63	0,72	0,67	0,95	0,69	0,35	0,29	0,32	0,42	0,58	0,42	0,89	2,14	0,57	1,50	0,22	0,38
Al_2O_3	0,89	0,36	0,22	0,25	1,42	0,77	1,63	1,73	0,47	0,16	0,14	0,20	0,99	1,21	1,08	2,43	4,45	0,14	3,09	0,20	0,38
FeO	21,16	30,12	30,26	26,24	12,25	17,68	13,09	10,77	28,52	28,92	30,25	30,72	18,41	15,98	16,06	10,73	11,90	27,76	11,42	29,60	29,99
MnO	0,68	0,36	1,46	0,41	0,66	0,79	0,43	0,29	1,32	1,24	1,17	1,27	0,93	0,83	0,58	0,00	0,40	1,11	0,39	1,23	1,29
MgO	7,61	0,02	0,42	0,04	11,78	8,17	12,66	14,33	0,96	0,34	0,11	0,12	7,92	10,45	10,09	14,39	13,01	1,04	11,65	0,80	0,57
CaO	19,76	0,40	17,90	2,98	20,94	20,99	20,55	20,12	18,93	17,90	18,52	18,53	20,34	20,45	20,49	18,07	19,03	14,51	21,51	18,60	16,77
Na_2O	0,14	13,21	1,15	11,46	0,51	0,42	0,35	0,34	0,71	1,62	1,21	1,20	0,44	0,42	0,36	0,21	0,52	4,36	0,45	0,78	0,95
Total	100,09	97,23	100,61	98,32	99,34	100,59	100,67	99,97	99,12	99,29	99,28	99,99	99,44	100,73	99,89	99,13	99,78	99,18	99,96	99,60	98,27
Formula based on 4 cations 6 oxygens																					
Si	1,93	1,99	1,99	2,00	1,95	1,97	1,92	1,92	1,96	2,00	1,97	1,96	1,96	1,94	1,95	1,98	1,82	1,99	1,89	1,99	2,00
Al^{iv}	0,04	0,01	0,01	0,00	0,05	0,03	0,07	0,08	0,02	0,00	0,01	0,01	0,04	0,05	0,05	0,02	0,18	0,01	0,11	0,01	0,00
Al^{vi}	0,00	0,00	0,00	0,01	0,01	0,01	0,00	0,00	0,00	0,01	0,00	0,00	0,00	0,00	0,00	0,08	0,02	0,00	0,03	0,00	0,02
Ti	0,02	0,03	0,02	0,14	0,02	0,02	0,02	0,03	0,02	0,01	0,01	0,01	0,01	0,02	0,01	0,03	0,06	0,02	0,04	0,01	0,01
Fe^{+3}	0,08	0,94	0,07	0,55	0,05	0,01	0,07	0,05	0,07	0,09	0,13	0,15	0,05	0,07	0,06	0,00	0,08	0,32	0,03	0,07	0,03
Fe^{+2}	0,61	0,02	0,96	0,29	0,35	0,57	0,34	0,28	0,92	0,90	0,92	0,91	0,55	0,44	0,46	0,34	0,29	0,61	0,33	0,95	1,02
Mn	0,02	0,01	0,05	0,01	0,02	0,03	0,01	0,01	0,05	0,04	0,04	0,04	0,03	0,03	0,02	0,00	0,01	0,04	0,01	0,04	0,05
Mg	0,45	0,00	0,03	0,00	0,67	0,47	0,71	0,80	0,06	0,02	0,01	0,01	0,46	0,59	0,58	0,81	0,73	0,06	0,66	0,05	0,04
Ca	0,83	0,02	0,78	0,12	0,85	0,87	0,83	0,81	0,84	0,79	0,82	0,82	0,85	0,83	0,84	0,73	0,77	0,62	0,87	0,82	0,75
Na	0,01	0,98	0,09	0,85	0,04	0,03	0,03	0,02	0,06	0,13	0,10	0,10	0,03	0,03	0,03	0,02	0,04	0,34	0,03	0,06	0,08
Total	4,00	4,00	4,00	3,99	4,00	4,00	4,00	4,00	4,00	3,99	4,00	4,00	4,00	4,00	4,00	4,00	4,00	4,00	4,00	4,00	3,99
Ae	5,02	97,92	7,20	65,33	4,68	0,63	6,72	5,31	5,69	9,74	11,08	12,68	5,34	6,38	5,79	0,00	8,95	33,37	3,49	6,53	2,86
Aug	94,98	1,97	92,80	33,37	94,28	98,43	93,28	94,69	94,31	89,42	88,92	87,32	94,35	93,62	94,21	91,38	89,32	66,63	93,76	93,47	95,12
Wo	41,67	1,61	41,39	12,54	44,18	44,87	42,16	41,32	43,47	42,72	42,85	42,42	43,79	42,49	43,11	38,91	40,69	37,67	45,81	42,47	39,98
En	22,34	0,10	1,32	0,20	34,56	24,29	36,14	40,97	3,06	1,09	0,37	0,42	23,72	30,21	29,54	43,07	38,73	3,76	34,54	2,53	1,87
Fs	35,99	98,29	57,29	87,26	21,26	30,84	21,69	17,71	53,47	56,20	56,78	57,17	32,49	27,31	27,34	18,02	20,58	58,57	19,64	54,99	58,16
Mg#	39,07	0,10	2,36	0,24	63,14	45,16	63,27	70,37	5,65	1,98	0,66	0,75	43,42	53,81	52,84	70,51	66,06	6,26	64,50	4,58	3,24

Basalts (Figure 5.8.c) are lacking of clinopyroxene phenocrysts, instead nucleating microlites and (sometimes dendritic) laths are observed in the groundmass. In the Wo-En-Fs diagram they exhibit scatter on (titanian) diopside, augite and hedenbergite fields. Their compositions are between $Wo_{48}En_{22}Fs_{30}$ and $Wo_{42}En_{40}Fs_{17}$. Magnesium numbers [Mg #: 100 x Mg / ($Mg+Fe^{+2}$)] vary between 43 -70.

Clinopyroxene in mugearites (SID: 1050) is augite with compositions between $Wo_{40}En_{32}Fs_{29}$ and $Wo_{33}En_{41}Fs_{16}$ (Figure 5.8.d). Mg-numbers are between 72 - 53. Microlites (ø < 100 µm) are more evolved corresponding to the phenocrysts. Augite inclusions in plagioclase are compositionally similar with co-existing phenocrysts. Mugearites bear microcrystalline cumulates with slightly higher Mg-numbers (~70). The transition from cumulates to host rock is gradual without any evidence for disequilibrium.

Clinopyroxene in mugearites frequently exhibit disequilibrium (Figure 5.9.a) by resorption and reverse zoning with increasing Mg-numbers ($100*Mg/Mg+Fe^{+2}$) towards the rims (Figure 5.9.b). Mg-numbers of texturally unstable clinopyroxene are around 50, whereas in stable ones between 60 and 72.

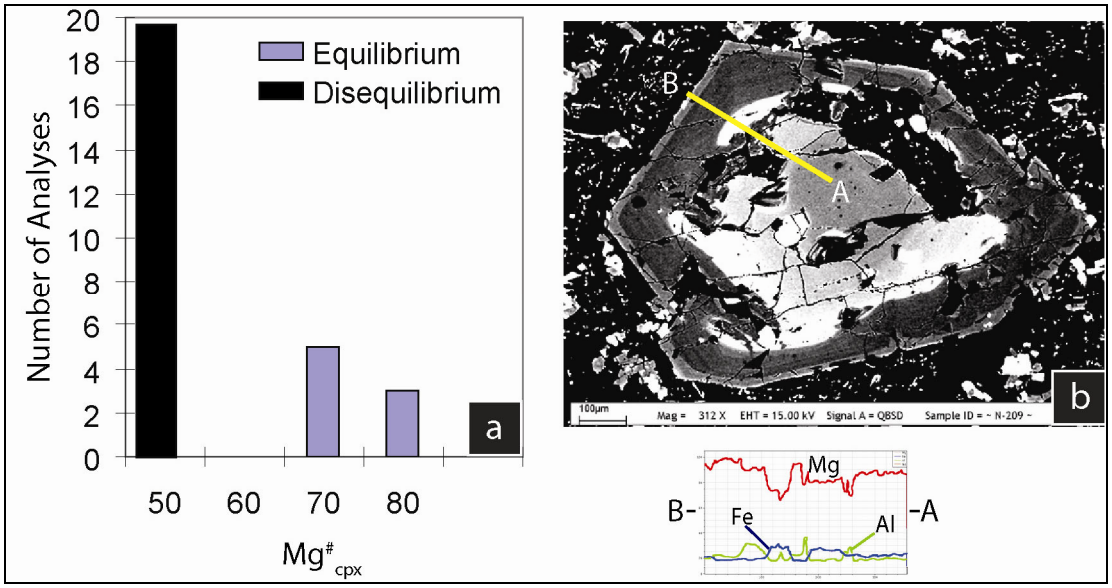

Figure 5.9: (a) Clinopyroxenes of mugearites with disequilibrium textures are frequently evolved (Mg# < 50). (b) EDS profile of an unstable reversely zoned resorbed clinopyroxene in mugearite.

Metaluminous trachytic products of caldera forming trachytic pyroclastics exhibit a broad range of augite with Mg-numbers varying between 67 and 1 (Figure 5.10). Clinopyroxene in Kantaşı ignimbrite is dominantly reverse zoned augite with compositions between

$Wo_{43}En_2Fs_{55}$ and $Wo_{44}En_{34}Fs_{23}$ (Figure 5.8.g). Dark colored plinian fallout unit (SID: 1036) overlying Nemrut ignimbrite (SID: 1345) bears augite with average composition of $Wo_{43}En_{30}Fs_{27}$. Clinopyroxene in Nemrut ignimbrite (SID: 1033, 1034 and 1035) is augite within the compositional range between $Wo_{42}En_{39}Fs_{19}$ and $Wo_{45}En_1Fs_{55}$. They exhibit reverse zoning. Mg-numbers of Nemrut ignimbrite clinopyroxenes are 67 to 2. In dark colored, dark pumice rich plinian fallout unit (SID: 1032) augite is $Wo_{44}En_{24}Fs_{33}$. However, we observe sharp decrease in Mg content, thus average En component is as low as ~ 1 % in augites of pale colored lower plinian air fall unit (SID: 1031). We note a general trend of decreasing Mg-number towards the stratigraphically lowermost plinian units. In addition a wide compositional scatter in Nemrut Ignimbrite is noteworthy (Figure 5.10).

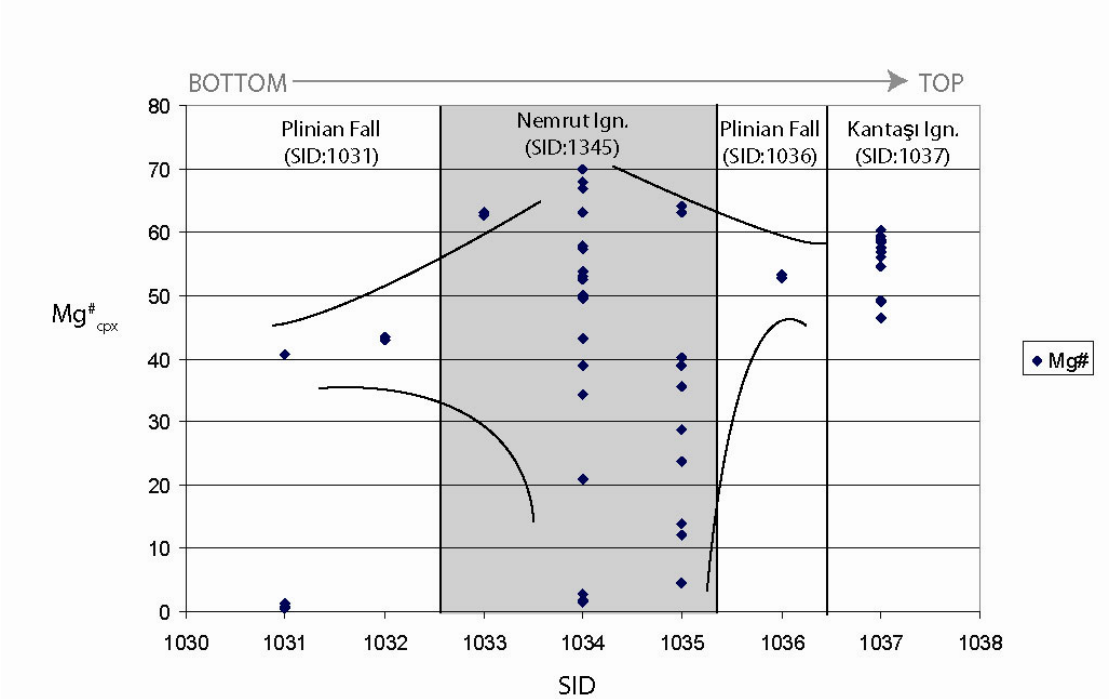

Figure 5.10: Stratigraphical distribution of clinopyroxene compositions in caldera forming eruptions. Plinian fall underlying the Nemrut Ignimbrite (SID: 1031) contain Mg-poor cpx. Diversification is evident in Nemrut Ignimbrite while plinian fall overlying (SID: 1036) comprise cpx with Mg-number ~ 54. In Kantaşı ignimbrite Mg-number$_{cpx}$ varies between 48 and 60.

Rare metaluminous trachyte lava flows (Agpaitic Index < 1) contain unstable clinopyroxene frequently. They are resorbed and reversely zoned with multiple variations throughout their growth (Figure 5.11). In pre-caldera trachytic lava flows and domes (Agpaitic Index < 1.12), clinopyroxene phenocrysts (ø > 100 µm) dominantly belongs to Ca-Mg-Fe chemical group (augite) and exhibit no significant enrichment in Ae component (Figure 5.8.f). Their compositional window is between $Wo_{44}En_{35}Fs_{21}$ (Mg-number: 63) and $Wo_{41}En_1Fs_{58}$ (Mg-number: 2). However, sporadic aegirine-augite (Ae_{80-20}) microphenocrysts and microlites of

aegirine-augite and aegirine (Ae > 80 mol %) (Ø < 75 µm) are omnipresent in pantelleritic trachytes and comendites with Agpaitic indices between 1.12 and 1.32. Rhyolites of both pre- and post-caldera stage contains normally zoned augite between $Wo_{44}En_{13}Fs_{43}$ (Mg-number: 24) and $Wo_{43}En_{0}Fs_{57}$ (Figure 5.8.g). We note slightly higher Mg content in augites of post-caldera comendites compared with the pre-caldera counterparts.

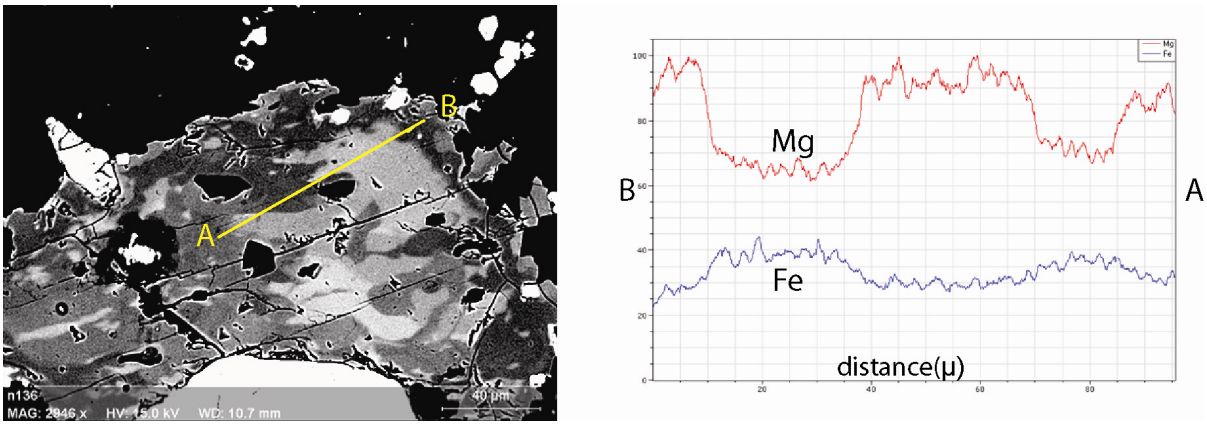

Figure 5.11: Anhedral resorbed cpx in metaluminous (A.I. <1) trachytes exhibit oscillatory reverse zoning revealed by EDS profile.

Enclaves

Benmoreitic Type I enclaves (Figure 5.8.e) within post-caldera comendites contain normally zoned augite microphenocrysts between $Wo_{43}En_{42}Fs_{15}$ (Mg-number: 74) and $Wo_{37}En_{38}Fs_{25}$ (Mg-number: 61). In microcrystalline interface between enclave and the comendite host, augite exhibits no major compositional variation. Furthermore, we could not observe any in-situ crystallized clinopyroxene in pumiceous boundary excluding crystal fragments resembling to those in the enclaves.

Type II enclaves (Figure 5.8.e) contain relatively evolved clinopyroxene with a broad range in Mg number (11 and 70). They dominantly exhibit disequilibrium with slightly reverse oscillatory zoning which points out the chemical fluctuation of the melt during crystal growth. Microlites represent more evolved clinopyroxene compositions with lower Mg-numbers exhibiting a somewhat bimodal distribution (Figure 5.12).

Post-caldera phreatomagmatic trachytic ejecta

In the granular holocrystalline lithic fragments (Type G) ejected from intra-caldera vents during post-caldera phreatomagmatic activity, clinopyroxene is normally zoned augite (Figure 5.13.a) between $Wo_{45}En_{22}Fs_{33}$ (Mg-number: 41) and $Wo_{44}En_{12}Fs_{45}$ (Mg-number: 21).

Whereas, porphyritic ejecta (Type P) frequently contains strongly resorbed clinopyroxene (Figure 5.13.b) and their composition is between $Wo_{37-45}En_{25-35}Fs_{37-20}$.

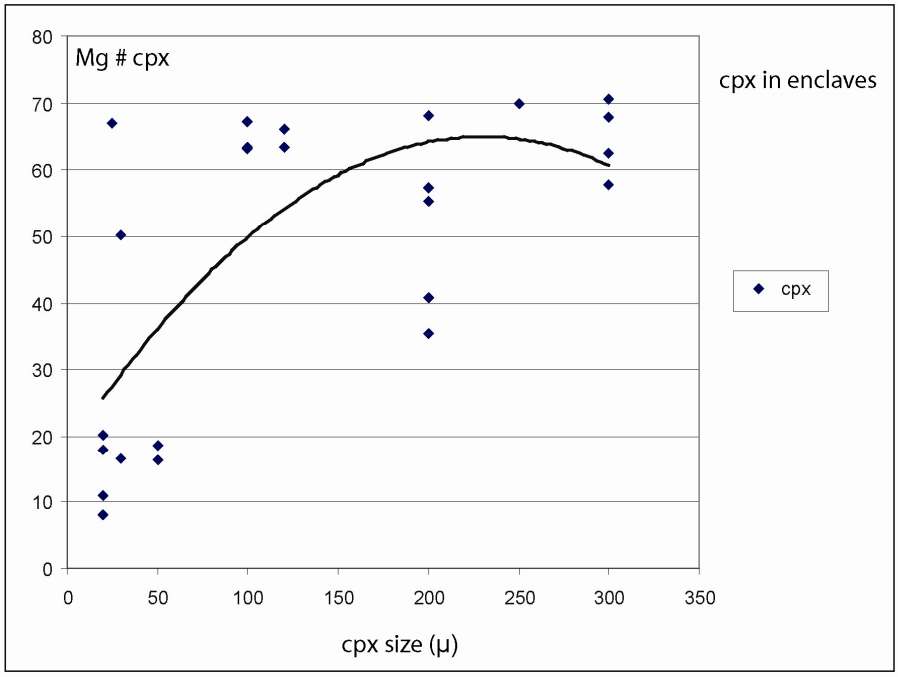

Figure 5.12: Clinopyroxene phenocrysts of Type II benmoreitic enclaves are significantly Mg-richer than the microlites in the groundmass exhibiting bimodal distribution between Mg# 50 and 20.

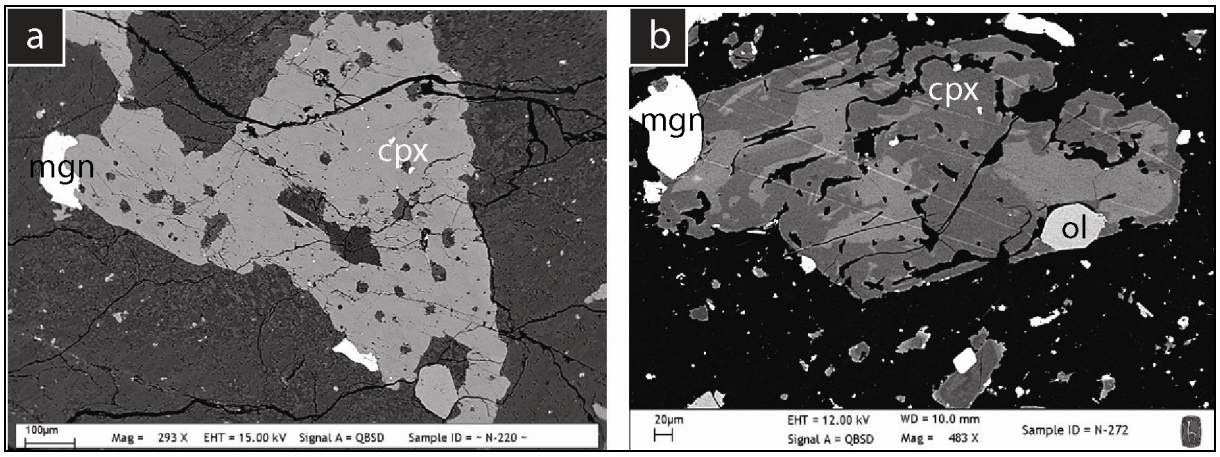

Figure 5.13: Cpx in post-caldera phreatomagmatic ejecta (a) Type G porphyritic ejecta contains subhedral normally zoned augite (b) Type P ejecta contains strongly resorbed anhedral cpx

5.1.3 Olivine

Olivine displays a wide compositional spectrum from forsteritic (~Fo_{80}) to nearly pure fayalite end-member throughout the eruptive units of Nemrut volcanism (Figure 5.14.a). Some typical analyses of olivine of Nemrut rocks are listed on Table 5.4.

Olivine in basalts (Figure 5.14.b) is forsteritic with varying content between Fo_{76} to Fo_{50}. They exhibit normal zoning with an increase in Fa content towards the rims. Centers of phenocrysts (ø > 100 µm) are richer in Fo (73 - 75 %) than their rims (75 - 55 %) and microlites (66 - 50 %).

Mugearites (Figure 5.14.c) comprise slightly evolved olivine between $Fo_{68}Fa_{32}Tp_{0}$ and $Fo_{36}Fa_{63}Tp_{1}$. Although frequently resorbed (Figure 5.15), they are normally zoned with a decrease in Fo rimwards. Centers and mid-zones of phenocrysts (ø > 100 µm) are usually richer in Fo (68 - 55 %) compared to the rims (63 - 47 %) and to the microlites (46 - 36 %).

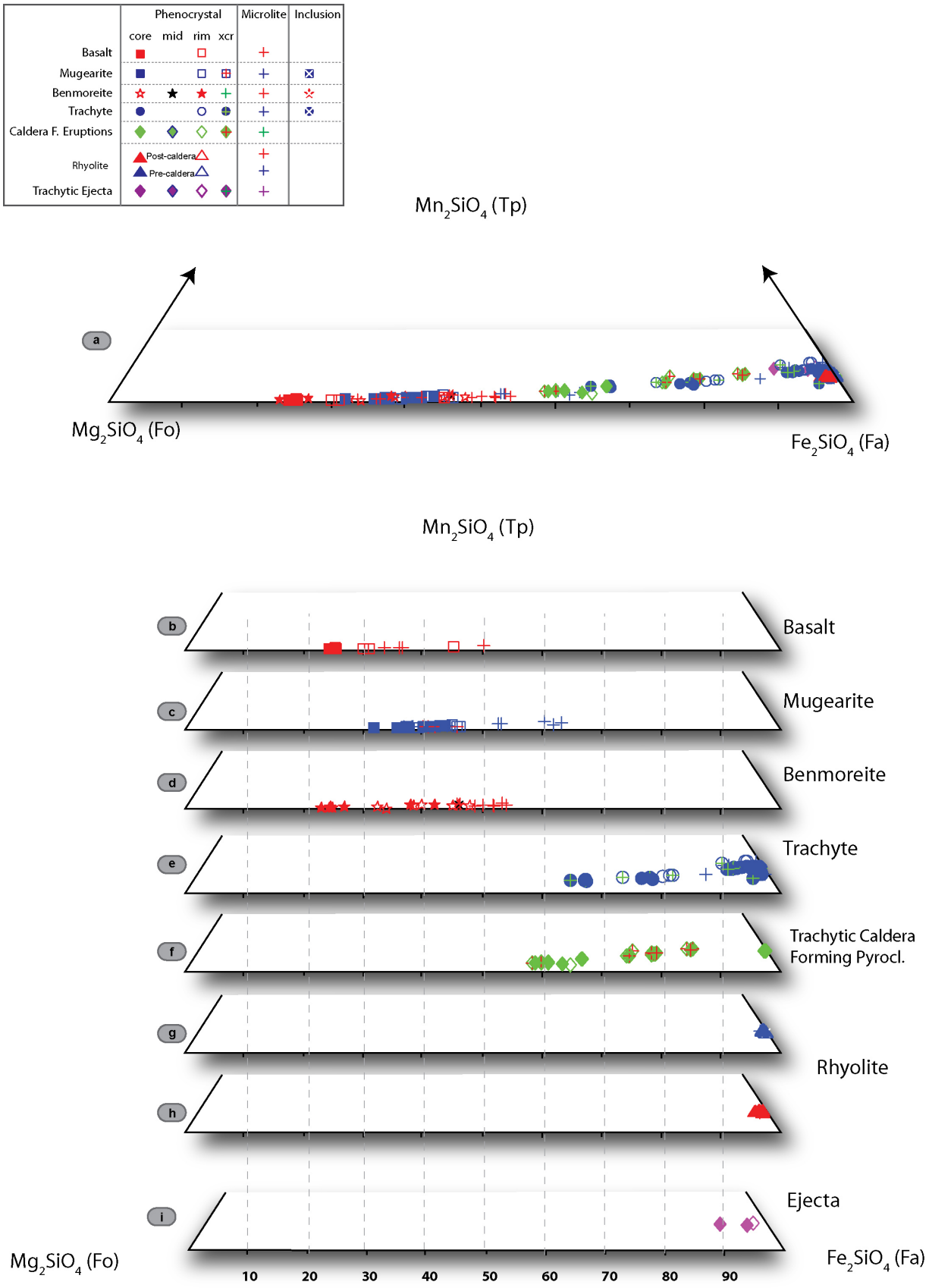

Figure 5.14: Distribution of olivine compositions in Nemrut eruptive units plotted on Tp-Fo-Fa triangular diagram. (Tp: Tephroite, Fo: Forsterite, Fa: Fayalite)

Table 5.4: Selected olivine analyses. SID: Stratigraphic ID, emid: Electron Microprobe ID, Location (0: center, 9: border), Stability (0: disequilibrium, 9: stable). B: Basalt, M: Mugearite, BM1/2 (Benmoreitic enclave Type 1 or 2), (C) T: (Comenditic) Trachyte, C: Comendite, P: Pantellerite. End members, Fo: Forsterite, Fa: Fayalite, Tp: Tephroite

	Pre-Caldera Rocks										Nemrut Ign.					Kantaşı I.	Post-Caldera Rocks					
Sample	**N-188**	**N-188**	**N-136**	**N-136**	**N-239**	**N-209**	**N-209**	**N-181**	**N-098**	**N-246**	**N-022**	**N-247**	**N-023**	**N-233**	**N-036**	**N-259**	**N-065**	**N-220**	**N-258**	**N-257**	**N-011**	**N-256**
SID	1070	1070	1060	1060	1060	1050	1050	1040	1040	1040	1031	1033	1034	1035	1036	1037	1020	1020	1010	1010	1010	1010
Rock	P	P	T	T	CT	M	M	CT	P	C	T	T	T	T	T	T	C	T	B	B	BM1	BM1
emid	1112	1113	1172	1171	1358	493	492	1086	1012	620	158	1457	218	561	247	714	345	526	825	707	5	682
Location	0	9	9	0	0	9	0	0	0	0	0	0	0	0	9	9	0	0	0	0	0	0
Stability	9	9	0	0	0	0	0	9	9	9	9	9	0	0	9	9	9	9	9	9	9	9
Size (µ)	300	300	200	200	200	1500	1500	250	200	250	300	750	800	200	500	1500	250	300	750	50	200	250
SiO_2	28,03	29,92	30,99	31,22	30,39	35,51	36,18	29,46	29,40	29,08	28,83	33,30	30,89	31,24	32,79	32,02	28,97	29,72	37,86	36,15	38,44	36,32
TiO_2	0,03	0,06	0,05	0,21	0,09	0,05	0,08	0,01	0,03	0,04	0,03	0,03	0,03	0,08	0,04	0,12	0,06	0,03	0,00	0,18	0,06	0,07
Al_2O_3	0,00	0,00	0,03	0,05	0,01	0,05	0,03	0,00	0,00	0,04	0,00	0,01	0,08	0,00	0,02	0,03	0,00	0,01	0,07	0,04	0,00	0,04
FeO	67,19	65,15	58,15	56,77	62,38	38,64	35,75	64,76	65,93	67,32	66,97	47,41	57,30	57,49	50,15	55,05	67,18	65,50	22,17	31,19	22,41	32,49
MnO	3,86	4,05	2,74	2,53	3,61	0,64	0,62	4,11	3,37	2,99	3,08	1,70	2,89	3,05	1,19	2,66	2,89	4,05	0,40	0,51	0,37	0,80
MgO	0,31	0,27	6,63	8,41	2,45	25,61	27,74	1,10	0,20	0,06	0,02	16,61	7,87	7,71	15,08	9,89	0,38	1,30	39,05	31,23	39,11	29,88
CaO	0,43	0,45	0,70	0,62	0,28	0,34	0,30	0,79	0,31	0,37	0,31	0,30	0,42	0,48	0,31	0,42	0,16	0,12	0,25	0,51	0,29	0,23
Total	99,85	99,89	99,27	99,81	99,22	100,85	100,70	100,23	99,25	99,90	99,23	99,36	99,48	100,06	99,57	100,19	99,64	100,73	99,80	99,80	100,67	99,84
Formula calculated for 4 oxygens																						
Si	0,96	1,01	1,00	0,99	1,01	1,00	1,00	0,99	1,00	0,99	0,99	1,00	0,99	1,00	1,00	1,00	0,99	0,99	0,99	0,99	0,99	1,00
Fe^{+2}	1,93	1,83	1,57	1,51	1,74	0,91	0,83	1,82	1,88	1,91	1,92	1,19	1,54	1,54	1,28	1,44	1,91	1,83	0,48	0,71	0,48	0,75
Mn	0,11	0,12	0,07	0,07	0,10	0,02	0,01	0,12	0,10	0,09	0,09	0,04	0,08	0,08	0,03	0,07	0,08	0,11	0,01	0,01	0,01	0,02
Mg	0,02	0,01	0,32	0,40	0,12	1,07	1,14	0,05	0,01	0,00	0,00	0,75	0,38	0,37	0,68	0,46	0,02	0,06	1,52	1,27	1,51	1,22
Ca	0,02	0,02	0,02	0,02	0,01	0,01	0,01	0,03	0,01	0,01	0,01	0,01	0,01	0,02	0,01	0,01	0,01	0,00	0,01	0,02	0,01	0,01
Fo	0,77	0,70	16,24	20,16	6,20	53,75	57,61	2,76	0,52	0,15	0,05	37,59	18,90	18,49	34,35	23,38	0,96	3,21	75,51	63,71	75,37	61,52
Fa	93,78	93,42	79,95	76,39	88,60	45,49	41,66	91,37	94,58	95,56	95,51	60,22	77,16	77,35	64,11	73,04	94,90	91,08	24,05	35,70	24,23	37,54
Tp	5,45	5,89	3,81	3,45	5,20	0,76	0,73	5,88	4,90	4,30	4,44	2,19	3,95	4,16	1,54	3,57	4,14	5,71	0,44	0,59	0,40	0,94

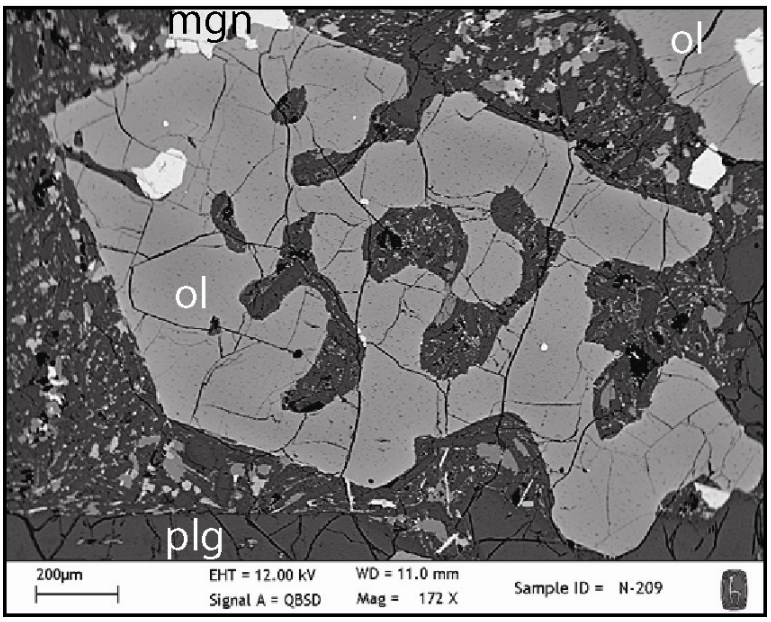

Figure 5.15: Normally zoned resorbed olivine in mugearite

Metaluminous caldera forming pyroclastic rocks contain olivine with varying compositions between $Fo_{40}Fa_{58}Tp_2$ and $Fo_0Fa_{96}Tp_4$ (Figure 5.14.f). Kantaşı ignimbrite (SID: 1037), representing the uppermost unit of pyroclastic sequence, bears both stable and destabilized olivine. Stable crystals are $Fo_{24}Fa_{73}Tp_3$ in average. Dark colored upper plinian phase (SID: 1036) is represented by $Fo_{35}Fa_{63}Tp_2$ with slightly normal zoning. In Nemrut ignimbrite (SID: 1345) olivine varies between $Fo_{40}Fa_{58}Tp_2$ and $Fo_{12}Fa_{83}Tp_{5.}$ Textures of disequilibrium are often associated with reverse zoning. However, normally zoned crystals are also present. The distribution of olivine, being relatively Fo-rich (> 20 %) and Fo-poor (< 20 %) in Nemrut ignimbrite is somehow chaotic. Upper sections (SID: 1035) bears both varieties, whereas middle section (SID: 1034) has olivine relatively confined to average composition of $Fo_{19}Fa_{77}Tp_4$. Lower section (SID: 1033) is represented by normally zoned olivine with an average composition of $Fo_{38}Fa_{60}Tp_2$. Dark colored plinian air fall unit underlying Nemrut ignimbrite (SID: 1032) has reversely zoned olivine with ~ $Fo_{19}Fa_{77}Tp_4$. However, we do observe an abrupt decrease in Fo component in the lowermost pale colored plinian phase (SID: 1031). Olivine is $Fo_0Fa_{95}Tp_5$. We note the compositional variation of olivine between plinian fallouts (SID: 1031 and 1036) and the extended range of compositions in Nemrut ignimbrite (Figure 5.16).

In the least evolved trachytes (0.93 < A.I. < 1.06) olivine varies from Fo_{31} to Fo_5 while these units bear xenocrysts with $Fa_{75\text{-}80}$ (Figure 5.14.e). Fayalite (Fa > 97 %) is frequently present in comenditic glassy rhyolites with cumulates of clinopyroxene and Fe-Ti oxides. However, a slight difference between post-caldera and pre-caldera rhyolites is noteworthy: Only pure

fayalite (Fa < 1 %) is observed in pre-caldera rhyolites whereas in post-caldera comendites Fa component varies between 1 and 2.5 % (Figure 5.14.g-h). Besides Tp (Mn_2SiO_4) mole fraction in olivines is positively correlated with Fa content but decreases abruptly from peralkaline trachytes (5-7 % Tp) to comendites (4.0 - 4.6 Tp %).

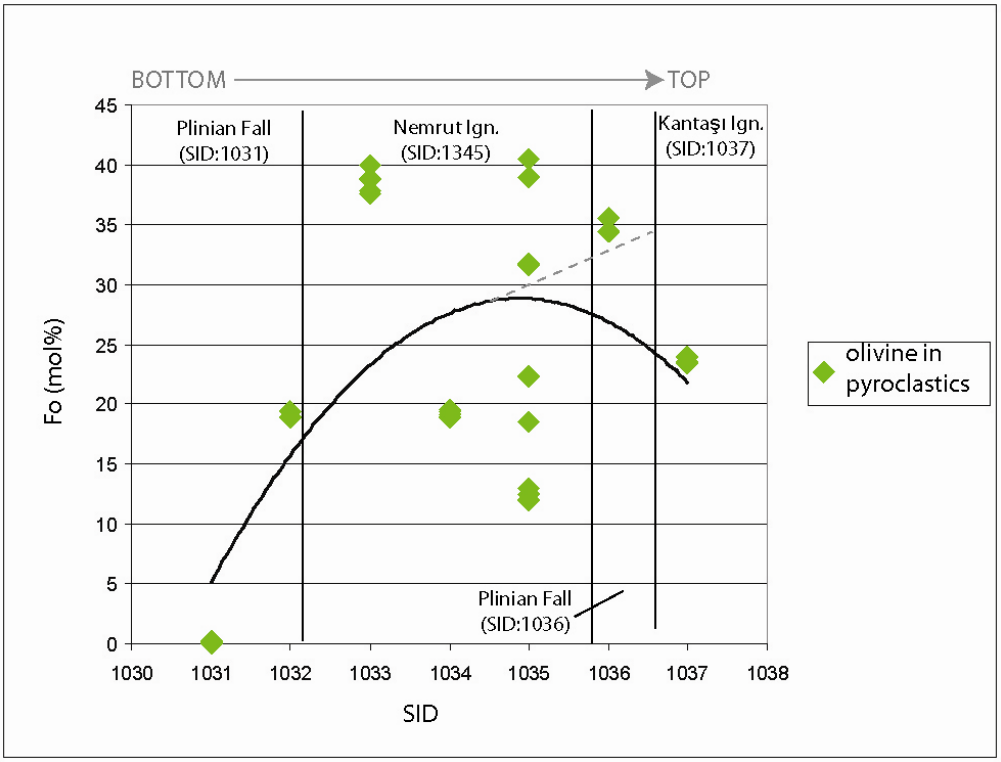

Figure 5.16: Stratigraphical distribution of olivine compositions in caldera forming eruptions. Plinian fall underlying the Nemrut Ignimbrite (SID: 1031) contains nearly pure fayalite. Diversification is evident in Nemrut Ignimbrite while plinian fall overlying (SID: 1036) comprises olivine with ~ Fo_{35}.

Enclaves

Benmoreitic enclaves in post-caldera comendite comprise olivine between $Fo_{77}Fa_{23}Tp_0$ and $Fo_{53}Fa_{46}Tp_1$ (Figure 5.14.d). They exhibit strong normal zonation with enrichment of Fa component by a factor up to 50 % compared to nominal compositions of respective center zone of the crystals. Microcrystalline interface between enclave body and the pumiceous boundary of rhyolite glass comprises slightly evolved olivine with ~$Fo_{48}Fa51Tp_1$. On the other hand, pumiceous interface bears both forsterite-rich (Fo_{50}) olivine and fayalite ($Fo_1Fa_{95}Tp_1$).

Post-caldera phreatomagmatic trachytic ejecta

Trachytic granular holocrystalline ejecta found in post-caldera phreatomagmatic deposits (Type G), contain destabilized olivine with an average composition of $Fo_4Fa_{90}Tp_6$ (Figure

5.14.i). They exhibit normal zoning. They are often observed to be mantled with amphibole (ferrorichterite) and clinopyroxene with aenigmatite at their rims (Figure 5.17).

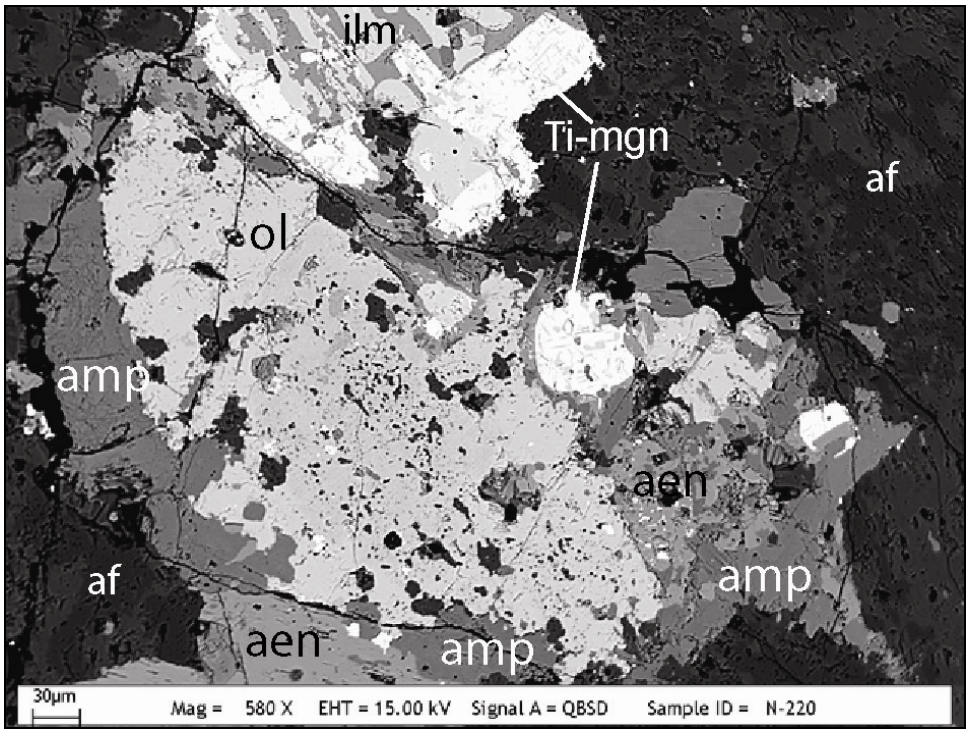

Figure 5.17: Olivine (Fa_{90}) in granular Type G ejecta decomposed into a mantling aggregate of amphibole (ferrorichterite), aenigmatite and clinopyroxene (not shown). Sandwich type (after Buddington and Lindsley, 1964) exsolution of magnetite and ilmenite is also observed (ilm).

5.1.4 Fe-Ti Oxides

Iron - Titanium oxides occur in all types of rocks throughout the volcanic history (Figure 5.18.a). Table 5.5.a, b depicts some typical analyses of Fe-Ti oxides. Fe_2O_3 and FeO recalculated stochiometrically as proposed by Carmichael (1967). Molecular fractions of ulvöspinel and ilmenite are calculated according to Stormer (1983).

Basalts (Figure 5.18.b) contain only subhedral titanomagnetite microcrystals in groundmass and as scarce inclusions in plagioclase and olivine with Usp_{96-64}. In mugearites (Figure 5.18.c) titanomagnetite is frequently oxy-exsolved to ilmenite and magnetite, exhibiting fine to coarse trellis-type exsolution (Figure 5.19.a terminology after Buddington and Lindsley, 1964). Microprobe analyses expected to be more reliable in the crystals with coarse exsolution lamellae, in which ilmenite content reach up Ilm_{100} whereas magnetite is Usp_{11}. However, in one phenocryst-free mugearite sample (N-240), exsolution lamellae of ilmenite and magnetite contents are Ilm_{84} and Usp_{79} respectively. In mugearites, apart from

the oxy-exsolved crystals, ilmenite and magnetite coexist. Magnetites vary from pure magnetite (Mgn_{100}) to titanomagnetite (Usp_{30-69}) whereas ilmenite compositions are restricted to Ilm_{83-96}.

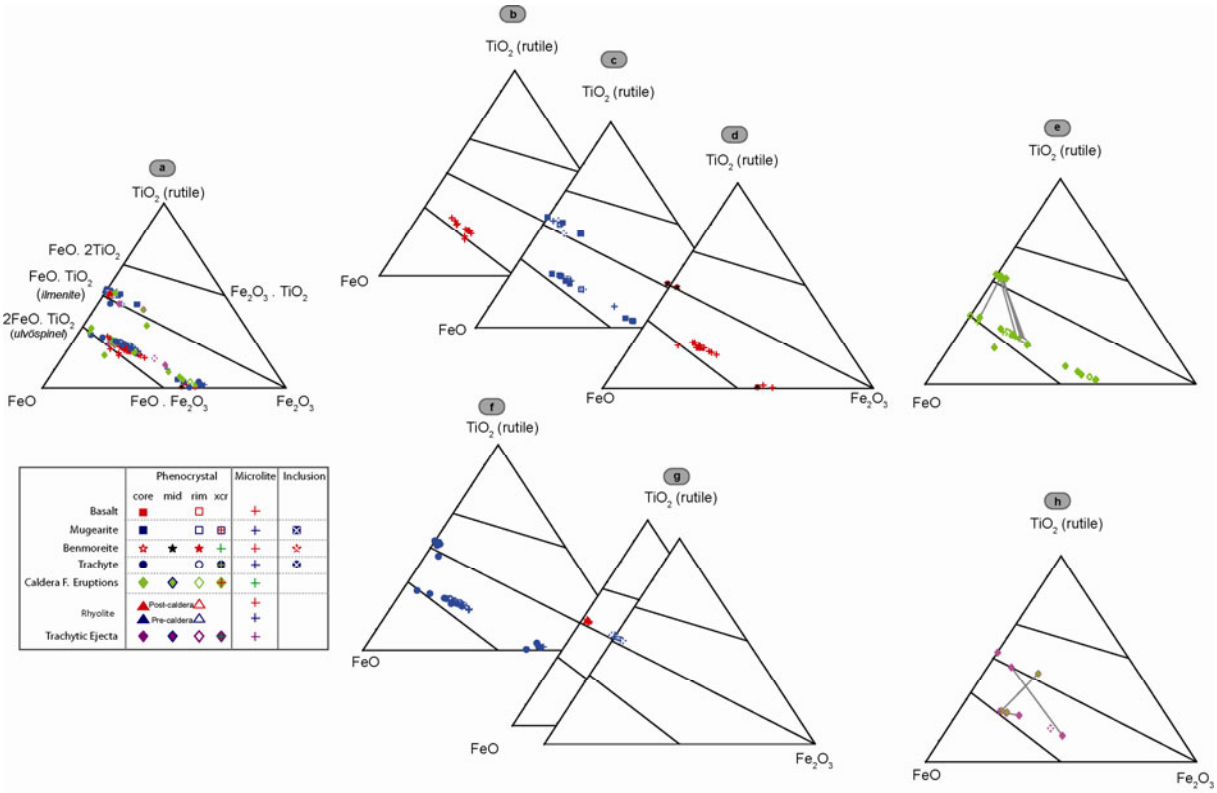

Figure 5.18: Distribution of Fe-Ti oxides in Nemrut eruptive units.

Kantaşı ignimbrite (SID: 1037) contains dominantly magnetite (Mag_{94-96}) and titanomagnetite / ulvöspinel (Usp_{26-100}) (Figure 5.18.e). However, sporadic ilmenite is also observed (Ilm_{71}). Plinian air fall underlying Kantaşı and overlying Nemrut ignimbrites (SID: 1036) bears titanomagnetite exsolved in trellis type into ilmenite (Ilm_{98-100}) and titanomagnetite (Usp_{68-72}) (Figure 5.19.b). In Nemrut ignimbrites, its upper sections (SID: 1035) contain trellis exsolution of titanomagnetite into ilmenite (Ilm_{97}) and magnetite ($Usp_{14}Mag_{86}$) and single grains of titanomagnetite (Usp_{72-92}) (Figure 5.19.c). Middle sections (SID: 1034) bear magnetite (Mag_{99-80}) and titanomagnetite (Usp_{71-80}). Lower sections of Nemrut ignimbrite and dark colored plinian phase below (SID: 1033 and 1032 respectively) contain titanomagnetite (Usp_{72-77}) sometimes exhibit exsolution into pure ilmenite and magnetite. However, pale colored plinian fallout unit, observed stratigraphically at the bottom of the pyroclastic sequence, contain only ilmenite (Ilm_{98-100}).

In the metaluminous trachytes (0.93 < A.I.), magnetite (Mag_{99}) and titanomagnetite (Usp_{71-57}) are present (Figure 5.18.f), however abundance of Fe-Ti oxides decreases with increasing differentiation. Comenditic trachytes contain titanomagnetite (Usp_{61-83}) sometimes oxy-exsolved into magnetite ($Mag_{94}Usp_6$) and ilmenite (Ilm_{98}). Pantelleritic counterparts have dominantly ilmenite (Ilm_{98}) and rare magnetite (Mag_{91}). Peralkaline rhyolites of both pre- and post-caldera stages have only ilmenite (Ilm_{100-97}) (Figure 5.18.g).

Table 5.5: Selected Fe-Ti oxide analyses. SID: Stratigraphic ID, emid: Electron Microprobe ID, Location (0: center, 9: border), Stability (0: disequilibrium, 9: stable). B: Basalt, M: Mugearite, BM1/2 (Benmoreitic enclave Type 1 or 2), (C) T: (Comenditic) Trachyte, C: Comendite, P: Pantellerite. End members, Usp: Ulvöspinel, Ilm: Ilmenite. Ferric – ferrous iron has been calculated stochiometrically.

Magnetite

	Pre-Caldera Rocks					Nemrut Ign.			Kantaşı Ign.	Post-Caldera Rocks		
Sample	**N-141**	**N-184**	**N-136**	**N-209**	**N-016**	**N-047**	**N-023**	**N-036**	**N-259**	**N-011**	**N-256**	**N-258**
SID	1080	1070	1060	1050	1050	1032	1034	1036	1037	1010	1010	1010
Rock	T	P	T	T	M	T	T	T	T	BM1	BM1	B
emid	1544	1140	1180	498	99	297	182	256	716	11	680	836
Location	0	0	0	0	0	0	0	0	0	0	0	0
Stable	9	9	9	9	9	9	9	9	9	9	9	9
Size	250	250	10	1300	250	1000	150	30	200	100	100	50
TiO2	25,25	3,33	21,18	24,79	3,40	24,29	25,78	23,36	2,21	22,45	1,39	24,84
Al_2O_3	0,47	0,09	0,41	2,10	5,42	1,32	1,40	1,47	2,66	2,16	0,53	2,55
FeO	53,76	32,01	48,87	50,30	32,27	51,26	52,30	48,27	29,05	47,61	31,50	50,87
Fe_2O_3	17,59	62,69	26,18	19,21	56,13	20,04	17,27	21,54	61,95	22,18	58,72	16,02
MnO	1,12	2,28	1,17	0,56	0,17	1,44	1,29	0,85	2,35	0,54	0,16	0,72
MgO	0,02	0,04	0,22	2,35	1,66	0,64	0,94	1,21	1,36	2,35	1,27	1,79
Total	98,21	100,44	98,02	99,30	99,05	99,00	98,98	96,69	99,58	97,29	93,58	96,80
Formula based on 3 cations and 4 oxygens												
Ti	0,72	0,10	0,61	0,68	0,09	0,68	0,72	0,66	0,06	0,63	0,04	0,69
Al	0,02	0,00	0,02	0,09	0,24	0,06	0,06	0,06	0,12	0,09	0,02	0,11
Fe^{+2}	1,70	1,02	1,56	1,54	1,00	1,61	1,63	1,51	0,91	1,48	1,03	1,58
Fe^{+3}	0,50	1,80	0,75	0,53	1,56	0,57	0,49	0,61	1,75	0,62	1,73	0,45
Mn	0,04	0,07	0,04	0,02	0,01	0,05	0,04	0,03	0,07	0,02	0,01	0,02
Mg	0,00	0,00	0,01	0,13	0,09	0,04	0,05	0,07	0,08	0,13	0,07	0,10
Total	2,97	3,00	2,99	2,99	2,99	3,00	3,00	2,94	2,99	2,97	2,91	2,95
Usp%	73,64	9,77	61,42	68,73	9,74	68,78	72,62	66,27	6,59	63,13	11,87	71,78

Ilmenite

	Pre-Caldera Rocks					Nemrut Ignimbrite					Post-Caldera Rocks		
Sample	**N-188**	**N-281**	**N-016**	**N-080**	**N-227**	**N-098**	**N-022**	**N-047**	**N-268**	**N-036**	**N-220**	**N-146**	**N-255**
SID	1070	1070	1050	1040	1040	1040	1031	1032	1033	1036	1020	1020	1010
Rock	P	CT	M	CT	C	P	T	T	T	T	T	C	C
emid	1109	771	87	1046	808	1018	143	296	756	255	536	924	1220
Location	9	0	0	0	0	0	9	0	0	0	0	0	0
Stable	9	9	9	9	9	9	9	9	9	9	9	9	9
Size	150	300	300	150	50	150	50	1000	200	50	200	50	50
TiO2	51,80	53,45	45,42	51,75	50,58	52,15	51,61	52,46	54,58	53,20	52,93	50,34	50,71
FeO	44,64	44,53	32,85	44,48	43,49	45,16	44,85	43,28	45,22	43,21	43,82	43,69	43,94
Fe_2O_3	1,78	-0,15	16,38	2,60	3,28	0,92	1,78	1,91	-2,15	-0,01	0,17	2,86	2,99
MnO	1,99	3,19	1,19	1,91	1,98	1,73	1,58	1,83	0,75	0,72	3,72	1,35	1,54
MgO	0,01	0,19	3,88	0,08	0,00	0,00	0,00	1,18	1,75	2,09	0,00	0,12	0,06
Total	100,22	101,22	99,72	100,82	99,32	99,96	99,82	100,66	100,15	99,21	100,65	98,37	99,25
Formula based on 2 cations and 3 oxygens													
Ti	0,98	1,00	0,84	0,97	0,97	0,99	0,98	0,98	1,02	1,00	1,00	0,96	0,97
Fe^{+2}	0,94	0,93	0,68	0,93	0,93	0,95	0,95	0,90	0,94	0,90	0,92	0,93	0,93
Fe^{+3}	0,03	0,00	0,30	0,05	0,06	0,02	0,03	0,04	-0,04	0,00	0,00	0,05	0,06
Mn	0,04	0,07	0,02	0,04	0,04	0,04	0,03	0,04	0,02	0,02	0,08	0,03	0,03
Mg	0,00	0,01	0,14	0,00	0,00	0,00	0,00	0,04	0,06	0,08	0,00	0,00	0,00
Total	2,00	2,00	1,99	2,00	2,00	2,00	2,00	1,99	2,00	1,99	2,00	1,97	2,00
Ilm	98,206	100,010	84,364	97,489	96,832	99,048	98,271	98,002	101,866	99,680	99,837	96,273	97,049

Enclaves

Benmoreitic enclaves of post-caldera comendites contain titanomagnetite (Usp_{54-73}), sometimes trellis-type oxy-exsolved into magnetite (Mag_{96-99}) and ilmenite (Ilm_{97}) (Figure 5.18.c).

Post-caldera phreatomagmatic trachytic ejecta

Trachytic holocrystalline ejecta of post-caldera phreatomagmatic activity contain titanomagnetite (Usp_{45}) and ilmenite (Ilm_{100}) (Figure 5.18.h). In addition, sandwich type trellis exsolution of titanomagnetite into magnetite ($Usp_{35}Mag_{65}$) and ilmenite (Ilm_{91}) is frequent (Figure 5.19.d).

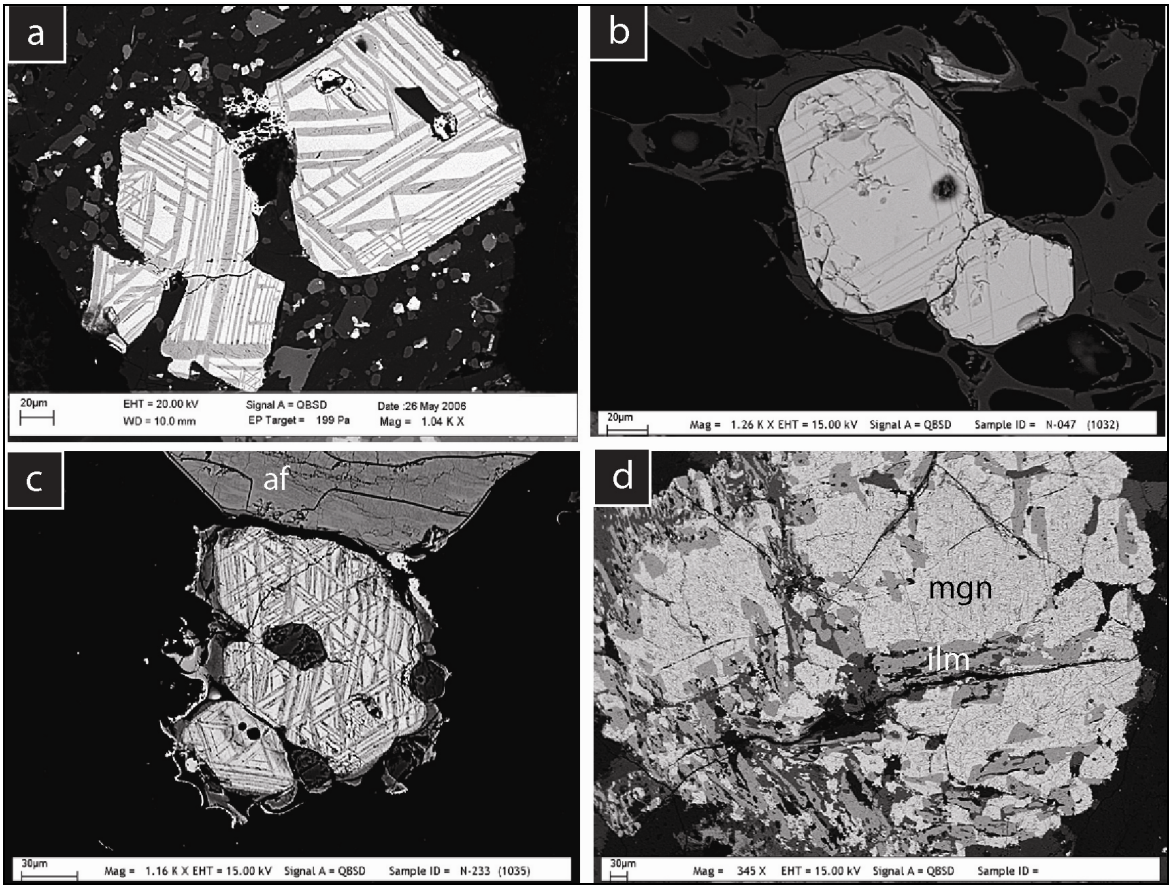

Figure 5.19: Exsolution textures of Fe-Ti oxides in Nemrut eruptive units. (a) Coarse trellis type exsolution in mugearite. (b) Very fine trellis in dark colored plinian airfall underlying Nemrut ignimbrite (SID: 1032). (c) Fine-to-coarse trellis exsolution in Nemrut ignimbrite. (d) Sandwich trellis in post-caldera phreatomagmatic trachytic ejecta (Terminology after Buddington and Lindsley, 1964)

5.1.5 Amphibole

Occurrence of amphibole is relatively restricted to some pre-caldera rhyolites and trachytes, on the other hand subordinate occurrence of amphibole is observed rarely in mugearites and Type II benmoreitic enclaves (Table 5.6). In some of the rhyolites, no ideal stochiometric crystal - chemical formulae for amphibole could be acquired (Si_{pfu} > 8). Furthermore, the total weight of analyzed oxides is generally lower than 97 %. Regarding the fact that Na-amphibole from peralkaline granites commonly contains significant Li in the octahedral sites (e.g. Hawthorne, 1993), a practice proposed by Tribuzio and Giacomini (2002), which requires adding 0.75% Li and recalculating the cation proportions could have been applied. Although, such an addition into total weight of oxides leads to acquire some acceptable results (Si_{pfu} ~ 8), without the presence of any analyses of F, which reaches up to 3.67 % in synthesized amphiboles in peralkaline rhyolites (cf. Scaillet and Macdonald, 2003), modification of original analyses would be insufficient. Thus, original amphibole analyses are calculated without any modification and minerals are named “as is” according to Leake et al. (1997). However, the reader should be cautious about the facts stated above.

Compositional range and names of the amphiboles are illustrated on Si_{pfu} versus Ca_{pfu} diagram (Figure 5.20 after Mitchell, 1990).

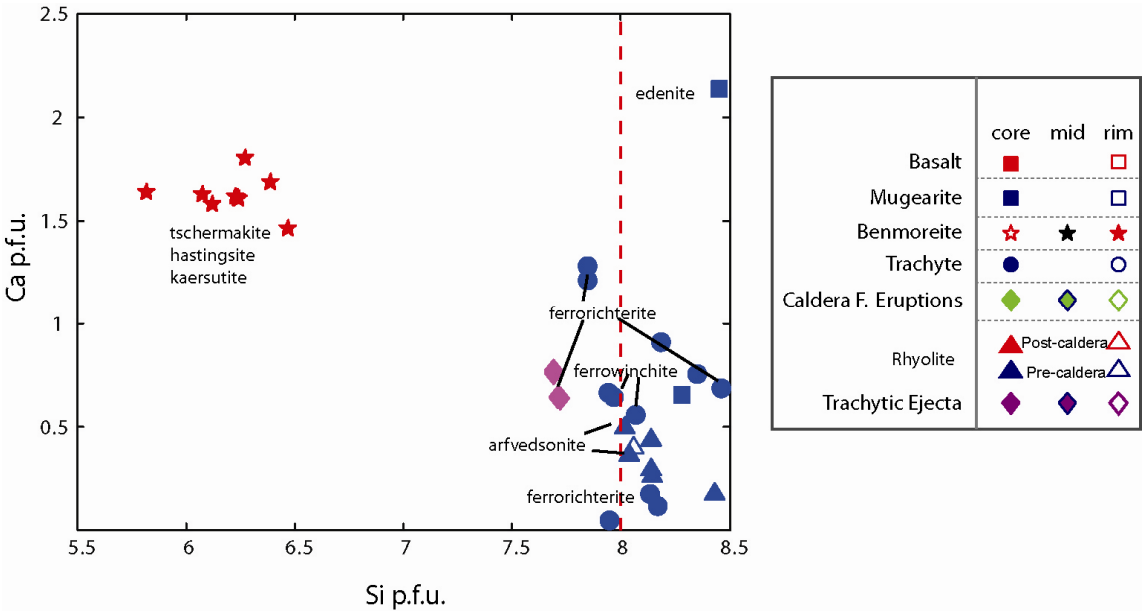

Figure 5.20: Compositional range and nomenclature of amphiboles in Nemrut eruptive units (after Mitchell, 1990). Most of the amphiboles in peralkaline rocks exceed ideal crystal – chemical formulae (Si_{pfu}>8) a common feature of peralkaline rocks due to their conventionally not-analyzed element content. Significant discrepancy is observed between the modal amphiboles of silicic rocks and the amphiboles in intracrystalline ponds of the enclaves.

In mugearites, scarce microphenocrysts of calcic amphibole (edenite) and sodic-calcic amphibole (ferrorichterite) in destabilized feldspar are observed (section 4.1.1). In pre-caldera comenditic trachytes (especially in SID: 1040 and 1060) amphibole belongs to dominantly sodic-calcic amphiboles. Microphenocrysts and microlites of ferrorichterite and ferrowinchite are observed. In addition, sporadic sodic amphibole (arfvedsonite) microphenocrysts are also present (Figure 5.21.a). In pre-caldera comendites, amphibole is sodic with phenocrysts of riebeckite and arfvedsonite. They are observed to mantle resorbed olivine (Figure 5.21.b).

Enclaves

In benmoreitic Type II enclaves of post-caldera comendites, formation of subordinate calcic amphibole is observed especially along the Ca-rich phases with disequilibrium textures. Particularly, in the “ponds” and along the inner rims of cellular plagioclase, acicular calcic amphiboles are observed. They exhibit various compositions due to their alkali (NA+K) content in their A sites. They are ferroactinolite, ferrohornblende and tschermakite when $(Na+K)_A < 0.50$ whereas, hastingsite and kaersutite when $(Na+K)_A > 0.50$. These amphiboles exhibit strong evidence for being derived from the plagioclase intracrystal melt. Their occurrence is restricted to the inner confined ponds of cellular plagioclase and not to the actual groundmass. (Figure 5.21.c).

Holocrystalline Ejecta

Holocrystalline granular (Type G) lithic ejecta of post-caldera phreatomagmatic activity contain both sodic-calcic and calcic amphiboles. Sodic-calcic and calcic amphiboles are ferrorichterite. They are observed to mantle destabilized olivine (Figure 5.21.d). Further resorption of amphiboles yields aenigmatite and sometimes clinopyroxene.

Table 5.6: Selected amphibole analyses. SID: Stratigraphic ID, emid: Electron Microprobe ID, Location (0: center, 9: border), Stability (0: disequilibrium, 9: stable). B: Basalt, M: Mugearite, BM1/2 (Benmoreitic enclave Type 1 or 2), (C) T: (Comenditic) Trachyte, C: Comendite, P: Pantellerite. Nomenclature; Arf: Arfvedsonite, Fwc: Ferrowinchite, Frch: Ferrorichterite, Rbc: Riebeckite, Kaer: Kaersutite, Hst: Hastingsite, Fhb: Ferrohornblende, Fac: Ferroactinolite, Tsch: Tschermakite

	Pre-Caldera rocks								Post-Caldera rocks						
Sample	**N-149**	**N-149**	**N-239**	**N-083**	**N-209**	**N-227**	**N-227**	**N-227**	**N-220**	**N-256**	**N-256**	**N-050**	**N-050**	**N-050**	**N-050**
SID	1060	1060	1060	1060	1050	1040	1040	1040	1020	1010	1010	1010	1010	1010	1010
Rock	C	C	CT	CT	M	C	C	C	CT	BM1	BM1	BM2	BM2	BM2	BM2
emid	423	431	1319	393	479	801	802	798	556	1522	1521	1500	1496	1499	1497
Location	0	0	0	0	0	0	1	0	9	0	0	0	0	0	0
Stability	9	0	9	9	9	9	9	9	9	9	9	9	9	9	9
Size (µ)	750	300	75	90	20	200	200	400	400	25	30	50	30	50	50
Na_2O	7,22	6,87	4,08	4,43	4,18	7,90	5,18	6,40	6,17	2,23	2,23	2,63	0,95	0,80	2,34
MgO	0,01	0,08	1,72	0,77	2,48	0,00	0,00	0,02	4,65	9,53	10,48	7,54	8,15	6,53	9,47
K2O	1,21	1,42	1,45	4,33	3,51	1,40	1,44	1,57	1,18	0,73	0,74	0,80	0,26	1,15	0,67
CaO	2,06	2,79	3,74	0,72	4,30	1,47	1,64	1,00	3,78	10,84	9,63	9,58	14,88	12,37	10,21
TiO_2	0,28	0,58	3,49	1,74	1,81	0,39	0,36	0,67	0,78	5,11	3,88	3,70	1,46	0,77	1,95
FeO_t	34,55	34,04	30,13	13,49	15,49	33,78	34,19	31,57	29,31	18,79	18,05	21,42	19,53	16,22	19,98
MnO	1,52	1,64	0,91	0,63	0,24	1,23	1,10	1,20	1,14	0,26	0,10	0,52	0,77	0,93	0,63
SiO_2	49,64	49,26	50,26	52,92	55,89	50,07	50,35	52,07	49,68	40,81	40,74	39,19	43,48	50,67	42,44
Al_2O_3	0,21	0,15	0,50	14,46	11,58	0,21	0,19	0,21	0,90	8,30	8,93	10,40	7,68	6,68	9,42
Total	96,69	96,85	96,28	93,47	99,47	96,45	94,49	94,75	97,59	96,61	94,79	95,78	97,17	96,11	97,10
Formula calculated for 23 oxygens															
T															
Si	8,04	8,02	7,97	8,17	8,28	8,15	8,14	8,43	7,71	6,27	6,23	6,08	6,83	7,92	6,39
^{iv}Al	0,00	0,00	0,03	0,00	0,00	0,00	0,00	0,00	0,16	1,50	1,61	1,90	1,17	0,08	1,61
Ti	0,00	0,00	0,00	0,00	0,00	0,00	0,00	0,00	0,09	0,22	0,16	0,02	0,00	0,00	0,00
Sum_T	8,04	8,02	8,00	8,17	8,28	8,15	8,14	8,43	7,97	8,00	8,00	8,00	8,00	8,00	8,00
C															
^{vi}Al	0,04	0,03	0,06	2,63	2,02	0,04	0,04	0,04	0,00	0,00	0,00	0,00	0,25	1,15	0,06
Ti	0,03	0,07	0,42	0,20	0,20	0,05	0,04	0,08	0,00	0,37	0,29	0,41	0,17	0,09	0,22
Fe^{+3}	0,58	0,35	0,32	0,00	0,00	0,28	1,08	0,25	0,86	0,39	1,05	0,93	0,00	0,00	0,98
Mg	0,00	0,02	0,41	0,18	0,55	0,00	0,00	0,01	1,08	2,18	2,39	1,74	1,91	1,52	2,12
Fe^{+2}	4,09	4,28	3,67	1,74	1,92	4,32	3,55	4,02	2,94	2,02	1,26	1,85	2,57	2,12	1,53
Mn	0,21	0,23	0,12	0,08	0,03	0,17	0,15	0,16	0,12	0,03	0,01	0,07	0,10	0,12	0,08
Sum_C	4,96	4,98	5,00	4,83	4,72	4,85	4,86	4,57	5,00	5,00	5,00	5,00	5,00	5,00	5,00
B															
Mg	0,00	0,00	0,00	0,00	0,00	0,00	0,00	0,00	0,00	0,00	0,00	0,00	0,00	0,00	0,00
Fe^{+2}	0,00	0,00	0,00	0,00	0,00	0,00	0,00	0,00	0,00	0,00	0,00	0,00	0,00	0,00	0,00
Mn	0,00	0,00	0,00	0,00	0,00	0,00	0,00	0,00	0,03	0,00	0,00	0,00	0,00	0,00	0,00
Ca	0,36	0,49	0,64	0,12	0,68	0,26	0,28	0,17	0,63	1,78	1,58	1,59	2,50	2,07	1,65
Na	1,64	1,51	1,25	1,32	1,20	1,74	1,62	1,83	1,34	0,22	0,42	0,41	0,00	0,00	0,35
Sum_B	2,00	2,00	1,89	1,44	1,88	2,00	1,91	2,00	2,00	2,00	2,00	2,00	2,50	2,07	2,00
A															
Na	0,62	0,65	0,00	0,00	0,00	0,75	0,00	0,18	0,52	0,45	0,24	0,38	0,29	0,24	0,33
K	0,25	0,30	0,29	0,85	0,66	0,29	0,30	0,32	0,23	0,14	0,14	0,16	0,05	0,23	0,13
Sum_A	0,87	0,95	0,29	0,85	0,66	1,04	0,30	0,51	0,75	0,59	0,38	0,54	0,34	0,47	0,46
Sum	15,87	15,95	15,18	15,30	15,54	16,04	15,20	15,51	15,72	15,59	15,38	15,54	15,85	15,54	15,46
Name	Arf	Arf	Fwc	Frch	Frch	Arf	Rbc	Arf	Frch	Kaer	Tsch	Hst	Fhb	Fac	Tsch

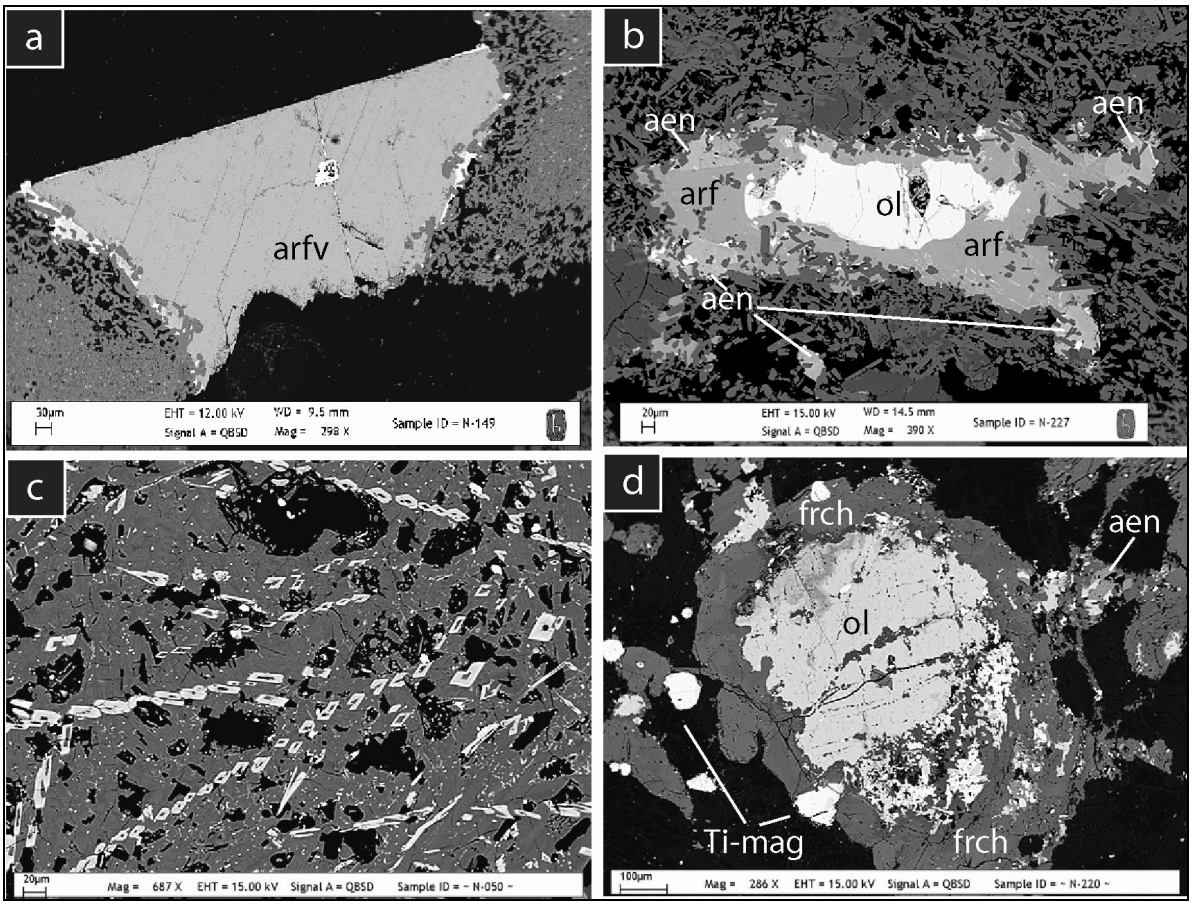

Figure 5.21: Amphibole in Nemrut eruptive units. (a) Subhedral arfvedsonite in pre-caldera comendite (SID: 1060). Ilmenite and Fs-rich cpx is observed at the rims. Groundmass is comprised of anorthoclase. (b) Decomposition of olivine into arfvedsonite and aenigmatite in pre-caldera comendite (SID: 1040). (c) Acicular spindles of tschermakite in intracrystalline ponds of benmoreitic enclaves exhibiting late-stage rapid crystallization. (d) Decomposition of fayalite into ferrorichterite and aenigmatite dominant mantling aggregate.

5.1.6 Aenigmatite

Aenigmatite is a common mineral of peralkaline magmatic rocks worldwide. Aenigmatite is present only in more differentiated (1.08 < A.I. < 1.52) silica over-saturated trachytes and pre-caldera rhyolites (Table 5.7). They are frequently observed as anhedral – subhedral microcrysts / microlites (φ < 250 μm, except one phenocryst, φ ~ 700 μm in holocrystalline ejecta fragment, N-220). Aenigmatite usually coexists with stable / relict amphibole in peralkaline trachytes. In amphibole-bearing peralkaline trachytes and pre-caldera rhyolites aenigmatite is observed to have been formed along rims of amphibole (Figure 5.21.b, d). Such occurrence of aenigmatite could be explained by the following reaction (Marks and Markl, 2003):

$$4\ \text{arfvedsonite} + 2\ Na^{+} + 2\ Ti^{4+} + H_2O + O_2 \rightarrow 10\ \text{aegirine} + 2\ \text{aenigmatite} + 10\ H^{+}$$

Furthermore, aenigmatite forms at the expense of Fe-Ti oxides (Figure 5.22) by the following reaction (Schönenberger et al., 2006):

$$\text{Ulvöspinel} + 2\ Na+ + 3\ Fe^{2+} + 6\ SiO_2{}^{(fluid)} + 4\ H_2O \rightarrow \text{aenigmatite} + 8\ H^+$$

Table 5.7: Selected analyses of aenigmatite from Nemrut pre-caldera units

	Pre-Caldera				
Sample	**N-149**	**N-151**	**N-098**	**N-080**	**N-188**
Rock	*Comendite*	*Comendite*	*Pantellerite*	*Comenditic Trachyte*	*Pantellerite*
Type	*Lava Flow*	*Dike*	*Lava Flow*	*Lava Flow*	*Lava Flow*
Na2O	6,91	7,05	7,16	6,90	7,14
MgO	0,05	0,10	0,06	0,05	0,00
K2O	0,07	0,09	0,25	0,02	0,13
CaO	0,33	0,20	0,62	0,22	0,31
TiO2	8,49	6,86	7,84	6,16	6,71
Cr2O3	0,00	0,01	0,01	0,04	0,00
FeO	38,83	37,03	36,64	38,01	35,94
Fe2O3	1,01	6,25	4,03	5,30	6,53
MnO	1,48	1,04	0,94	1,05	1,04
NiO	0,00	0,02	0,01	0,00	0,00
SiO2	41,01	40,78	40,77	41,35	40,51
Al2O3	0,40	0,24	1,18	0,13	0,27
Total	98,59	99,66	99,50	99,23	98,57
Formulae based on 20 oxygen atoms					
Si	5,96	5,89	5,85	6,00	5,90
Ti	0,93	0,75	0,85	0,67	0,74
Al	0,07	0,04	0,20	0,02	0,05
Fe_2	4,72	4,47	4,40	4,61	4,38
Fe_3	0,11	0,68	0,44	0,58	0,72
Mn	0,18	0,13	0,11	0,13	0,13
Mg	0,01	0,02	0,01	0,01	0,00
Ca	0,05	0,03	0,10	0,03	0,05
Na	1,95	1,97	1,99	1,94	2,02
K	0,01	0,02	0,05	0,00	0,02

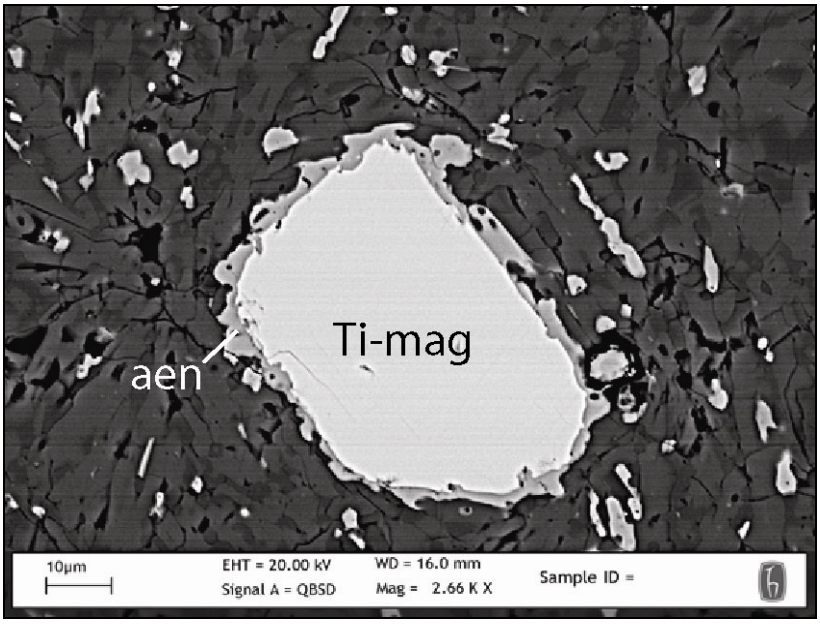

Figure 5.22: Aenigmatite forms at the expense of Fe-Ti oxides in pre-caldera comendite (SID: 1040)

5.1.7 Accessory Phases

Although in a recent study based on polarized microscopy, Özdemir et al. (2006), report occasional occurrences of biotite for Nemrut lavas, our thin-section observations and microprobe analyses revealed none. Quartz is a common accessory phase in silica-oversaturated pre-caldera comenditic trachytes and crystalline rhyolites. They are observed as subhedral subordinate crystals and as euhedral inclusions in fayalite and / or augite. Apatite is omnipresent in mugearites, trachytes and rhyolites. Plinian fallout (SID: 1036) overlying Nemrut Ignimbrite, contains apatite as inclusions in feldspar and titanomagnetite. Within the Nemrut ignimbrite sequence, free minute crystals of apatite have been observed. Pre-caldera trachytes and rhyolites bear apatite as inclusions in ilmenite, olivine and feldspar.

Post-caldera comendites (SID: 1010 and 1020) contain REE-silicate chevkinite-group [(Ce, La, Ca)$_4^-$ (Fe^{2+}, Mg)$_2$ (Ti, Fe^{3+})$_3$ Si$_4$O$_{22}$] mineral as inclusions in fayalite and as free crystals along the rims of fayalite and ilmenite. Chevkinite is regarded as a "REE sink" with strong attraction to all REE to the extent that these are readily accommodated in the structure (Troll et al., 2003). Some chevkinite analyses realized by energy dispersive spectrometry are given in Table 5.8. Zircon and apatite occasionally occurs together with chevkinite (Figure 5.23). Apatite is observed to be enriched in REE when it is adjacent to chevkinite, probably because of its strong preference for these elements.

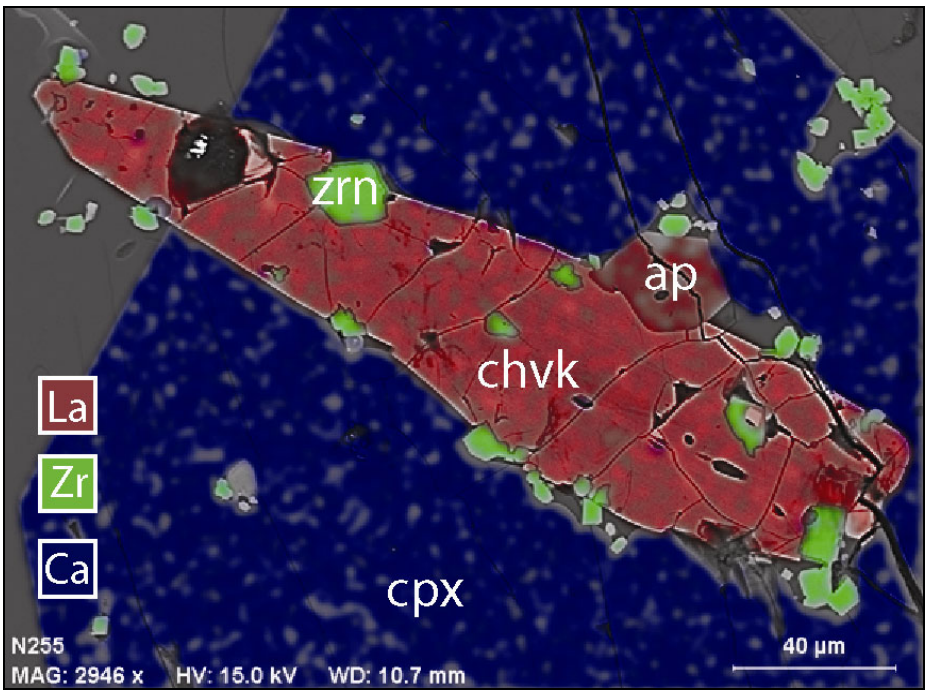

Figure 5.23: Compositional map of subhedral chevkinite (chvk) together with zircon (zrn), apatite (ap) and cpx in post-caldera vitric comendite (SID: 1010).

Table 5.8: Selected analyses of chevkinite in post-caldera comendites, performed by full quantitative EDS analyses.

Sample	SiO_2 (%)	CaO (%)	TiO_2 (%)	Fe_2O_3 (%)	La (%)	Ce (%)	ZrO_2 (%)
N-255	21.0	2.6	20.1	17.4	13.7	25.3	
N-255	18.8	3.4	21.2	16.8	14.1	25.7	
N-255	19.9	3.3	22.1	15.5	14.0	25.2	
N-255	16.8	3.6	22.2	17.4	14.5	25.4	
N-255	19.8	3.7	21.3	16.5	14.2	24.5	
N-255	22.2	3.2	21.0	16.3	13.5	23.7	
N-255	22.5	3.7	21.3	15.4	13.2	23.9	
N-255	21.6	3.1	20.4	17.0	13.4	24.5	
N-255	18.8	2.1	20.9	18.7	13.7	25.9	
N-255	19.5	2.9	21.1	17.2	13.9	25.5	
N-255	22.7	2.9	19.9	16.3	12.7	23.2	2.3

5.2 Crystal - Liquid Equilibria

Phenocryst compositions and mineral-melt equilibria are sensitive to variations in the critical intensive parameters of magmatic systems and these variations can be used to constrain the crystallization environments (Damasceno et al, 2002). Therefore, using both phenocryst and corresponding whole rock compositions, we can deduce whether mineralogic evolution paths follow liquid line of descent.

5.2.1 Olivine - Liquid Equilibrium

Chemical equilibrium between olivine and silicate liquid has been the subject of considerable attention. In multi-component systems the temperature dependence of Mg and Fe partitioning between olivine and liquid are very similar (Toplis, 2005). The ratio of the partition coefficients of iron and magnesium is called the exchange coefficient:

$$K_{DOl-liq}^{Mg-Fe} = \frac{X_{liq}^{Mg} / X_{Ol}^{Mg}}{X_{liq}^{Fe^{+2}} / X_{Ol}^{Fe^{+2}}}$$

where X represents the molar fractions of respective components in either liquid (liq) or olivine (ol). The exchange partition coefficient between olivine and basaltic liquid is experimentally well constrained being constant 0.3 ± 0.03 (Roeder and Emslie, 1970).

However, recent studies show that it depends on melt compositions ranging between 0.15 and 0.45 (Mysen, 2007 and references therein).

Olivine-melt equilibrium relations are best shown in a plot (Figure 5.24.a) of whole rock Mg-number [100 x ($Mg^{+2}/Mg^{+2} + Fe^{+2}$)] versus forsterite content of olivine (e.g. Garcia, 1996) with the equilibrium field (K_D = 0.3 ± 0.03) is depicted as the shaded band (Damasceno et al, 2002). Also depicted by the arrows are the relative effects of high Mg xenocryst addition and groundmass crystallization. This plot mainly illustrates the magmatic evolution from basalts to metaluminous trachytes, as highly differentiated units are significantly poor in Mg.

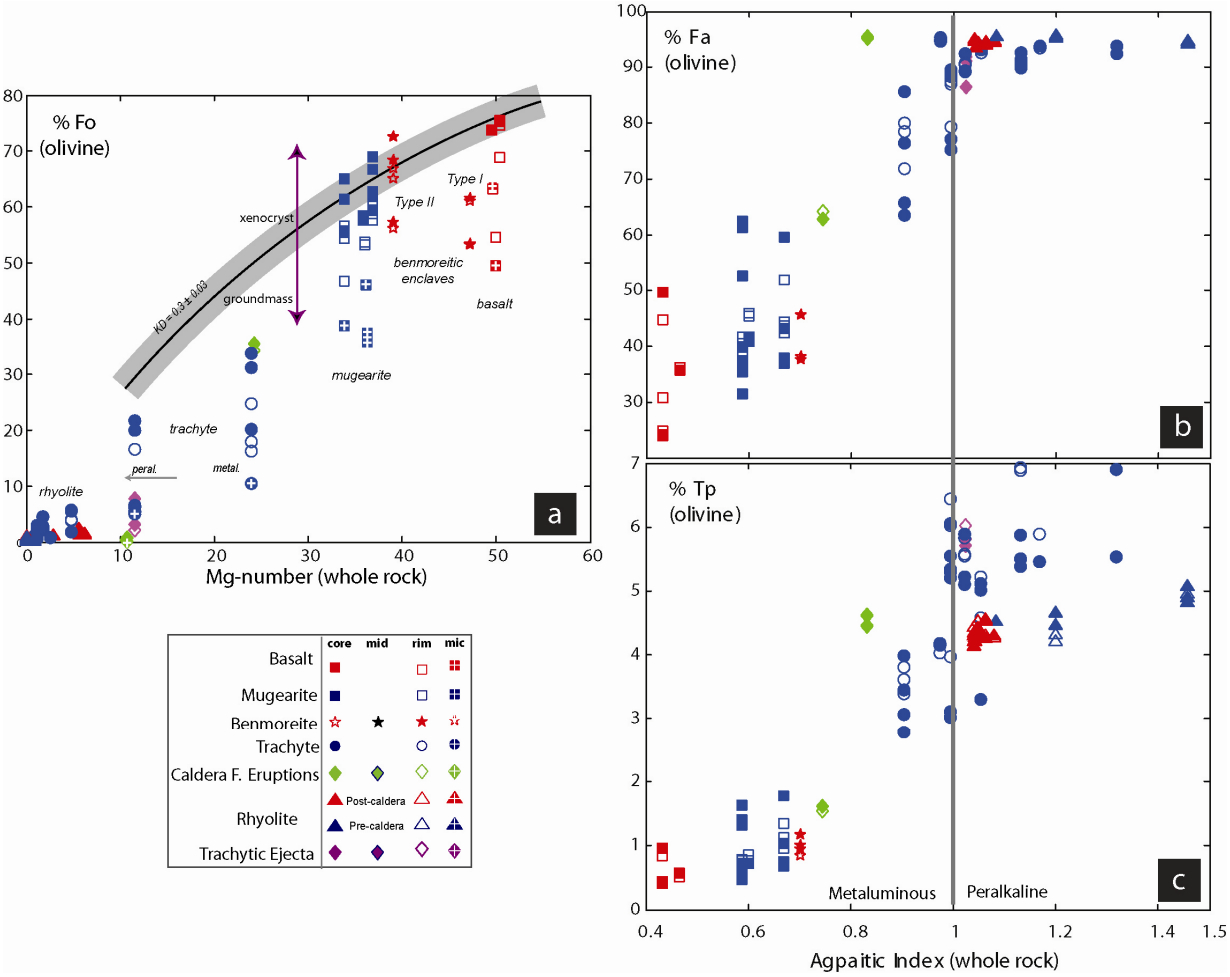

Figure 5.24: Variation of olivine compositions versus nominal whole rock geochemistry (a) Olivine – melt Fe/Mg equilibrium diagram. Whole rock Mg-numbers versus Fo content of olivine is plotted, where Mg-number = $100*Mg^{+2}/ (Mg^{+2} + Fe^{+2})$ is calculated assuming Fe^{+3}/Fe^{+2} = 0.1. The equilibrium field for Fe/Mg exchange between olivine and the melt (0.3 ± 0.03; Roeder and Emslie, 1970) is shown. Arrows indicate the relative effects of xenocryst addition and groundmass crystallization. (b) Fa content and (b) Tp content variation versus the degree of peralkalinity of the rock (Agpaitic Index). (mic: microlite)

Figure 5.24.a depicts the relationship between Mg-number and Fo content of phenocryst cores, rims and microlites. Core compositions of phenocrysts in basalts lie within the equilibrium field, whereas respective rims and groundmass microlites shift towards groundmass area. In Type I benmoreitic enclaves Fo contents of olivines fall below the equilibrium field indicating that these are not equilibrium compositions. Type II benmoreitic enclaves and mugearites however exhibit scatter on olivine compositions. The petrographical observation of resorbed olivine (see section 4.1.2 and 4.1.3) in these units is confirmed by the analyses which plot over the equilibrium field representing an exotic origin. However rim and microlite compositions are towards groundmass field. Metaluminous trachytes (Sample N-036: SID 1036 plinian and Sample N-136: SID 1060 lava flow) bear olivine which plot significantly below the equilibrium field indicating that they are not true equilibrium compositions. Marginally peralkaline trachytes tend to lie along the equilibrium field. More evolved rhyolites (Mg-number < 10) have fayalite. For these highly evolved rock compositions, the proposed equilibrium field ($K_D \approx 0.3$) tends to yield erroneous estimations. It is yet unclear the relative roles of increased silica activity and alkali content of the melt on iron - magnesium partitioning (Toplis, 2005). Besides, $K_{D\ Mg/Fe}^{olivine/melt}$ becomes sensitive to the increasing degree of melt polymerization and melt composition (Mysen, 2007).

Nevertheless, we can infer that the evolution in olivine compositions in basaltic and rare intermediate products towards the least differentiated metaluminous trachytes conforms to a general crystal fractionation trend. However, olivine compositions in mugearite and benmoreitic enclaves strongly suggest the interference (mixing) between mafic and felsic melts.

Tephroite (Tp mol %) and fayalite mole fractions in olivine are positively correlated with the degree of peralkalinity (Figure 5.24.b, c). Peralkaline rocks bear solely fayalite (Figure 5.24.b). Elevated MnO content and X_{Fe}, often seen in peralkaline silicic rocks indicate the decrease in temperature (Scaillet and Macdonald, 2003). Tp content of olivine is < 2 % in basalt, mugearite and benmoreitic enclaves, but reaches up to 7% in peralkaline trachyte. However in comendites, Tp is confined to 4 - 5 % (Figure 5.24.c).

5.2.2 Clinopyroxene - Liquid Equilibrium

The Fe/Mg exchange partition coefficient between clinopyroxene and basaltic liquid is less well constrained than that for olivine-liquid, principally because of the presence of ferric iron in clinopyroxene and in the melt (Damasceno et al., 2002). However, experimental studies (Grove and Bryan, 1983; Toplis and Carroll, 1995) suggest that a value of 0.23 ± 0.05 for

exchange partition coefficient is consistent while there might be slight compositional effects (Hoover and Irvine, 1977; Damasceno et al., 2002).

Figure 5.25.a illustrates the relationships between Mg-numbers of whole rock and clinopyroxenes. Equilibrium field is drawn according to $K_D = 0.23 \pm 0.05$ (Toplis and Carroll, 1995). Relative effects of xenocryst addition and groundmass crystallization are shown by the arrows. As clearly seen, this plot demonstrates the evolution of clinopyroxene and melts relatively better for basaltic to intermediate compositions as the exchange coefficient better represents the equilibria between clinopyroxene and basaltic magma.

Basalts and Type I benmoreitic enclaves, as stated before, bear clinopyroxene only as microlites, which fall well below the equilibrium field (Figure 5.25.a). However some clinopyroxenes in mugearites (especially in sample N-209) which plot significantly below the equilibrium field are not microlites. Rather, they are unstable resorbed phenocrysts mentioned earlier (see section 4.1.2) suggesting a more evolved exotic origin. Metaluminous trachytic lavas (sample N-136) and upper plinian airfalls (sample N-036) bear clinopyroxene which plot within the equilibrium field. Clinopyroxenes of porphyritic Type P trachytic ejecta (sample N-272) of post-caldera phreatomagmatic activity, exhibit scatter with microlites within the equilibrium field, Mg-rich rims due to reverse zoning and strongly resorbed xenocrysts. This indicates the probable interference of two magmas with evolved and less evolved compositions. As the rock compositions evolve towards more peralkaline side, clinopyroxene compositions plot significantly below the equilibrium field. This is expected, as suggested K_D does not represent exchange equilibria between clinopyroxene and the melt in highly evolved peralkaline compositions.

Furthermore, Mg-numbers of clinopyroxenes tend to decrease slightly form basalts to metaluminous trachytes but an abrupt decrease is observed as soon as the rock composition becomes peralkaline (Figure 5.25.b). Total Al content per formula unit (pfu) of clinopyroxenes exhibits gradual decrease towards evolved compositions. However, clinopyroxenes of Type II benmoreitic enclaves and Type P trachytic ejecta display deviation from the general trend, strongly due to their heterogeneous nature (Figure 5.25.c). Mn in QUAD clinopyroxenes is positively correlated with the degree of peralkalinity. Nevertheless, Type P trachytic ejecta bear clinopyroxenes with 0.01 – 0.05 Mn pfu (Figure 5.25.d).

Aegirine component of clinopyroxenes is relatively constant in metaluminous rocks (<15 mol%). However peralkaline ($1 < A.I. < 1.3$) trachytes and rhyolites bear aegirine-augite microphenocrysts and pure aegirine in groundmass (Figure 5.25.e). Sharp depletion of Ti in clinopyroxene is observed from basalts to mugearites and benmoreitic enclaves (Figure

5.25.f). However, the abrupt increase of Ti in aegirine microlites in aenigmatite bearing peralkaline rocks can be explained by the decomposition of aenigmatite to Ti-rich aegirine (Larsen, 1977; Schönenberger et al, 2006) by the following formula:

$$2\ \text{aenigmatite} + 2\ Na^{+} + 1.5\ O_2 + H_2O \rightarrow 2\ \text{ulvöspinel} + 6\ \text{aegirine} + 2\ H^{+}$$

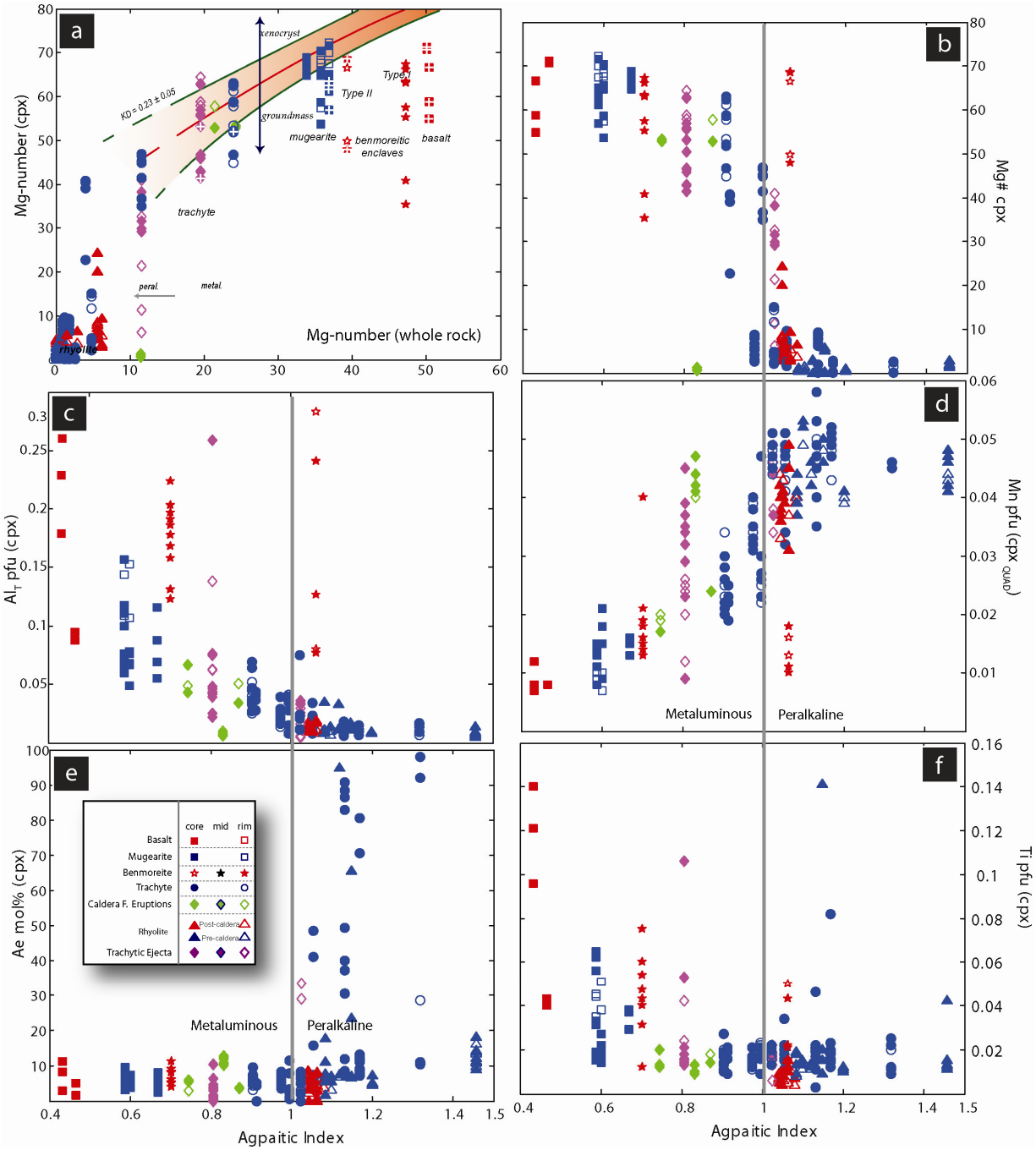

Figure 5.25: Variation of clinopyroxene compositions versus nominal whole rock geochemistry (a) Cpx - melt Fe/Mg equilibrium diagram. Whole rock Mg-numbers versus Mg-numbers of cpx are plotted, where Mg-number = $100*Mg^{+2}/(Mg^{+2} + Fe^{+2})$ is calculated assuming $Fe^{+3}/Fe^{+2} = 0.1$. The equilibrium field for Fe/Mg exchange between cpx and the melt (0.23 ± 0.05; Toplis and Carroll, 1995) is shown. Arrows indicate the relative effects of xenocryst addition and groundmass crystallization. Variation of (b) Mg-numbers (c) Total Al pfu (d) Mn pfu (e) Aegirine content and (f) Ti pfu in cpx versus degree of peralkalinity of nominal rocks.

5.2.3 Feldspar - Liquid Equilibrium

In Figure 5.26.a, plagioclase with equilibrium textures of basalts, mugearites, benmoreitic enclaves, trachytic caldera related products and, to a lesser degree, metaluminous trachytes could be considered as in equilibrium with a liquid similar to the whole rock composition, under almost dry conditions (K_D = 1-3) and at low pressure (< 2 kbar) (Sisson and Grove, 1993; Feeley and Dungan, 1996; Ferla and Meli, 2006). However, as stated earlier, disequilibrium feldspars are omnipresent in mugearites, benmoreitic enclaves, Type P trachytic ejecta and in the least evolved metaluminous trachytes.

Feldspars are mainly represented by plagioclase and alkali feldspar phenocrysts in metaluminous and peralkaline rocks respectively. Nemrut feldspars conform to the experimental studies (i.e. Scaillet and Macdonald, 2001) as plagioclase (An > 20%) crystallization is suppressed as soon as the melt becomes peralkaline, whatever its CaO or volatile contents (Figure 5.26.b). An overall tendency of gradually decreasing An content is observed from basalt to rhyolite. However, significant scatter is evident in some highly heterogeneous mugearites (N-209), Type II benmoreitic enclaves and Type P trachytic ejecta as well as some metaluminous trachytes (N-136). The crystals in benmoreitic enclaves, metaluminous trachyte and Type P ejecta, which deviate from the general trend, are highly resorbed xenocrysts. Omitting the Ab-Or perthitic exsolution in Type G trachytic ejecta (not shown), peralkaline rocks contain dominantly Na-sanidine. Metaluminous rocks, however, display dispersed curvilinear increase in Or towards peralkaline rocks, where plagioclase is replaced by alkali feldspar (Figure 5.26.c). Again, scattered analyses which deviate from the general trend are observed in rocks with disequilibrium textures (mugearite N-209, Type P trachytic ejecta N-272 and benmoreitic enclaves).

Omitting the feldspars with disequilibrium textures, it is fair to state that the feldspar compositional evolution is positively correlated with that of the melt, via liquid line of descent.

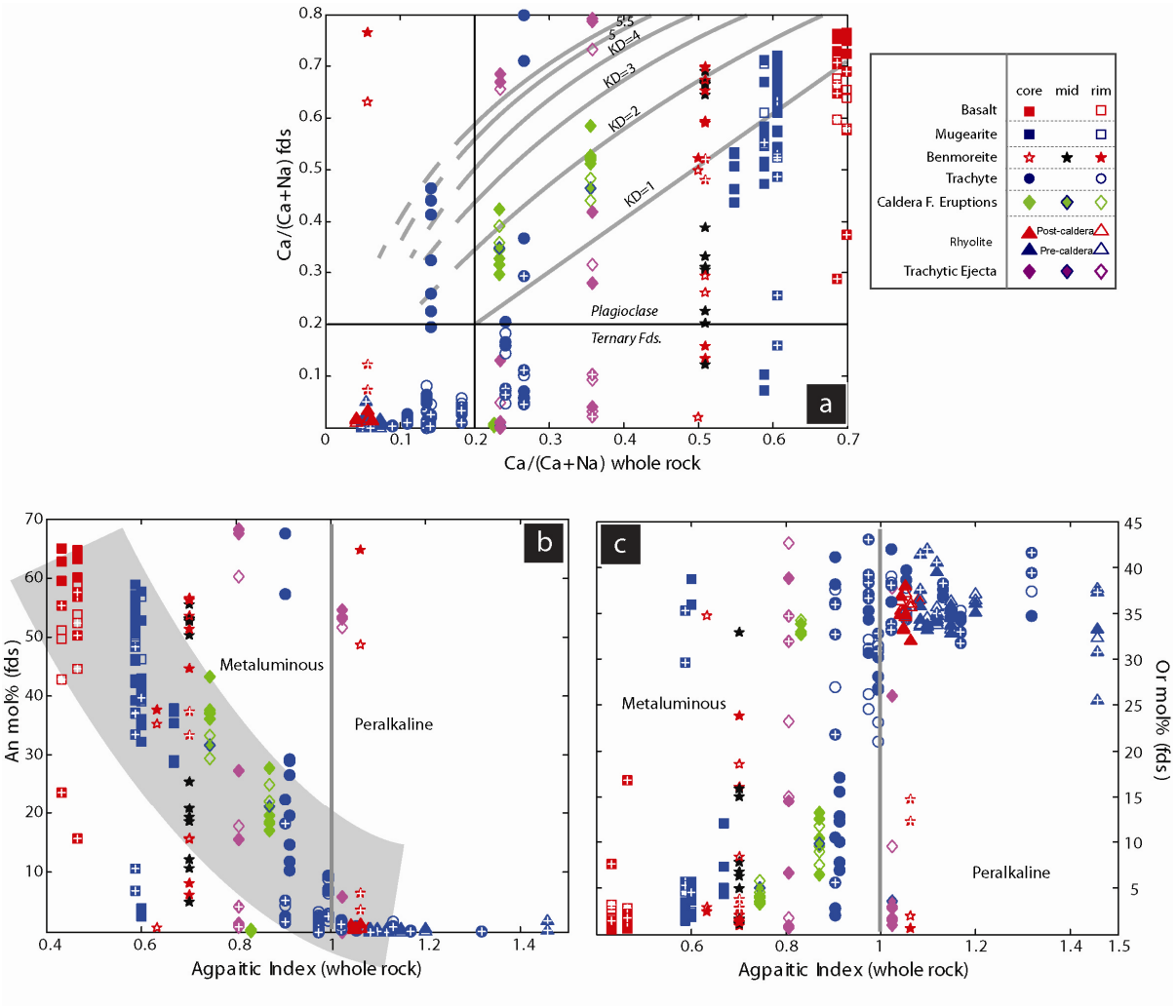

Figure 5.26: Feldspar - melt equilibria. (a) Plagioclase - melt equilibria of Nemrut eruptive units; K_D values are from Sisson and Grove (1993), (b) An content and (c) Or content variation versus the degree of peralkalinity of the nominal rocks.

5.3 Intensive Reservoir Parameters

Petrographical observations supported by mineralogical and geochemical data indicate two basic differentiation processes for the petrologic evolution of Nemrut volcanism: Fractional crystallization and magma mixing. Fractional crystallization is believed to be the prevailing mechanism for the complete evolution from mafic to felsic compositions. On the other hand, fingerprints of magma mixing would be limited to the melts having physical contact.

With the purpose of revealing the effects and the results of these dominant processes as well as the possible differentiation paths, geochemical data have been used for modelling fractional crystallization (see Chapter 6). Some of these models (essentially fractional crystallization by least squares mass balance model) have benefited from the chemical

compositions of the actual modal associations, thanks to extensive microprobe dataset generated during this study.

Modelling is literally the use of mathematical equations to simulate and predict real events and processes. A model should be consistent with the actual circumstances in which the simulated processes occur. Hence, before testing the hypotheses on petrologic differentiation (Chapter 6), it seems beneficial to constrain the intensive parameters of the magmatic reservoir. With the intention of constraining the magma chamber for consistent modelling, intensive state variables (density, pressure, temperature, viscosity and oxygen fugacity) have been calculated using thermodynamic equilibria. Thermodynamic models are based on the assumption that the natural systems are energy-conserving open composite systems, sealed off adiabatically from the rest of their surroundings (Spera and Bohrson, 2001).

5.3.1 Density

The density of the melts, especially in peralkaline bimodal suites, is believed to play an important role for explaining the Daly Gap. Liquid densities calculated from the major element concentrations assuming a dry magma (McBirney, 1993) illustrate the systematic decrease in density with respect to the degree of peralkalinity (Figure 5.27). Basalts are the densest units followed by mugearites, benmoreitic compositions, trachytes and rhyolites. Besides, thermodynamic modelling of density variation according to Ghiorso and Sack (1995), which conforms to the calculated patterns, illustrates the drastic decrease in density when fractional crystallization under varying conditions from a basaltic parent (sample N-258) is assumed as the dominant differentiation process.

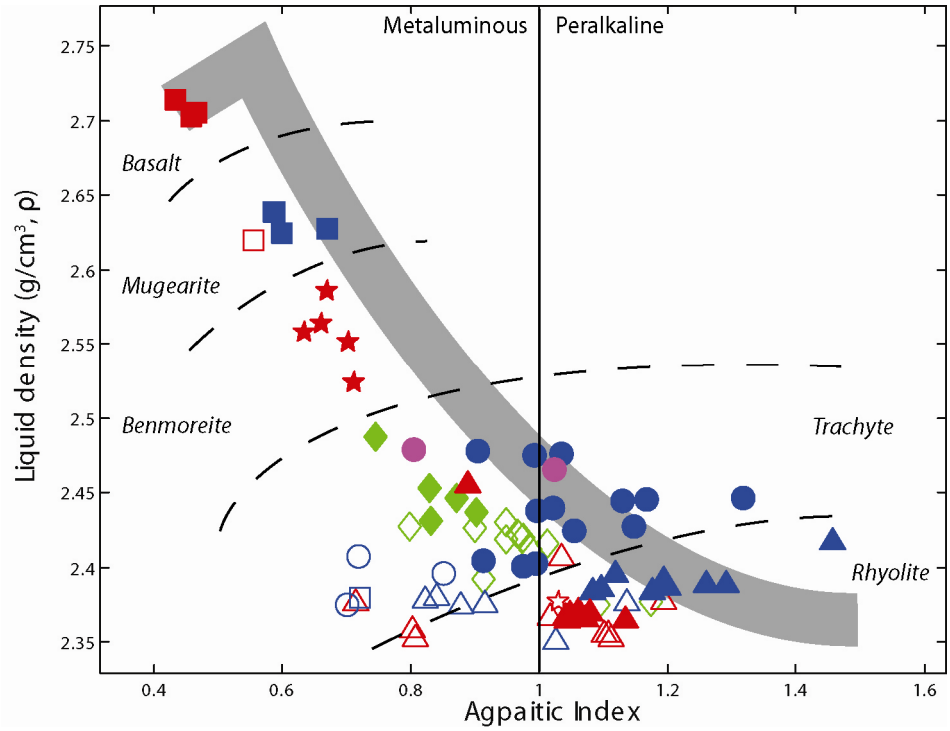

Figure 5.27: Variation of calculated density (ρ) (McBirney, 1993) versus the degree of peralkalinity in Nemrut eruptive units. Open symbols indicate EPMA realized glass analyses. Thick gray line is the average trend of MELTS produced FC models (Section 5.4)

5.3.2 Pressure

Nemrut mafic and silicic rocks bear typical low-pressure phenocryst mineralogy, observed in peralkaline suites worldwide (Mahood and Baker, 1986; Caroff et al., 1993; Scaillet and Macdonald, 2001; Peccerillo et al., 2003). Besides, a brief estimation of pressure using pressure dependence of plagioclase composition and calculated average melt temperatures, (see 5.3.3.) (Housh and Luhr, 1991; Tomiya and Takahashi, 2005) depicts that even plagioclase bearing mugearitic melts, ponding probably at the lowermost levels of the magmatic reservoir are under < 1,000 bar (Figure 5.28). Furthermore, experimental phase equilibrium studies on Kenya peralkaline trachytes and rhyolites (Bailey et al., 1974) show that alkali feldspar is the liquidus phase at pressures of about 1 kbar, where it is joined by quartz, which is on the liquidus at higher pressures (Macdonald, 1987). Quartz is accessory in Nemrut trachytes and rhyolites and it is always together with alkali feldspar. Hence, 1 kbar can be considered as the upper limit for equilibration pressure. Nonetheless, in order to simulate crystallization paths under low-pressure isobaric conditions, pressure is fixed to 1000 bar (1 kbar) according to the further practice of White et al. (2005), which is based on the experiments of Mahood and Baker (1986).

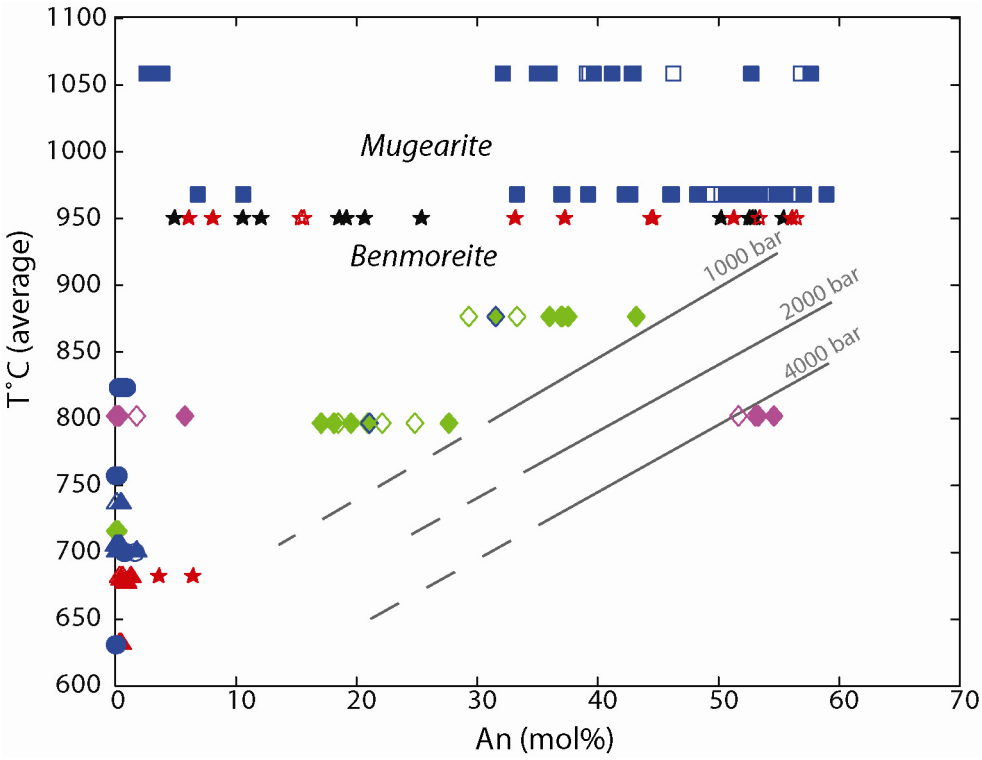

Figure 5.28: Pressure dependence of plagioclase compositions depict that even mafic Nemrut magmas crystallized under 1 kbar. (Pressure gradients from Housh and Luhr, 1991)

5.3.3 Temperature

As stated in section 5.3.2, thermodynamic models utilized are based on isobaric (= 1 kbar) calculations of phase equilibria. In order to estimate the temperature range of crystallization in Nemrut eruptive units, various thermodynamic expressions calibrated based on experimental data have been used. Among numerous geothermometer expressions; clinopyroxene - liquid thermometer based on jadeite crystallization and jadeite - diopside + hedenbergite exchange equilibria (Putirka et al., 2003) and plagioclase thermobarometer based on plagioclase - liquid equilibria (Putirka, 2005) were applied. Plagioclase – liquid equilibria was implemented only for metaluminous rocks due to the lack of plagioclase in peralkaline units. Olivine - liquid thermometers of Beattie (1993) and Putirka (1997) were also applied incorporating either nominal glass or whole rock compositions. Furthermore, using QUILF95 software (Andersen et al., 1993) QUILF thermometry (Frost et al., 1988; Lindsley and Frost, 1992; Frost and Lindsley, 1992) was applied on modal mineral compositions. QUILF temperature estimation is based on Fe, Mg and Ca exchange between olivine and clinopyroxene. Clinopyroxene, olivine and plagioclase thermometries were calculated for a fixed pressure of 1000 bar according to the practice of White et al. (2005), based on the experiments of Mahood and Baker (1986) (see Section 7.1.2). For such

estimations based on mineral - melt equilibria of ignimbrites, of which whole rock composition could not be determined, electron microprobe analyses of juvenile glasses were used.

In order to avoid the effects of subsolidus cation transfer, representative crystal core compositions were chosen. Besides, thermometers were tried to be applied on phenocrysts analyses which fall within the equilibrium fields of Mg - Fe exchange in olivine (Figure 5.24.a; K_D = 0.3 ± 0.03) and clinopyroxene (Figure 5.25.a; 0.23 ± 0.05) in order to strengthen the equilibrium conditions in basaltic and intermediate melts. The same procedure is also applied, for plagioclase analyses (Figure 5.26.c) as a precautious practice, although plagioclase – liquid thermometer uses additionally Al and Si (Putirka, 2005).

Basalt

Plagioclase - liquid equilibria yielded an interval between 1081 and 1138°C for plagioclase crystallization in basalts (Figure 5.29.a). Olivine crystallization is slightly higher and confined to 1147 -1157°C (not shown). Clinopyroxene geothermometer was not applicable due to the lack of clinopyroxene phenocrysts (Figure 5.29.b).

Mugearite

In mugearites, plagioclase temperatures vary between 992 - 1110°C (Figure 5.29.a). In aphyric sample (N-240) microcrysts of plagioclase yielded 927 - 1020°C, suggesting the colder portion of mugearitic melt is crystal free in conformity with fractional crystallization. Clinopyroxene and olivine geothermometers (Figure 5.29.a) gave 994 - 1062°C and 1031 - 1040°C respectively. QUILF resulted in 968 - 1058°C for porphyritic counterparts (Figure 5.29.c). All four geothermometers yielded comparable results.

Benmoreitic Enclaves

Plagioclase crystallization in Type I and Type II benmoreitic enclaves was calculated to occur between 846 - 1137°C and 795 - 1102°C respectively. Clinopyroxene thermometer was applied only on Type II enclaves, because of the absence of clinopyroxene phenocrysts in basalt-like Type I, and gave 1083 - 1132°C. Olivine equilibria yielded 1037 - 1167°C and 1068 - 1075°C in Type I and II enclaves respectively. QUILF equilibria, however, yielded 1000°C and 950°C for Type I and II respectively.

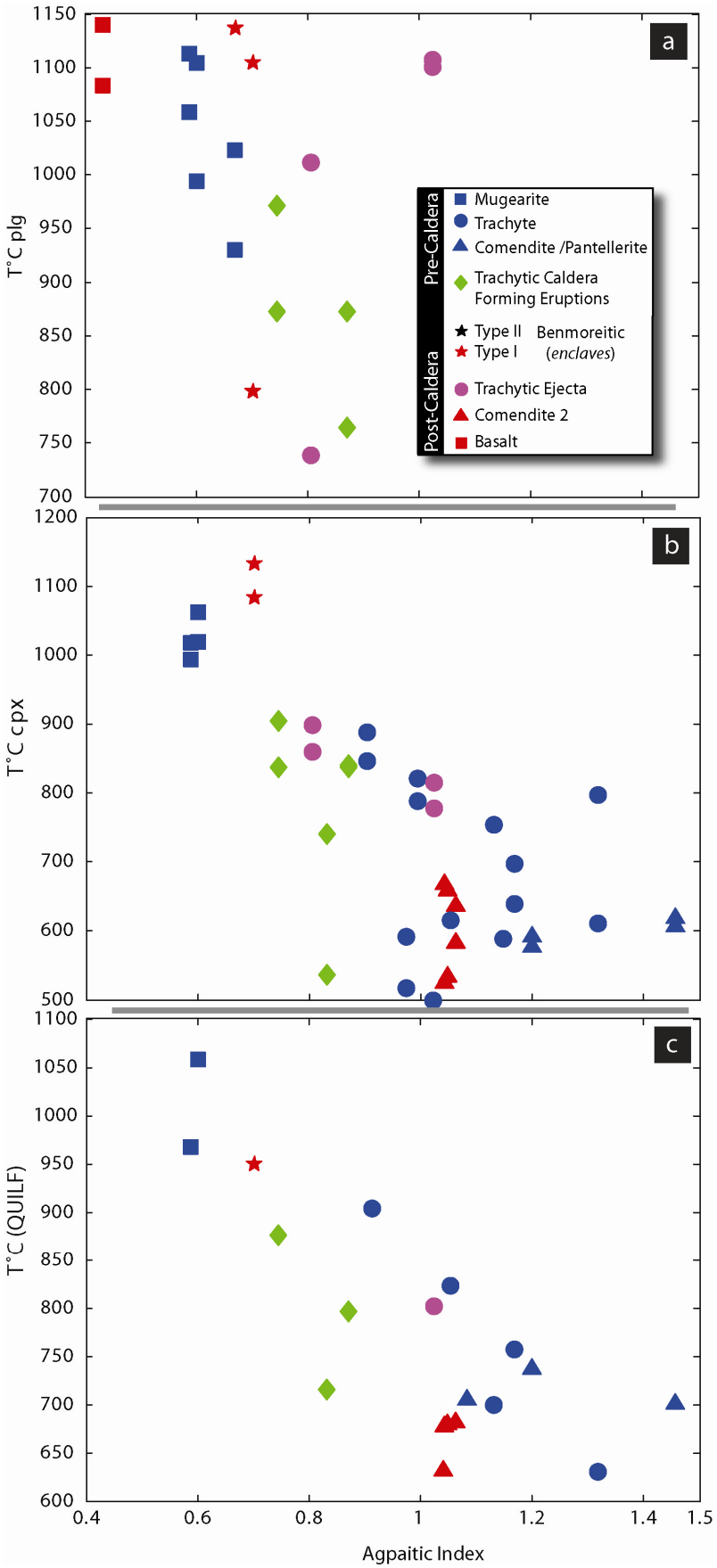

Figure 5.29: Calculated crystallization temperatures via mineral compositions versus AI (a) plagioclase (b) cpx (Putirka, 2003) (c) QUILF equilibria (Andersen and Lindsley, 1993)

Trachyte

Hereafter, olivine thermometers will not be applied because its sole dependence on Mg - Fe exchange. As seen in Figure 5.24.a, olivine compositions are not in the equilibrium field. Besides, such application gave inconsistent results as high as 1400°C (not shown) for fayalitic olivine crystallization in highly evolved peralkaline melts.

The plagioclase - melt and clinopyroxene - melt equilibria gave 870 - 969°C and 837 - 904°C respectively for the plinian fallout (N-036; SID: 1036) overlying the syn-caldera ignimbrite sequence, whereas QUILF equilibria yielded 876°C. Temperatures for the ignimbrites, calculated by various methods stated above, exhibit a gradual decrease towards the lowermost sections of the sequence (Figure 5.29.a, b, c). QUILF equilibria gave an interval of 818 - 728°C for ignimbrites, however clinopyroxene thermometry was not comparable due to the lack of Jd bearing clinopyroxene. QUILF yielded 715°C for the plinian fallout (SID: 1031) stratigraphically overlain by the ignimbrites (N-022).

Rhyolite

Pre-caldera comenditic trachytes exhibit lower temperatures with increasing degree of differentiation. For the least evolved comenditic trachytes (A.I. < 1.0, SiO_2 < 61.6 wt %), QUILF thermometer yielded 927°C (sample N-083) whereas clinopyroxene equilibria gave 847 - 888°C (sample N-136). Temperatures for slightly differentiated comenditic trachytes (1.0 < A.I. < 1.2) vary between 699 - 823°C. However in pre-caldera pantellerites (A.I. > 1.3), calculated temperatures are from 757°C to as low as 630°C. Pre-caldera comendites are calculated to be somehow in a relatively narrow interval of 737 - 697°C. Post-caldera comendites, although they have lower A.I. than the pre-caldera comendites (1.04 < A.I. < 1.06), gave relatively lower temperatures of 630 - 650°C, conforming to the relatively lesser abundance of Tp in nominal olivines (see Section 6.1).

5.3.4 Viscosity

In determining the behavioral aspects of silicate melts in magma chambers, viscosity has a direct effect due to its influence on kinetics and hence compositional setting of the reservoir. Although whole rock geochemical data will be discussed on Chapter 6, which have been utilized to calculate the melt viscosities, it seems more reasonable to state briefly a priori in this section.

Viscosities of Nemrut volcanic rocks have been calculated according to the non-Arrhenian silicate melt model of Giordano et al. (2006). Temperature values needed to calculate the

viscosity have been gathered from temperature estimations based on mineral equilibria (see Section 5.3.3). A plot of density (see Section 5.3.1) versus viscosity (Figure 5.30) illustrates two different correlation trends. Viscosity of mafic melts exhibit a steady increase from basalt to mugearite, however, as soon as the melt becomes silica-rich starting from trachyte, a sharp increase in viscosity is observed.

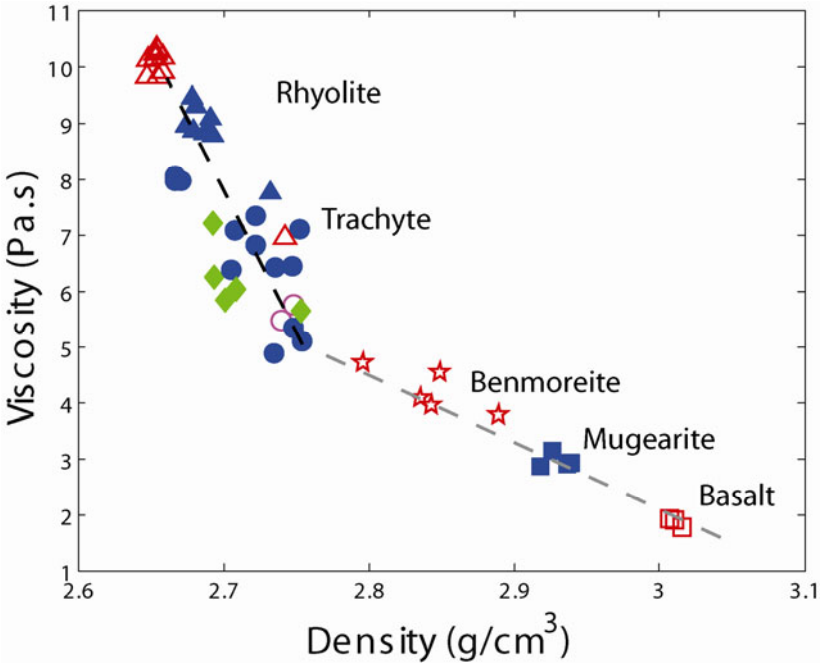

Figure 5.30: Calculated density (McBirney, 1993) versus viscosity (Giordano et al., 2006) values of Nemrut volcanic rocks. Hollow symbols are pre-, solid symbols are post-caldera.

As clearly seen on Figure 5.30, we can infer that there may be at least two physically distinct zones within the magmatic chamber. Basalts and mugearites, being the densest and the least viscous units would likely to occupy the lowermost portions, whereas silica oversaturated rhyolites and trachytes occupy the uppermost portions of the reservoir. These two chemically and physically diverse zones are traversed by benmoreites, which are only observed as enclaves. Regarding the significant disequilibrium textures in both mugearites and benmoreitic enclaves and to a lesser degree in metaluminous trachyte lavas, these heterogeneous textures might probably due to the kinetic interaction between fluid mafic and the denser zones of viscous felsic melts along benmoreitic compositions. Furthermore, the compositional gap observed in peralkaline suites has been proposed to be a result of the high viscosity of the crystal rich intermediate magmas (Mungall and Martin, 1995; Avanzinelli et al., 2004).

5.3.5 Oxygen Fugacity

Oxygen fugacity is an important parameter which controls the evolution of magmatic systems, determining the crystallizing mineral assemblage and thereby governs the path of fractional crystallization (Ryabchikov and Kogarko, 2006).

QUILF 6.42 was used to calculate oxygen fugacity (fO_2) from the equilibria between Fe - Mg silicate and Fe - Ti oxide minerals. The absence of clinopyroxene and ilmenite prevented the estimation of oxygen fugacity in basalts.

Oxygen fugacity exhibits steady decrease with differentiation (Figure 5.31). Estimated fO_2 for mugearites and benmoreites are above the synthetic NNO (Nickel - Nickel Oxide) buffer indicating relatively oxidizing conditions. In mugearites log fO_2 varies between - 9.8 and -8.7 (ΔQFM +1.6 – 1.4). Type I basalt-like benmoreitic enclaves reflect the most oxidized conditions calculated with log fO_2 -7.8 (ΔQFM +3.1) falling well above synthetic NNO buffer. Type II enclaves are relatively reduced with log fO_2 -11.3 (ΔQFM +0.4).

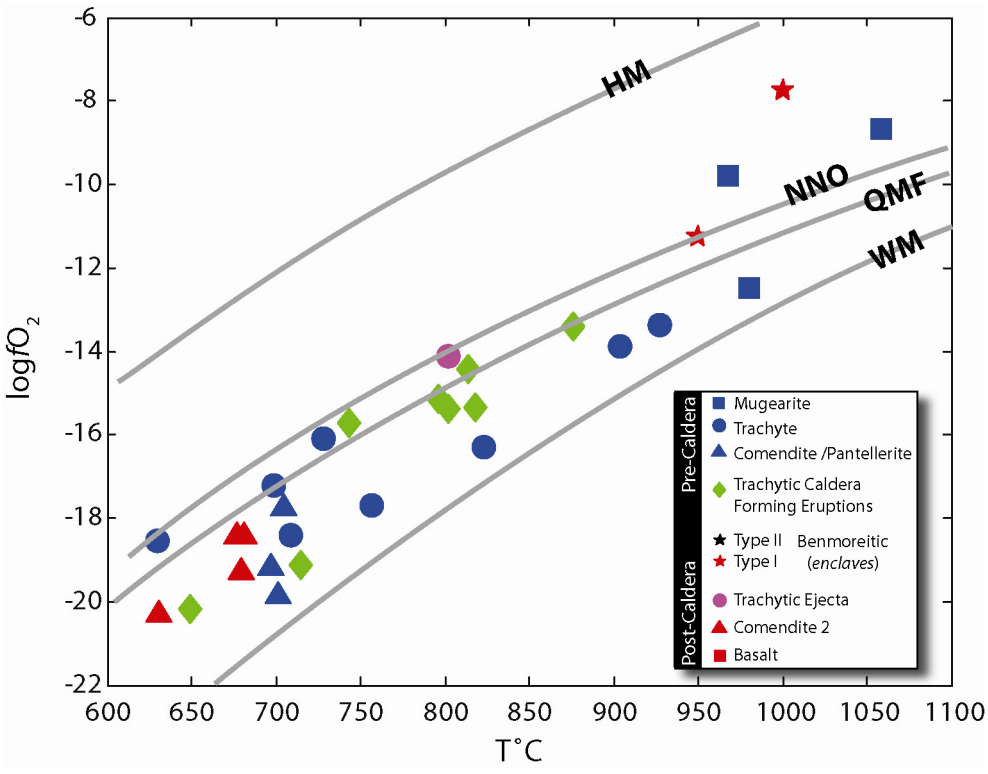

Figure 5.31: Calculated oxygen fugacities versus temperature from QUILF equilibria

Caldera related trachytic pyroclastics represent the gradual transition to reducing conditions lying along the QFM boundary (Figure 5.30). Oxygen fugacity decreases from -13.4 to -19.16 (ΔQFM -0.4 to -2.6) from the uppermost (SID: 1036) to the lowermost (SID: 1031) plinian

fallouts limiting the Nemrut Ignimbrite. The gradual decrease of oxygen fugacity as well as the temperature (see Section 7.1.2) highly depends on the stratigraphical position within the Nemrut Ignimbrite. Samples collected from the upper and middle sections of Nemrut Ignimbrite (SID: 1035-1034) have log fO_2 -14 to -16 and fall between the values of aforementioned limiting fallouts. However, in Nemrut ignimbrite pumice with significant mingling textures exist (see Chapter 3). Mafic portions of a mingled pumice revealed log fO_2 – 14.4 (ΔQFM -0.2), whereas felsic portion yielded log fO_2 – 20.2 (ΔQFM -1.8).

Metaluminous trachyte lavas yielded log fO_2 – 13.4 and -13.9 (ΔQFM -1.3 and -1.4 respectively), whereas peralkaline counterparts.

In pre-caldera comenditic trachytes (A.I. < 1.2) log fO_2 varies between -17.2 and -13.4 (ΔQFM -0.3 – 2.3), however in pantellerites (A.I. > 1.2) is between -18.6 and -17.7 being 0.3 log units above and 2.2 log units below the QFM buffer respectively. In pre-caldera peralkaline rhyolites, log fO_2 has been calculated between -13.4 and -22.9 (ΔQFM -1.3 – -6.9). Log fO_2 in post-caldera peralkaline rhyolites are from -18.4 to -20.3 (ΔQFM -0.9 – -1.5) (Figure 5.30).

5.4 Mineralogical Modeling

Fractional crystallization models have been established using various data and simulation methods. Mineralogical evolution paths via liquid line of descent have been simulated by MELTS algorithm (Ghiorso and Sack, 1995). Isobaric fractional crystallization under varying conditions from different parents (Table 8.1) has been modeled stepwise. MELTS is better calibrated in mafic systems and reproduces better results for MORBs and mafic alkaline magmas. Phase equilibria involving hornblende and biotite are not modeled well by the MELTS package (Ghiorso and Sack, 1995); however Nemrut mineralogical assemblages indicate the absence of hornblende and biotite as major phases, conforming to these caveats.

Table 5.9: Parent rocks, fixed pressures, starting temperatures and oxygen buffer parameters for various runs utilized during isobaric fractional crystallization modeling with MELTS algorithm (Ghiorso and Sack, 1995)

Model	Parent	Rock Type	Pressure	Starting Temperature	Oxygen Buffer
1	N-258	Basalt	0,5 Gpa	1200	QMF
2	N-258	Basalt	0,5 GPa	1170	QMF
3	N-264	Basalt	0,5 Gpa	1200	QMF
4	N-258	Basalt	0,5 Gpa	1200	NNO
5	N-258	Basalt	0,1 Gpa	1200	QMF
6	N-240	Mugearite	0,1 Gpa	1100	QMF
7	N-016	Mugearite	0,1 Gpa	1100	QMF
8	N-240	Mugearite	0,1 Gpa	1100	NNO
9	N-281	Comenditic Trachyte	0,1 Gpa	1030	QMF

Simulated fractionated feldspar compositions, when a basaltic parent is selected (Models 1-5), correlate well with the nominal feldspar evolution paths in basalts, mugearites, benmoreites and metaluminous trachytes (Figure 5.31.a). Models 6, 7 and 8, exhibit shift towards more potassic trends. Reproduced general patterns of isobaric fractional crystallization models are comparable to the observed feldspar evolution. The observed slight shift towards more potassic compositions in calculated trends might due to the volatile effects during actual crystallization conditions which are not simulated by MELTS. Volatiles tend to shift silicate melts towards more sodic compositions (Baker, 1987).

Clinopyroxene evolution paths are somehow comparable with the MELTS reproduced models. However, evident scatter among unstable clinopyroxenes of benmoreitic enclaves, mugearites and to a lesser degree metaluminous trachytic lavas led to the spread of their respective fields (Figure 5.31.b). Nonetheless, we can infer that evolution of clinopyroxene compositions, at least the equilibrium crystals, roughly conform to those of MELTS reproduced isobaric fractional crystallization models.

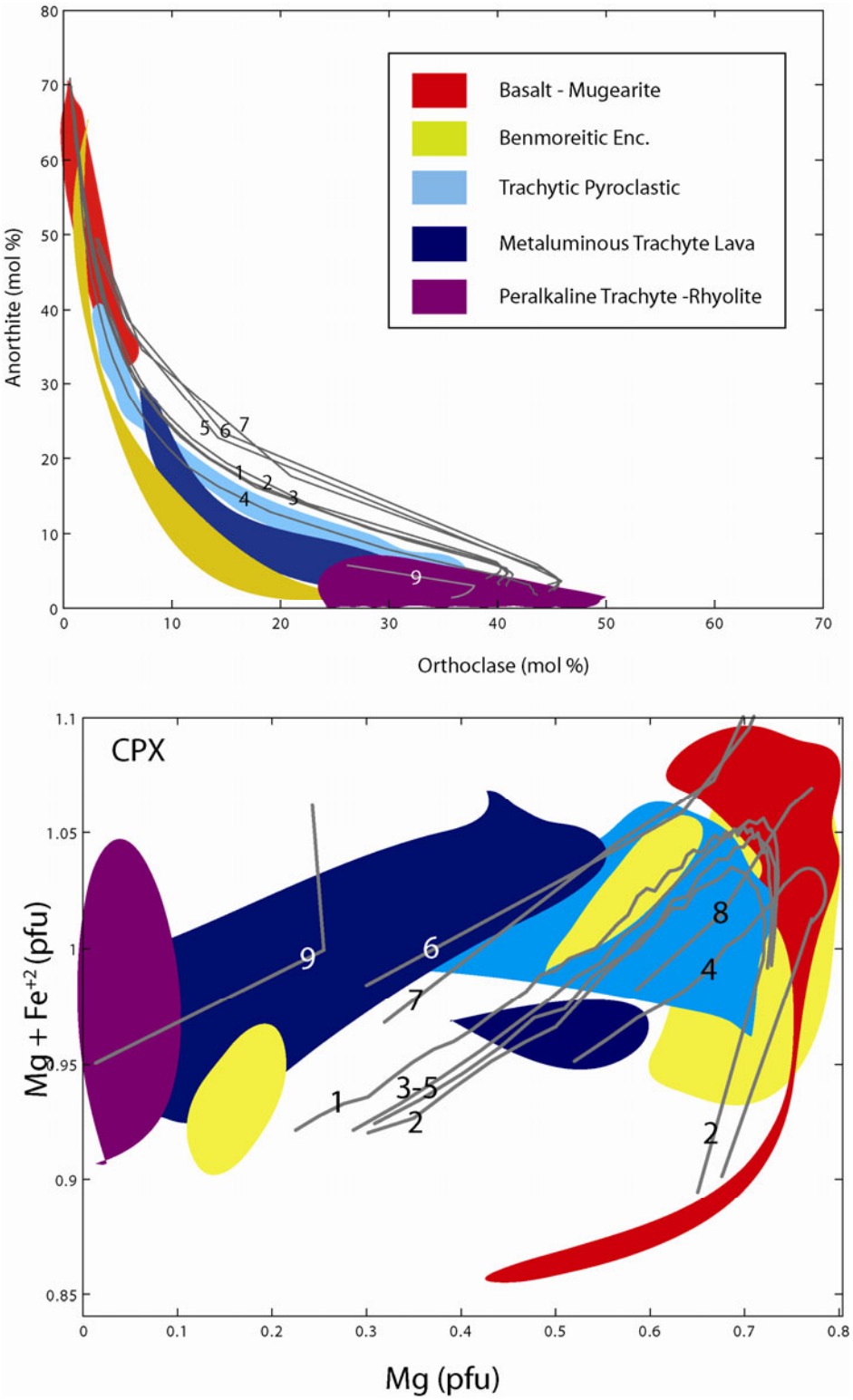

Figure 5.32: Chemical evolution paths (1-9) calculated with various conditions (see Table 5.9) for isobaric fractional crystallization using MELTS algorithm (Ghiorso and Sack, 1995) (a) Orthoclase vs. Anorthite content of observed (filled areas) and calculated trends (gray lines) of feldspars (b) Mg vs. $Mg+Fe^{+2}$ (pfu) plot of observed (filled areas) and calculated trends (gray lines) of clinopyroxenes. Numbers indicate the Model No.

5.5 Conclusions of Mineralogical Analyses

5.5.1 Compositional Continuum in Mineral Species

Extensive EPMA studies supported with crystal-liquid equilibria on all Nemrut eruptive units revealed an evident compositional continuity especially in solid-solution mineral species. Although whole rock geochemistry of these units conform to the Daly Gap, typical of continental extensional peralkaline magmatism, major mineral phases exhibit remarkable gradual variation from basalt to rhyolite. However, caldera related pyroclastic rocks play the key role for the transition from mafic units (basalt, mugearite and benmoreite) to more evolved trachytes and rhyolites. Feldspars, clinopyroxenes and olivines of mafic rocks evolve in equilibrium towards the transitional compositions of caldera related rocks.

Feldspar is represented by labradoritic plagioclase and exhibits normal zoning in basalts. Phenocryst rims and microlites are observed to be richer in Ab, reaching andesine. Feldspars of mugearite and benmoreitic enclaves of post-caldera comendites however, span from labradorite to oligoclase. Furthermore, remarkable textures of instability and presence of xenocrystic alkali feldspar indicate interference with more evolved magma. The significant transition from oligoclase to An-rich (~10% mole) anorthoclase is observed exceptionally in pyroclastic rocks. Having mildly calcic plagioclase (andesine) in stratigraphically uppermost plinian fallout, syn-caldera ignimbrite progressively evolves to comprise Ca-poor anorthoclase towards lowermost sections. Such zonation reflects a zoned magma chamber. Magmas erupted from a stratified magma chamber would normally be drawn from the top and could give rise to compositionally ‘inverted’ gradation in ash flow tuffs or frequently erupted lavas (Baker, 1987). Trachytes comprise anorthoclase with An contents scatter up to 10 % mole whereas comendites only contain anorthoclase with An < 1% mole.

Like feldspar, clinopyroxene exhibits similar evolution trend with increasing degree of differentiation. Although basalts lack of phenocrysts, clinopyroxene microlites are present in the groundmass. Mugearites and benmoreitic enclaves comprise compositionally similar (Mg# 72 - 56) phenocrysts of clinopyroxene. Furthermore, the least differentiated pre-caldera comenditic trachytes (A.I. < 1.0, SiO_2 < 61.6 wt %) consist of clinopyroxene with Mg# 64 - 44. In pre-caldera comenditic trachytes (A.I. > 1.0), clinopyroxene is Mg# < 10. A steady decrease of Mg# (63 - 1) is observed in pyroclastic rocks towards the earliest eruptive units. Comendites have clinopyroxene with 1 < Mg# < 24.

Olivine, like feldspars and clinopyroxenes, displays compositional continuum from forsterite in mafic to pure fayalite in silicic rocks, although some scatter has been observed in middle sections of Nemrut ignimbrite, probably due to intense kinetics during eruption.

5.5.2 Variation in Mineral Assemblages and Crystallization Conditions

Nemrut eruptive units display evident variability in mineral assemblages. Basalts, mugearites and benmoreites (A.I. < 0.70, SiO_2 < 59.5 wt %) consist primarily of plagioclase + olivine + magnetite phenocryst assemblage. Augite is present as minute microlites in basalts and observed to be replaced by larger phenocrysts in mugearites and benmoreites. However, in mugearites and benmoreites, textures of instability and existence of xenocrystic feldspar (either plagioclase or anorthoclase) and amphibole is interpreted to be the result of possible interference with evolved magma batches. Ilmenite is observed as oxy-exsolved lamellae in magnetite; in mugearites and benmoreites. Such assemblage (omitting the instability textures) conforms to the calculated temperatures (up to 1138°C) and oxygen fugacity above the synthetic QFM buffer.

Plinian fallout (SID: 1036) overlying the ignimbritic sequence (0.74 < A.I. < 0.87, SiO_2 < 61.5 wt %) comprise a similar assemblage with plagioclase + clinopyroxene + olivine + magnetite ± ilmenite. Calculated temperatures (870°C - 969°C), oxygen fugacity (ΔQFM -0.4) and the mineral assemblage of this fallout could represent a colder portion of basaltic magma. Mineralogical content of upper ignimbritic sequence comprises plagioclase + anorthoclase + clinopyroxene + olivine + magnetite ± ilmenite. In the lower sections of the sequence, plagioclase is very rare and anorthoclase represents the only feldspar phase. In these lower sections, typical mineral assemblage can be defined as: anorthoclase + clinopyroxene + olivine ± magnetite ± ilmenite. We note a decrease in the abundances of Fe - Ti oxides towards the bottom.

The least differentiated pre-caldera comenditic trachytes (A.I. < 1.0, SiO_2 < 61.6 wt%) comprise anorthoclase + clinopyroxene + olivine + magnetite ± ilmenite with calculated temperatures of 876 - 927°C and log fO_2 ~ -13. In some samples amphibole (ferrorichterite) microlites (φ < 75μ) are scarcely present in the groundmass. The presence of ferrorichterite only in the groundmass is meaningful as ferrorichterite is stable under lower temperatures (c.f. White et al., 2005) than our calculations based on phenocryst assemblages. As the peralkalinity increases (1.0 < A.I. < 1.2) this mineralogical assemblage, extend to contain ± amphibole (arfvedsonite, 75 < φ < 200 μ) ± aenigmatite ± aegirine – augite ± aegirine. In the experimental studies of Scaillet and Macdonald (2001), arfvedsonite (and riebeckite) appears

only in the more peralkaline rocks, at temperatures below 750°C (dry) and below 670°C (H_2O saturated) which conform to the minimum calculated temperatures for these rocks. Aenigmatite was observed along the rims of amphibole indicating the possible link between presence of arfvedsonite and aenigmatite formation. However, pre-caldera pantellerites (A.I. > 1.2) are lack of amphibole. Under oxidizing conditions, amphibole breaks down to aegirine (Scaillet and Macdonald, 2001). Concerning the oxygen fugacity, which varies between ΔQFM 0.3 - 2.2, the break down of amphibole above QFM buffer is meaningful. Pre-caldera rhyolites (A.I. > 1.1, 70.7 < SiO_2 < 72.9 wt %), which are formed under reducing conditions and lower temperatures, mineral assemblage consist of anorthoclase + clinopyroxene + olivine + ilmenite ± amphibole ± aenigmatite ± aegirine ± quartz. Amphibole is arfvedsonite - riebeckite - ferrorichterite, regarding the presence of aenigmatite; this indicates the equilibrium at low temperature (< 750°C) and low oxygen fugacity (Scaillet and Macdonald, 2001). This observation is consistent with our calculations for pre-caldera peralkaline rhyolites (697 - 737°C; ΔQFM -1.3 – -6.9). Post-caldera comendites (A.I < 1.1, 73.4 < SiO_2 < 74.8 wt %) comprise anorthoclase + clinopyroxene + olivine ± ilmenite under QFM buffer with < 700°C.

5.5.3 Zonation of Magma Chamber

Both compositional continuum of mineral species from mafic to silicic melts and gradual variation of calculated intensive state parameters strongly suggest the existence of a spatially zoned shallow magmatic reservoir beneath Nemrut volcano.

Progressive decrease in temperature towards the upper zones of the reservoir is accompanied by decrease in density and oxygen fugacity and increase in viscosity. Furthermore, viscosity is observed to increase abruptly from 5 to ~ 11 Pa as the density becomes 2.73 g/cm^3, which coincides with the compositional transition into trachytic melts. If we assume crystal segregation due to fractional crystallization, then this point would correspond to a crystal rich zone consisting of dominantly labradorite - andesine plagioclase, as their specific gravities are between 2.72 - 2.78 g/cm^3. Considering the lower viscosity of fluidal mafic melts, their convection would be beneath this zone. This proposal can be supported by several facts observed in Nemrut volcanic rocks. Benmoreites, especially of Type II and mugearites frequently display disequilibrium textures due to the change in crystallization environments, which in fact, bear dominantly labradorite and andesine. Including the andesine (and to a lesser degree oligoclase) with evident instabilities in metaluminous trachytes, continuous convection of mafic melts along this viscosity-density boundary between metaluminous trachytes would lead to the heterogeneous growth

conditions for plagioclase. Furthermore, recalling the inner ponds and discrepant intracrystal assemblages within calcic plagioclase in mugearites and benmoreites (Figure 5.6) suggest that, crystallization environments of calcic plagioclase change continuously. Upon crystallization in mafic zone, they are brought into trachytic zone and become unstable with well developed cellular texture (Figure 5.33). During this process, trachytic melt is entrapped within crystal. As soon as the crystal returns back to mafic zone due to kinetic processes, the crystals mantled with plagioclase again (which in turn well explains the oscillatory zoning) and the entrapped liquid crystallizes in a hotter medium. This also explains the existence of Tschermakitic amphibole, which definitely does not conform to the nominal amphibole compositions of Nemrut volcano (and also to the other peralkaline suites).

Hence, regarding the compositional spectrum of mineral phases of all eruptive units and calculated intensive parameters of crystallization conditions, we suggest the existence of a compositionally and physically zoned magma reservoir. Such zonation, with the probable existence of a filtering layer, would explain the bimodality of erupted products, which will be discussed later.

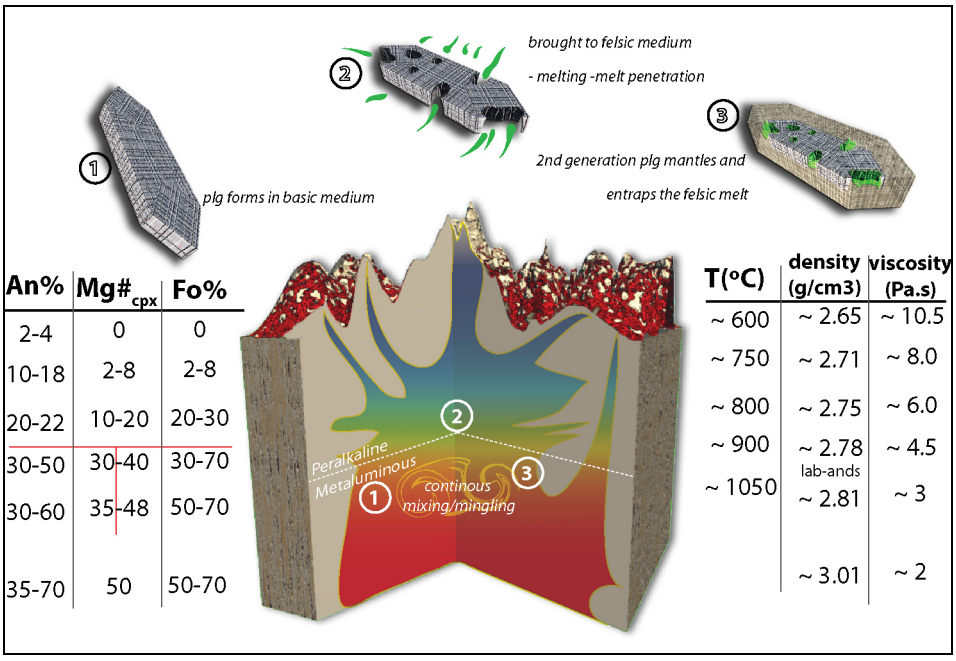

Figure 5.33: Synthetic sketch illustrating the zonation of magma chamber and the simplified evolution of an unstable plagioclase with discrepant intracrystal assemblage in its ponds. Numbers represent the possible position and the step of the evolution. (1) Plg crystallizes in mafic medium (2) Due to kinetics it is brought up to the silicic layer, separated from the mafic medium by the density zone. Here plg is in disequilibrium and contiguous cells are formed due to either thermal or decompressional factors. Trachytic melt penetrates into intracrystal ponds (3) Plg then settles back to the mafic environment and further crystallization of 2nd generation plg mantles the crystal. Trachytic melt is entrapped and forms different crystal assemblages in intracrystal pond

5.5.4 Effects of Fractional Crystallization

The compositional continuum of solid-solution mineral species in a zoned magma chamber indicates that Fractional Crystallization would be the prevailing mechanism for the magmatic evolution of Nemrut eruptive units. This suggestion is cemented by the crystal-liquid equilibria, which denote that crystals should have been formed under equilibrium conditions following the liquid line of descent.

Furthermore, calculated mineral compositional evolution trends with mathematical fractional crystallization models conform to the observed evolution trends of nominal mineral phases, when a basaltic parent (basalt N-258) undergoes continuous fractionation. However, the geochemical evolution of nominal bulk rock compositions, including major and trace elements together with Sr-Nd isotopic ratios, will be tested in the next chapter

CHAPTER 06

GEOCHEMISTRY OF NEMRUT VOLCANIC ROCKS

6 GEOCHEMISTRY OF NEMRUT VOLCANIC ROCKS

In order to reveal petrologic processes governing the Nemrut volcanism, a total of 52 samples have been chosen for whole rock geochemical analyses (see Chapter 2 - Methodology for Analytical Conditions). Our principal concern is to improve our understanding of the 1) nature of eruptive products, 2) temporal evolution of geochemical characteristics, 3) probable differentiation processes, and 4) genesis of Nemrut magmas.

6.1 Major Elements

Major element analyses and calculated CIPW norms of eruptive products throughout the volcanic history are given in Table 6.1. Also presented is the Agpaitic Index (molecular [$(Na_2O+K_2O)/Al_2O_3$]) of each rock. Nomenclature of the rocks, which have been re-calculated on a water free basis, has been realized according to the TAS (Total Alkali versus Silica) scheme of Le Bas et al (1986). Peralkaline (Agpaitic Index: A.I.>1.0) trachytes and rhyolites are also discriminated according to Macdonald (1974) classification and presented in Table 6.1. Basalts, one mugearite sample (N-209) and two trachyte samples (N-136 and N-238) exhibit “Gain on Ignition” with negative values of L.O.I due to the oxidation of Fe^{+2}.

According to the calculated CIPW norms, basalts are nepheline normative, and transitional to mildly alkaline. In worldwide locations, where basalts are exposed, the silicic peralkaline volcanic rocks are almost always associated with transitional to mildly alkaline basalts, strongly suggesting that the basalts may be parental (Bohrson and Reid, 1997). Mugearites are silica saturated with normative hypersthene up to 14%. Excluding two lava samples (*ne*-normative N-136 and marginally peralkaline N-238) all the trachytes and rhyolites of Nemrut volcanism are silica oversaturated with quartz in the norms. Oversaturation of silica is positively correlated with Agpaitic Index.

Total Alkali versus Silica classification diagram (Figure 6.1) depicts that volcanic products consist dominantly of trachytes and rhyolites with minor mugearites (Na_2O -2.0 ≥ K_2O) and transitional-to-mildly alkaline olivine basalts. A compositional gap (Daly Gap) between 53% and 59% SiO_2 is partly filled with benmoreitic (Na_2O - 2.0 ≥ K_2O; LeBas et al., 1986) enclaves of peralkaline rhyolites (SiO_2 > 74%). Excluding the enclaves, rocks of Nemrut volcanism show bimodal distribution. The scarcity of such intermediate compositions conforms to the observations of bimodality in numerous peralkaline volcanic series (e.g. Peccerillo et al, 2003; Ferla and Meli, 2006; Macdonald and Scaillet, 2006).

Table 6.1: Major element concentrations and calculated CIPW norms of Nemrut samples. Agpaitic Index = [molar ($Na_2O+K_2O)/Al_2O_3$]. SID represents the "Stratigraphic ID" C: Comendite / Comenditic, P: Pantellerite (Macdonald, 1974). Tr: Trachyte, R: Rhyolite, BM: Benmoreite, M: Mugearite, B: Basalt (LeBas et al, 1986). I, II: Type I and II benmoreitic enclaves respectively. b.d.l: below detection limit

	Pre-Caldera																								
Sample	N-141	N-162	N-281	N-184	N-188	N-151	N-064	N-135	N-136	N-239	N-238	N-185	N-149	N-178	N-240	N-016	N-191	N-209	N-222	N-181	N-080	N-098	N-224	N-172	N-194
SID	1080	1070	1070	1070	1070	1070	1070	1070	1060	1060	1060	1060	1060	1060	1050	1050	1050	1050	1040	1040	1040	1040	1040	1040	1040
McDonald		C	C	P	P	C		C		C	C	C	C	C					II	C	C	P	C	C	C
TAS	Tr	Tr	Tr	Tr	Tr	Tr	Tr	R	Tr	Tr	Tr	Tr	R	R	M	M	M	M	BM	Tr	Tr	R	R	R	R
SiO_2	67,77	65,37	66,42	66,90	66,97	68,60	68,84	71,27	59,82	61,59	61,79	68,58	72,19	72,46	51,46	51,85	52,56	53,05	59,48	65,99	67,24	70,73	72,43	72,48	72,48
Al_2O_3	15,14	15,31	13,96	11,97	11,62	12,71	14,66	12,12	17,09	15,22	15,53	14,28	12,09	12,13	15,32	15,64	15,69	15,57	16,92	13,67	14,28	10,00	11,07	11,72	11,99
Fe_2O_3	3,36	5,52	6,20	7,94	7,48	6,40	3,44	4,51	6,35	7,42	7,58	3,38	3,79	3,64	12,60	12,32	12,51	11,90	7,48	6,90	5,44	6,96	4,48	4,42	3,95
MgO	0,06	0,30	0,14	0,04	0,09	0,02	0,01	*b.d.l*	0,91	0,44	0,47	0,04	*b.d.l*	0,06	2,94	3,27	3,32	3,07	1,59	0,06	0,03	*b.d.l*	*b.d.l*	*b.d.l*	0,01
CaO	0,91	1,29	1,24	0,68	0,91	0,48	0,87	0,33	2,47	1,93	1,92	1,28	0,28	0,34	5,85	6,89	6,76	6,43	4,44	1,06	0,75	0,36	0,26	0,35	0,31
Na_2O	5,27	5,69	5,32	6,54	5,33	5,74	5,32	5,18	6,53	5,82	6,41	5,28	5,10	5,58	4,61	4,30	4,32	4,30	5,77	6,13	5,86	5,98	5,69	5,46	5,72
K_2O	4,76	5,46	5,09	4,63	4,44	4,74	5,11	4,65	4,35	5,13	5,10	5,10	4,51	4,70	2,46	1,94	1,95	2,10	2,36	4,95	5,01	4,37	4,57	4,62	4,59
TiO_2	0,41	0,50	0,49	0,51	0,47	0,51	0,24	0,29	0,84	0,82	0,87	0,23	0,23	0,22	2,34	2,49	2,63	2,36	1,22	0,43	0,37	0,38	0,25	0,28	0,23
MnO	0,02	0,19	0,21	0,21	0,22	0,13	0,08	0,10	0,17	0,20	0,21	0,08	0,10	0,08	0,22	0,19	0,19	0,18	0,19	0,23	0,16	0,18	0,10	0,11	0,09
P_2O_5	0,06	0,09	0,06	0,04	0,06	0,05	0,03	*b.d.l*	0,29	0,17	0,18	0,03	0,02	0,02	1,04	0,53	0,53	0,52	0,46	0,06	0,04	0,04	0,01	0,02	0,02
H_2O^+				0,16							0,06			0,08			0,20		0,09				0,05		0,11
H_2O^-				0,08							-0,21			0,32			-0,12		0,04				0,21		0,40
LOI	0,92	0,25	0,97	0,24	1,67	0,59	0,06	0,51	-0,12	0,13	-0,15	1,26	0,28	0,40	-0,03	0,17	0,08	-0,03	0,13	0,10	0,35	0,02	0,26	0,24	0,51
Total	98,68	99,95	100,09	99,71	99,26	99,97	98,66	98,95	98,69	98,87	99,91	99,56	98,58	99,64	98,81	99,59	100,54	99,44	100,12	99,56	99,51	99,01	99,13	99,69	99,91
CIPW Norms																									
Quartz	15,66	6,96	11,65	15,24	17,68	17,06	15,52	23,45		1,68		15,25	25,29	24,84					3,93	9,89	11,14	26,46	27,35	25,64	25,04
Plagioclase	48,19	48,25	43,47	35,79	35,05	38,98	46,04	36,45	57,69	49,50	51,49	44,88	37,08	36,22	52,85	54,03	54,22	53,37	62,12	42,75	45,56	27,11	31,50	34,56	36,12
Orthoclase	28,13	32,27	30,08	27,36	26,24	28,01	30,20	27,48	25,71	30,32	30,14	30,14	26,65	27,78	14,54	11,46	11,52	12,41	13,95	29,25	29,61	25,83	27,01	27,30	27,13
Nepheline									1,10																
Corundum																									
Diopside	0,47	4,99	5,10	2,77	3,66	1,83	2,75	1,46	5,05	7,19	7,31	5,29	1,12	1,38	7,09	11,01	10,44	9,71	4,85	4,33	3,08	1,36	1,09	1,43	1,25
Hypersthene	3,15	4,04	4,79	8,66	7,81	6,94	2,28	4,15		5,87	1,84	0,97	3,58	3,41	4,36	8,01	10,80	14,37	9,42	6,68	5,31	7,03	4,37	4,10	3,72
Olivine									5,08		3,72				10,19	6,06	4,31	1,14							
Acmite			1,37	4,60	4,34	3,70		3,91			2,43		3,30	3,15						3,99	3,15	6,05	3,88	3,85	3,41
Na_2SiO_3				3,33	1,19	1,25		0,69					0,54	1,73						1,07	0,10	3,87	2,85	1,69	1,96
Ilmenite	0,78	0,95	0,93	0,97	0,89	0,97	0,46	0,55	1,60	1,56	1,65	0,44	0,44	0,42	4,44	4,73	4,99	4,48	2,32	0,82	0,70	0,72	0,47	0,53	0,44
Magnetite	0,97	1,59	1,11				1,00		1,38	1,61	0,44	0,99			1,83	1,78	1,81	1,73	1,62						
Apatite	0,14	0,21	0,14	0,09	0,14	0,12	0,07		0,67	0,39	0,42	0,07	0,05	0,05	2,41	1,23	1,23	1,20	1,07	0,14	0,09	0,09	0,02	0,05	0,05
Anorthite	3,60	0,11					1,03		4,47	0,25		0,20			13,84	17,64	17,66	16,98	13,30						
Albite	44,59	48,15	43,47	35,79	35,05	38,98	45,02	36,45	53,22	49,25	51,49	44,68	37,08	36,22	39,01	36,39	36,55	36,39	48,82	42,75	45,56	27,11	31,50	34,56	36,12
Agpaitic Index	0,91	1,00	1,02	1,32	1,17	1,15	0,97	1,12	0,90	0,99	1,03	0,99	1,10	1,18	0,67	0,59	0,59	0,60	0,71	1,13	1,05	1,46	1,29	1,19	1,20

Table 6.1: (continued)

			Caldera Related Rocks					Post-Caldera																			
Sample	N-092	N-227	N-036	N-037	N-232	N-046	N-022	N-033	N-050	N-272	N-220	N-146	N-131	N-051	N-063	N-305	N-065	N-032	N-035	N-258	N-264	N-010	N-013	N-256	N-014	N-255	N-254
SID	1040	1040	1036	1034	1033	1032	1031	1020	1020	1020	1020	1020	1020	1020	1020	1020	1020	1020	1020	1010	1010	1010	1010	1010	1010	1010	1010
McDonald	C	C						II	II		C	C	C	C	C	C	C	C	C				I	I	C	C	C
TAS	R	R	Tr	Tr	Tr	Tr	Tr	BM	BM	Tr	Tr	R	R	R	R	R	R	R	R	B	B	B	BM	BM	R	R	R
SiO_2	72,94	73,66	60,25	61,55	63,66	62,40	63,73	56,75	57,12	60,63	63,76	73,40	73,61	73,85	73,90	74,04	74,11	74,59	74,81	46,75	46,91	47,69	56,44	59,51	67,35	74,02	74,45
Al_2O_3	10,89	12,30	16,02	17,05	16,70	16,96	15,30	16,99	17,19	16,75	14,75	12,66	12,33	12,68	12,33	12,31	12,42	12,52	12,45	16,36	15,91	15,72	14,61	14,35	13,32	12,57	12,40
Fe_2O_3	4,59	3,68	6,57	4,54	4,40	4,73	4,34	8,84	8,52	5,74	7,01	1,91	2,23	2,36	2,21	2,26	2,27	2,23	2,27	14,06	13,75	13,46	9,51	8,47	5,35	2,47	2,41
MgO	*b.d.l*	*b.d.l*	0,96	0,56	0,27	0,42	0,26	2,22	2,26	0,63	0,42	0,05	*b.d.l*	0,03	0,04	0,02	*b.d.l*	0,01	0,03	6,49	6,28	6,21	3,97	3,45	1,62	0,07	0,07
CaO	0,25	0,34	2,78	1,92	1,86	2,43	1,42	5,55	5,53	3,35	1,96	0,32	0,27	0,31	0,25	0,23	0,28	0,23	0,29	9,13	8,98	8,97	5,80	4,90	2,51	0,33	0,34
Na_2O	5,45	5,06	4,81	6,05	6,09	5,86	4,68	5,51	5,30	5,77	6,14	4,99	4,94	5,36	5,14	5,00	4,93	5,14	5,12	3,77	3,95	3,80	4,52	4,53	4,86	5,21	4,96
K_2O	4,39	4,62	3,72	4,53	4,65	4,08	4,65	2,00	2,02	3,70	4,62	4,61	4,47	4,50	5,11	4,35	4,45	4,41	4,56	0,81	0,86	0,88	2,17	2,44	3,56	4,41	4,47
TiO_2	0,25	0,22	0,85	0,57	0,45	0,54	0,42	1,61	1,56	0,74	0,65	0,13	0,13	0,14	0,13	0,13	0,14	0,14	0,13	2,85	2,81	2,59	1,83	1,54	0,82	0,16	0,16
MnO	0,10	0,08	0,13	0,12	0,15	0,15	0,09	0,20	0,19	0,17	0,23	0,04	0,05	0,05	0,05	0,05	0,05	0,05	0,05	0,20	0,20	0,19	0,15	0,13	0,09	0,05	0,05
P_2O_5	*b.d.l*	*b.d.l*	0,24	0,14	0,10	0,12	0,08	0,51	0,53	0,18	0,17	0,02	*b.d.l*	0,02	0,01	0,02	*b.d.l*	0,02	0,01	0,43	0,39	0,39	0,26	0,22	0,12	0,02	*b.d.l*
H_2O^+					0,28			0,06	0,10			0,12		0,04	0,04	0,31		0,05	0,10	0,19	0,13		0,12	0,31	0,01	0,01	
H_2O^-					1,75			0,05	0,03			1,27		0,50	0,81	1,62		0,43	0,73	-0,37	-0,84		0,04	-0,19	0,16	0,58	
LOI	0,48	0,40	3,04	1,82	2,03	1,44	4,73	0,11	0,13	0,87	-0,09	1,39	1,19	0,54	0,85	1,93	0,44	0,48	0,83	-0,18	-0,71	-0,90	0,16	0,12	0,17	0,59	0,44
Total	99,33	100,36	99,37	98,84	100,34	99,14	99,69	100,37	100,43	98,51	99,62	99,52	99,23	99,85	100,03	100,34	99,10	99,82	100,56	100,67	99,32	99,00	99,45	99,69	99,79	99,92	99,76
CIPW Norms																											
Quartz	28,63	26,12	8,25	2,72	5,11	5,45	13,21	0,50	2,35	3,78	4,29	26,34	27,47	26,09	27,16	28,00	27,70	27,81	28,01				2,40	7,34	17,38	26,63	27,78
Plagioclase	31,57	37,54	51,83	57,18	56,03	57,51	46,12	62,34	61,99	57,70	50,15	39,45	38,53	40,17	34,97	39,10	39,11	39,84	38,65	51,51	51,23	51,20	51,41	49,95	45,14	40,10	38,89
Orthoclase	25,94	27,30	21,98	26,77	27,48	24,11	27,48	11,82	11,94	21,87	27,30	27,24	26,42	26,59	30,20	25,71	26,30	26,06	26,95	4,49	4,90	5,20	12,82	14,42	21,04	26,06	26,42
Nepheline																				2,48	2,03	2,27					
Corundum							0,18																				
Diopside	1,11	1,50	0,93	2,26	3,56	2,91		7,16	5,73	5,68	7,55	1,29	1,19	1,25	1,04	0,90	1,24	0,90	1,22	13,63	15,87	15,47	11,54	9,31	6,38	1,33	1,49
Hypersthene	4,49	3,25	9,17	5,32	3,44	4,98	5,68	12,04	11,44	5,08	5,88	1,53	1,83	2,01	1,98	2,06	1,83	1,98	1,93				14,77	12,53	5,85	2,17	2,01
Olivine																				17,87	16,65	16,77					
Acmite	3,99	3,18									1,59	1,65	1,94	2,05	1,91	1,97	1,97	1,94	1,97							2,14	2,08
Na_2SiO_3	2,33	0,39										0,21	0,25	0,66	1,48	0,23	0,09	0,34	0,57							0,36	0,17
Ilmenite	0,47	0,42	1,61	1,08	0,85	1,03	0,80	3,06	2,96	1,41	1,23	0,25	0,25	0,27	0,25	0,25	0,27	0,27	0,25	5,13	4,99	4,92	3,48	2,92	1,56	0,30	0,30
Magnetite			1,44	0,99	1,28	1,03	0,94	1,28	1,86	1,25	0,72									1,99	1,94	1,96	1,38	1,84	1,55		
Apatite			0,56	0,32	0,23	0,28	0,19	1,18	1,23	0,42	0,39	0,05		0,05	0,02	0,05		0,05	0,02	0,93	0,95	0,90	0,60	0,51	0,28	0,05	
Anorthite			11,13	5,99	4,50	7,92	6,52	15,72	17,15	8,88										25,88	23,60	23,24	13,17	11,61	4,01		
Albite	31,57	37,54	40,70	51,19	51,53	49,59	39,60	46,62	44,85	48,82	50,15	39,45	38,53	40,17	34,97	39,10	39,11	39,84	38,65	25,64	27,64	27,96	38,25	38,33	41,12	40,10	38,89
Agpaitic Index	1,26	1,08	0,75	0,87	0,90	0,83	0,83	0,66	0,63	0,81	1,02	1,04	1,05	1,08	1,13	1,05	1,04	1,06	1,07	0,43	0,47	0,46	0,67	0,70	0,89	1,06	1,05

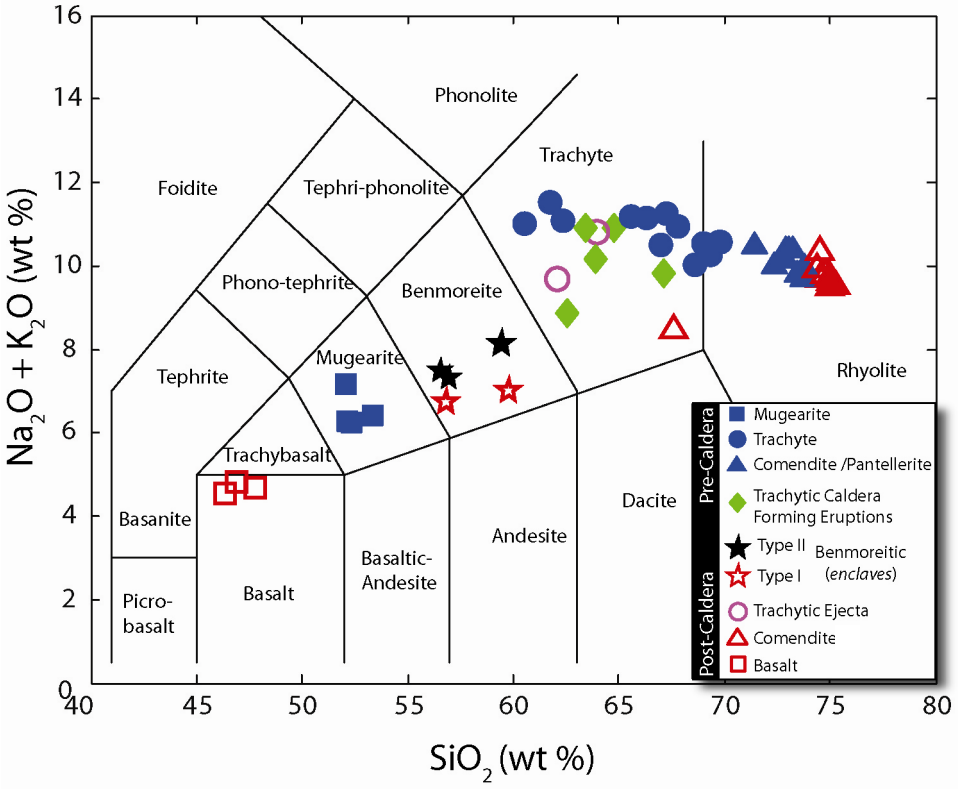

Figure 6.1: Total Alkali versus Silica diagram of Nemrut samples after LeBas et al., 1986. (recalculated on a water-free basis)

The great majority of the felsic rocks are peralkaline (A.I. > 1.0) except the trachytic pyroclastic products of caldera forming eruptions, metaluminous trachyte lavas (samples N-141 SID: 1080, N-064 SID: 1070 and N-136 SID: 1060) of pre-caldera period and Type P ejecta in post-caldera phreatomagmatic products (N-272). Peralkaline trachytes and rhyolites are dominantly comenditic trachytes and comendites respectively, according to the classificatory diagram of Macdonald (1974) (Figure 6.2). However, pantellerites are very rare and confined to the pre-caldera stage (in SID: 1070 and 1040).

Prior to detailed investigation of major and trace element patterns, it is vital to detect, if present, any sample suffered from post-eruptive alkali loss, a common phenomenon in peralkaline rocks (Ren et al., 2006). For peralkaline rocks (A.I > 1), plotted the molar concentrations of less mobile elements Fe, K and Al against Agpaitic Index (A.I.) and the correlation A.I. = 0.6727 $(FK/A)_{molar}$ + 0.5954 (Figure 5.3, White et al., 2003). Samples deviate from the correlation line can be thought as they have experienced alkali modification. Here, all the samples lie on the correlation line, indicating no significant alkali loss has taken place for the investigated samples.

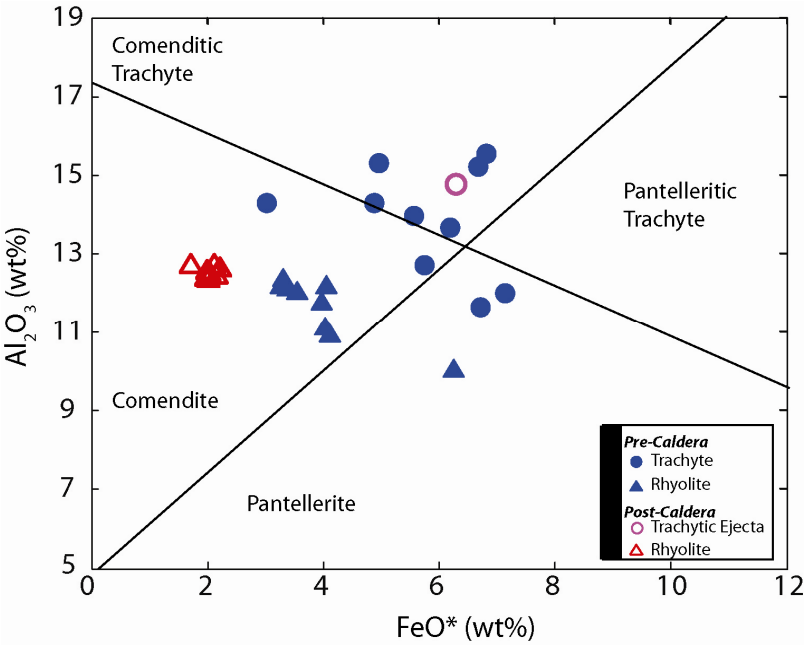

Figure 6.2: Nomenclature of silica rich (SiO_2>62 wt %) peralkaline rocks after Macdonald, 1974. Total iron is expressed as FeO*.

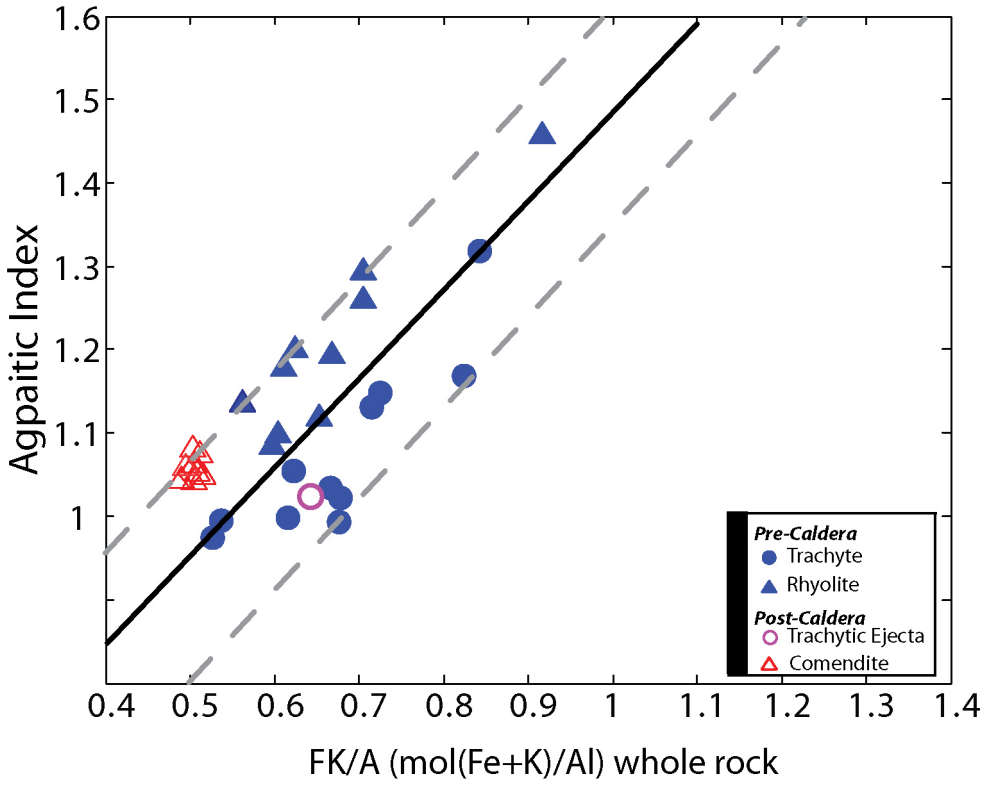

Figure 6.3: FK/A (mol Fe+K/Al) vs. A.I. (mol Na+K/Al) diagram for peralkaline rocks (A.I.>1), depicting the alkali variation based on criteria by White et al. (2003). (Solid line: A.I. = 0.6727(FK/A) +0.5954; dashed line: 95% confidence interval).

The degree of peralkalinity increases with increasing SiO_2 content (Figure 6.4). However, we note a slight decrease in A.I. as the SiO_2 content exceeds 73% in post-caldera comendites (SID: 1010 and 1020) compared to those of pre-caldera counterparts. The most peralkaline sample (N-098) is a pre-caldera (SID: 1040) pantellerite with A.I. = 1.52. As we have stated before, caldera forming pyroclastic sequence produced metaluminous trachytic pumice. Porphyritic (Type P) trachytic ejecta (sample N-272) of post-caldera phreatomagmatic activity is metaluminous (A.I. = 0.83), whereas granular (Type G) ejecta (sample N-220) is comenditic trachyte.

According to the Harker variation diagrams of major elements (Figure 6.5), a continuous decrease in MgO, TiO_2, CaO, Fe_2O_3 is observed. Al_2O_3 displays slight decrease from basalts towards mugearites and increases towards trachytic caldera related products, sharply decreasing afterwards. Na_2O positively correlates with silica but decreases significantly towards rhyolites, exhibiting significant scatter in benmoreitic (Type II) and trachytic compositions. K_2O increases with increasing silica but remains constant in rhyolites. MnO exhibit scatter with respect to silica and trachytic lavas with 61-67% SiO_2 bear the highest content (> 0.2 %), whereas metaluminous pyroclastic products fits the general linearly decreasing trend. However, MnO sharply decreases after SiO_2 exceeds 70%. P_2O_5 exhibit minor enrichment from basalt to benmoreitic enclaves and a curvilinear decrease towards more evolved rocks. Aphyric mugearite sample (N-240) exhibits significant deviation with 1.04% P_2O_5. It should be regarded as the contaminant effect of Paleozoic apatite bearing magnetite deposits in the vicinity (Ercan et al., 1990).

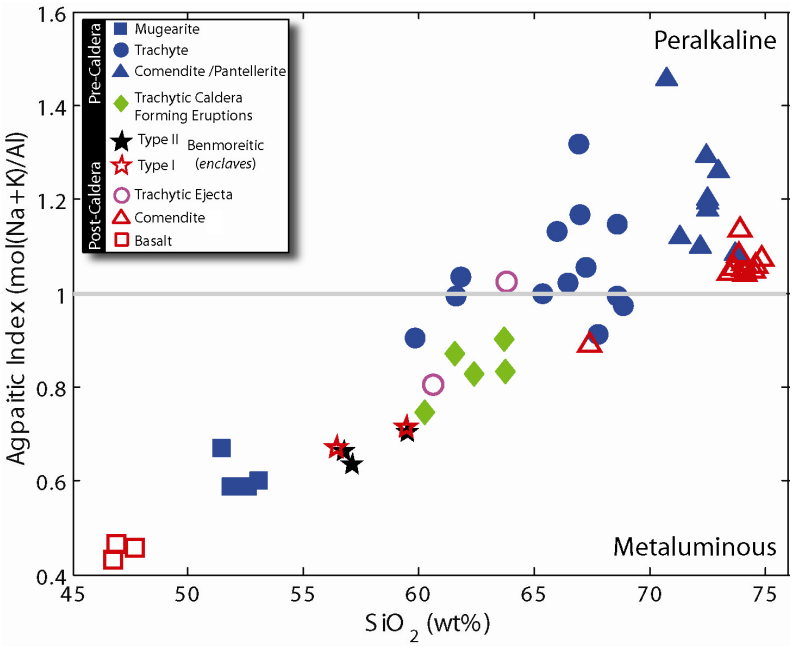

Figure 6.4: Variation of peralkalinity as a function of silica content in Nemrut samples.

Peralkaline (A.I.>1) trachytes and rhyolites of pre-caldera stage are ferriferous (3 < Fe_2O_3 < 8%), contrary to post-caldera comendites (Fe_2O_3 < 3%). The most primitive basalts bear MgO with ~ 6 %. The greatest diversity among global silica saturated peralkaline suites is found in the variation of K_2O (Nekvasil et al., 2004) and Na_2O content. Na_2O versus K_2O plot (Figure 6.6) shows that products of Nemrut volcanism are sodic with K_2O/Na_2O ratio is < 1.

Systematic variation patterns in major oxides likely to indicate that magmatic evolution is dominated by fractional crystallization, crustal contamination and limited magma mixing. Pre-caldera samples are represented by crystal fractionation and crustal contamination; whereas magma mixing is more pronounced in post-caldera samples. In pre-caldera stage, abrupt depletion of Mg, Fe, Ca and P from mugearite and to more evolved rocks indicates olivine, clinopyroxene, (plagioclase) feldspar and apatite fractionation. Starting from pre-caldera least evolved trachytes, depletion of Na, Al and to some degree K indicates that crystal fractionation is governed by alkali feldspar-rich assemblage. From pre-caldera mugearite to marginally peralkaline trachyte, initial enrichment in Al, Na and K shows the varying degrees of contamination. On the other hand, strongly bimodal post-caldera samples plot on the straight mixing line between basalt and comendite.

Significant discrepancy is observed between Type I and II benmoreitic enclaves. Type II samples are richer in Al_2O_3, Na_2O, MnO and P_2O_5 and poorer in Fe_2O_3, MgO and TiO_2 than Type I enclaves. Furthermore, Type I enclaves define a striking mixing trend between post-caldera comendites. Type I enclave-hosting sample N-014 has been defined as comendite based on field and petrographical observations. Hence, the lineation among basalt-Type I enclaves - N-014 - post-caldera comendite is strongly likely to indicate in-conduit mixing between basalt and rhyolite end members.

Major element trends in Nemrut volcano, despite obvious scatter due to varying degrees of crustal contamination, conform to those of the well-documented silica-saturated peralkaline suites worldwide. Whether situated in ocean island or continental environments, the basic trends of compositional change with silica content for all major oxides appear substantially the same for silica saturated alkaline series (Nekvasil et al., 2004). Besides, the scarcity of intermediate compositions (Daly Gap) and the relatively lesser abundance of mafic members compared to the dominant silica oversaturated peralkaline compositions are significant, especially in a collision dominated setting.

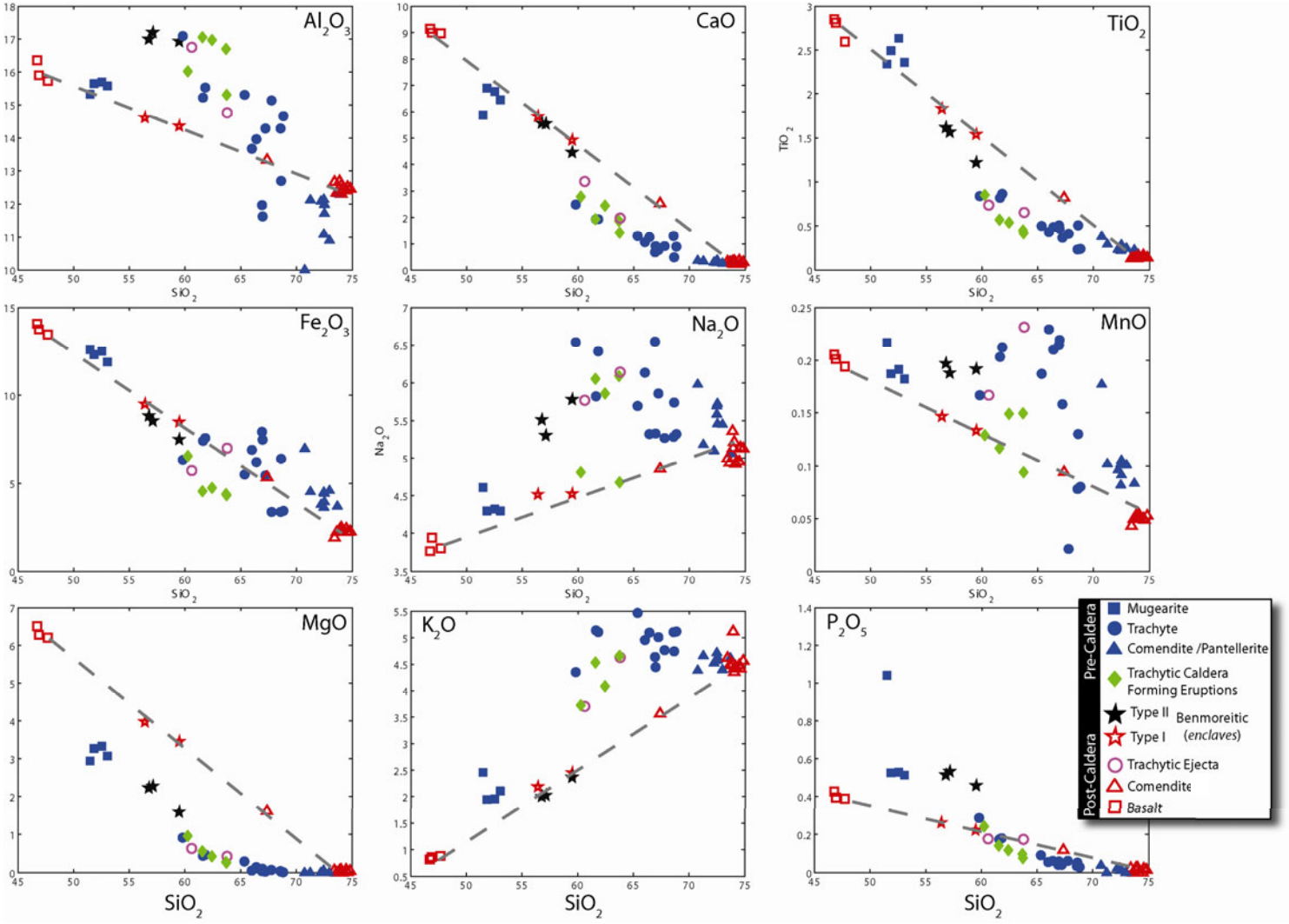

Figure 6.5: Harker variation diagrams of major oxides versus SiO_2 in Nemrut samples. Gray dashed lines represent the mixing line between basalt and post caldera comendite. Notice that Type I benmoreitic enclaves generally plot on the mixing lines

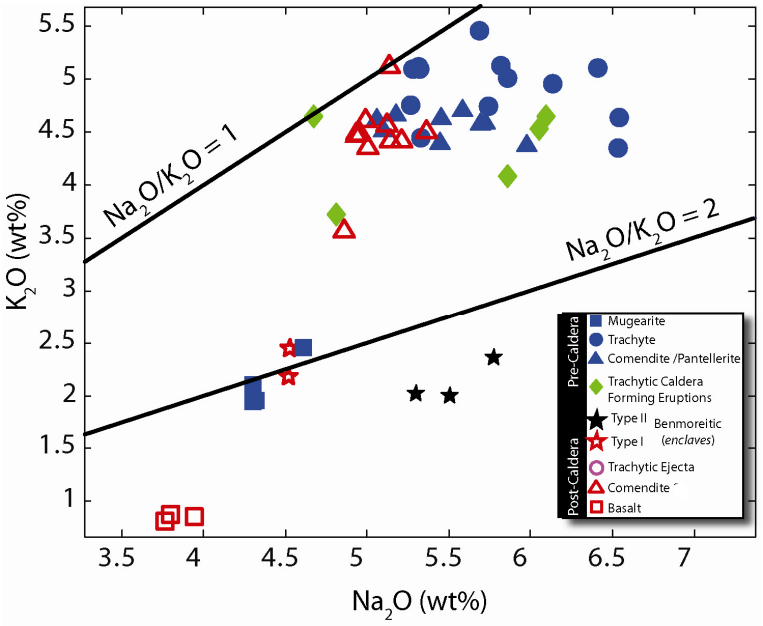

Figure 6.6: Na_2O versus K_2O diagram of Nemrut samples, depicting that vast majority of the samples are sodic ($Na_2O/K_2O < 1$)

6.2 Trace Elements

Trace element analyses of Nemrut volcanism are given in Table 6.2. Concentrations of various trace elements versus SiO_2 are plotted in Figure 6.7. Compatible elements (Sr, Ni, and V) exhibit significant depletion from basalt to rhyolite (Figure 6.7.a). However, Ni and Cr content of basalts depicts that they are not primitive (Ni: ~50 ppm, Cr: ~60 ppm) and that they have experienced some degree of olivine fractionation en route to the surface (Wilson, 1989). Ba increases from basalts to mugearites, to Type II benmoreitic enclaves and metaluminous to marginally peralkaline trachytes (N-136, N-141 and N-239). Trachytic pumice and post-caldera trachytic ejecta of phreatomagmatic eruptions show the highest concentrations of Ba followed by metaluminous trachytic lavas and some peripheral trachytic domes. Ba is almost depleted in peralkaline rhyolites and trachytes. Such variation in Ba content depicts that crustal contamination may be significant in caldera related trachytes, followed by abrupt depletion due to feldspar fractionation. Cr is negatively correlated with differentiation index (SiO_2) excluding its highest contents in easternmost peripheral trachytic lava/dome flows (N-162 and N-281, SID: 1070).

Table 6.2: Trace and rare earth element concentrations in Nemrut samples. SID represents “Stratigraphic Id”. R: Rhyolite, C: Comendite, T: Trachyte, CT: Comenditic Trachyte, P: Pantellerite, M: Mugearite, Bm1/2: Benmoreite Type I/II, B: Basalt, b.d.l: below detection limit

	Pre-Caldera																		
Sample	**N-141**	**N-281**	**N-064**	**N-135**	**N-151**	**N-162**	**N-188**	**N-149**	**N-185**	**N-239**	**N-136**	**N-016**	**N-209**	**N-240**	**N-098**	**N-080**	**N-092**	**N-227**	**N-172**	**N-181**
SID	1080	1070	1070	1070	1070	1070	1070	1060	1060	1060	1060	1050	1050	1050	1040	1040	1040	1040	1040	1040
Rock	T	CT	T	C	CT	CT	P	C	CT	CT	T	M	M	M	P	CT	C	C	C	CT
A.I.	0,91	1,02	0,97	1,12	1,15	1,00	1,17	1,10	0,99	0,99	0,90	0,59	0,60	0,67	1,46	1,05	1,26	1,08	1,19	1,13
V	b.d.l	1,15	b.d.l	b.d.l	b.d.l	1,156	b.d.l	b.d.l	b.d.l	0,96	8,00	188,30	190,90	86,25	b.d.l	b.d.l	b.d.l	b.d.l	b.d.l	b.d.l
Cr	b.d.l	101,2	b.d.l	b.d.l	5,186	78,14	5,311	b.d.l	4,957	46,41	b.d.l	11,74	61,33	41,05	b.d.l	b.d.l	b.d.l	7,84	7,94	5,44
Co	17,17	1,00	13,73	13,79	9,34	1,30	13,94	18,73	27,04	2,36	18,11	33,98	24,85	24,56	14,05	13,1	14,33	13,97	10,93	20,84
Ni	b.d.l	5,29	b.d.l	b.d.l	b.d.l	3,983	3,243	b.d.l	3,283	6,712	b.d.l	7,915	9,539	8,13	b.d.l	b.d.l	b.d.l	4,60	4,08	3,74
Cu	3,51	4,79	b.d.l	b.d.l	b.d.l	4,44	3,66	b.d.l	b.d.l	5,58	3,55	10,93	11,50	27,81	3,60	b.d.l	3,58	3,25	b.d.l	b.d.l
Zn	125,60	143,10	127,10	173,00	162,60	121,80	227,70	167,10	112,70	163,90	117,90	136,50	125,20	153,30	251,10	99,33	218,90	161,40	176,60	152,90
Ga	28,75	29,75	32,22	34,89	36,62	27,45	36,27	35,65	29,13	31,72	27,26	24,44	24,56	27,53	35,30	28,70	35,87	33,76	31,84	30,89
Rb	153,50	113,00	184,50	220,30	132,50	101,40	123,80	191,30	169,40	160,60	134,80	43,87	52,40	67,90	234,40	102,90	243,20	219,10	188,50	119,60
Y	80,39	66,46	82,41	111,90	115,00	52,51	127,20	74,00	78,68	77,66	54,93	42,63	42,01	65,47	140,30	27,78	135,30	105,20	107,20	73,08
Cs	3,95	3,58	5,39	2,24	7,25	1,67	3,35	1,63	6,00	4,01	5,19	1,43	1,73	0,77	9,92	0,51	9,60	2,66	6,89	1,99
Sr	78,53	5,22	8,25	1,96	3,04	9,57	19,63	b.d.l	10,83	45,76	210,80	357,20	332,60	339,30	b.d.l	1,862	b.d.l	2,58	b.d.l	2,624
Ba	608,80	193,10	260,10	5,97	9,75	220,60	13,42	b.d.l	211,70	396,40	465,40	380,20	398,40	330,50	6,40	19,14	b.d.l	6,25	4,84	64,74
Zr	709,20	561,60	846,90	1057,00	1010,00	589,70	1173,00	1031,00	766,40	906,80	600,80	303,20	318,80	630,00	1196,00	651,00	1366,00	1145,00	1008,00	618,00
Hf	17,37	12,43	18,20	26,63	21,38	12,77	24,68	24,93	17,13	18,49	13,53	6,75	6,95	12,41	28,64	14,09	28,86	24,76	22,05	13,30
Nb	39,14	32,82	43,22	66,78	58,88	30,88	66,44	58,95	39,36	51,07	41,66	18,16	18,29	31,76	70,38	35,13	73,56	60,57	49,65	36,22
Ta	3,22	2,47	3,55	5,41	4,68	2,31	5,34	4,69	3,53	3,95	3,44	1,58	1,45	2,41	5,68	2,92	6,08	5,01	4,16	3,10
Pb	16,81	16,24	21,31	26,27	27,76	15,13	30,73	25,51	21,72	30,86	17,98	6,50	7,19	12,25	36,02	19,41	34,94	31,76	28,16	28,23
Th	19,84	13,75	22,31	31,02	22,69	11,29	26,48	24,59	21,29	20,17	17,00	6,92	7,28	10,44	30,96	15,96	34,14	30,46	25,17	13,17
U	5,97	4,01	7,07	7,47	8,23	2,41	5,32	2,76	6,72	6,11	5,69	2,06	2,27	3,47	10,36	1,36	11,10	4,27	7,70	2,18
La	83,03	55,06	70,53	118,50	88,38	51,66	96,52	54,02	67,83	66,94	51,99	32,00	31,24	52,48	107,50	41,99	109,50	88,75	90,01	53,64
Ce	142,40	116,60	145,70	178,90	172,90	107,50	197,40	158,10	138,50	138,60	110,80	74,88	70,92	117,80	226,50	114,50	229,90	210,60	183,60	114,70
Pr	18,76	14,18	17,43	28,16	21,96	13,13	24,41	14,76	16,53	16,77	12,19	9,02	8,77	14,68	27,14	11,50	27,13	23,16	21,99	13,89
Nd	70,75	55,08	63,81	104,00	85,04	50,40	93,30	57,59	61,44	62,59	45,09	36,62	36,00	59,99	104,00	42,05	100,80	86,46	83,87	53,94
Sm	14,28	11,93	13,75	21,18	18,88	10,65	20,58	12,55	13,09	13,33	9,15	8,37	8,14	13,28	23,11	8,58	21,92	18,75	18,08	11,77
Eu	2,29	2,18	1,11	1,13	1,77	1,56	1,52	0,40	1,00	2,38	1,97	2,57	2,50	3,50	1,55	0,72	0,85	0,54	1,33	1,69
Gd	13,23	11,41	12,96	19,04	18,40	9,91	20,04	11,65	12,24	12,47	8,41	8,39	8,05	12,97	22,71	6,70	20,73	18,02	17,19	11,72
Tb	2,17	1,92	2,23	3,25	3,17	1,63	3,47	2,01	2,12	2,11	1,43	1,29	1,27	2,00	3,91	1,09	3,63	3,12	2,95	1,98
Dy	13,12	11,87	13,80	19,80	20,31	9,77	21,98	12,82	13,38	13,25	8,96	7,69	7,55	11,84	24,54	6,13	22,52	19,78	18,50	12,48
Ho	2,55	2,36	2,80	3,92	4,07	1,92	4,53	2,63	2,72	2,71	1,85	1,52	1,47	2,31	5,01	1,14	4,62	4,04	3,77	2,53
Er	7,23	6,93	8,42	11,56	11,93	5,49	13,24	8,11	8,03	8,05	5,66	4,29	4,17	6,48	14,67	3,36	13,78	11,95	10,96	7,40
Tm	1,07	1,04	1,30	1,81	1,83	0,85	2,04	1,35	1,26	1,28	0,91	0,62	0,61	0,95	2,26	0,56	2,12	1,87	1,68	1,14
Yb	6,98	7,25	9,04	12,61	12,20	6,13	13,80	9,97	8,62	8,96	6,37	4,24	4,09	6,38	15,03	4,36	14,64	13,00	11,19	7,74
Lu	1,04	1,14	1,42	2,01	1,85	1,02	2,09	1,66	1,31	1,39	1,04	0,66	0,63	0,98	2,32	0,74	2,23	1,95	1,70	1,20

Table 6.2: (continued)

	Caldera-Related Rocks				Post-Caldera													
Sample	**N-036**	**N-037**	**N-046**	**N-022**	**N-272**	**N-220**	**N-131**	**N-051**	**N-305**	**N-065**	**N-254**	**N-014**	**N-256**	**N-010**	**N-258**	**N-050**	**N-264**	**N-013**
SID	1036	1034	1032	1031	1020	1020	1020	1020	1020	1020	1010	1010	1010	1010	1010	1020	1010	1010
Rock	T	T	T	T	T	CT	C	C	C	C	C	C	B	B	B	Bm2	Bm1	Bm1
A.I.	0,75	0,87	0,83	0,83	0,81	1,02	1,05	1,08	1,05	1,04	1,05	0,89	0,70	0,46	0,43	0,63	0,47	0,67
V	23,12	2,53	10,00	1,45	32,17	4,75	b.d.l	b.d.l	b.d.l	b.d.l	2,55	72,82	143,50	278,30	281,90	75,63	286,10	172,40
Cr	9,63	b.d.l	b.d.l	5,91	9,06	5,25	b.d.l	b.d.l	5,041	b.d.l	12,72	15,92	28,89	55,38	64,11	4,69	59,90	33,33
Co	21,51	16,45	10,28	48,71	18,34	18,53	24,92	170,30	68,26	9,23	8,19	279,30	167,70	55,14	56,65	68,40	60,15	271,40
Ni	9,30	b.d.l	3,50	4,22	6,08	5,14	b.d.l	b.d.l	3,13	3,11	6,37	13,88	25,46	44,55	50,98	4,90	48,14	29,15
Cu	16,70	26,22	3,23	22,65	6,54	b.d.l	b.d.l	b.d.l	b.d.l	b.d.l	b.d.l	13,70	19,86	30,14	42,74	8,70	35,58	23,55
Zn	109,90	82,68	83,79	97,11	91,14	126,00	130,30	119,00	114,10	137,90	128,70	128,10	123,70	128,90	125,00	103,30	131,10	122,60
Ga	25,84	22,63	25,52	26,85	25,48	27,86	31,10	29,82	27,37	31,57	30,71	29,44	27,18	24,31	24,27	24,09	25,47	26,32
Rb	109,20	93,96	58,89	136,30	53,15	94,79	202,20	194,60	185,10	211,50	200,10	158,00	99,96	18,99	12,55	43,65	16,78	83,74
Y	58,76	33,77	33,55	56,63	34,70	49,19	102,70	99,45	94,79	107,20	103,00	90,73	67,06	37,36	34,04	41,16	37,37	60,62
Cs	3,96	3,24	2,03	4,94	1,27	3,20	8,56	8,08	7,98	8,88	8,44	6,66	4,24	0,73	0,45	1,96	0,62	3,53
Sr	179,70	137,80	151,70	84,12	186,30	76,19	b.d.l	1,68	2,02	b.d.l	4,27	100,40	202,80	388,10	395,20	337,40	398,60	244,10
Ba	658,70	966,30	952,30	685,50	863,40	793,40	12,12	13,09	11,09	11,14	9,52	27,34	46,05	69,88	83,93	430,80	82,90	49,69
Zr	488,60	360,20	297,40	635,30	266,20	460,40	577,00	691,40	660,80	694,90	694,00	674,70	484,10	250,30	227,00	360,10	243,50	430,40
Hf	10,42	7,15	6,09	13,37	5,72	9,51	17,59	16,61	16,54	17,86	18,07	14,96	10,87	5,40	4,87	6,60	5,48	9,61
Nb	25,47	22,52	18,41	29,22	16,61	27,06	55,68	54,62	51,60	57,77	56,20	47,99	35,61	13,07	11,26	17,25	12,60	30,94
Ta	2,20	1,99	1,49	2,91	1,39	2,28	5,09	5,96	5,09	5,07	4,96	6,04	3,76	1,18	0,99	1,72	1,19	4,47
Pb	13,53	12,52	8,47	16,56	7,77	10,60	27,62	27,08	26,75	27,81	26,96	21,81	15,00	3,24	3,84	8,13	3,85	12,51
Th	13,50	10,02	6,73	17,17	6,02	10,07	26,84	26,21	25,99	27,18	26,11	21,60	14,00	3,05	2,15	5,63	2,83	11,94
U	4,19	3,62	2,30	5,23	2,07	3,07	9,42	9,17	9,08	9,46	9,14	7,44	4,82	1,00	0,65	2,11	0,91	4,10
La	50,36	34,33	27,81	52,16	26,95	41,31	70,18	68,88	64,26	72,10	66,40	61,08	42,35	18,54	16,50	28,01	18,40	37,19
Ce	101,90	74,02	61,87	105,00	56,17	90,72	145,30	141,60	132,90	149,70	137,20	126,60	89,97	46,37	40,22	60,79	44,56	79,40
Pr	12,87	8,18	7,18	12,70	6,84	10,80	16,63	16,63	15,70	17,14	16,44	15,12	10,91	5,92	5,36	7,90	5,91	9,81
Nd	49,33	29,61	27,88	45,37	27,35	42,09	61,74	61,00	57,78	63,50	59,71	56,25	42,21	25,18	23,67	33,43	25,87	38,35
Sm	10,58	6,09	6,00	9,51	6,00	9,09	13,92	13,74	13,17	14,53	13,75	12,84	9,97	6,34	5,89	7,82	6,51	9,23
Eu	2,20	2,20	2,91	1,47	2,97	2,69	0,30	0,31	0,28	0,32	0,29	0,74	1,21	1,99	2,08	3,00	2,11	1,39
Gd	10,11	5,61	5,85	8,89	5,92	8,59	14,03	13,61	13,31	14,44	14,03	12,77	9,93	6,83	6,49	7,92	7,12	9,49
Tb	1,65	0,93	0,95	1,52	0,97	1,40	2,58	2,47	2,41	2,64	2,57	2,28	1,77	1,10	1,03	1,23	1,12	1,64
Dy	10,00	5,57	5,75	9,37	5,90	8,66	16,66	15,84	15,60	17,01	16,78	14,50	11,06	6,71	6,18	7,20	6,88	10,24
Ho	2,03	1,14	1,17	1,91	1,16	1,73	3,48	3,31	3,28	3,54	3,46	3,00	2,27	1,32	1,21	1,43	1,35	2,11
Er	5,94	3,44	3,37	5,77	3,41	5,11	10,45	9,95	9,85	10,74	10,48	9,03	6,72	3,72	3,38	4,01	3,78	6,18
Tm	0,89	0,53	0,52	0,90	0,51	0,80	1,65	1,60	1,56	1,68	1,64	1,42	1,04	0,54	0,48	0,59	0,55	0,94
Yb	6,23	3,80	3,64	6,38	3,57	5,66	11,25	10,74	10,68	11,69	11,34	9,57	7,08	3,65	3,20	3,96	3,67	6,39
Lu	0,98	0,62	0,60	1,03	0,57	0,91	1,73	1,63	1,61	1,77	1,69	1,48	1,08	0,57	0,49	0,62	0,56	0,98

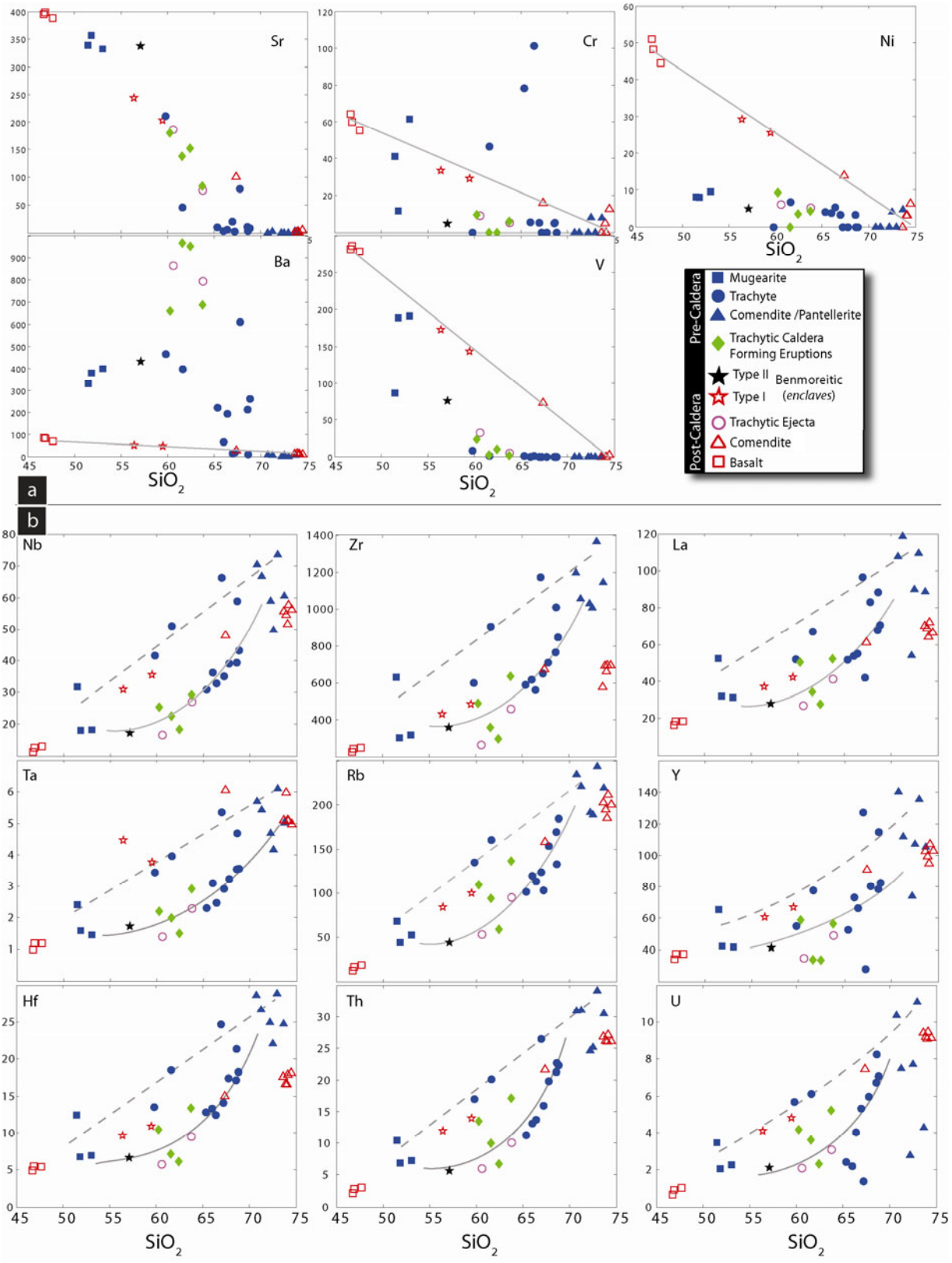

Figure 6.7: Trace element abundances (ppm) versus silica content (wt %) of Nemrut samples. (a) Compatible elements. Mixing line between post-caldera basalt and comendite is shown with solid line (b) Incompatible elements. Dashed and solid gray lines represent the first and the second trends respectively (refer to text)

Incompatible elements define positive correlations with the degree of silica saturation. Various incompatible elements versus SiO_2 have been plotted (Figure 6.7.b). Two positively correlated similar but shifted trends for pre-caldera stage from mugearite to peralkaline rhyolite are significant in each plot. In order to improve our understanding on possible causes for such diversification, a brief glance on the effects of crustal contamination would be helpful.

6.2.1 Crustal Contamination

The effects of possible crustal contaminants have been pronounced regarding the varying Ba contents of Nemrut volcanic rocks. A plot of Th vs. Ba (Figure 6.8.a) depicts two different evolutionary paths can be achieved with varying degrees of crustal assimilation: from mugearite and from metaluminous (caldera related) trachytes. Mugearites represent significant crustal contamination, whereas caldera related metaluminous trachytes signify the highly contaminated magmas of Nemrut volcanism. Fractionation of feldspar dominated mineral assemblages from either mugearites or metaluminous caldera related trachytes would be suggested. The similarity between Type II benmoreitic enclaves and mugearites and also their discrepancy with the Type I counterparts have also been emphasized. Besides, post-caldera trachytic ejecta (both Type P and G) represent significant crustal contamination.

However, assuming an only one type of crustal contaminant in this highly disrupted geological context would be too simplistic. Although it exceeds the perspectives of this study, we believe that demonstrating our evidence for the existence of possible multiple contaminants would be a basis for future research. Recalling the anomalous Cr contents of some trachytes, we suggest the existence of a Cr-rich contaminant (possibly ophiolitic origin), located on the easternmost margin of Nemrut volcanic field. Figure 6.8.b shows that distant (> 13km) eastern domes (and a lava flow) exhibit positive correlation between Cr content and their distance to the caldera center. Last, but not least, as differing Nb/U ratios would indicate various crustal contaminants (c.f. Krienitz et al., 2006 and references therein), we plot U versus Nb (Figure 6.8.c). Although a general trend characterizes the prevailing crystal fractionation; two different trends (represented by some pre-caldera trachytes and comendites) are evident. If we assume the existence of a possible contaminant with the illustrated composition, then these two trends can be explained by local crustal assimilation.
Hence, we propose the existence of various crustal contaminants which contribute with varying degrees to the geochemical evolution of Nemrut volcanism. Yet, with the absence of a comprehensive and up-to-date geochemical data for the basement rocks in the vicinity, only rough estimations on the nature of the contaminants for the shallow magmatic reservoir can be performed.

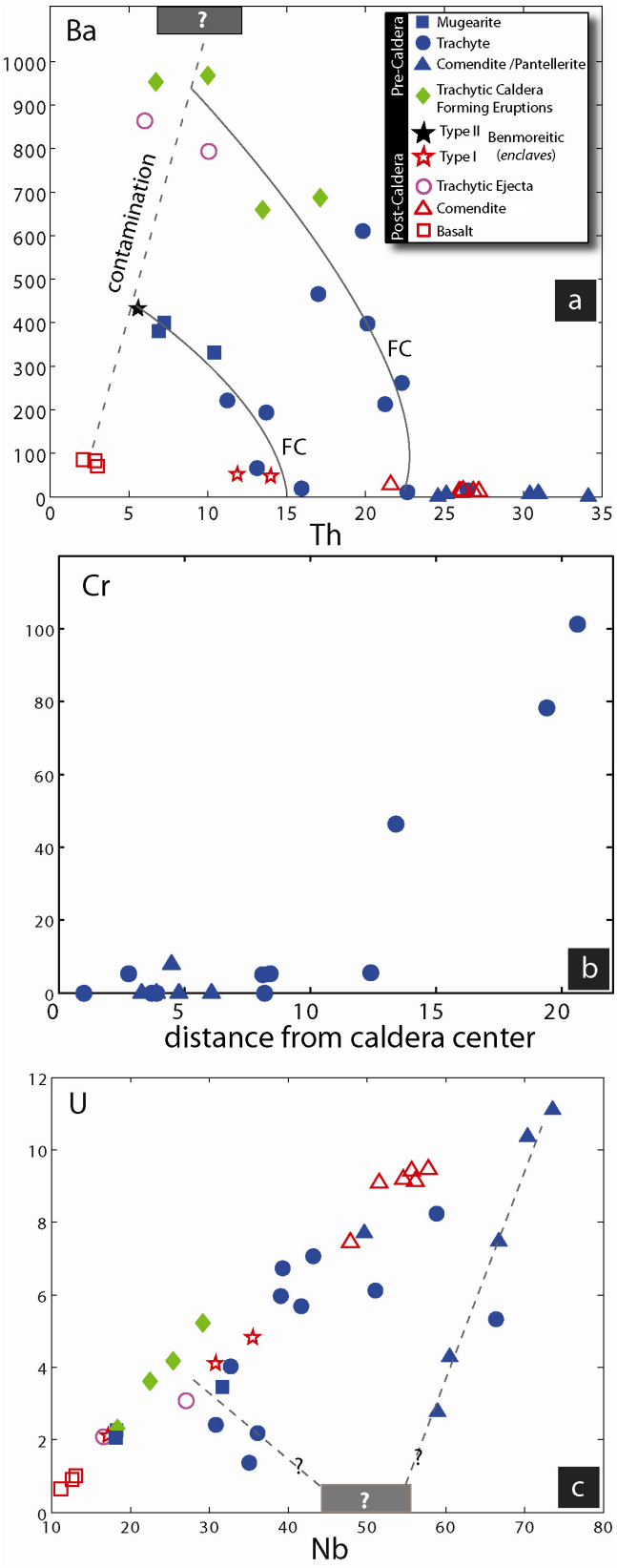

Figure 6.8: Effects of crustal contamination (a) Ba vs. Th plot depicting varying degrees of assimilation of a possible (?) crustal contaminant and associated FC trends (b) Cr abundance increases in towards the easternmost margin of Nemrut volcanic field (c) U-Nb plot showing assimilation trends of a possible (?) contaminant.

6.2.2 Incompatible Elements

Pre-caldera rocks exhibit systematic increase in incompatible elements from mugearites and benmoreitic enclaves to comendites via metaluminous pumice and peralkaline trachytes. On the other hand, when compared to more peralkaline pre-caldera counterparts, post-caldera comendites are slightly poor in incompatible elements The discrepancy in these elements between post- and pre-caldera comendites may indicate a different magmatic evolution process after the caldera collapse, than that of the pre-caldera stage.

Correlations of various incompatible elements versus highly incompatible Th define general linear trends for especially for pre-caldera stage (Figure 6.9). However, slight-to-moderate scattering of pre-caldera samples is also observed. Such dispersion is likely to be the result of varying degrees of crustal contamination. Besides, basalt and comendite (including post-caldera benmoreitic enclaves) of post-caldera stage seem to define another lineation. Basalts are significantly deviate from general linear trend, exhibiting enrichment in incompatible elements. This might be due to the evolved (and contaminated) nature of post-caldera basalts, compared to probable parental basalts of pre-caldera stage.

However, evident anomalies are observed in bivariate incompatible element plots (Figure 6.9). Two pre-caldera samples (N-080 trachyte, N-149 comendite) deviate from the correlation line in Y and Lu concentrations. These variations, however, are not systematic and confined only to those two elements. Relative depletions of REE, Y and Cs in silicic peralkaline volcanic rocks have been attributed to expulsion at near-solidus temperatures (Baker and Henage, 1977; Weaver et al., 1990; Bohrson and Reid, 1997). Relative depletions of Lu and Y in these two samples have probably suffered from this effect.

On the other hand, apparent systematic anomalies have been observed for post-caldera comendites (Figure 6.9). Besides, in plots of Hf and to some degree La and Ce, post-caldera comendites are situated together with metaluminous and the least evolved peralkaline trachytes. Considering Th as the differentiation index, their locations on these plots are somehow peculiar. Furthermore, there is no observed significant difference between post- and pre-caldera comendites, except relatively low Fe_2O_3 in post-caldera comendites. Hence, regarding the considerably lower Zr, La, Ce and Hf contents of post-caldera comendites (Figure 6.7.b) evident displacement is a matter of concern. In highly evolved peralkaline liquids such as post-caldera comendites, one might expect higher contents of incompatible elements. Nonetheless, the principal difference between post- and pre-caldera comendites is in their modal crystal assemblages. In Nemrut volcanic units only post-caldera comendites

bear modal REE-Ti silicate chevkinite (see Chapter 5). Chevkinite is characterized by a strong preference for REE, Nb, Zr and Y in the crystal structure and is thought to greatly influence the budget of evolved magmas by reducing the relative concentrations of these elements (Troll et al., 2003). Post-caldera comendites bear chevkinite microphenocrystals (~ 200 μ) in synneusis with zircon and apatite (See Chapter 5, Figure 5.29 and Table 5.8) which are in equilibrium with the comendite glass. Chevkinite (which is together with zircon and apatite in Nemrut post-caldera samples) is a crystallizing phase in comenditic magma as it is stable only in peralkaline melts (Vlach and Gualda, 2007). Hence, we may assume its removal by gravitational settling or retention in the source of comenditic melt due to its high specific gravity (ρ = 4.61 g/cm^3: www.webmineral.com and references therein) than comendite (ρ < 2.65 g/cm^3: calculated in the previous chapter, section 5.3.1). Moreover, chevkinite has exceptionally high partition coefficients (e.g. K_{DLa}= 988, K_{DCe} =806; Troll et al., 2003 and Table 6.5) and can be responsible for the anomalous elemental concentrations of post-caldera comendites. Furthermore, segregation of modal zircon would decrease the Zr (and Hf) content drastically. Finally, the difference of Fe_2O_3 contents between post- and pre-caldera comendites could be attributed to possible chevkinite fractionation. Chevkinite in Nemrut post-caldera comendites contain 16-19 % Fe_2O_3, and thus its possible fractionation would result in low Fe2O3 concentrations.

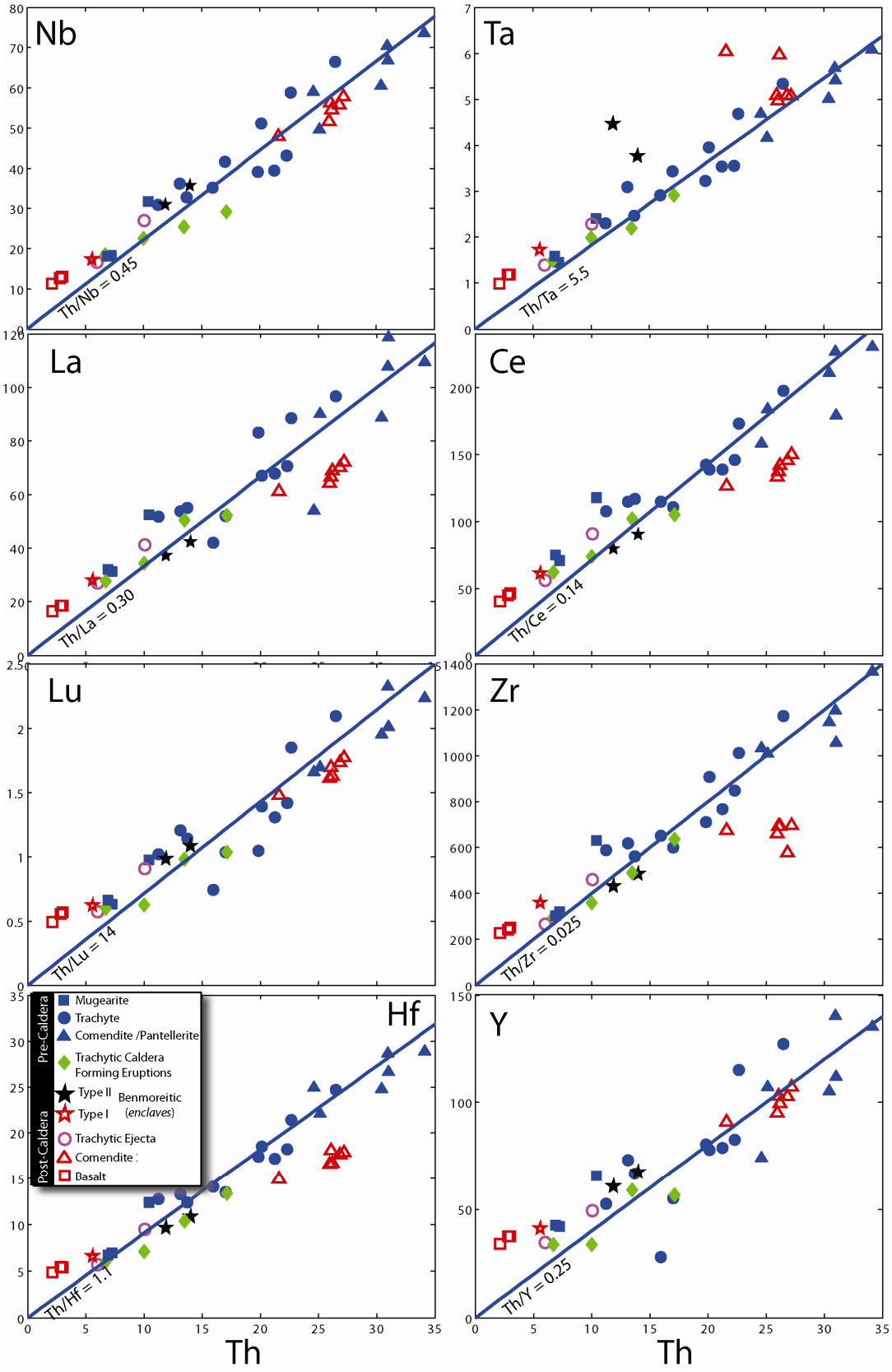

Figure 6.9: Incompatible elements versus Th plots of Nemrut volcanism. Incompatible element ratios are drawn by solid lines passing through origin. Notice the anomalous concentrations in post-caldera comendites (see text for explanation).

In the N-type MORB normalized (Hart et al., 1999; Ta from Hoffman, 1988) multi element spider diagrams (Figure 6.10.a), the most primitive samples of Nemrut volcanism, post-caldera basalt exhibits enrichment in LIL elements (Sr, K, Rb, Ba, Th) relative to N-MORB abundances. Rb and Th present a humped pattern with Ba and Nb troughs. The absence of Ta and Ti troughs accompanying Nb indicates a lesser contribution from subduction component in the mantle source or crustal assimilation. Besides the presence of a negative Nb anomaly has also been proposed to be the characteristic for magmas derived from the subcontinental lithospheric mantle (Halama et al., 2004 and the references therein). Also Rb and Th peaks can indicate contamination by upper crustal amphibolite (Wilson, 1989). Nemrut volcano displays somewhat similar multi element patterns with Muş and Tendürek; however Kars and Ararat patterns indicate a slightly enriched mantle source either by subduction component and/or crustal contamination (Pearce et al., 1990).

Mugearite defines marked negative anomalies of Nb, Sr, Ti and slightly Sm. Benmoreitic enclaves of Type I represent similar trends with basalts, whereas Type II enclaves exhibit significant depletion in Ba, K, Nb, Sr, P and Ti. Trachytes emphasize the systematic fractional enrichment of incompatible elements with significant negative anomalies in Ba, Sr, P and Ti from metaluminous to peralkaline trachytes. Pre-caldera comendites display the depletion of these elements. Fractional crystallization of feldspars, Ti-oxides and apatite may create such trend. Caldera forming eruptions exhibit lowest Sr, P and Ti content in plinian phase underlying Nemrut ignimbrite (SID: 1031) and highest content in upper plinian overlying Nemrut ignimbrite (SID: 1036). This may testify to the zonation of the magmatic chamber. Post-caldera rhyolites are comparable to the pre-caldera counterparts. However, one sample (N-014) exhibits relatively higher concentrations of Ba, Sr, P and Ti. Considering the fact that this sample bears abundant mafic material (i.e. sample N-013 enclave), such trend should be considered with caution. The probability of the inadequate removal of mafic material from the host during sample preparation could reflect such effect. However, it is utile to see such patterns as they illustrate the magma mixing process literally. Trachytic ejecta of post-caldera phreatomagmatic eruptions bear similar multi-element patterns with slight enrichment in K and marked negative anomalies in Sr, P and Ti. The rocks of Nemrut volcanism display parallel multi-element patterns, excluding the systematic depletion of Ba, Sr, P and Ti by fractionating phases, indicator of the same parental source.

6.3 Rare Earth Elements

Chondrite normalized (Nakamura, 1974) rare earth element (REE) patterns for post-caldera basalt are slightly LREE (light - REE) enriched (Figure 6.10.b). LREE/HREE fractionation is weak with $[La/Yb]_N$ ratio is nearly 3. HREE (heavy - REE) abundances are ~ 20 times chondritic indicating the absence of residual garnet in the source (Wilson, 1989).

Rare earth element patterns of felsic rocks of Nemrut volcanism lie sub-parallel to the patterns of basic rocks and have large Eu anomalies, typical of amphibole-free POAM (plagioclase olivine clinopyroxene magnetite) fractionation. This trend is comparable with Muş and Tendürek volcanoes. On the other hand, Kars, Ararat, Bingöl and Süphan volcanoes are dominated by amphibole fractionation (Pearce et al., 1990).

Mugearites are relatively LREE enriched with $[La/Yb]_N$ ratio is approximately 5. Type I benmoreitic enclaves exhibit Eu positive anomaly and $[La/Yb]_N$ is 5. On the other hand
Type II enclaves illustrate a marked negative anomaly in Eu and the overall pattern is slightly shifted upwards compared to Type I enclaves. Trachytes exhibit significant depletion in Eu from metaluminous to peralkaline samples. $[La/Yb]_N$ in trachytes is between 4.5 and 8. Pre-caldera comendites define a significant Eu depletion and $[La/Yb]_N$ is 3.5 - 5.5. Trachytic caldera forming pyroclastic units exhibit mixed behavior for Eu. However, plinian fall underlying the Nemrut ignimbrite (SID: 1031, sample N-022) bears Eu trough indicating its fractionated nature. SID 1036 plinian fall overlying the Nemrut ignimbrite exhibits similar patterns without a significant Eu anomaly. Juvenile pumices of Nemrut ignimbrite exhibit Eu enrichment. For the caldera forming pyroclastics $[La/Yb]_N$ is ~5. In post-caldera comendites Eu depletion is significant where LREE/HREE fractionation is comparable with $[La/Yb]_N$ being approximately 4. In holocrystalline granular ejecta Eu negative anomaly has not been observed, however porphyritic ejecta define a positive Eu spike. Ejecta have weakly enriched LREE with $[La/Yb]_N$ is 5.

The effect of REE-Ti silicate chevkinite in post-caldera comendites compared with pre-caldera counterparts is apparent in chondrite normalized patterns. As chevkinite is more influential in the LREE budget than HREE (Troll et al., 2003), possible presence of chevkinite in fractionating assemblage will shift LREE contents towards chondritic abundances. Pre-caldera comendites are ~ 1.5 – 2 times enriched in LREE than post-caldera comendites. LREE are 280 -380 times chondritic in pre-caldera comendites, whereas post-caldera comendites have 195 – 215 times chondritic LREE abundances. Moreover, chevkinite will also contribute to the Eu anomalies as bulk K_D for Eu in chevkinite is $K_{D\ Eu}$ = 225 (Troll et al.,

2003). Post-caldera comendites have only ~4 times chondritic Eu, whereas pre-caldera comendites reach up to 21 times the chondritic Eu abundances.

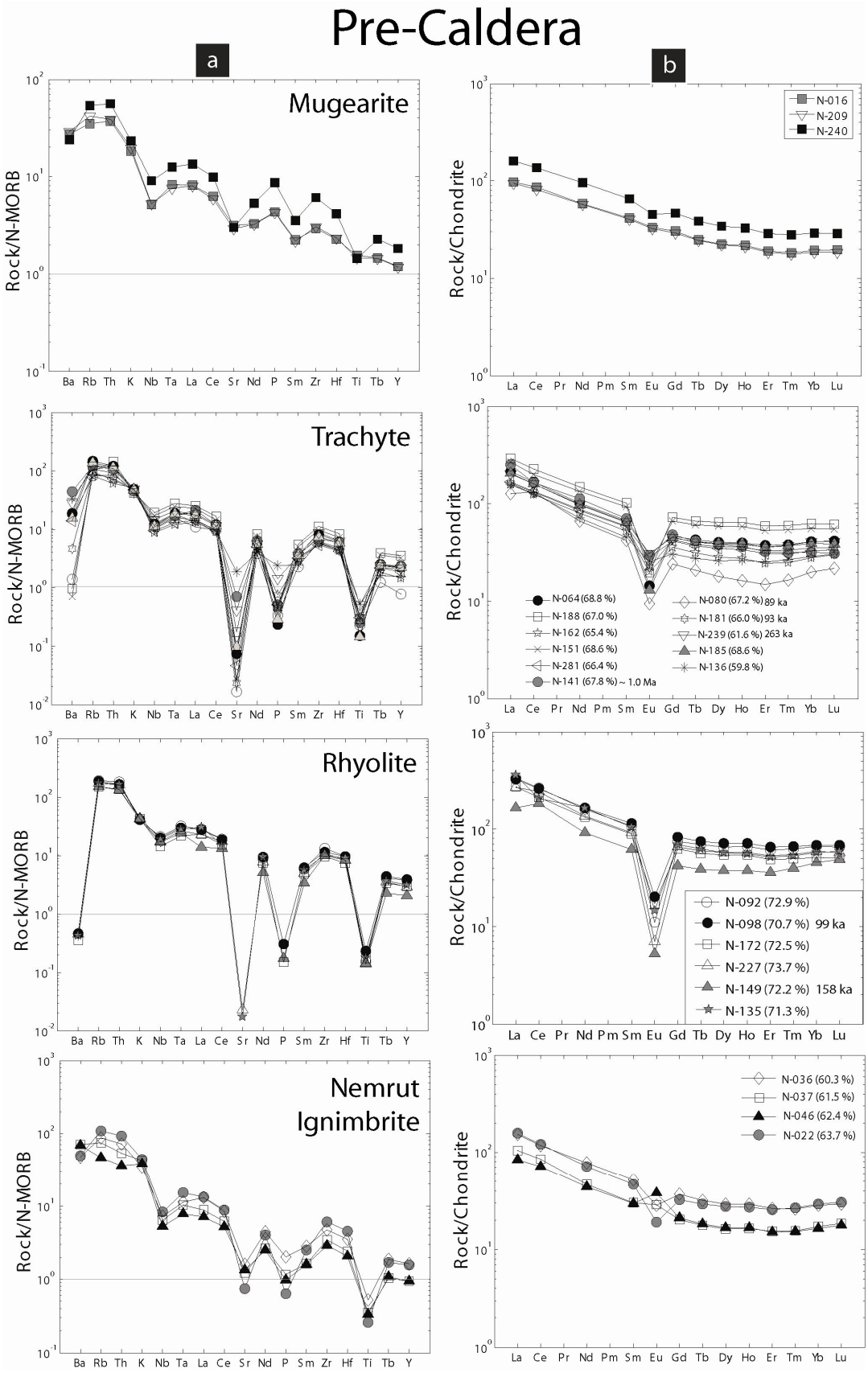

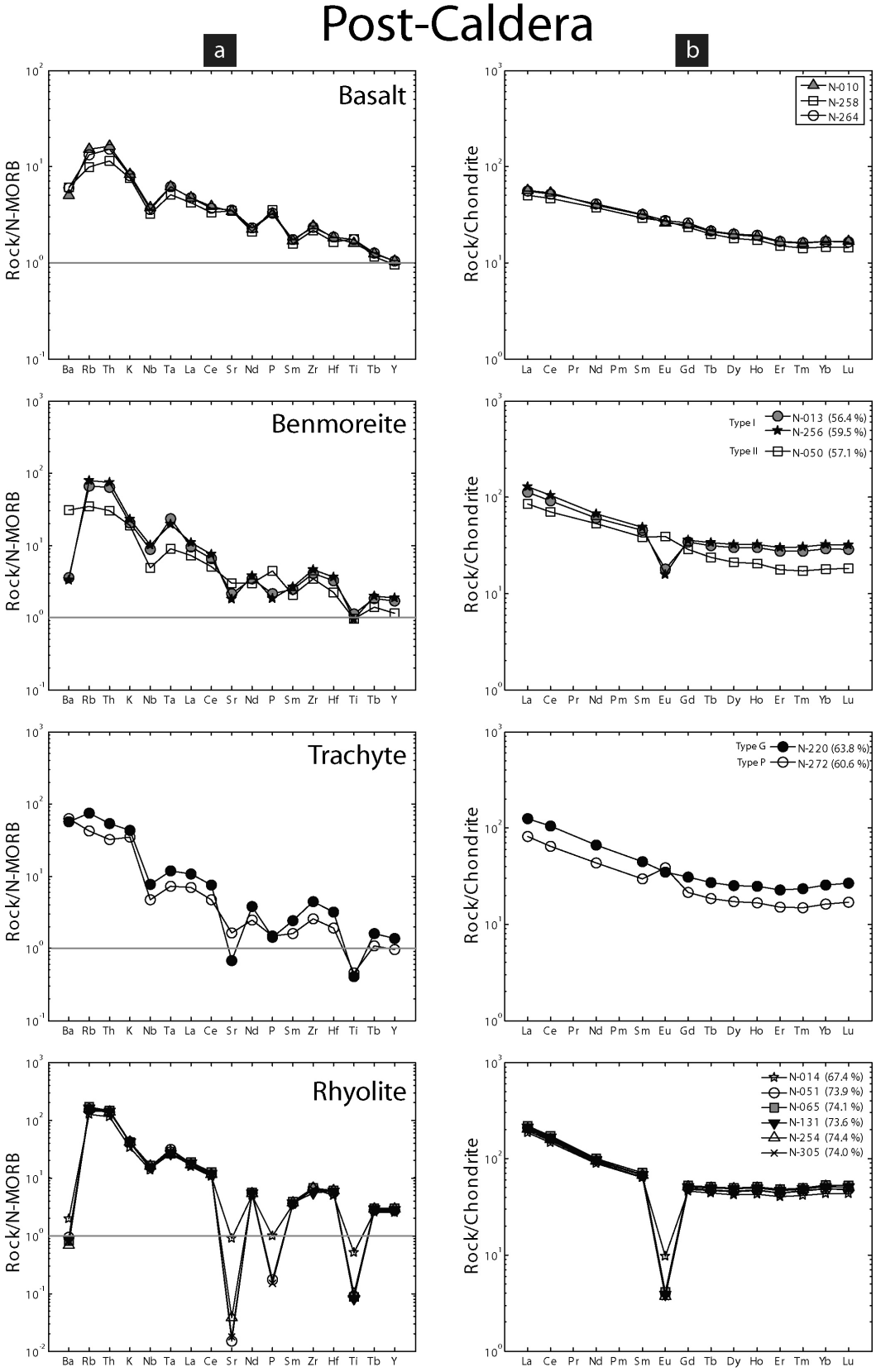

Figure 6.10: Normalized trace element concentrations of Nemrut samples. a) Chondrite normalized (Nakamura, 1974) REE abundances b) Primordial Mantle normalized multi element spidergrams (PM: McDonough, 1992; P from Sun, 1980) Numbers in parentheses indicate the SiO_2 content.

6.4 Sr and Nd Isotopes

Sr isotopic ratios have been determined for a total of 5 samples being 2 basalts and 3 mugearites, whereas Nd ratios have been obtained for a total of 14 samples from various rock types (Table 6.3 and see Chapter 2 - Methodology and Analytical Conditions).

Table 6.3: $^{87}Sr/^{86}Sr$ and $^{143}Nd/^{144}Nd$ isotopic compositions of selected samples from Nemrut eruptive units. NBS 987 standard gave an average value of $^{87}Sr/^{86}Sr$ = 0.710260 ± 0.0000015 and the AMES standard gave an average value of $^{143}Nd/^{144}Nd$ = 0.511957 ± 0.000005

	Pre-Caldera									
SID	1070		1060	1060		1050	1050		1040	1040	1040
Type	Dyke		Lava Flow	Lava Flow		Lava Flow	Lava Flow		Lava Flow	Lava Flow	Lava Flow
Rock	Comenditic Trachyte		Comenditic Trachyte	Comendite		Mugearite	Mugearite		Comenditic Trachyte	Comenditic Trachyte	Pantellerite
Sample	*N-151*		*N-239*	*N-149*		*N-016*	*N-209*		*N-181*	*N-080*	*N-098*
$^{87}Sr/^{86}Sr$						0,705827	0,705908				
$^{143}Nd/^{144}Nd$	0,512637		0,512690	0,512658		0,512634			0,512652	0,512647	0,512657
	Post-Caldera										
SID	1010	1010	1010		1010	1020		1010	1010		
Type	Lava Flow	Lava Flow	Lava Flow		Pumice	Lava Flow		Ejecta	Ejecta		
Rock	Basalt	Basalt	Basalt		Comendite	Comendite		Comenditic Trachyte	Trachyte		
Sample	*N-258*	*N-010*	*N-264*		*N-305*	*N-51*		*N-220*	*N-272*		
$^{87}Sr/^{86}Sr$	0,703564	0,703503	0,703519								
$^{143}Nd/^{144}Nd$	0,512894	0,512878	0,512884		0,512766	0,512759		0,512657	0,512736		

Sr isotopic ratios have been measured for basaltic rocks only and range from 0.70350 to 0.70591. The vast majority of trachytes and rhyolites have very low concentrations of Sr (< 15 ppm) as they would have been highly susceptible to the effects of contamination. Hence, they are not analyzed for their $^{87}Sr/^{86}Sr$ ratios. However, Sr isotopic ratios from literature (Gülen 1984; Notsu et al., 1995) have been normalized to the standards and their obtained average values used in this study and incorporated into various diagrams in order to demonstrate the magmatic evolutionary trends.

$^{87}Sr/^{86}Sr$ isotopic ratios of basalts (SiO_2 < 48%) are between 0.70350 and 0.70416, whereas their $^{143}Nd/^{144}Nd$ ratios plot between 0.512878 and 0.512927. Mugearites (48<SiO_2<55%; and two marginal hawaiites in Gülen, 1984) plot between 0.70463 and 0.70591 for $^{87}Sr/^{86}Sr$, however a drastic decrease in $^{143}Nd/^{144}Nd$ is observed from 0.512907 to 0.512634. Two obvious $^{87}Sr/^{86}Sr$ variation trends are identified from mugearite to rhyolite. Pre-caldera rhyolites exhibit definite (curvi)linear increase in $^{87}Sr/^{86}Sr$ isotopic ratios plotting between 0.70608 and 0.70823. On the contrary, post-caldera comendites are within a relatively narrow interval of 0.70457 – 0.70522. Pre-caldera trachytes and rhyolites define somewhat curvilinear decreasing $^{143}Nd/^{144}Nd$ trend from basalt when post-caldera trachytic ejecta are included. Especially Type P ejecta (N-272) lie on a mixing line between pre-caldera rhyolites

and basalt. On the other hand, pre-caldera silicic rocks lie along a relatively flat line drawn from mugearite (N-016). Post-caldera comendites again represent higher $^{143}Nd/^{144}Nd$ ratios compared to the pre-caldera counterparts. This testifies that post-caldera comendites have been subjected to relatively lesser degrees of crustal contamination.

Variations of $^{87}Sr/^{86}Sr$ and $^{143}Nd/^{144}Nd$ isotopic ratios with respect to SiO_2 (Figure 6.11) indicate that significant crustal assimilation should have occurred from basalt to mugearite, possibly ruling out an evolution via mere crystal fractionation. This conforms to our observations depicted in Figure 6.8.a. Besides, striking discrepancy in Sr and Nd isotopic ratios is evident between post-caldera and pre-caldera rhyolites indicating different paths should have been responsible for their evolution. Post-caldera comendites seem to have been less affected from crustal contamination. During the construction of the volcano and its magmatic chamber, inevitable crustal contamination should have occurred resulting in more contaminated pre-caldera lavas. Post-caldera lavas, on the other hand, could have been less subjected to such contamination as their ascent paths in the crust have possibly been plastered by pre-caldera predecessors.

Starting from mugearite; pre-caldera silicic isotopic ratios could be obtained via fractional crystallization with limited crustal assimilation. However, intermediate compositions (trachytic ejecta and least evolved trachyte, N-239) could indicate probable interaction between basaltic and felsic melts, as evidenced earlier by petrographical - mineralogical observations.

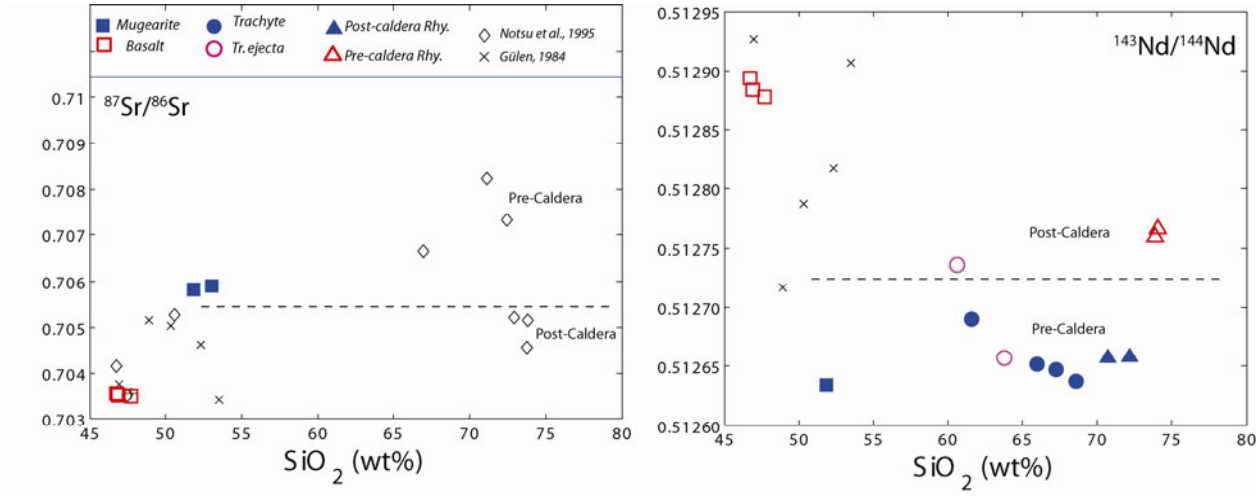

Figure 6.11: Variation of $^{87}Sr/^{86}Sr$ and $^{143}Nd/^{144}Nd$ isotopic compositions versus silica content of selected Nemrut samples. Data from literature and discrimination between post- and pre-caldera comendites are also plotted.

6.5 Source Characteristics

Covariation diagram for $^{87}Sr/^{86}Sr$ and $^{143}Nd/^{144}Nd$ isotopic ratios (Figure 6.12) has been plotted, on which East Anatolian volcanics (Gülen, 1984; Pearce et al., 1990), Afar, Main Ethiopian Rift (Hart et al., 1989; Deniel et al., 1994; Trua et al., 1998) and Kenya Rift (Naivasha, Davies and Macdonald, 1987) has also been shown for comparison. Nemrut basalts, as well as other east Anatolian volcanics clearly plot within OIB field as East African volcanics (Afar plume, Main Ethiopian Rift and Naivasha of Kenya Rift). Also shown is the average granitic upper crust (Wedepohl, 1995). However, regarding the fairly evolved character of Nemrut basalts (e.g. Ni = 45 - 51 ppm, Cr = 64 - 55 ppm), we might expect considerable shift in Nd and Sr isotopic ratios compared to their sources.

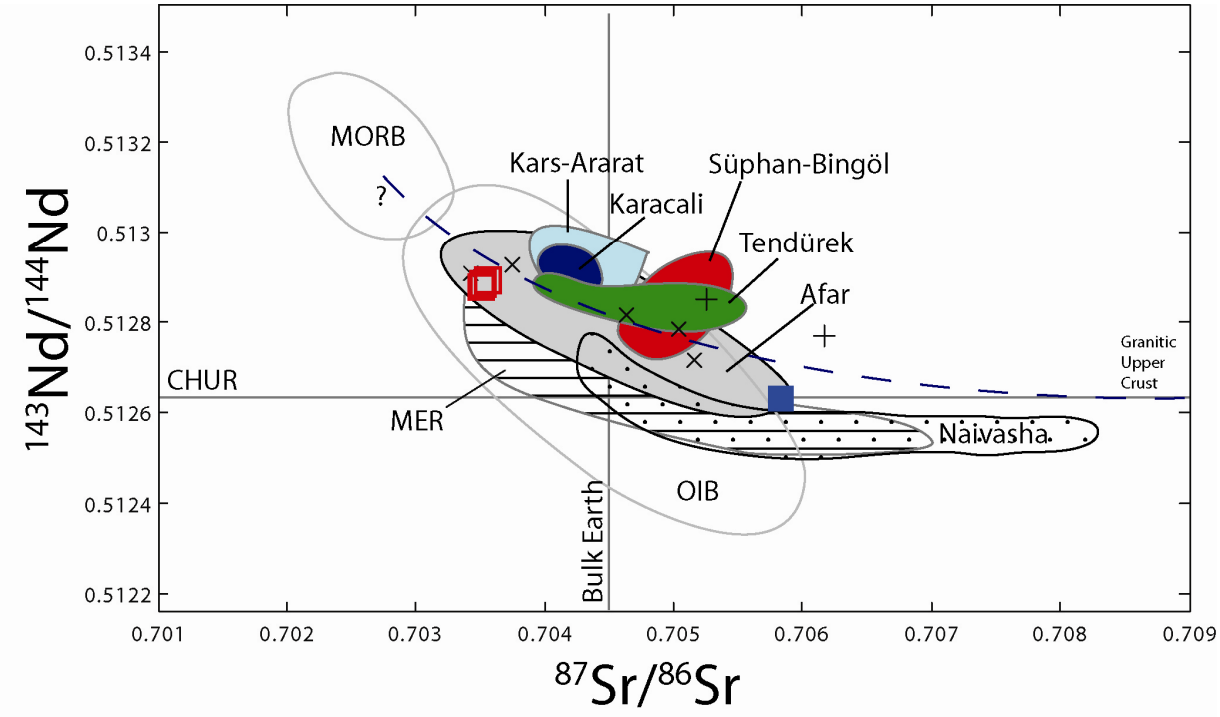

Figure 6.12: $^{143}Nd/^{144}Nd$ versus $^{87}Sr/^{86}Sr$ plot. Data for East Anatolian volcanics from Gülen, 1984and Pearce et al., 1990. For Afar, Main Ethiopian Rift: Hart et al., 1989; Deniel et al., 1994; Trua et al., 1998 and for Kenya Rift (Naivasha), Davies and Macdonald, 1987.

In order to approximate the nature of the source magmas, revised tectonic discrimination diagrams (Figure 6.13), based on classification trees have been used (Vermeesch, 2006). Three of the best performing discriminant analysis diagrams have been used, however the fields onto which Nemrut basalts plot, exhibit variation. In 50xSm-Ti/50-V and Si/1000-Ti/40-Sr triangular plots, Nemrut basalts fall into OIB field (Figure 6.13.a, c), whereas in 100xEu-500xLu-Sr diagram they plot within MORB field (Figure 6.13.b). Considering the actual overlaps between the geochemistry of different tectonic settings, tectonic discrimination would not be possible. Nonetheless, given the complex geodynamic and structural context

with multiple possible source regions, and the absence of true primitive basaltic compositions, suggesting an absolute origin for Nemrut volcanic rocks would be highly controversial.

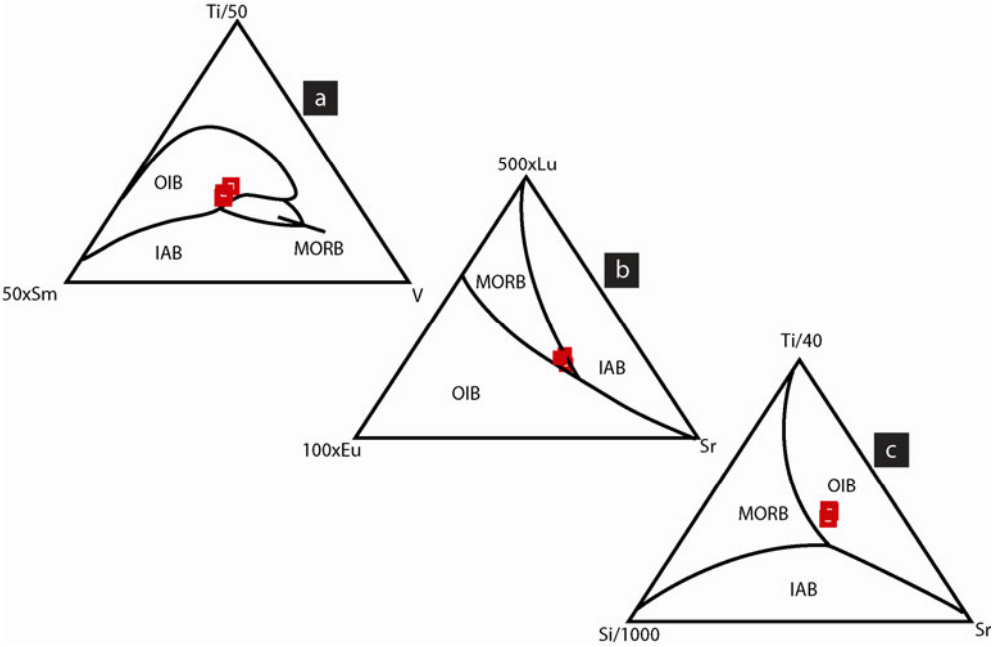

Figure 6.13: Tectonic discrimination diagrams based on classification trees (Vermeesch, 2006). See text for further explanation

6.6 Geochemical Modeling

Henceforth, our primary focus for modeling the intra-crustal petrologic evolution processes will be mainly on fractional crystallization, which is shown to be the dominated differentiation process. Furthermore, the effects of crustal assimilation will also be investigated. Besides, mixing models between mafic and felsic end-members will be also utilized in order to shed light on to the origin of rocks with significant disequilibrium textures.

6.6.1 Whole Rock Major Element Modeling

Major element data have been used in order to reproduce similar outlines of fractional crystallization by using both 'least squares mass balance estimations (Bryan et al., 1969)' and 'Rayleigh Fractionation (Arth, 1976)'. The probable effects of crustal assimilation is also modeled (DePaolo, 1981) and depicted on various bivariate plots.

Mass Balance Estimations

The objective of the least squares analysis is to determine whether an assumed residual liquid might be derived from assumed parent magma by removal or addition of components which have the compositions of mineral phases or contaminants (Bryan et al, 1969). Since a

well-constrained assumption of two end-members is the key for a comparable calculated trend, representative samples have been chosen according to their mineralogical and geochemical properties. Removed phases are compiled from the microprobe data of each sample. Besides, intensive parameters of the crystallization medium were considered.

The path for fractional crystallization is tested assuming a zoned magma chamber with probable crystal-rich density layer(s) between mafic and felsic compositions. Therefore, the setting of the reservoir is as follows: Basalts pond at the bottom (estimated temperature and density) for relatively longer time than that for felsic melts (high porphyritic indices). Benmoreitic Type II enclaves and to some degree mugearites represent the dynamic transition between trachytic melts. Fractionation is chemically linear but somehow chaotic according to petrographic/mineralogic data. Trachytes display smooth differentiation to rhyolites with traces of disequilibrium on its metaluminous counterparts. However some distinct compositions have also been reached in trace elements.

Basalts, although not primitive (low Cr and Ni content), have been used as starting melts (Sample N-258). Mugearites represent the next step (Sample N-016). Metaluminous trachytic pumice (N-036) is chosen for its juvenile nature. Comenditic trachyte sample N-080 represents the transition into peralkaline compositions with its marginal Agpaitic Index (1.05). Comendite end member is a pre-caldera glassy lava flow N-092. Pantellerites are not incorporated into mass balance calculations as they exhibit subsolidus crystallization under low temperature, relatively oxidized conditions. Post-caldera comendites, however, are not primarily considered due to (1) significant deviation in incompatible elements and REE because of probable chevkinite/zircon fractionation/retention in the source (see previous section) (2) the possible physical / chemical variations of magma chamber following the caldera collapse (3) lack of representative intermediate compositions other than basalt and benmoreitic enclaves in post-caldera stage.

The primary goal was to test whether mugearite-like whole rock compositions via fractional crystallization of basalt could be achieved, as we rule out a mere FC process between them, but intense crustal contamination. For various combinations of end members, the best approximations are insufficient to reproduce similar concentrations for CaO. Mass balance models (Table 6.4) indicate that 58% crystallization of plagioclase (30%), olivine (14%) and magnetite (6%) from the chosen basaltic composition yields mugearitic compositions without the accuracy in CaO, conforming to our suggestion. Removal of 31% plagioclase, 13% clinopyroxene, 3% olivine and %7 accessory phases (magnetite, ilmenite and apatite) leads to a composition similar to metaluminous trachyte glass (sample N-036). Further 34%

crystallization of alkali feldspar dominant (27%) assemblage with minor clinopyroxene, olivine and magnetite reproduces comparable results with marginally peralkaline comenditic trachyte (N-080). Increased alkali feldspar crystallization with minor clinopyroxene, olivine and titanomagnetite will result in comendite compositions comparable to sample N-092. ΣR^2 for all steps are << 1, hence acceptable, excluding basalt - mugearite calculation (ΣR^2 = 1.61).

Early crystallization of olivine accompanied by clinopyroxene in mugearites, testifies to the early depletion of Mg, Fe and Ca. Feldspar fractionation is marked with negative Eu anomalies in differentiated lavas.

MELTS Modeling

MELTS (Ghiorso and Sack, 1995) yields analogous major element variation trends with the observed data. Given the starting compositions listed in Table 5.9, major element concentrations evolve during crystal fractionation represent similar variation (Figure 6.14).

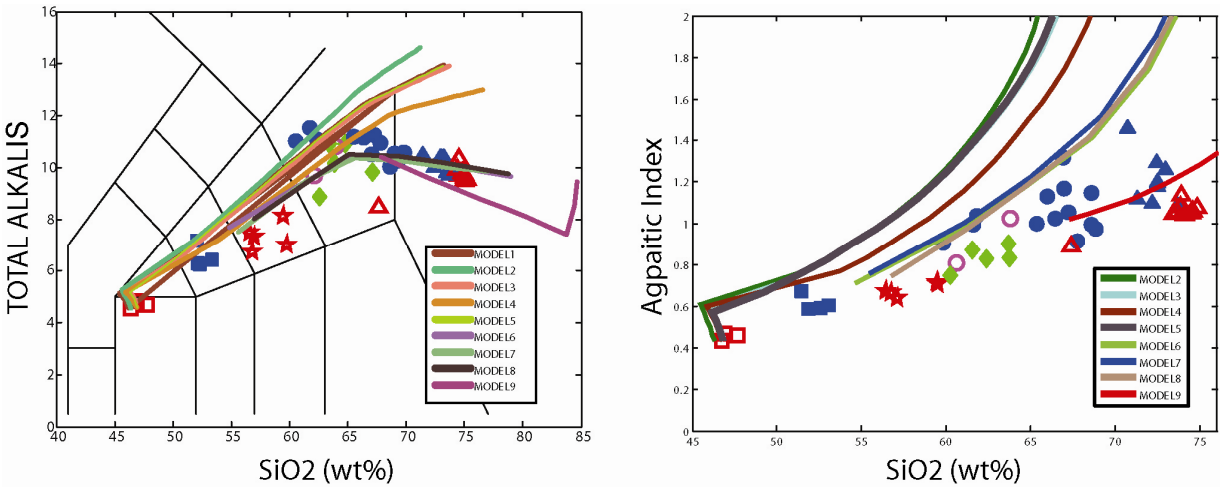

Figure 6.14: Major element variation calculated by MELTS under isobaric FC conditions depicted on (a) TAS b) Agpaitic Index versus silica (SiO2) diagrams.

MELTS modeling indicate that it is not possible to reach highly evolved felsic compositions from a basaltic parent via single fractionation stage. Rather, if a stepwise fashion is implemented by consecutive starting compositions (Basalt – mugearite – trachyte – comenditic trachyte – comendite), peralkaline rhyolitic compositions can be obtained. Hence, regarding the zonation of the magmatic chamber, in which crystallization occur, step-by-step geochemical modeling is logical.

Table 6.4: Least-squares mass balance calculations for major elements for the derivation by fractional crystallization of basalt → mugearite → metaluminous trachyte → comenditic trachyte → comendite. Chemical compositions of fractionating phases are given. ΣR^2 is the sum of least squares representing error. Calculated bulk K_Ds for trace elements for respective melt compositions have also been shown. See Table 6.5 for the partition coefficients of trace elements.

	Basalt		Mugearite		Trachyte		Com. Trachyte		Comendite
	Obs.	Calc.	Obs.	Calc.	Obs.	Calc.	Obs.	Calc.	Obs.
Sample	**N-258**		**N-016**		**N-036**		**N-080**		**N-092**
SiO_2	46,75	46,77	51,85	51,85	60,25	60,25	67,24	67,23	72,93
Al_2O_3	16,36	17,08	15,64	15,71	16,02	15,86	14,28	14,20	10,89
Fe_2O_3	14,06	14,11	12,32	12,31	6,57	6,66	5,44	5,44	4,59
MgO	6,49	6,45	3,27	3,27	0,96	0,66	0,03	0,05	0
CaO	9,13	7,55	6,89	6,89	2,78	2,86	0,75	0,77	0,25
Na_2O	3,77	3,36	4,30	4,01	4,81	5,32	5,86	6,06	5,45
K_2O	0,81	1,02	1,94	2,09	3,72	3,54	5,01	5,14	4,39
TiO_2	2,85	2,61	2,49	2,50	0,85	0,60	0,37	0,36	0,25
MnO	0,21	0,20	0,19	0,16	0,13	0,19	0,16	0,19	0,1
Melt Fraction	**50,43**		**43,13**		**66,03**		**42,64**		
Cryst. Fraction	**49,57**		**56,87**		**33,97**		**57,36**		
Feldspar	**29,53**		**30,95**		**26,93**		**50,81**		
SiO_2	52,04		57,62		58,90		67,15		
Al_2O_3	30,28		26,04		25,50		18,86		
Fe_2O_3	0,56		0,78		0,34		0,49		
CaO	13,54		8,50		7,53		0,13		
Na_2O	3,98		5,95		6,97		7,36		
K_2O	0,09		1,47		0,75		6,46		
Clinopyroxene			**12,46**		**1,93**		**3,07**		
SiO_2			50,44		50,47		48,23		
Al_2O_3			2,36		1,11		0,38		
Fe_2O_3			11,76		15,82		28,88		
MgO			13,69		10,04		1,08		
CaO			19,82		20,29		18,92		
Na_2O			0,36		0,39		0,84		
TiO_2			1,11		0,51		0,57		
Olivine	**14,04**		**3,13**		**3,30**		**2,50**		
SiO_2	36,77		35,90		32,82		29,38		
Fe_2O_3	28,29		34,81		49,86		65,87		
MgO	32,76		28,79		15,41		0,78		
Fe-Ti Oxides	**6,00**		**6,64**		**1,79**		**0,98**		
Al_2O_3	3,93		3,86		1,69		0,11		
Fe_2O_3	62,70		80,24		68,82		73,09		
MgO	2,73		1,32		1,26		0,04		
TiO_2	21,61		7,97		23,28		22,56		
MnO	0,62		0,29		0,79		1,38		
Apatite			**0.92**						
Agpaitic Index	0,43	0,39	0,59	0,56	0,75	0,79	1,05	1,09	1,26
ΣR^2		1,61		0,01		0,00		0,09	
Used Bulk KD									
Rb	0,033		0,074		0,247		0,338		
Sr	1,757		2,121		2,368		1,654		
Zr	0,310		0,117		0,014		0,076		
La	0,148		0,184		0,028		0,170		
Lu	0,023		0,184		0,027		0,336		
Ba	0,309		0,288		2,904		15,804		
Y	0,017		0,193		0,008		0,185		
Yb	0,215		0,453		0,059		0,164		
Ce	0,058		0,260		0,008		0,149		
Nd	0,087		0,385		0,028		0,549		

6.6.2 Trace Element Modeling

In order to test the proportions of fractionating assemblages and the remaining melt obtained from the major element mass balance models (Table 6.4.), trace element modeling has been applied. Rayleigh fractionation equation was used for fractional crystallization (FC). Moreover, the effects of crustal assimilation (AFC) were simulated using the equations of De Paolo (1981) and Powell (1984).

The main approach was to simulate fractional crystallization in a multi-stage fashion. As we suggested before, magma chamber is zoned with spatial variation in crystallization conditions. Besides, chemical compositions of removed phases vary remarkably depending on the portion of the magma chamber in which crystallization occurs. Moreover, the Nernst partition coefficients for the distribution of trace elements are significantly affected by the chemical composition of the melt. Hence, in a chemically zoned chamber, fractional crystallization from a basaltic parent to rhyolitic daughter via single stage would unlikely to occur.

As a consequence, the same evolutionary steps with the major element mass balance models have been used. Parent and daughter couples are also the same. Proportions of fractionating phases have been taken as is. This helped us to verify whether both models are consistent, with the obtained F (the fraction of melt remaining) values. Bulk partition coefficients (Table 6.4) are calculated according to the calculated assemblages for each step with the Nernst coefficients (compiled from www.earthref.org Table 6.5) of the respective melt compositions. Due to the great diversification among published partition coefficients for trace elements; we tried to choose, whenever possible, recent mineral/nominal rock groundmass values for (per)alkaline compositions.

Table 6.5: Partition coefficients of trace elements in various melt compositions. Nernst coefficients are compiled from www.earthref.org. Chevkinite data are from Troll et al. (2003).

Melt	Mineral	Sc	V	Rb	Sr	Y	Zr	Nb	Ba	La	Ce	Pr	Nd	Sm	Eu	Gd	Tb	Dy	Ho	Er	Tm	Yb	Lu	Hf	Th	U	Ta	Cr	Co	Ni
BASALT - MUGEARITE	Clinopyroxene	1,42	3,4	0,011	0,449	0,245	0,195	0,2	0,05	0,11	0,1	0,3	0,329	0,49	0,36	0,46	0,73	0,9	0,66	0,566	1	0,9	0,9	0,375	0,0127	0,004	0,261	1,8	1,8	2,2
	Olivine		0,09	0,04	0,02	0,009	0,06	0,01	0,03	0,01	0,01	0,005	0,0023	0,01	0,01	0,0041	0,0041		0,0047		0,009	0,394	0,03	0,04	1E-05	1E-05	0,01	0,49	5,3	16
	Magnetite	0,73	6,85	0,11			0,71	1,8		0,015	0,016		0,026	0,024	0,025	0,018	0,019		0,017			0,018					2,53	30	3,4	31
	Ilmenite	1,8	12				0,28	2	0,0003	0,098	0,11	0,0002	0,14	0,0006	0,1	0,14	0,14	0,01	0,13		0,1	0,17	0,084	0,38	0,0006	0,0082	2	6	2,2	4
	Amphibole	6		0,31	0,12	1,3	1,2	0,21	6,4	0,195	0,367	0,6	0,44	0,93	1,08	1,19	1,29	0,78	0,73	0,68	0,64	0,98	0,82	1,8	0,11	0,15	0,21	0,1	1,35	16
	Apatite	0,22							0,05	8,6	11,2		14	14,6	1,08	15,8	15,4		13,3			8,1							0,03	
	Plagioclase	0,008	0,1	0,016	3,5	0,023	0,13	0,01	1,45	0,24	0,09	0,142	0,14	0,106	1,23	0,05	0,06	0,055	0,048	0,01	0,036	0,17	0,025	0,05	0,05	0,1	0,11	0,08	0,58	0,5
MUGEARITE - TRACHYTE	Clinopyroxene	1,49	4,82	0,02	0,449	0,8	0,16	0,2	0,05	0,2	0,1	0,3	0,888	0,49	0,36	0,46	0,37	0,9	0,66	0,566	1	0,9	0,75	0,23	0,05	0,03	0,2	1,8	1,8	2,2
	Olivine		1,2	0,02	0,02	0,02	0,06	0,01	0,03	0,02	0,01	0,005	2,6	0,01	0,01	0,0041	0,03		0,0047		0,009	0,394	0,03	0,01	0,01	0,01	0,01	0,49	5,3	16
	Magnetite	2,99	63	0,49			0,51	1,8		0,11	0,016		0,026	0,024	0,24	0,018	0,16		0,017			0,018		0,48	0,1	0,11	1,8	30	3,4	31
	Ilmenite	1,8	12				0,28	2	0,0003	0,098	0,11	0,0002	0,14	0,0006	0,1	0,14	0,14	0,01	0,13		0,1	0,17	0,084	0,38	0,0006	0,0082	2	6	2,2	4
	Amphibole	1,28		0,08	0,12	1,3	0,13	0,21	6,4	0,07	0,367	0,6	0,44	0,93	0,34	1,19	0,46	0,78	0,73	0,68	0,64	0,98	0,82	0,19	0,01	0,02	0,21	0,1	1,35	16
	Apatite	0,22							0,05	8,6	11,2		14	14,6	1,08	15,8	15,4		13,3			8,1							0,03	
	Plagioclase	0,01	0,1	0,02	3,715	0,03	0,01	0,01	1,45	0,02	0,09	0,142	0,14	0,106	0,06	0,05	0,01	0,055	0,048	0,01	0,036	0,17	0,025	0,01	0,01	0,01	0,01	0,08	0,58	0,5
PERALKALINE TRACHYTE	Alkali Feldspar			0,29	2,79	0,01	0,0001	0,0001	3,43	0,01				0,01	0,52								0,0001				0,0001			
	Clinopyroxene	27		0,15	0,52		0,5		0,22	0,69	0,48		3,06	3,78	1,69		3,06	3,77		3,94		2,16	2,68	0,98	0,06	0,17		6	7	6
	Olivine									0,1	0,01											0,35								
	Magnetite	2,5	25		0,1		0,25		0,01	0,07	0,07			0,08	0,07		0,07					0,05	0,08	0,25	0,03			8	21	
	Apatite	0,3			8		2		0,45	27	31			38	30		30					10	7	0,07	1,6	2,6			2	
	Plagioclase	0,009		0,7	3,18		0,17		3,4	0,1	0,223		0,219	0,221	2,5		0,03	0,22		0,219		0,004	0,0024	0,0001	0,001	0,003		0,3	0,04	0,18
	Chevkinite				84	74	3,55	15		988	806	626	615	392	225	142		72						8,5	50					
COMENDITE - PANTELLERITE	Alkali Feldspar	0,029		0,4	1,68	0,028	0,036	4,8	18,9	0,129	0,065		0,054	0,026	6,5	0,011	0,06	0,04		0,162		0,03	0,02	0,034	0,022	0,04	4,8		0,39	1,3
	Clinopyroxene	44		0,039	2,1	1,7	0,42	0,036	0,1	0,51	0,81		5,2	1,7	1,7	1,3	4,6	4,5		1,14		1,3	3,3	0,4	0,1	0,6	0,036	4,13	17	
	Olivine				1,1	0,12	0,049																							
	Magnetite	5		0,01	0,01		0,24		0,1	0,8	1,02		1,5	1,9	0,91		2	4,4				1	0,91	0,95	0,32	0,83		54	80	
	Ilmenite	5,9			0,74	0,024	0,074	50,9		7,1	7,8		7,6	6,9	2,5		6,5	4,9				4,1	3,6	3,1	7,5	3,2	50,9	3	26	6,2
	Amphibole	2,4	17	11,1	0,38	0,017	0,05	0,76	0,3	0,05	0,06		5,19	0,06	3,2		2,4	12,3		8,2		4,41	1,8	0,04	0,45	1,6	0,76	43	37	2
	Chevkinite				84	74	3,55	15		988	806	626	615	392	225	142		72						8,5	50					

We aimed to investigate trace element distribution starting from basalt (N-258), mugearite (N-016), metaluminous trachyte (N-036) and peralkaline trachyte (N-080). Theoretical distribution of selected trace elements in each step has been depicted in Figure 6.15. For comparison, calculated trends of each step are given in different plots. Also depicted the effects of crustal assimilation for different ratios of assimilation/fractionation (r = 0.3 and 0.8). Crustal assimilant is assumed as the upper crustal composition of Wedepohl, 1995.

According to the calculated tendencies, multi-stage fractional crystallization with varying degrees of crustal assimilation is the dominant process for the magmatological evolution of Nemrut volcanics.

Trace element modeling does not satisfy the fractionation of suggested assemblage from basalt to reproduce mugearites. Calculated mugearites are LREE-poor and sometimes HREE-rich than the observed mugearites (Figure 6.15).

Theoretical crystal fractionation accompanied with assimilation (r=0.3) reproduces similar trends for trace elements with the observation, from mugearite to metaluminous trachyte (Figure 6.15). Remaining melt fractions for both FC and AFC processes are fairly consistent with the mass balance models, being dominantly 40 – 60% (43% is presumed in mass balance models). Calculated REE patterns are comparable, excluding the absence of Eu trough. Pumices of Nemrut ignimbrite exhibit Eu enrichment whereas upper and lower plinian airfalls (SID: 1036 and 1031 respectively) exhibit depletion. The absence of Eu anomaly in theoretical compositions might be due to the partition coefficients for mugearitic melts.

The following step is to test whether 30% fractionation of alkali feldspar-rich assemblage with minor olivine, clinopyroxene and Fe-Ti oxides reproduce marginal comenditic trachytes (N-080, A.I. = 1.02). For 10 – 20% removal of given assemblage (Table 6.4) with crustal assimilation (r = 0.3), most trace element contents of comenditic trachyte can be reached. On the other hand, some LIL elements (Sr and Ba) exhibit evident deviation from calculated trends (not shown) probably due to varying degrees of crustal contamination. Calculated and observed REE patterns match remarkably.

The final step is performed in order to reach comenditic compositions. Rayleigh fractionation of given assemblage (Table 6.4) from a marginally peralkaline trachyte (N-080) generally represents the trace element variation relatively better than AFC process. Bivariate plots of various elements exhibit that 40 - 50% fractionation of an alkali feldspar-rich assemblage could produce typical comendite magmas. Moreover, calculated and observed REE patterns

are overlapped, except the stronger depletion of Eu in theoretical melt. However, this error might be related to the selection of partition coefficient for Eu.

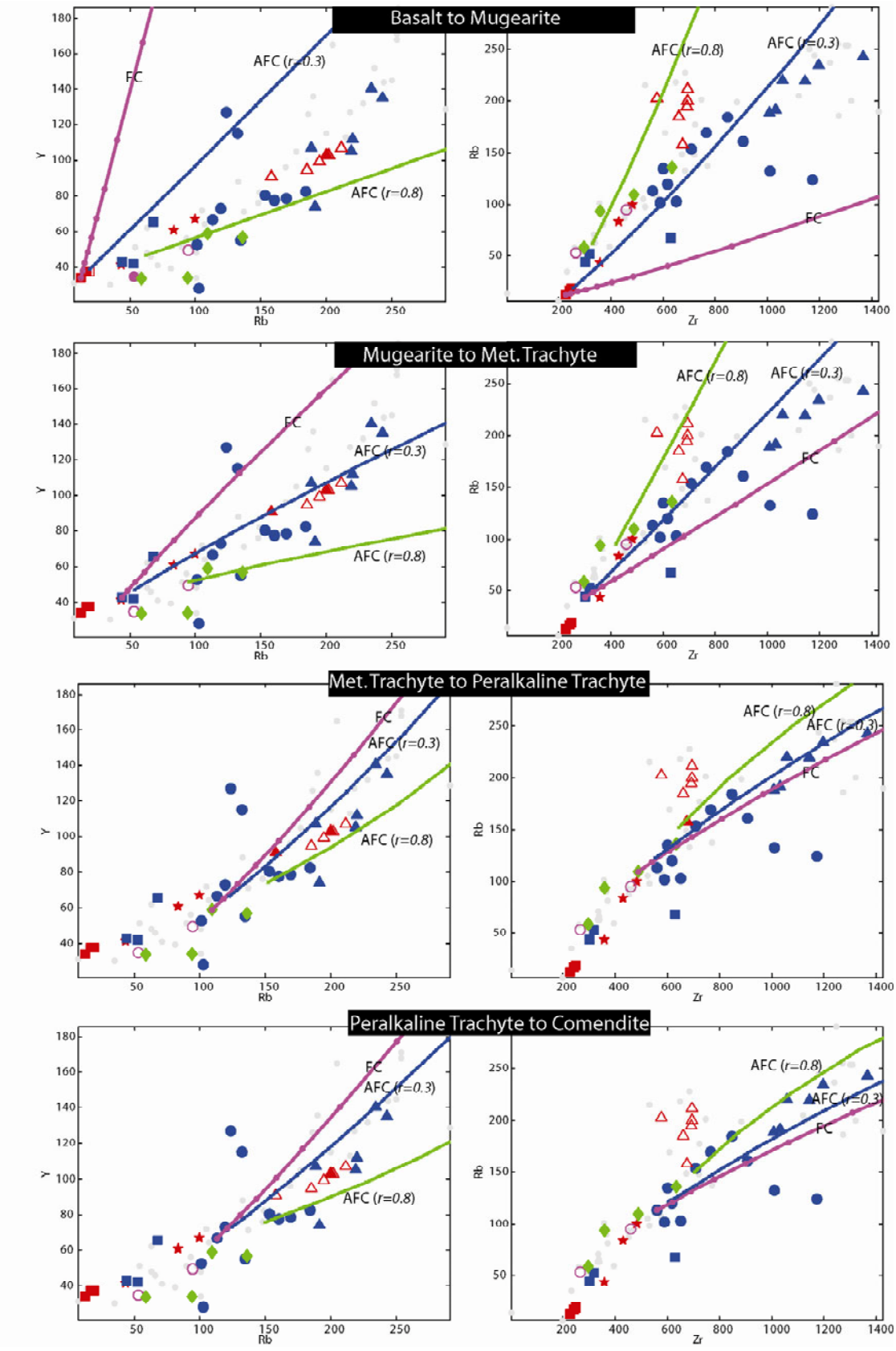

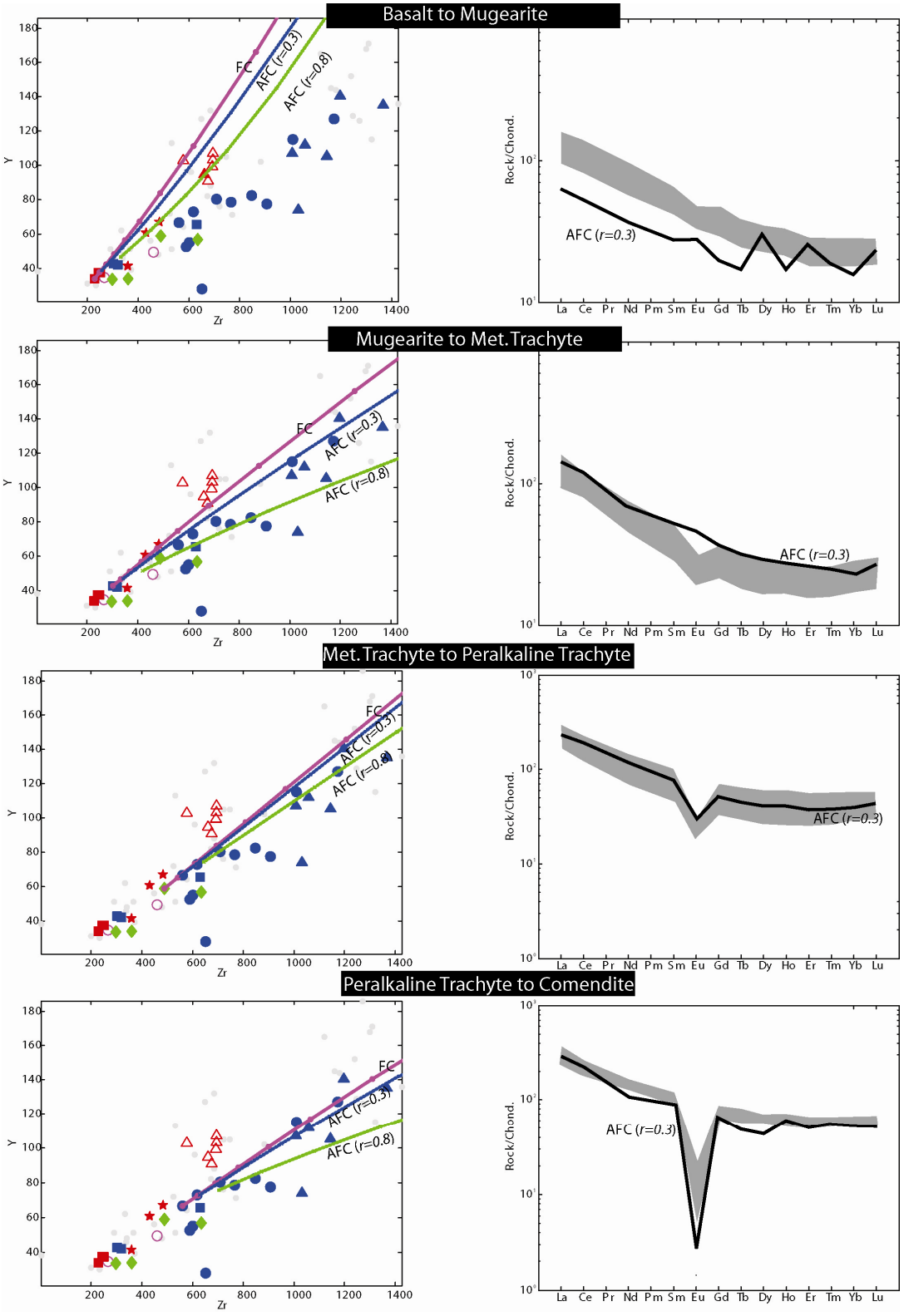

Figure 6.15: Trace element modeling of fractional crystallization (FC) and assimilation fractional crystallization (AFC) starting from various compositions. Bulk K_Ds for trace elements have been calculated for mineral assemblages obtained from least squares mass balance models (Table 6.4). Assimilation of a typical upper crust composition (Wedepohl, 1995) has been simulated for r=0.3 and r=0.8. Observed REE content of Nemrut volcanic rocks have been depicted by gray fields. Black lines represent average compositions reached by AFC (r=0.3). Gray dots represent data from literature (Gülen, 1984; Pearce et al., 1990; Yılmaz et al., 1998). Symbols are as Figure 6.7

6.6.3 Testing AFC Processes with EC-AFC Modeling

In order to test the consistency of the obtained results from major element mass-balance models and trace elements Rayleigh fractional crystallization models (combined with AFC equations: DePaolo, 1981; Powell, 1984), EC-AFC (Energy Conserved - Assimilation Fractional Crystallization) modeling (Spera and Bohrson, 2001) has been realized. Compared with '*classical*' models that conserve mass and species only, energy-constrained models represent more complete assessments of the complex physicochemical dynamics governing the geochemical evolution of open-system magma bodies (Spera and Bohrson, 2001).

The underlying idea in our EC-AFC calculations was selecting reasonable ranges of initial parameters required and performing iterative calculations using the EC-AFC spreadsheet provided by respective authors (http://magma.geol.ucsb.edu) systematically changing the parameter set within constrained ranges until a best fitting trend was obtained. For a rigorous application of EC-AFC modeling, the reader is advised to read Bohrson and Spera (2001) and Guo et al. (2006) from which we have been inspired significantly.

Thermal and compositional parameters utilized during EC-AFC calculations are given in Table 6.6. Concerning the requirement of significant crustal assimilation of basalts to reproduce mugearites and possible existence of a stratified magma chamber with a crystal-rich filtering layer between basaltic and trachytic melts (see Chapter 5), in order to reach rhyolitic compositions of the pre-caldera stage, EC-AFC calculations are performed starting from pre-caldera mugearite. Post-caldera comendites are believed to be significantly affected by possible chevkinite fractionation and will be discussed in section 6.6.4. For the purpose of demonstrating the possible evolution paths of isotope ratios, mugearites have been selected as the starting magma compositions (Table 6.6). According to the calculated intensive reservoir parameters (Chapter 5), magma stagnation and evolution take place at upper crustal levels. Hence, due to the absence of any crustal xenoliths (and analysis), the assimilant is chosen to be the "granitic" standard upper crust and EC-AFC parameters for standard upper crustal case (Bohrson and Spera, 2001) have been performed (Table 6.6). However, it is noteworthy to remember Nemrut magmas have been affected by the assimilation of local basement rocks (Figure 6.8). Nonetheless, a standard upper crustal assimilant, compositionally conformant to basement metamorphics, is assumed throughout the calculations.

Calculated liquidus temperatures of magmas (see Chapter 5) have been performed with liquidus temperature of standard upper crustal assimilant (Bohrson and Spera, 2001). Solidus and equilibration temperatures are estimated by iterative calculations. Values for the isobaric specific heat of the magmas and the assimilant as well as enthalpies of crystallization and fusion are taken from Bohrson and Spera (2001) and are assumed to be constant (Guo et al., 2006). Trace element bulk partition coefficients are calculated for possible crystallizing phases during AFC processes (taken from Table 6.4), whereas for assimilant bulk coefficients have been calculated for partially melting assemblage.

Table 6.6: Thermal and compositional parameters utilized in EC-AFC calculations. Magma is mugearite (N-016). Assimilant is the standard upper crustal case from Bohrson and Spera (2001)

Thermal Parameters						
Magma liquidus temperature	1160 °C		Isobaric specific heat of magma			1484 J/kg K
Magma initial temperature	1160 °C		Isobaric specific heat of assimilant			1370 J/kg K
Assimilant liquidus temperature	1000 °C		Crystallization enthalpy			396000 J/kg
Assimilant initial temperature	300 °C		Fusion enthalpy			270000 J/kg
Solidus temperature	850 °C					
Equilibration temperature	885°C					
Compositional Parameters	**Sr**	**Nd**	**La**	**Rb**	**Y**	
Magma (Mugearite)						
initial concenration (ppm)	357	37	32	44	42,63	
isotope ratio	0,705827	0,512634				
trace element distribution coefficient	2,22	0,67	0,184	0,08	0,21	
Assimilant						
initial concenration (ppm)	316	26	32,3	110	20,7	
isotope ratio	0,722	0,5118				
trace element distribution coefficient	2,79	0,25	0,01	0,29	0,01	

Since an exact quantification of AFC processes is limited due to heterogeneous geochemical nature of the upper crust and uncertainties of the bulk distribution coefficients (especially for Sr) (Krienitz et al., 2006), we demonstrate the results of EC-AFC calculations on various qualitative plots (Figure 6.16). Starting from mugearite, peralkaline trachytic - rhyolitic compositions can be achieved via prolonged crystal fractionation with limited degrees (<6%) of upper crustal assimilation. Assimilation will be initiated once the crustal rocks achieve specific heat of fusion. Hence, as it can be seen from the plots (Figure 6.16) the amount of assimilation increases with respect to the amount of fractionation and thus magmatic evolution.

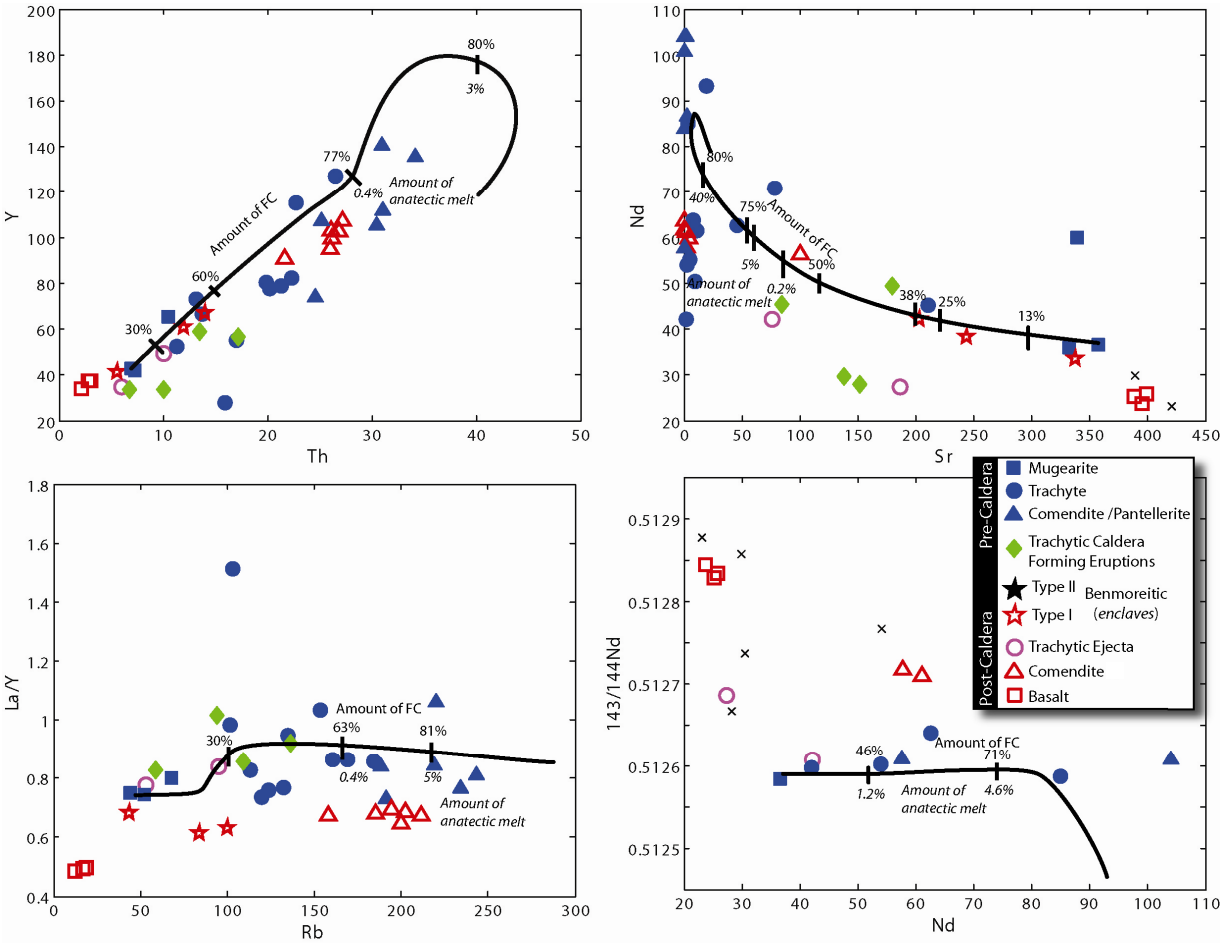

Figure 6.16: Results of EC-AFC modeling. Calculations are performed starting from mugearite. Percentage of crystallized cumulates are depicted by "Amount of FC", whereas assimilated anatectic melt percentages have been given in italic numbers. X symbols are recalculated data from Gülen, 1984. EC-AFC calculations indicate the dominance of prolonged Fractional Crystallization with slight contribution from upper crustal anatectic melts

As a result, we state that the prolonged crystal fractionation of feldspar, clinopyroxene, olivine and Fe-Ti oxide bearing assemblage in varying proportions and with slight upper crustal anatectic melts (<6%) would reproduce similar trends as observed in Nemrut volcanic rocks.

6.6.4 Testing the Role of Chevkinite Fractionation in Post-Caldera Comendites

Anomalous REE content of post-caldera comendites compared with the pre-caldera counterparts have been debated to be the result of possible retention or fractionation of REE-Ti-silicate chevkinite (and synneusis zircon). In order to demonstrate the effect of chevkinite fractionation we performed standard Rayleigh fractionation from a highly evolved pre-caldera comendite (N-092). The rationale behind our calculation is as follows: If a highly evolved pre-caldera comendite undergoes chevkinite fractionation, could similar compositions with post-

caldera comendites be achieved? Thus, we assumed a “null” fractionating assemblage with only 0.01% chevkinite. Bulk partition coefficients (elemental Nernst coefficients from Troll et al., 2003) are calculated for 0.01% chevkinite. As Figure 6.17 clearly indicates, even 3-6% fractionation of an assemblage consisting of 0.01% chevkinite would reproduce significantly comparable compositions with post-caldera comendites. Hence, we propose even minimal fractionation of chevkinite, if present in any magmatic suite, would deviate the compositional trends significantly. Bohrson and Reid (1997) discuss anomalous Ce and REE content of peralkaline rhyolites from Socorro Island, Mexico. Although, they do not report modal chevkinite, the trends presented in their paper remind the likely effect of chevkinite fractionation. Hence, we do need to emphasize the importance of modal mineralogy in petrogenetic studies.

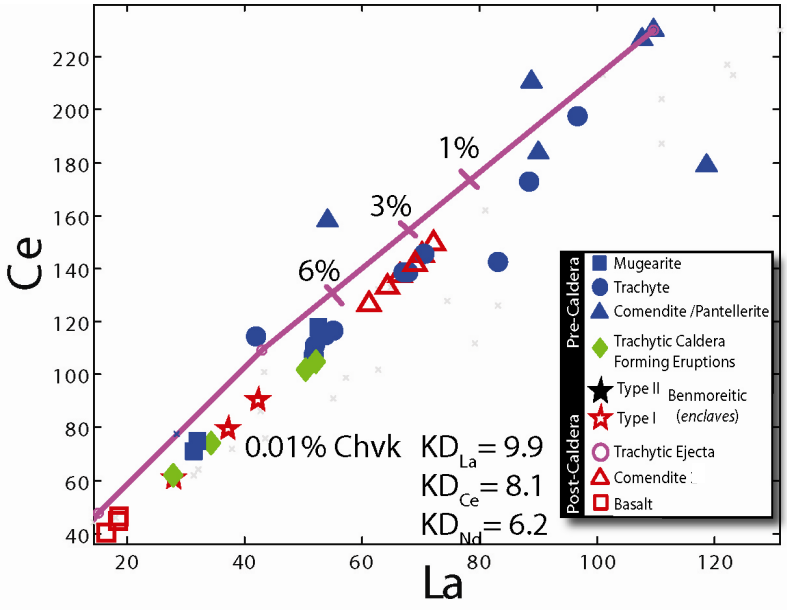

Figure 6.17: Calculated chevkinite fractionation trend starting from pre-caldera comendite N-092

6.7 Conclusions

Throughout its evolution Nemrut volcanism produced mafic to silica oversaturated peralkaline rocks with an evident scarcity of intermediate compositions (Daly Gap), which is a common phenomenon in peralkaline suites of continental extension. Basalts are nepheline normative, being mildly alkaline to transitional in character. Mugearites and metaluminous trachytes are rare by volume compared to the widespread trachytes and rhyolites. The degree of peralkalinity of felsic rocks varies from marginal comendites (Agpaitic Index ≈ 1) to scarce pantellerites (A.I = 1.45). Intermediate compositions are benmoreites and confined only to the enclaves observed in comendites. Caldera forming pyroclastic activity, on the other hand, has produced metaluminous trachytic ignimbrite.

Basalts should have been subjected to intense crustal assimilation in order to reproduce mugearitic compositions. It is suggested that protracted fractionation of feldspar dominated, clinopyroxene, olivine and Fe-Ti oxides bearing assemblage from mugearitic melts with sometimes significant crustal assimilation to evolve into pre-caldera lavas. Both major and trace element systematics, especially those of pre-caldera stage, indicate a fractional crystallization of mainly feldspar and accompanied with clinopyroxene, olivine, Fe-Ti oxides and apatite from a mugearitic parent is the prevailing differentiation process for Nemrut volcanic rocks. However, crustal contamination from possibly multiple sources is pronounced especially for pre-caldera lavas. Post-caldera lavas, on the other hand seem to be less affected by contamination, probably due to the plastering of pre-caldera magmas onto the ascent paths. Geochemical modeling using both major and trace elements show that assimilation of typical upper crust compositions with varying degrees contribute to the geochemical evolution of Nemrut volcano. However, local mixing of mafic and felsic melts is represented by Type I benmoreitic enclaves, which is not accepted as a primary differentiation process. Post-caldera comendites, however, exhibit significant depletion in REE, Nd and Zr compared to the pre-caldera counterparts, which can be explained by the fractionation and/or retention of REE-Ti silicate chevkinite accompanied with zircon.

Slight upper crustal assimilation and concomitant fractional crystallization of a minor subduction enriched mantle source would create parental magmas for Nemrut volcanism (Figure 6.18). Trace element data and Sr-Nd isotopic ratios conform to a slightly enriched asthenospheric mantle source.

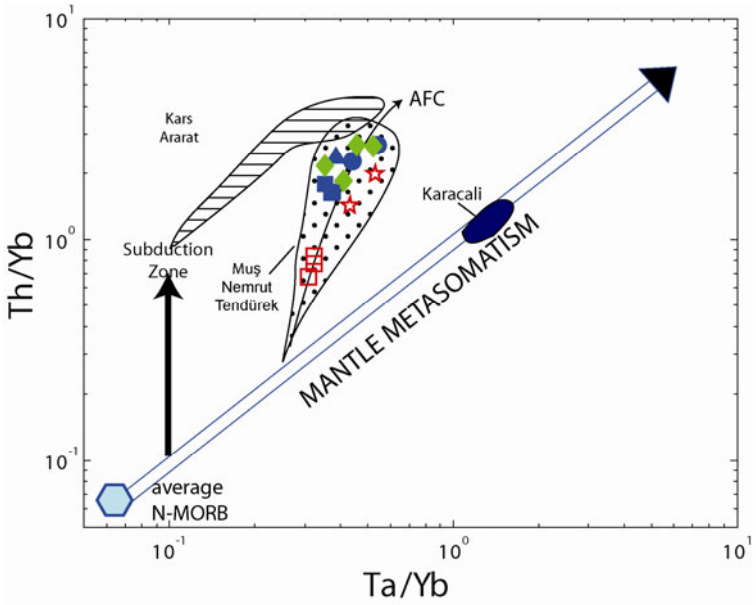

Figure 6.18: Th/Yb versus Ta/Yb diagram for Nemrut and other east Anatolian volcanic centers (after Pearce et al., 1990). Nemrut basalts are depicted to be formed from a slightly enriched mantle source with AFC processes.

CHAPTER 07

DISCUSSION AND CONCLUSIONS

When I examine myself and my methods of thought, I come to the conclusion that the gift of fantasy has meant more to me than any talent for abstract, positive thinking.

Albert Einstein

7 DISCUSSION AND CONCLUSIONS

In order to emphasize its significance and to reveal several problems prescribed for Nemrut volcano should be discussed in terms of the data, findings and interpretations presented throughout this study.

Quaternary Nemrut volcano exhibits distinguishing magmatological features of a typical silica oversaturated peralkaline suite from transitional olivine basalt to rhyolite: **(a)** Predominance by erupted volume of peralkaline (Agpaitic Index >1) acidic volcanic rocks with respect to basic varieties with evident scarcity of intermediate compositions (Daly Gap), which are partly represented by inclusions in highly evolved rocks **(b)** Characteristic peralkaline accessory mineral assemblages composed of aenigmatite, alkali amphibole (arfvedsonite, riebeckite, ferrorichterite), aegirine, fayalite and REE-Ti silicate chevkinite **(c)** Existence of a small (diameter < 10 km) collapsed caldera indicator of a shallow magma chamber, in which crystallization thought to occur at ~1 kbar pressure.

7.1 Genesis of Peralkaline Magmas in a Continental Collision Setting

Alkaline rocks such as peralkaline quartz trachyte and rhyolite are generally considered to be characteristic of intraplate magmatism (Bowden, 1974) as perfectly exemplified in continental East African Rift system. However, occurrences of peralkaline magmatism have also been reported for local extensional regimes in convergent margins (e.g. D'Entrecasteaux Island, Papua New Guinea; Mayor Island, New Zealand; Bohrson and Reid, 1997; White et al., 2006 and references therein). Tectonic setting of east Anatolia and hence, Nemrut volcano, seems analogous with Pine Canyon caldera in Trans-Pecos Texas, USA (White et al., 2006) and Cambrian post-collisional Iforas province, Mali (Liégois and Black, 1987).

Post-collisional magmatism in Trans-Pecos magmatic province is generally summarized in four basic evolutionary steps (Bonin, 2004; White et al., 2006): **1)** Collision (flat subduction of Laramide plate resulting in lithospheric stacking and orogenic growth). **2)** Post-collisional relaxation, following the roll-back or break-off of subducting slab resulted in asthenospheric upwelling, partial melting of lithospheric mantle and crust. **3)** Post-orogenic, early stage of continental rifting and asthenospheric magmatism, represented by bimodal and peralkaline volcanism because of delamination and the sinking of the detached lithosphere. **4)** Relaxation with a clear extensional intra-plate regime, and magmatism with a greater influence from the asthenosphere.

Iforas province (Mali) displays similar geodynamic evolutionary steps (Liégois and Black, 1987). Starting with subduction of passive continental margin of West African craton and related calc-alkaline island arc magmatism, initiation of alkaline magmatism after a major uplift and the break off of the subducted plate, asthenospheric mantle induced alkaline - peralkaline magmatism along lithospheric mega-shear zones and related wrench faults producing distension.

Geodynamics of East Anatolia presents similarities with both Trans-Pecos and Iforas magmatic provinces. Neotectonics of East Anatolia has been dominated by the collision between Arabian and Anatolian plates along Bitlis – Zagros suture zone. Eastern Anatolia comprised of remnants of Tethyan oceanic lithosphere and Gondwana derived continental blocks or microplates, still being squeezed and experienced a compressional – extensional tectonic regime in connection with westward extrusion of the Anatolian plate (Elitok and Dolmaz, 2007).

Following the initial continental collision between Eurasia and Arabian plates and the subduction of northern margin of Arabian plate (Figure 7.1), the final continental collision and suturing of Arabia with Eurasia plates is thought to have happened in the Middle Miocene (Yılmaz, 1993). Subducting oceanic lithosphere, has began to get steepened (Keskin, 2003) and caused upwelling in the surrounding asthenosphere (Krienitz et al., 2006). The slab has been detached from Arabian continent due to its downward force probably 11 Ma ago (Şengör et al., 2003). Upon the break off of the subducting slab, tectonic regime in the region changes from compressional - contractional to compressional - extensional (Koçyiğit et al., 2001). Meanwhile, hot subduction-unmodified asthenosphere residing beneath the Arabian Foreland, might have migrated towards the slab window which was opened during the detachment and invaded the mantle wedge beneath East Anatolian Collision zone (Figure 7.1) (Keskin, 2003; Şengör et al., 2003; Elitok and Dolmaz, 2007). Furthermore, Faccenna et al. (2006) proposes that slab break off might be responsible for the formation of North and East Anatolian Transform Fault zones (NATFZ and EATFZ). The westward extrusion and counterclockwise rotation of Anatolian plate via NATFZ and EATFZ have been accompanied by the intracrustal deformations; the present crust between east Anatolian plate and Arabian foreland gets thinner from north (44km) to south (~36km) (Elitok and Dolmaz, 2007). Although S-wave receiver interpretations suggest that eastern Anatolia is indeed a mélange of several lithospheric fragments, it is difficult to observe whether the crust also shows similar fragmentation with deep faults extending into lower crust, which would be expected for a region composed of several crustal blocks (Angus et al., 2006). Besides, rapid westward extrusion of Anatolia and its counterclockwise rotation following the slab break off

eased by the amalgamated crustal structure of east Anatolian region, where stretching and crustal thinning dominated by wrench tectonics (Elitok and Dolmaz, 2007).

The present state of lithosphere beneath Eastern Anatolia is not clear. Al-Lazki et al. (2003) interpret the anomalies of attenuated Sn wave propagation and the very low Pn velocity, as the existence of a partially molten or eroded mantle lid beneath easternmost portion of NATFZ. Keskin (2003) further argues the possibility of an almost normal-thickness crust resides on an extremely thin mantle lithosphere or even directly on asthenosphere. Angus et al (2006) demonstrate the absence of lithosphere-asthenosphere boundary under East Anatolia Accretionary Complex within the depth of 60 - 80 km, where late Miocene to recent volcanism is significant. Recent Curie Point Depth studies indicate that mantle lithosphere under Arabian Foreland gets thinner towards Bitlis suture, probably due to the removal of the lithospheric mantle at the northernmost margin of the Arabian Foreland (Elitok and Dolmaz, 2007). Hence, it is plausible to think of a very thin or partially absent mantle lithosphere accompanied by hot asthenospheric upwelling beneath Nemrut volcano and its vicinity.

The peralkaline character of Nemrut volcano, compared to its neighboring coeval volcanoes (i.e. Süphan) is appealingly distinct. It is reasonable to believe that similar processes of magma genesis have been operating beneath both volcanoes within the aforementioned geodynamic framework. Süphan volcano, being transitional in character and located just between Tendürek and Nemrut volcanoes, seems somehow contradictory with the suggestion of a spatial discrimination between calc-alkaline and alkaline volcanism (c.f. Keskin, 2003). Süphan produced calc-alkaline to transitional products during the same timespan while Nemrut was effusing dominantly peralkaline lavas. Unfortunately Süphan is not very well documented and data is lacking for its basic lavas, which inhibits us to make a comparison between Nemrut, in terms of primitive magmas. Still, we know that Süphan evolved into more alkali-poor felsic rocks than Nemrut did. Evidently different differentiation mechanisms, operating under different physical conditions would be responsible for the distinct trends observed in these two volcanoes. Süphan lavas, compared to Nemrut, bear completely dissimilar mineral associations including orthopyroxene, hornblende and biotite, highly likely to point out a deeper magma chamber. Besides, absence of a collapsed caldera conforms to this suggestion. Hence, we can conclude that depth difference between magma chambers of these two volcanoes would result in different evolution trends, but why? Why Nemrut has a high level reservoir (or vice versa)?

Nemrut volcano is situated on the north of Muş basin, the deformed and dissected remnant of the WNW trending Oligocene – Miocene Muş-Van ramp basin located at the northern foot of the Bitlis suture zone (Koçyiğit et al., 2001). A ramp basin is an intermountain basin where outward directed active thrusts bound its opposite sides (Cunningham, 2005) representing syntectonic depression. Although Muş basin seems to retain its earlier nature of ramp basin, its northern margin bounding reverse fault has a considerable dextral strike-slip component, implying an inversion in the tectonic regime in Pliocene (Koçyiğit et al., 2001). Consequently, right lateral movement of the northern margin of Muş basin with respect to the southern marginal thrust, would result in localized extension on the northern margin, where Nemrut volcano is located. The existence of prevailing extension in the Nemrut region is obvious with the rift associated with post-caldera activity of the volcano.

Whilst the source of alkaline magmatism is to be sought in the deep mantle, its location and nature are largely controlled by the structure, composition and dynamics of the overlying continental lithosphere (Black et al., 1985) or of the crust in Nemrut case, where mantle lithosphere is extremely thin or even absent. During its evolution, Muş basin is though to be deformed and dissected (Koçyiğit et al., 2001), while deep shear zones have been likely to develop. Following the slab break off and the emplacement and ascension of partial melts in the middle crust of the region, pre-existing shear zones and neotectonic extensional fractures would have eased the magmas to reach uppermost levels due their buoyant nature. Further magmatic differentiation in upper level magmatic reservoirs such as in Nemrut, would be the probable reason for its unique peralkaline character in the region.

Furthermore, Nemrut volcano represents analogous structural settings with the intracontinental rifting sites. Extensive thinning of the lithosphere produces significant asthenospheric mantle contribution to the developing melt zone (Wilson, 1989). Besides, silicic peralkaline volcanoes are typically situated in tectonic settings characterized by moderate rates of extension (Mahood, 1984). Peralkaline magmatism can occur pre-rifting (epeirogenic doming), initial rifting (development of linear fractures and the beginning of crustal attenuation) and continued rifting (extensive crustal attenuation leaving little or no sialic crust on the rift floor) (Bowden, 1974). Comendites occur in subvolcanic ring complexes associated with non-peralkaline volcanics during pre-rifting, whereas in rift valleys they are more closely linked with peralkaline trachytes and pantellerites during initial rifting. However, abundance of comendites diminishes and they become virtually absent, and replaced by pantellerites, in well-developed, continued rifts where crustal attenuation is more extensive (c.f. Mohr, 1970; Bowden, 1974). Thus, it should be emphasized that pantelleritic volcanism is directly related to the extent of rifting. However, the more the rift evolves, the less the

abundance of peralkaline rhyolites, which are replaced by intermediate basalts between alkaline and tholeiitic nature, and minor trachytes. We suggest that, due to the predominance of comenditic products and the regional tectonic settings, Nemrut volcano bears imprints of intracontinental pre-rifting. Further scrutinized studies on the eastern Anatolian volcanoes, which seem compulsory in every manner, would help us to understand the developing magmatism in the region better. Finally, we suggest that following the slab break-off and the emplacement of asthenosphere contributed partial melts in the lower crust, both pre-existing shears and developing extensional features in Muş basin eased the formation of high level reservoirs, resulting in peralkaline magmatism in Nemrut volcano.

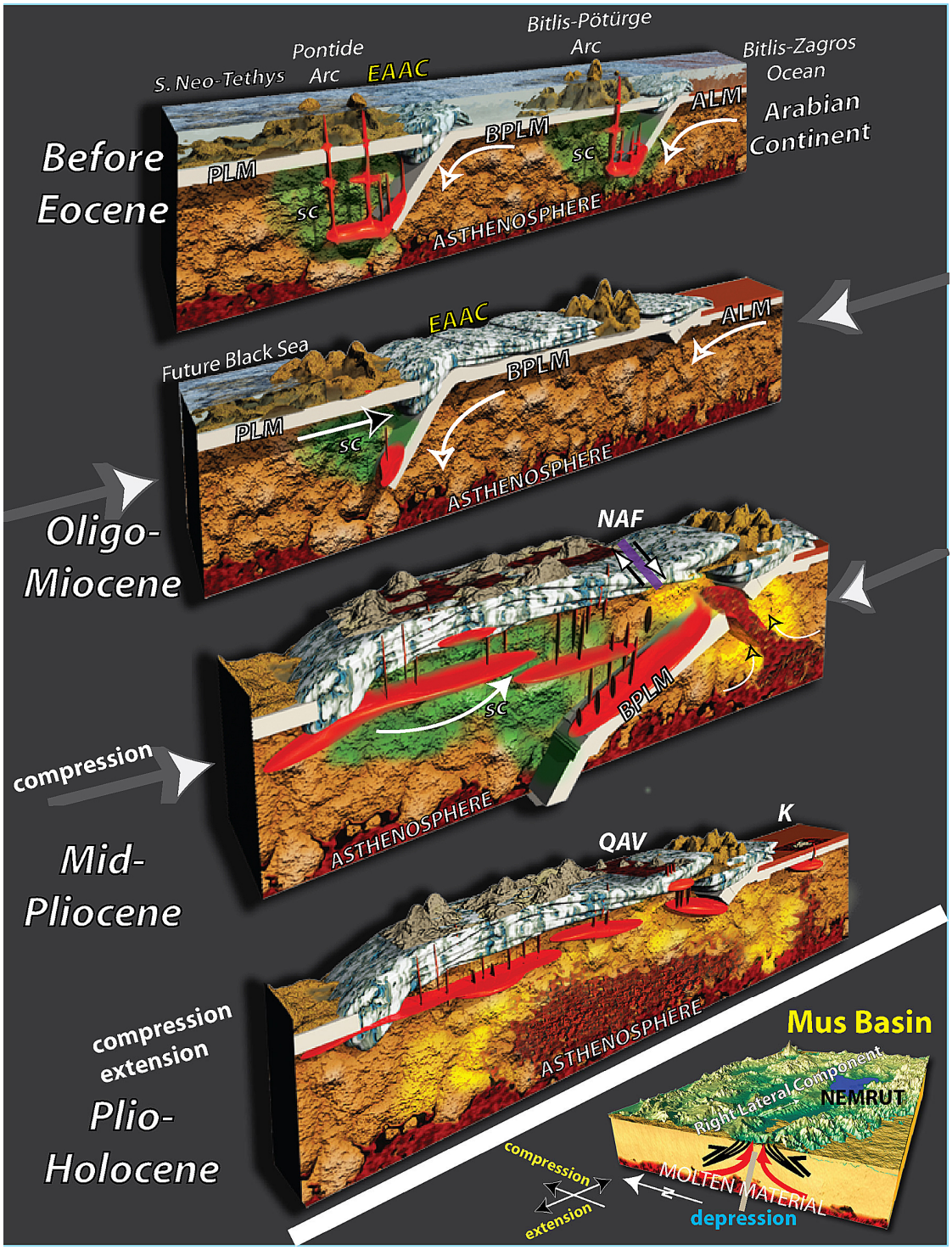

Figure 7.1: Block diagram of tectonic evolution of East Anatolia. Modified from Gülen (1984), Keskin (2003), Angus et al. (2006), Şengör et al. (2003). Under compression Arabian lithospheric mantle subducts under Bitlis - Pötürge Lithospheric Mantle. Arabian lithosphere ceases in Oligocene. Continuing collision leads EAAC (East Anatolian Accretionary Complex) to be formed. In mid-Pliocene Bitlis Pötürge Lithosphere gets steeper and breaks off accompanied with asthenospheric upwelling. During this time NAF and EAF were formed. In southeastern Anatolia, ramp basins attains strike slip component (Muş basin is also illustrated. From 6 Ma and on (Plio-Holocene), break-off causes asthenospheric mantle to interact with crust of EAAC.

7.2 Crystal Fractionation in a Stratified Shallow Magma Chamber

7.2.1 Shallow Magma Chamber

Mineralogical investigations of Nemrut eruptive units concerning phase equilibria depict that crystallization occurs in a low pressure shallow magma chamber. Besides, existence of small (<10 km in diameter) collapsed caldera indicates that the chamber have to be located in shallow levels.

Experimental studies suggest that peralkaline magmas in rift environments are indicative for differentiation under relatively low oxygen fugacity conditions in an extensional environment characterized by a high degree of crustal fracturing that allows rapid upward migration of mafic parental magmas and formation of shallow magma reservoirs (Caricchi et al., 2006). Experiments on anhydrous pantellerites from Eburru showed that at P<1 kbar, alkali feldspar is the sole phase on the liquidus; at ≈1 kbar, alkali feldspar is joined by quartz on the liquidus; and at P>1 kbar, quartz replaces alkali feldspar as the sole liquidus phase (Bailey et al., 1974; Ren et al., 2006). Nemrut eruptive units always bear alkali feldspar with occasional quartz and never quartz alone, suggesting that crystallization of Nemrut magmas, at least in the highly evolved liquids, should have occurred below 1 kbar pressure. Low oxygen fugacity and low temperature mineral assemblages (ferrorichterite, aenigmatite) reflect that the medium, in which such crystals are formed, should be under low pressures. Furthermore, a shallow chamber is implied by experiments which demonstrate that differentiation of mildly alkaline basalt at 1 kbar produces silica-saturated (pantelleritic) magmas whereas at moderate pressures, silica-undersaturated (phonolitic) magmas are produced (Mahood and Baker, 1986). Thus, isobaric phase equilibria modelling with a fixed pressure of 1 kbar realized in this study is consistent with the probable pressure conditions during crystallization.

Moreover, volcano-seismic data obtained from three seismometers (courtesy of Hacettepe University, Dept. Geological Engineering) dedicated to monitor the volcanic activity of Nemrut volcano indicates that shallow, magma chamber related volcanic earthquakes are concentrated within a depth range of 0 – 5 km; roughly corresponding to 1.5 kbar (Figure 7.2; lithostatic gradient ≈ 0.3kbar/km). Regarding the descent of roof of magma chamber after caldera collapse; we suggest that reservoir would probably be at shallower depths during pre-caldera stage, consistent with the findings and the assumptions for crystallization pressure stated above.

Hence, we suggest that one of the primary parameters for developing peralkaline magmatism is the existence of a shallow magma chamber, which is the case in Nemrut volcano. However, further studies on other Quaternary volcanoes of East Anatolia would reveal their reservoir characteristics, which, at this point, we only presume (due to their reported modal mineralogies) and believe to be different than those of Nemrut.

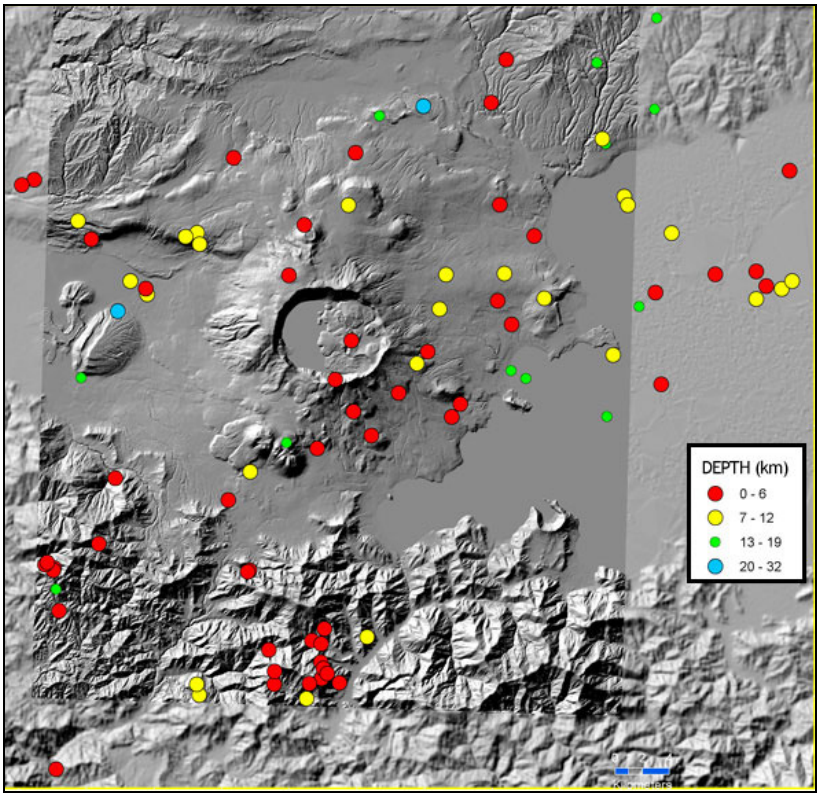

Figure 7.2: Focal points of volcanogenic earthquakes in Nemrut volcano and its vicinity. Data collected from October 2003 to October 2005 by Hacettepe University Geological Engineering Department Nemrut Monitoring Station.

7.2.2 Stratification of the Reservoir and Daly Gap

Regarding the compositional spectrum of mineral phases of all eruptive units and calculated intensive parameters of crystallization conditions, we suggest the existence of a compositionally and physically stratified magmatic reservoir (Chapter 5). Compositional zonation of the magmatic chamber is pronounced in caldera forming eruptive units which are somewhat compositionally inverted, highly evolved plinian fall being at the bottom, whereas the least evolved plinian at the top of the main Nemrut ignimbrite.

We also suggest that temperature, density, viscosity and oxygen fugacity in the magma chamber exhibit progressive variation from lower to upper zones of the chamber (Figure 7.3). Besides, we proposed the probable existence of a crystal rich (labradorite – andesine

plagioclase) layer between mafic and trachytic melts based on our evidence on benmoreitic enclaves.

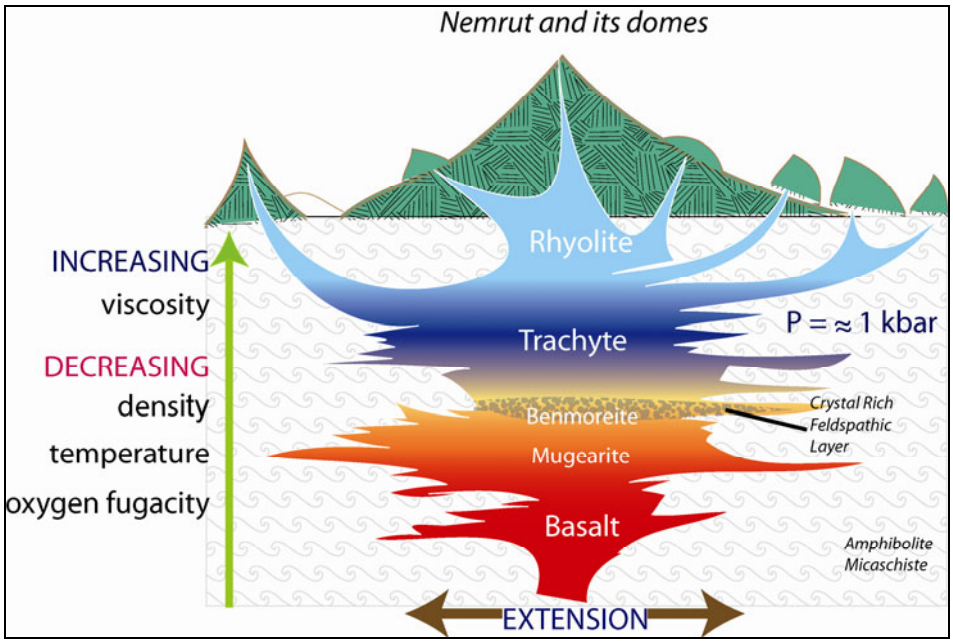

Figure 7.3: Schematic illustration of stratification of Nemrut magmatic reservoir

Assuming crystal fractionation is the continuous process in the chamber from basalt to more evolved liquids, several models have been realized using MELTS (Ghiorso and Sack, 1995). When a basaltic parent like sample N-258 is selected, density of the melt, crystallizing phases and their proportions to the total mass changes abruptly from basalt-mugearite to trachyte (Figure 7.4) in MELTS simulations. Density tends to increase at first but when the temperature falls below 1150 °C, a sharp decrease is observed (Figure 7.4.c). Besides, within the same temperature interval, mass of liquid also decreases with a sharp increase in total mass of crystallized phases (Figure 7.4.a, b). Yet, when the temperature decreases, mass of crystallizing phases and the remaining melt tend to decrease progressively. In a sense, this model is consistent with the observed mineralogical and petrographical textures: chaotic disequilibrium textures in benmoreitic enclaves, which represent the intermediate compositions in Nemrut volcanics. However, Mahood and Baker (1986) suggest that benmoreitic enclaves in Pantelleria are feldspathic cumulates and are not representative of intermediate magma compositions in the Daly Gap. Indeed, Nemrut benmoreitic enclaves (especially Type II) exhibit evidence for several generations of minerals with significant disequilibrium textures and deviant crystal chemistry (i.e. anorthoclase and trachytic ponds of plagioclase in benmoreites). This indicates that magma mixing/mingling is a major process in Daly Gap, occurring between basic and the acidic portions of the magma body, resulting with mingled/mixed benmoreites.

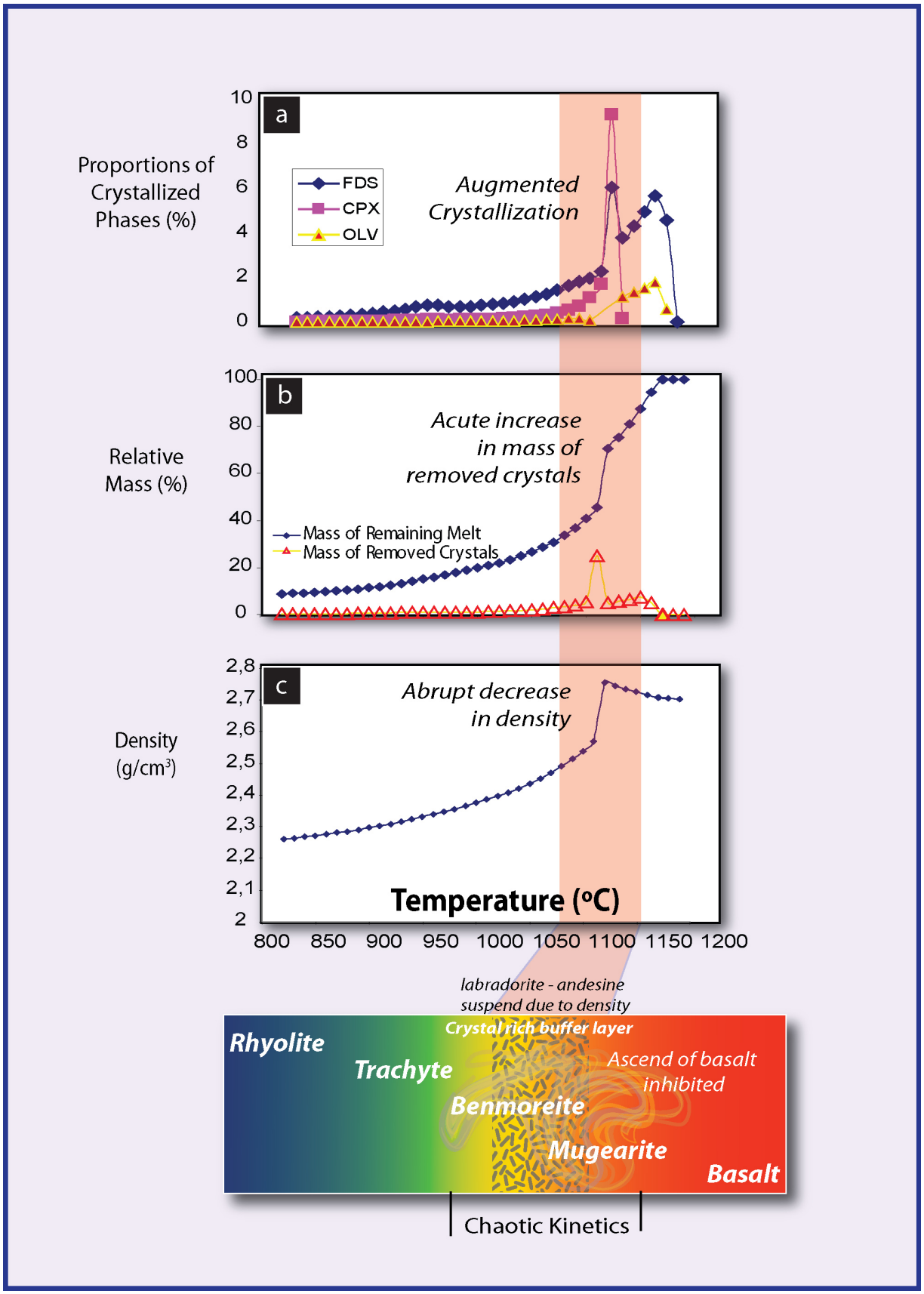

Figure 7.4: MELTS modeling of fractional crystallization (a) proportions of fractionating phases (b) Relative masses of removed crystals and remaining melt (c) Variation of density. Schematic setting of the magma chamber is also illustrated

Although fractionation of basalts produces a continuum of compositions, the problem of the absence or scarcity of intermediate rocks (Daly Gap) requires an explanation (Peccerillo et al., 2003). As we have proposed before, mass of residual liquid decreases sharply during transition towards the crystallization conditions of trachytic compositions, coinciding with the benmoreitic compositional field (Figure 7.4.b). These data, as previously suggested by Peccerillo et al (2003), point out that only little quantity of intermediate melt will be produced while fractionating basaltic magma pass rapidly through the intermediate stages.

To sum up; in a compositionally and physically stratified magma chamber, such as in the peralkaline Nemrut volcano, basalts would pond at the bottom and the most evolved rhyolites would occupy the top of the magma chamber, in which progressive decrease in temperature, density and an increase in viscosity towards the upper zones are observed. Undergoing fractionation, basalts would produce small amounts of intermediate melts only within a narrow temperature interval which is accompanied by augmented crystallization dominated by feldspar and clinopyroxene. Due to the density difference, these crystal rich layers would be stuck between trachytic and basaltic melts, where they are mingled/mixed with either basalt or trachyte. Finally, they are entrapped within evolved liquids due to probable pre-eruptive dynamic conditions and observed only as enclaves.

7.2.3 Fractional Crystallization

Petrogenetic models proposed to explain the generation of peralkaline felsic magmas include the evolution from alkali basaltic or mugearitic magmas by fractional crystallization (Nelson and Hegre, 1990; Mungall and Martin, 1995; Bohrson and Reid, 1997; Civetta et al 1998), which is probably associated with moderate assimilation of crust (Peccerillo et al., 2003), partial melting of lower crustal gabbros (Lowenstern and Mahood, 1991) and partial melting of heterogeneous source regions, including metasomatized subcontinental mantle (Bailey and Macdonald, 1987) and upper crustal lithologies (Davies and Macdonald, 1987; Macdonald et al, 1987; Black et al 1997). However, no experimental study of crustal anatexis has yet produced peralkaline melts (Scaillet and Macdonald, 2003).

Our mineralogical - geochemical data and realized mathematical models for crystal-liquid equilibria, major and trace elements, represent complete consistency with a differentiation process of fractional crystallization with moderate (r=0.3) assimilation of crustal material, from mildly alkaline transitional olivine basalt to comendite, at least for the continuous series of pre-caldera stage. Post-caldera comendites, on the other hand, exhibits systematic depletion in Zr, Nd and REE compared to the pre-caldera counterparts. We report modal

existence of REE-Ti silicate chevkinite with zircon in post-caldera comendites. As partition coefficients for REE in chevkinite exceeds 800, only 3% segregation of chevkinite alone from rhyolitic melt would effect the residual composition with a bulk KD ≈ 30. Hence, probable retention or segregation of chevkinite and zircon would likely to produce similar compositions observed in post-caldera comendites. It is also notable that post-caldera comendites have been affected from lesser degrees crustal contamination compared to pre-caldera counterparts.

7.3 Temporal / Petrological Evolution of Nemrut Volcano

According to the all findings obtained, interpreted and discussed in this study, we suggest the following evolution scenario for Nemrut volcano:

Upon the emplacement of asthenosphere induced partial melts into upper crust beneath Nemrut volcano, their ascension in high level storage reservoirs would have been eased by right lateral strike slip extension of pre-existing shears of Muş basin. The oldest rocks (~1.0 Ma) were slightly immature metaluminous trachytes/rhyolites, indicating their evolution has predated their eruption (SID: 1080). Meanwhile magma chamber should have evolved into stratified settings. Between 570 -160 ka (SID: 1070-1060), Nemrut volcano produced preferentially peralkaline trachytes and rhyolites, of which the degree of peralkalinity in some trachytes extends into pantelleritic affinity. This testifies that magma chamber has completely zoned and its upper levels, consisting of rhyolites and trachytes, were being continuously tapped, volatile content should have been increased. Peripheral doming has been intensified suggesting that magma chamber has expanding laterally, perhaps via extensional crack network, producing occasional distant domes (up to 18 km radii) with slightly assimilation modified trace element contents (i.e. elevated Cr contents of dome flows in Adabag peninsula). During 100 ka timespan (SID: 1050), mugearite have reached surface. However, the reason for the mugearitic flows can be controversial; either due to evacuation of the upper zones of the chamber by extensive felsic eruptions, or due to the distension of chamber boundaries helping low level mugearites to reach towards the surface via cracks. Subsequently, Nemrut continues to produce peralkaline rhyolites and trachytes with comenditic affinity (100 - 90 ka; SID: 1040). During this time interval, a relatively fresh batch of replenishment causes an acute change in chamber dynamics as an eruption trigger. This resulted in paroxysmal pyroclastic eruptions, which produced extensive ignimbritic flows (SID: 1030). According to our radiometric dating of preceding units, we suggest this pyroclastic activity should have likely to occur between 89 and 30 ka ago. Intense pyroclastic flows resulted in the evacuation of the magma chamber and thus, the collapse of the its roof

forming Nemrut caldera. Volcanic activity begins in intracaldera region with comenditic domes and flows (SID: 1020). Phreatomagmatic eruptions take place suggesting the existence of a water body in the caldera. Meanwhile N-S extending rift on the northern flank of the volcano has been formed, from which historic bimodal basalt -comendite eruption has occurred.

7.4 Suggestions

Although we have done our best to reveal the primary petrological features of Nemrut volcano, we believe there are still a plenty of research that can be carried out, as in all geological studies.

The more excursions on caldera walls, the more petrologic data for the evolution!

In order to define and investigate the effects of volatiles (F, Cl, S…) to magmatic evolution, mineral and whole rock chemistry should be extended to include such elements.

As the enclaves represent the only intermediate compositions produced dominantly by mixing/mingling of mafic and felsic melts, a scrutinized study and classification of enclaves should have been realized to improve our understanding the interrelations within the magmatic reservoir of peralkaline volcanoes and the existence of abundant enclaves. Investigating trace element behaviour and partitioning between mafic enclaves and felsic hosts along hybridized interfaces would be an interesting topic which provides chemical interactions that likely to occur in Daly Gap. Furthermore, TEM studies especially on the entrapped melt in destabilized plagioclases of benmoreites might provide clues for the causes of the formed discrepant mineral assemblages.

A more detailed stratigraphical sampling from ignimbrites would provide much more information than we would expect. Especially, pumices should be dated, thus proper sampling must be realized.

Petrological studies should be extended to cover Bitlis valley basalts, Incekaya tuff cone, Mazik dome, and the most importantly Bilican Volcano, which represents evident structural continuum with Nemrut in terms of N-S directed rifting.

Radar research on the floor of Van Lake would provide structural evidence of the regional tectonics, would help us understand the dynamic framework, and may shed light onto the causes of peralkaline volcanism in such context.

Although the anomalous Zr, REE, Nd content of post-caldera comendites can be well explained by chevkinite-zircon fractionation, it can be modeled whether partial melting of Nemrut cone forming trachytes that incorporated into magma chamber during caldera collapse would produce melts with similar geochemical characteristics.

Investigating the trace element contents of metamorphic xenoliths especially in ignimbrites would provide realistic estimations for the actual crustal contaminants.

Increasing the quantity of isotopic analyses would yield remarkable data for better assessing the petrological processes responsible for the origin, development and the evolution of peralkaline magmatism in Nemrut volcano.

7.5 Conclusions

1. Nemrut is a Quaternary peralkaline volcano situated at 12 km north of the Bitlis Suture, within a domain governed by collisional tectonics. It has an elliptical caldera with 6x8 km in diameter.
2. Its products form typical peralkaline series: mildly alkali transitional olivine basalt - mugearite - (peralkaline) trachyte - (peralkaline) rhyolite. Felsic rocks predominate, basaltic rocks are scarce and intermediate compositions are almost absent or confined to inclusions in evolved melts conforming to a Daly Gap.
3. Mineralogical studies depict that Nemrut volcano bears typical low pressure peralkaline mineral assemblages including aenigmatite, arfvedsonite, chevkinite, aegirine and fayalite. Phase equilibria emphasize a shallow magma chamber ≤ 1kbar pressure and low oxygen fugacity.
4. Calculated intensive crystallization parameters depict that the shallow magma chamber is compositionally stratified with a crystal-rich buffer layer with intermediate compositions between mafic and felsic melts.
5. The absence of intermediate compositions is ascribed to the rapid evolution of basalts through intermediate to felsic melts, accompanied with acute intense crystallization of plagioclase + clinopyroxene dominant assemblage.
6. Geochemical (major and trace) and mineralogical mathematical simulations depict that a protracted crystal fractionation dominated by alkali feldspar, clinopyroxene, olivine and Fe-Ti oxides with varying but significant degrees of crustal assimilation would produce peralkaline rhyolites from the actual basalt is taken as parent.
7. Trace element contents and Sr-Nd isotopic ratios indicate that Nemrut magmas have been derived from a slightly subduction modified asthenospheric mantle with slight crustal assimilation.
8. The genesis of Nemrut peralkaline magmatism in this collisional context has been ascribed to the penetration and ascension of asthenospheric partial melts into upper crustal high level reservoirs under Muş ramp basin, whose pre-existing shears have gained strike slip component thus leading localized extensions where Nemrut volcano has been located.
9. Our radiometric data indicates that the age of Nemrut caldera collapse is younger than 89 ka, which is also younger than hitherto believed.

APPENDIX

Sample	Description	X	Y	Maj	Trc	WDS	isotp
N-001	lithic fragment from phreatomagmatic deposit.			☐	☐	☐	☐
N-002	Felsic lithic fragment from phreatomagmatic deposi			☐	☐	☐	☐
N-003	Welded Ignimbrite			☐	☐	☐	☐
N-004	Welded Ignimbrite			☐	☐	☐	☐
N-005	Pumiceous transition between enclave and rhyolite			☐	☐	☐	☐
N-006	Historic basalt			☐	☐	☐	☐
N-007	Rif zone obsidian + enclave	258664	4284739	☐	☐	☐	☐
N-008	Rif zone obsidian + enclave	258604	4285023	☐	☐	☐	☐
N-009	Welded ignimbrite	258575	4284885	☐	☐	☑	☐
N-010	Rhyolite in the rift zone	258664	4284739	☑	☑	☐	☑
N-011	Pumiceous rhyolite + enclave	258672	4284313	☐	☐	☑	☐
N-012	Rhyoliye with abundant enclaves	258838	4283643	☐	☐	☐	☐
N-013	Enclave of N-014	258872	4284394	☑	☑	☐	☐
N-014	Aphyric rhyolite glass	258872	4284394	☑	☑	☐	☐
N-015	Felsic Lava flow	259199	4284793	☐	☐	☐	☐
N-016	Mafic lava flov wi	258936	4270139	☑	☑	☑	☑
N-017	ignimbrite	258936	4270139	☐	☐	☐	☐
N-018	Outer shell of glassy rhyolite flow	254318	4273327	☐	☐	☐	☐
N-019	Pumiceous - fibrious? İnner zone of rhyolite	254318	4273327	☐	☐	☐	☐
N-020	Bottom pumice of plinian underlying ignimbrite	253517	4273346	☐	☐	☑	☐
N-021	Middle pumice of plinian underlying ignimbrite	253517	4273346	☐	☐	☐	☐
N-022	upper pumice of plinian underlying ignimbrite	253517	4273346	☑	☑	☑	☐
N-023	ignimbrite	253517	4273346	☐	☐	☑	☐
N-024	trachytic lava flow	253094	4273720	☐	☐	☐	☐
N-025	Base surge sequence (with sub-samples)			☐	☐	☐	☐
N-026	Rheomorphic ignimbrite?			☐	☐	☐	☐
N-027	Aphyric glassy rhyolite (obsidian)			☐	☐	☐	☐
N-028	Base surge sequence (with sub-samples)			☐	☐	☐	☐
N-029	Crystal-rich glassy rhyolite	262623	4276696	☐	☐	☐	☐
N-030	Vesicular glassy obs.	262524	4276639	☐	☐	☐	☐
N-031	Obsidian	262468	4276557	☐	☐	☐	☐
N-032	fluvial banded obsidian.	262419	4276507	☑	☐	☐	☐
N-033	Enclave of N-032	262290	4276546	☑	☐	☐	☐
N-034	Aphyric glassy rhyolite	262122	4276384	☐	☐	☐	☐
N-035	Obsidian with scacr fluvial bands	261904	4276292	☑	☐	☐	☐
N-036	Plinian pumice overlying Ignimbrite	260291	4271498	☑	☑	☑	☐
N-037	Juvenile clast from ignimbrite	260291	4271498	☑	☑	☑	☐
N-038	Plinian Pumice underlying ignimbrite.	260291	4271498	☐	☐	☐	☐
N-039	Pumice Flow (lahar-like)	260471	4270412	☐	☐	☐	☐
N-040	Lithic fragment from Nueé?	266229	4268353	☐	☐	☐	☐
N-041	Pumice	271841	4275772	☐	☐	☐	☐
N-042	Pumice	271457	4275867	☐	☐	☐	☐
N-043	Plinian Pumice underlying ignimbrite.	270168	4273674	☐	☐	☐	☐
N-044	Ignimbrite	271528	4272686	☐	☐	☐	☐
N-045	White pumice (plinian)	265738	4273627	☐	☐	☐	☐
N-046	Dark colored pumice (plinian)	265738	4273627	☑	☑	☐	☐
N-047	Dark pumice from dark colored sub-plinian under ig	264738	4269483	☐	☐	☑	☐
N-048	ignimbrite	264738	4269483	☐	☐	☐	☐
N-049	Juvenile fragment from Incekaya tuff cone	276132	4261403	☐	☐	☐	☐
N-050	Enclave of post-caldera rhyolite (N-050)	260567	4280781	☑	☑	☑	☐
N-051	Post-caldera aphyric rhyolite (obs)	260567	4280781	☑	☑	☑	☑
N-052	Altered obsidian with spherulites	260567	4280781	☐	☐	☐	☐

Sample	Description	X	Y	Maj	Trc	WDS	isotp
N-053	Complete alteration of obsidian	260567	4280781	☐	☐	☐	☐
N-054	Breccia	260351	4279491	☐	☐	☐	☐
N-055	Fragment within N-55	260351	4279491	☐	☐	☐	☐
N-056	Spherulitic obsidian	261357	4277818	☐	☐	☐	☐
N-057	Completely altered obsidian	261357	4277818	☐	☐	☐	☐
N-058	Aphyric rhyolite (obsidian)	260624	4278795	☐	☐	☐	☐
N-059	Aphyric rhyolite (obsidian)	260705	4278668	☐	☐	☐	☐
N-060	Scoria overlying base surge	263724	4279690	☐	☐	☐	☐
N-061	Outer shell zone of rhyolite (obs) flow	262421	4276022	☐	☐	☐	☐
N-062	Pre-caldera lava flow	261977	4275889	☐	☐	☑	☐
N-063	Obsidian	261690	4275872	☑	☐	☐	☐
N-064	Pre-caldera lava flow	260705	4278668	☑	☑	☑	☐
N-065	Rhyolite dome (north)	260570	4277411	☑	☑	☑	☐
N-066	Rhyolite glass dome	261945	4279049	☐	☐	☐	☐
N-067	Rhyolite glass dome	261945	4279049	☐	☐	☐	☐
N-072	ignimbirite	249804	4270603	☐	☐	☐	☐
N-073	altered intrusion	253189	4271897	☐	☐	☐	☐
N-074	Ignimbrite with obsidian fragments	253263	4271847	☐	☐	☐	☐
N-075	Lava Flow	253840	4271443	☐	☐	☐	☐
N-076	Dome flow of Kirkor	253750	4271518	☐	☐	☑	☐
N-077	Dome flow of Kirkor	253812	4271885	☐	☐	☐	☐
N-078	Glassy rhyolite bottom section	253986	4273795	☐	☐	☐	☐
N-079	Glassy rhyolite upper section	253986	4273795	☐	☐	☐	☐
N-080	Trachytic lava flow	253848	4273173	☑	☑	☑	☑
N-081	Dark colored ignimbrite	255045	4274143	☐	☐	☐	☐
N-082	Scarlet-red ignimbrite	255045	4274143	☐	☐	☐	☐
N-083	Pre-caldera trachytic lava flow	255178	4274371	☐	☐	☑	☐
N-084	Pre-caldera trachytic lava flow			☐	☐	☐	☐
N-085	Pre-caldera trachytic lava flow	258179	4271834	☐	☐	☐	☐
N-086	Pre-caldera glassy lava flow (rhyolite)	258655	4272225	☐	☐	☐	☐
N-087	Peripheral felsic dome flow	259627	4271526	☐	☐	☐	☐
N-088	Peripheral felsic dome flow	259650	4271606	☐	☐	☐	☐
N-089	Ash	258307	4269245	☐	☐	☐	☐
N-090	ignimbirite	256062	4271489	☐	☐	☐	☐
N-091	Aphyric rhyolite (obsidian)	261953	4273066	☐	☐	☐	☐
N-092	Aphyric rhyolite (obsidian)	262163	4274061	☑	☑	☐	☐
N-093	Coulmnar jointed trachyte	263279	4280378	☐	☐	☐	☐
N-094	Aphyric rhyolite (obsidian)	263951	4280829	☐	☐	☐	☐
N-095	Phreatomagmatic ash	264165	4281451	☐	☐	☐	☐
N-096	Base surge sequence over ignimbrite.	264165	4281451	☐	☐	☐	☐
N-097	Pumice	264165	4281451	☐	☐	☐	☐
N-098	Aphyric rhyolite (obsidian)	263991	4282132	☑	☑	☑	☑
N-099	Crystalline trachyte-rhyolite	263991	4282132	☐	☐	☐	☐
N-100	ignim.	263991	4282132	☐	☐	☐	☐
N-101	Lithic fragment from ignimbrite	265144	4283262	☐	☐	☐	☐
N-102	Aphyric rhyolite (obsidian)	277958	4283768	☐	☐	☐	☐
N-103	Aphyric rhyolite (obsidian)	269398	4270400	☐	☐	☐	☐
N-104	ignimbrite (direction marked)	257944	4268462	☐	☐	☐	☐
N-105	ignimbirite			☐	☐	☐	☐
N-106	Crystalline trachyte-rhyolite lava flow			☐	☐	☐	☐
N-107	Crystalline trachyte-rhyolite lava flow			☐	☐	☐	☐
N-108	Pre-caldera trachyte lava			☐	☐	☐	☐

Sample	Description	X	Y	Maj	Trc	WDS	isotp
N-109	Pre-caldera trachyte lava			☐	☐	☐	☐
N-110	Pre-caldera trachyte lava			☐	☐	☐	☐
N-111	Pre-caldera trachyte lava			☐	☐	☐	☐
N-112	Pre-caldera lava			☐	☐	☐	☐
N-113	Pre-caldera alterated intrusion			☐	☐	☐	☐
N-114	Trachyte lava flow			☐	☐	☐	☐
N-115	Glassy lenticules within trachyte			☐	☐	☐	☐
N-116	Lava flow - trachyte			☐	☐	☐	☐
N-117	Lava flow -trachyte			☐	☐	☐	☐
N-118	Oxidized samples			☐	☐	☐	☐
N-119	Intensively altered lava flow			☐	☐	☐	☐
N-120	Aphyric rhyolite (obsidian)			☐	☐	☐	☐
N-121	İgnimbirite			☐	☐	☐	☐
N-122	Rhyolitic Dome flow			☐	☐	☐	☐
N-123	Hidrotermally altered rock (unrecognizable)			☐	☐	☐	☐
N-124	Trachyte lava flow			☐	☐	☐	☐
N-125	Rhyolitic dome flow			☐	☐	☐	☐
N-126	Hidrotermally altered Dome			☐	☐	☐	☐
N-127	Holocrystalline fragment from post-caldera phreato.			☐	☐	☐	☐
N-128	Rhyolitic Dome	261130	4279092	☐	☐	☐	☐
N-129	Holocrystalline fragment from post-caldera phreato.	261130	4279092	☐	☐	☐	☐
N-130	Rhyolitic Dome	259765	4280951	☐	☐	☐	☐
N-131	Rhyolitic Dome	259707	4280794	☑	☑	☐	☐
N-132	İgnimbirite	260675	4270637	☐	☐	☐	☐
N-133	Pumice	260438	4270969	☐	☐	☐	☐
N-134	İgnimbirite	260427	4271730	☐	☐	☐	☐
N-135	Trachytic lava flow	257273	4280569	☑	☑	☑	☐
N-136	Trachytic lava flow	257273	4280569	☑	☑	☑	☐
N-137	Trachytic dyke			☐	☐	☐	☐
N-138	Trachytic lava flow on caldera wall	256514	4279116	☐	☐	☐	☐
N-139	Contact zone between dyke and host trachyte	256455	4278815	☐	☐	☐	☐
N-140	Trachytic dyke	256455	4278815	☐	☐	☐	☐
N-141	Trachytic host	256455	4278815	☑	☑	☐	☐
N-142	İgnimbiritic debris	256455	4278815	☐	☐	☐	☐
N-143	İgnimbiritic debris	256487	4278326	☐	☐	☐	☐
N-144	Vitriphied lamellae under trachytic lava flow	256487	4278326	☐	☐	☐	☐
N-145	Trachytic lava flow	256487	4278326	☐	☐	☐	☐
N-146	Rhyolite flow	257270	4277624	☑	☐	☑	☐
N-147	Phreatomagmatic	257255	4276479	☐	☐	☐	☐
N-148	Aphyric rhyolite (obsidian)	257255	4276479	☐	☐	☐	☐
N-149	Trachytic lava flow	257665	4276154	☑	☑	☑	☑
N-150	Breccia	257665	4276154	☐	☐	☐	☐
N-151	Trachytic dyke	258125	4276127	☑	☑	☑	☑
N-152	Enclave? in Trachytic dyke	258125	4276127	☐	☐	☐	☐
N-153	Trachytic lava flow	258307	4276085	☐	☐	☐	☐
N-154	Trachytic dyke	258614	4276012	☐	☐	☐	☐
N-155	İgnimbirite	264190	4281205	☐	☐	☐	☐
N-156	İgnimbirite	264161	4281434	☐	☐	☐	☐
N-157	Pumice	264199	4282027	☐	☐	☐	☐
N-158	İgnimbirite	266378	4284303	☐	☐	☐	☐
N-159	İgnimbirite	266378	4284303	☐	☐	☐	☐
N-160	Trachytic lava flow	278028	4283062	☐	☐	☐	☐

Sample	Description	X	Y	Maj	Trc	WDS	isotp
N-161	Trachytic lava flow	278028	4283062	☐	☐	☐	☐
N-162	Trachytic lava flow	278421	4282623	☑	☑	☐	☐
N-163	Trachytic lava flow	278421	4282623	☐	☐	☐	☐
N-164	Scoraceous zone in N-163	278421	4282623	☐	☐	☐	☐
N-165	Pumice	276592	4279501	☐	☐	☐	☐
N-166	Pumice	276592	4279501	☐	☐	☐	☐
N-167	Pumice	276592	4279501	☐	☐	☐	☐
N-168	Pumice	276592	4279501	☐	☐	☐	☐
N-169	Pumice	276592	4279501	☐	☐	☐	☐
N-170	Scoria	279559	4278982	☐	☐	☐	☐
N-171	Trachytic-Rhyolitic lava flow	279559	4278982	☐	☐	☐	☐
N-172	Glassy banded rhyo-trachytic lava flow	273546	4273927	☑	☑	☐	☐
N-173	Pumice	272735	4274018	☐	☐	☐	☐
N-174	Trachytic lava flow	272143	4276033	☐	☐	☐	☐
N-175	Glassy rhyolitc dome	269202	4273364	☐	☐	☐	☐
N-176	İgnimbirite	266508	4274361	☐	☐	☐	☐
N-177	Glassy rhyolitc dome	265854	4274403	☐	☐	☐	☐
N-178	Glassy rhyolitc dome	265854	4274403	☑	☐	☐	☐
N-179	İgnimbirite	271744	4274113	☐	☐	☑	☐
N-180	Pumice	271744	4274113	☐	☐	☐	☐
N-181	Trachytic lava flow	270245	4271721	☑	☑	☑	☑
N-182	Trachytic lava flow	269412	4269985	☐	☐	☐	☐
N-183	İgnimbirite	268971	4268940	☐	☐	☐	☐
N-184	(Glassy) rhyolitc dome	264467	4269357	☑	☐	☑	☐
N-185	(Glassy) rhyolitc dome	263218	4271055	☑	☑	☐	☐
N-186	Trachytic lava flow	261938	4268215	☐	☐	☑	☐
N-187	Trachytic lava flow (glassy part)	261938	4268215	☐	☐	☐	☐
N-188	Trachytic lava flow	260967	4270130	☑	☑	☑	☐
N-189	Glassy Rhyolite flow	262043	4274480	☐	☐	☐	☐
N-190	Altered spherulitic obsidian	262043	4274480	☐	☐	☐	☐
N-191	Vesicular basaltic? Pre-caldera lava -disequilibrium	259199	4271599	☑	☐	☐	☐
N-192	İgnimbirite	257882	4271855	☐	☐	☐	☐
N-193	Vesicular basaltic? Pre-caldera lava -disequilibrium	257875	4272084	☐	☐	☐	☐
N-194	Trachytic lava flow	256788	4274148	☑	☐	☑	☐
N-195	Trachytic lava flow (pumiceous)	256788	4274148	☐	☐	☐	☐
N-196	Trachytic lava flow	257412	4274038	☐	☐	☐	☐
N-197	Trachytic lava flow	257412	4274038	☐	☐	☑	☐
N-198	Vitric fragment within ignimbrite	257777	4273249	☐	☐	☐	☐
N-199	ignimbrite	257777	4273249	☐	☐	☐	☐
N-200	ignimbrite	257777	4273249	☐	☐	☐	☐
N-201	ignimbrite	257777	4273249	☐	☐	☐	☐
N-202	Scarlet - reddish ignimbrite	257904	4273327	☐	☐	☐	☐
N-203	Reddish-brown ignimbrite	255590	4273586	☐	☐	☐	☐
N-204	ignimbrite	254126	4272866	☐	☐	☐	☐
N-205	Ash	253883	4272953	☐	☐	☐	☐
N-206	ignimbrite	250817	4272284	☐	☐	☐	☐
N-207	Trachytic Lava flow (Kirkor Dome)	250856	4272170	☐	☐	☐	☐
N-208	ignimbrite	249751	4270418	☐	☐	☐	☐
N-209	Vesicular basaltic? Pre-caldera lava -disequilibrium	248134	4270434	☑	☑	☑	☑
N-210	Pumice	249047	4269534	☐	☐	☐	☐
N-211	ignimbrite	249047	4269534	☐	☐	☐	☐
N-212	Metamorphic basement - micaschist	252491	4266032	☐	☐	☐	☐

Sample	Description	X	Y	Maj	Trc	WDS	isotp
N-213	Limestone?	252491	4266032	☐	☐	☐	☐
N-214	ignimbrite	252595	4266150	☐	☐	☐	☐
N-215	ignimbrite	252595	4266150	☐	☐	☐	☐
N-216	ignimbrite	252595	4266150	☐	☐	☐	☐
N-217	Trachytic banded lava flow			☐	☐	☐	☐
N-218	Trachytic banded lava flow (aphyric-vitric section)			☐	☐	☐	☐
N-219	Trachytic banded lava flow (crystalline section)			☐	☐	☐	☐
N-220	Holocrystalline ejecta within phreat. Base surge.			☑	☑	☑	☑
N-221	Trachytic Lava + its enclave	260523	4280818	☐	☐	☐	☐
N-222	Enclave of N-221	260523	4280818	☑	☐	☐	☐
N-223	Trachytic banded lava flow	264229	4277608	☐	☐	☐	☐
N-224	Trachytic banded lava flow	264229	4277608	☑	☐	☐	☐
N-225	Trachytic Lava + its enclave	264145	4277577	☐	☐	☐	☐
N-226	Enclave of N-225	264145	4277577	☐	☐	☐	☐
N-227	Trachytic lava flow	264093	4277568	☑	☑	☑	☐
N-228	Transition zone into aphyric lava flow (upper zone)	262586	4275733	☐	☐	☑	☐
N-229	Transition zone into aphyric lava flow (lower zone)	262685	4275780	☐	☐	☑	☐
N-230	Crystalline trachytic lava flow with fluvial bands	262647	4275728	☐	☐	☐	☐
N-231	Trachytic lava flow	262337	4273861	☐	☐	☐	☐
N-232	Black pumice in black-brown ignimbrite	262251	4267705	☑	☐	☐	☐
N-233	Black pumice in yellowish ignimbrite	262251	4267705	☐	☐	☑	☐
N-234	ignimbrite	262251	4267705	☐	☐	☐	☐
N-235	ignimbrite	262251	4267705	☐	☐	☐	☐
N-236	ignimbrite	248627	4283118	☐	☐	☐	☐
N-237	Scoria	248627	4283118	☐	☐	☐	☐
N-238	Trachytic lava flow	249849	4285325	☑	☐	☐	☑
N-239	Trachytic lava flow	249849	4285325	☑	☑	☑	☐
N-240	Aphyric intermediate? lava flow	248751	4285789	☑	☑	☑	☐
N-241	ignimbrite	248751	4285789	☐	☐	☐	☐
N-242	ash	248751	4285789	☐	☐	☐	☐
N-243	ignimbrite	264582	4283439	☐	☐	☐	☐
N-244	ignimbrite	264251	4283169	☐	☐	☐	☐
N-245	Trachytic lava flow	264251	4283169	☐	☐	☐	☐
N-246	Aphyric glassy rhyolite flow	264251	4283169	☐	☐	☑	☐
N-247	ignimbrite	264251	4283169	☐	☐	☑	☐
N-248	ignimbrite	264251	4283169	☐	☐	☑	☐
N-249	ignimbrite	264126	4284490	☐	☐	☐	☐
N-250	ignimbrite	264126	4284490	☐	☐	☐	☐
N-251	ignimbrite	264126	4284490	☐	☐	☐	☐
N-252	Scoria in N-251	264126	4284490	☐	☐	☐	☐
N-253	Glassy Rhyolite dome	264224	4284874	☐	☐	☐	☐
N-254	Glassy Rhyolite flow	258948	4287309	☑	☑	☑	☐
N-255	Glassy Rhyolite flow	258904	4287467	☑	☐	☑	☐
N-256	Mafic enclave within N-255	258904	4287467	☑	☑	☑	☐
N-257	Historic basalt flow	258904	4287467	☐	☐	☑	☐
N-258	Historic basalt flow	258771	4287477	☑	☑	☑	☑
N-259	Welded ignimbrite	260133	4282071	☐	☐	☑	☐
N-260	Fall-back (caldera wall)	260133	4282071	☐	☐	☐	☐
N-261	Fall-back (caldera wall)	260133	4282071	☐	☐	☐	☐
N-262	Glassy fiamme in ignimbrite	260133	4282071	☐	☐	☐	☐
N-263	?	260139	4282198	☐	☐	☐	☐
N-264	Historic basalt flow	260139	4282198	☑	☑	☑	☑

Sample	Description	X	Y	Maj	Trc	WDS	isotp
N-265	ignimbrite	252743	4262789	☐	☐	☐	☐
N-266	ignimbrite	252335	4262218	☐	☐	☐	☐
N-267	ignimbrite	248277	4255425	☐	☐	☐	☐
N-268	ignimbrite	248277	4255425	☐	☐	☑	☐
N-269	Ash			☐	☐	☐	☐
N-270	Lav	260463	4272190	☐	☐	☐	☐
N-271	Lav	261007	4272778	☐	☐	☐	☐
N-272	Porphyritic ejecta within phreatomagmatic	261248	4277456	☑	☑	☑	☑
N-273	Pomza	261248	4277456	☐	☐	☐	☐
N-274	Altered glassy rhyolite (obsidian)	261248	4277456	☐	☐	☐	☐
N-275	Porphyritic ejecta within phreatomagmatic	263839	4276836	☐	☐	☐	☐
N-276	Trachytic ejecta within phreatomagmatic	263839	4276836	☐	☐	☐	☐
N-277	Scoraceous fragment from fall back			☐	☐	☐	☐
N-278	Pale colore fall back			☐	☐	☐	☐
N-279	Vitric fragment within dark plinian			☐	☐	☐	☐
N-280	Basic fragment within dark colored fall back			☐	☐	☐	☐
N-281	Trachytic dome/lava flow - Adabag	280398	4278520	☑	☑	☑	☐
N-282	ignimbrite			☐	☐	☐	☐
N-305	Pumice from phreatomagmatic	261542	4278267	☑	☑	☑	☑

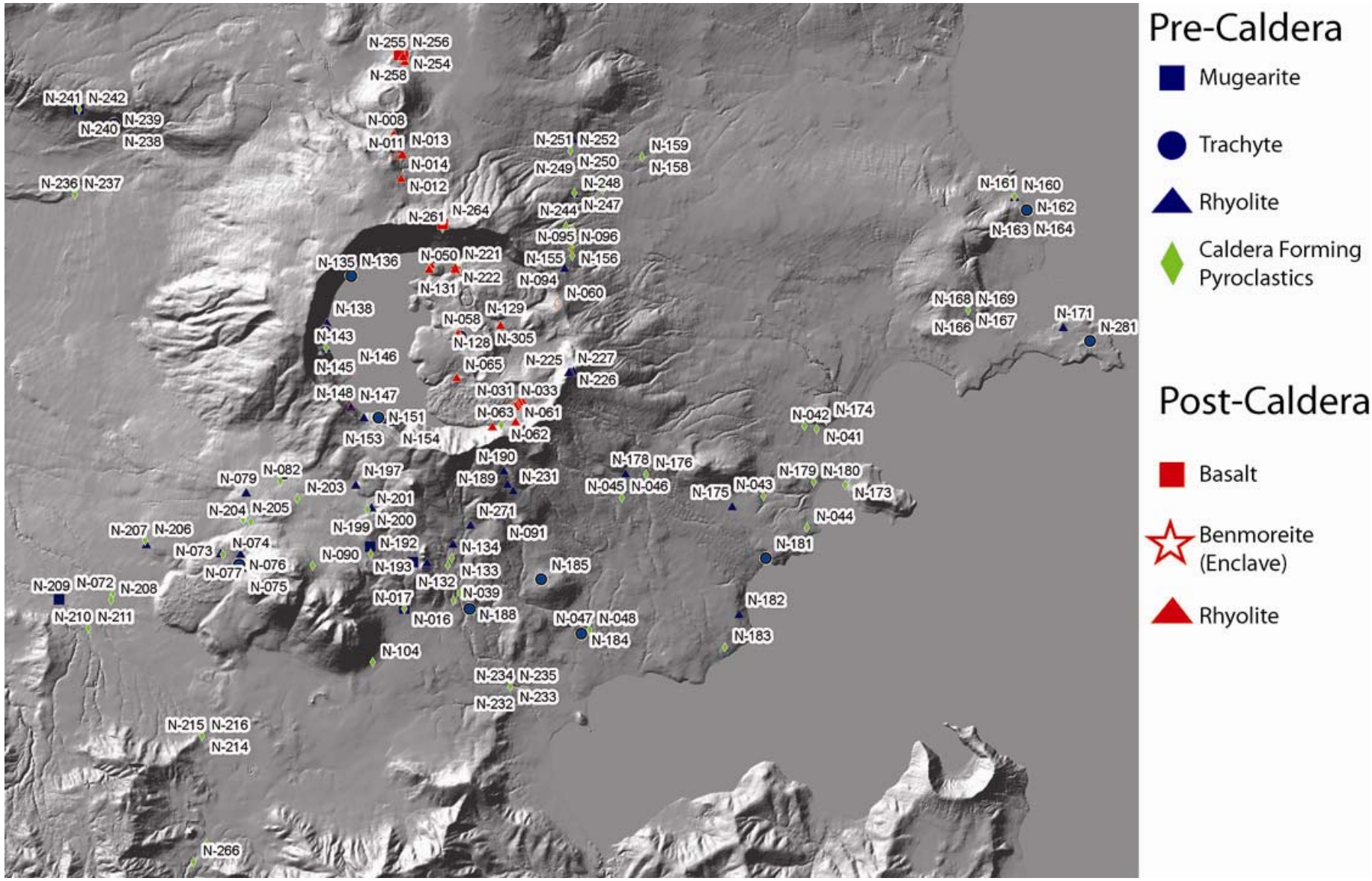

Appendix-2: Sample Locations

REFERENCES

Al-Lazki, A., Seber, D., Sandvol, E., Turkelli, N., Mohamad, R. & Barazangi, M. (2003). Tomographic Pn velocity and anisotropy structure beneath the Anatolian plateau (eastern Turkey) and the surrounding regions. *Geophysical Research Letters* **30** (24).

Andersen, D. J., Lindsley, D. H. & Davidson, P. M. (1993). QUILF: a Pascal program to assess equilibria among Fe–Mg–Ti oxides, pyroxenes, olivine and quartz. *Computers and Geosciences* **19**, 1333–1350.

Angus, D. A., Wilson, D.C., Sandvol, E. & Ni, J. F. (2006). Lithospheric structure of the Arabian and Eurasian collision zone in eastern Turkey from S-wave receiver functions *Geophysical Journal International* **166** (3). 1335–1346.

Arth, J.G., 1976. Behaviour of trace elements during magmatic processes — a summary of theoretical models and their applications. *J. Res. U. S. Geol. Surv.* **4**, 41– 47.

Atasoy, E., Terzioğlu, N. & Mumcuoğlu, Ç. (1989). Nemrut Volkanı Jeolojisi ve Jeotermal Olanakları, *TPAO Arama Grubu Başkanlığı, Rapor No*:**393**, (unpublished)

Avanzinelli, R., Bindi, L., Menghetti, S. & Conticelli, S. (2004). Crystallisation and genesis of peralkaline magmas from Pantelleria Volcano, Italy: an integrated petrological and crystal-chemical study. *Lithos* **73**, 41–69.

Aydar, E., Gourgaud, A., Ulusoy, I., Digonnet, F., Labazuy, P., Sen, E., Bayhan, H., Kurttas¸, T. & Tolluoğlu, A.Ü. (2003). Morphological analysis of active Mount Nemrut stratovolcano, eastern Turkey: evidences and possible impact areas of future eruption. *Journal of Volcanology and Geothermal Research* **123**, 301– 312.

Bailey, D. K. (1974). Origin of alkaline magmas as a result of anatexis. In: Sorensen, H. (ed.) *Alkaline Rocks*. New York: JohnWiley, pp. 427–442.

Bailey, D.K. & Macdonald, R. (1987). Dry peralkaline felsic liquids and carbon dioxide flux through the Kenya rift zone. In: Mysen BO (ed) Magmatic processes: physiochemical principles. *Geochem Soc Spec Publ* **1**:91–105

Baker, B.H. (1987). Outline of the petrology of the Kenya rift alkaline province. In: Fitton, J.G. & Upton, B.G.J. (eds) Alkaline Igneous Rocks. *Geological Society London Special Publications* **30**, 293-311.

Beattie, P., Drake, M., Jones, J., Leeman, W., Longhi, J., McKay, G., Nielsen, R., Shaw, D., Takahashi, E. & Watson, B., 1993. Terminology for trace-element partitioning. *Geochimica et Cosmochimica Acta* **57**, 1605-1606.

Bigazzi, G., Yeğingil, Z., Ercan, T., Oddone, M. & Özdoğan, M. (1993). New data for the chronology of central and northern Anatolia by fission track dating of obsidians. Bulletin Volcanologique 55, 588– 595.

Black, R., Lameyre, J. & Bonin, B. (1985). The structural setting of alkaline complexes. *Journal of African Earth Sciences* **3**. 5–16.

Black, S., Macdonald, R. & Kelly, M. R. (1997). Crustal origin of peralkaline rhyolites from Kenya: evidence from U-series disequilibria and Th-isotopes. *Journal of Petrology* **38**, 277-297.

Bohrson, W.A. & Spera, F.J. (2001). Energy-constrained open-system magmatic processes: II. Application of energy-constrained assimilation- fractional crystallization (EC-AFC) model to magmatic systems. *Journal of Petrology* **42**, 1019– 1041.

Bohrson, W.A.& Reid, M.R. (1997). Genesis of silicic peralkaline volcanic rocks in a ocean island setting by crustal melting and open system processes: Socorro Island, Mexico. *Journal of Petrology* **38**, 1137– 1166.

Bonin, B. (2004). Do coeval mafic and felsic magmas in postcollisional to within-plate regimes necessarily imply two contrasting, mantle and crustal, sources? A review. *Lithos* **78**, 1–24.

Bowden, P. (1974). Oversaturated alkaline rocks: granites, pantellerites and comendites. In: Sørensen, H. (Ed.), The *Alkaline Rocks. A Wiley-Interscience Publication. John Wiley and Sons, London- New York*, pp. 109–123.

Bozkurt E., Winchester J.A. & Piper J.D.A. (2000). Tectonics and Magmatism in Turkey and the Surrounding Area, vol 173. *Geological Society of London*. London, United Kingdom, pp 489–512

Bryan, W. B., Finger, L.W. & Chayes, F. (1969). Estimating proportions in petrographic mixing equations by least-squares approximation. *Science* **163**, 926–927.

Buddington, A. F. & Lindsley, D. H. (1964). Iron-titanium oxide minerals and synthetic equivalents. *Journal of Petrology* **5**, 310-357.

C – Ç – D

Caricchi, L., Ulmer, P. & Peccerillo, A. (2006). A high-pressure experimental study on the evolution of the silicic magmatism of the Main Ethiopian Rift, *Lithos* **91**, 46-58.

Carmichael, I.S.E. (1967): The iron–titanium oxides of salic volcanic rocks and their associated ferromagnesian silicates. *Contributions to Mineralogy and Petrology* **14**, 36-64.

Caroff, M., Maury, R. C., Leterrier, J., Joron, J. L. & Cotten, J. (1993). Trace element behavior in the alkalic basalt comenditic trachyte series from Mururoa atoll, French Polynesia. *Lithos* **30**, 1-22.

Cassignol, C. & Gillot, P.Y. (1982). Range and effectiveness of unspiked potassium–argon dating: experimental groundwork and applications. In: Odin, G.S. (Ed). *Numerical Dating in Stratigraphy. Wiley, Chichester*, pp. 159–179.

Christiansen, R. L. & Lipman, P. W. (1972). Cenozoic volcanism and plate-tectonic evolution of the Western United States. II Late Cenozoic: *Royal Society of London Philosophical Transactions A* **271**, p. 249-284.

Civetta, L., Cornette, Y., Crisci, G., Gillot, P.-Y., Orsi, G. & Requejos, C. S. (1984). Geology, geochronology and chemical evolution of the island of Pantelleria. *Geological Magazine* **121**, 541–668.

Civetta, L., D'Antonio, M., Orsi, G. & Tilton, G. R. (1998). The geochemistry of volcanic rocks from Pantelleria Island, Sicily channel: petrogenesis and characteristics of the mantle source region. *Journal of Petrology* **39**, 1453–1491.

Cole J.W., Milner D.M. & Spinks K.D. (2005). Calderas and caldera structures: a review. *Earth Sciences Reviews* **69**.1–26

Çubukçu, H. E., Aydar, E. & Gourgaud, A. (2007). Comment on "Volcanostratigraphy and petrogenesis of the Nemrut stratovolcano (East Anatolian High Plateau): The most recent post-collisional volcanism in Turkey" by 189–211. *Chemical Geology* **245**. 120-129.

Çubukçu, H. E., Ersoy, O., Aydar, E. & Çakır, Ü. (2006). WDS versus silicon drift detector EDS: A case report for the comparison of quantitative chemical analyses of natural silicate minerals. *Micron* (in press). doi:10.1016/j.micron.2006.11.004

Cunningham, D. (2005). Active intracontinental transpressional mountain building in the Mongolian Altai: Defining a new class of orogen. *Earth and Planetary Science Letters* **240**. 436-444.

Damasceno D., Scoates J.S., Weiss D., Frey F. & Giret A. (2002) Mineral chemistry of midly alkaline basalts from the 25 Ma Mont Crozier section, Kerguelen Archipelago : constraints on phenocryst crystallization environments. *Journal of Petrology* **43**, 1389-1413.

Davies, G.R. & Macdonald, R. (1987). Crustal influences in the petrogenesis of the Naivasha basalt–comendite complex: combined trace element and Sr–Nd–Pb isotope constraints. *Journal of Petrology* **28**. 1009–1031.

De Paolo, D. J. (1981). Trace element and isotopic effects of combined wall rock assimilation and fractional crystallization. *Earth and Planetary Science Letters* **53**, 189-202.

Deer, W. A., Howie, R.A. & Zussman, J. (2001). Rock Forming Minerals. Volume 4A. Framework Silicates: Feldspars, 2nd ed. *Geological Society of London. London* 972 pp. ISBN 1 86239 081 9.

Deniel, C., Vidal, P., Coulon, C., Vellutini, P. J. & Piguet, P. (1994). Temporal evolution of mantle source during continental rifting: the volcanism of Djibouti (Afar). *Journal of Geophysical Research* **99**, 2853-2869.

Dewey, J.F., Hempton, M.R., Kidd, W.S.F., Şaroğlu, F. & Şengör, A.M.C. (1986). Shortening of continental lithosphere: the neotectonics of Eastern Anatolia—a young collision zone. In: Coward, M.P., Riea, A.C. (Eds.), Collision Tectonics, *Geological Society of London Special Publications* **19**. pp. 3 – 36.

E – F – G

Elitok Ö. & Dolmaz, M. N. (2007). Mantle flow-induced crustal thinning in the area between the easternmost part of the Anatolian plate and the Arabian Foreland (E Turkey) deduced from the geological and geophysical data. *Gondwana Research* (in press)

Elmasri, R. & Navathe, S. B. (1989). Fundamentals of Database Systems. *Benjamin Cummings, Redwood City*, California.

Ercan, T., Fujitani, T., Matsuda, J., Notsu, K., Tokel, S. & Tadahide, U.I. (1990). Doğu ve Güneydoğu Anadolu Neojen-Kuvaterner volkanitlerine ilişkin yeni jeokimyasal, radyometrik ve izotopik verilerin yorumu. *MTA Dergisi* **110**, 143– 164.

Faccenna, C., Bellier, O., Martinod, J., Piromallo, C. & Regard, V. (2006). Slab detachment beneath eastern Anatolia: A possible cause for the formation of the North Anatolian fault. *Earth and Planetary Science Letters* **242**. 85-97.

Feeley, T. C. & Dungan, M. A. (1996). Compositional and dynamic controls on mafic– silicic magma interactions at continental arc volcanoes: evidence from Cordon El Guadal, Tatara–San Pablo Complex, Chile. *Journal of Petrology* **37**, 1547–1577.

Ferla, P. & Meli, C. (2006). Evidence of magma mixing in the 'Daly Gap' of alkaline suites: A case study from the enclaves of Pantelleria (Italy). *Journal of Petrology* **47**, 1467-1507.

Fitton, J.G. & Upton, B.G.J. (Eds.) (1987). Alkaline Igneous Rocks. Special Publication, vol. 30. *Geological Society, London*. 568 p.

Frost, B.R. & Lindsley, D.H. (1992). Equilibria among Fe–Ti oxides, pyroxenes, olivine, and quartz. II. Application. *American Mineralogist* **77**, 1004-1020.

Frost, B.R., Lindsley, D.H. & Andersen, D.J. (1988). Fe–Ti oxide–silicate equilibria: assemblages with fayalitic olivine. *American Mineralogist* **73**, 727-740.

Garcia, M.O. (1996). Petrography and olivine and glass chemistry of lavas from the Hawaiian Scientific Drilling Project, *Journal of Geophysical Research* **101**, 11701-11713.

Ghiorso, M.S. & Sack, R.O. (1995). Chemical mass transfer in magmatic processes. IV. A revised and internally consistent thermodynamic model for the interpretation and extrapolation of liquid-solid equilibria in magmatic systems at elevated temperatures and pressures. *Contributions to Mineralogy and Petrology* **119**. 197–212.

Giles, J. R. A. (ed.) (1995). Geological Data Management, *Geological Society Special Publication* **97**, pp. 81-90.

Giordano, D., Mangiacapra, A., Potuzak, M., Russell, J.K., Romano, C., Dingwell, D.B. & Di Muro, A. (2006). An expanded non-Arrhenian model for silicate melt viscosity: A treatment for metaluminous, peraluminous and peralkaline liquids, *Chemical Geology* **229**, 42-56.

Grove, T.L. & Bryan, W.B. (1983). Fractionation of pyroxene–phyric MORB at low pressure: An experimental study. *Contributions to Mineralogy and Petrology* **84**, 293–309.

Güleç, N., Hilton, D. R. & Mutlu, H. (2002). Helium isotope variations in Turkey: relationship to tectonics, volcanism and recent seismic activities. *Chemical Geology* **187**. 129-142.

Gülen, L. (1984). Sr, Nd, Pb isotope and trace element geochemistry of calc-alkaline and alkaline volcanics, Eastern Turkey. PhD thesis, *Massachutsetts Institute of Technology*. 232 p.

Guillou, H., Carracedo., J. C. & Day, S. J., (1998). Dating of the Upper Pleistocene–Holocene volcanic activity of La Palma using the unspiked K–Ar technique. *Journal of Volcanology and Geothermal Research* **86**. 137-149.

Gunderson, R. (1988). Geological summary of Nemrut volcano, Eastern Turkey: *UNOCAL Geothermal Geology Report*. 8 p.

Güner, Y. (1984). Nemrut yanardağının jeolojisi, jeomorfolojisi ve volkanizmanın evrimi. *Jeomorfoloji Dergisi* **12**. 23-63.

Guo, Z., Wilson, M., Liu., J. & Mao, Q. (2006). Post-collisional, potassic and ultrapotassic magmatism of the northern Tibetan Plateau: Constraints on characteristics of the mantle source, geodynamic setting and uplift mechanisms. *Journal of Petrology* **47**, 1177-1220.

H – I – K

Halama R., Waight T. & Markl G. (2002) Geochemical and isotopic zoning patterns of plagioclase megacrysts in gabbroic dykes from the Gardar Province, South Greenland: Implications for crystallization processes in anorthositic magmas. *Contributions to Mineralogy and Petrology* **144**, 109–127.

Hart, S.R., Blusztajn, J., Dick, H.J.B., Meyer, P.S. & Muehlenbachs, K. (1999). The fingerprint of seawater circulation in a 500-meter section of ocean crust gabbros. *Geochimica et Cosmochimica Acta* **63**. 4059-4080.

Hart, W. K., WoldeGabriel, G., Walter, R. C. & Mertzman, S. A. (1989). Basaltic volcanism in Ethiopia: constraints on continental rifting and mantle interaction. *Journal of Geophysical Research* **94**, 7731-7748.

Hawthorne, F. C., Ungaretti, L., Oberti, R., Bottazzi, P. & Czamanske, G. K. (1993). Li: an important component in igneous alkali-amphiboles. *American Mineralogist* **78**, 733–745.

Hibbard, M. J. (1994). Petrography to petrogenesis. *Engelwood Cliffs, New. Jersey, Prentice Hall*, 608. ISBN-13: 978-0023541452.

Hofmann, A.W. (1988). Chemical differentiation of the Earth: the relationship between mantle, continental crust, and oceanic crust. *Earth and Planetary Science Letters* **90**. 297-314. doi: 10.1016/0012-821X(88)90132-X.

Hoover, J.D. & Irvine, T.N. (1977). Liquidus relations and Mg–Fe partitioning in part of the system Mg_2SiO_4–Fe_2SiO_4–$CaMgSi_2O_6$–$CaFeSi_2O_6$–$KAlSi_3O_8$–SiO_2. *Carnegie Institute of Washington Yearbook* **77**. 774–784

Housh, T.B. & Luhr, J.F. (1991). Plagioclase-melt equilibria in hydrous systems. *American Mineralogist* **76**. 477-492.

Iddings, J. P. (1892). The origin of igneous rocks. *Bull Phil Soc Washington* **12**

İlhan, E. (1968). Dördüncü bölgeye dahil olan sahalarda yapılmış münferit jeolojik müşahadeler. *MTA Rapor* **439**. 26 p.

Innocenti, F., Manetti, P., Mazzuoli, R., Pasquare, G. & Villari, L. (1982). Anatolia and northwestern Iran. In: Thorpe, R.S. (Ed.), *Andesites: Orogenic Andesites and Related Rocks. Wiley, New York,* pp. 327–349.

Innocenti, F., Mazzuoli, R., Pasquare, G., Radicati di Brozolo, F. & Villari, L. (1976). Evolution of volcanism in the area of interaction between the Arabian, Anatolian and Iranian plates Lake Van, Eastern Turkey. *Journal of Volcanology and Geothermal Research* **1**. 103-112.

Innocenti, F., Mazzuoli, R., Pasquare, G., Serri, G. & Villari, L. (1980). Geology of the volcanic area north of Lake Van Turkey. *Geol. Rundsch*. **69**, 292–322.

Karakhanian, A., Djrbashian, R., Trifonov, V., Philip, H., Arakelian, S. & Avagian, A. (2002). Holocene-historical volcanism and active faults as natural risk factors for Armenia and adjacent countries. *Journal of Volcanology and Geothermal Research* **113**. 319-344.

Karaoğlu, Ö., Özdemir, Y., Tolluoğlu, A. Ü., Karabıyıkoğlu, M., Köse, O. & Froger, J.-L. (2005). Stratigraphy of the volcanic products around Nemrut Caldera: Implications for reconstruction of the caldera formation, *Turkish Journal of Earth Sciences* **14**. 123-143.

Keskin, M. (2003). Magma generation by slab steepening and breakoff beneath a subduction-accretion complex: An alternative model for collision related volcanism in Eastern Anatolia,Turkey. *Geophysical Research Letters* **30** (24), 8046, doi:10.1029/2003GL018019

Keskin, M., Pearce, J.A. & Mitchell, J.G. (1998). Volcanostratigraphy and geochemistry of collision-related volcanism on the Erzurum-Kars Plateau, North Eastern Turkey. *Journal of Volcanology and Geothermal Research* **85**. 355–404.

Klein, E.M. (2004). Geochemistry of the Igneous Oceanic Crust. In: Holland, H.D. and Turekian, K.K. (Eds). *Treatise on Geochemistry., Elsevier, Amsterdam* **3**. 433-463.

Koçyiğit, A., Yılmaz, A., Adamia, S. & Kuloshvili, S. (2001). Neotectonics of East Anatolian Plateau (Turkey) and Lesser Caucasus: Implication from transition from thrusting to strike-slip faulting. *Geodinamica Acta* **14**. 177– 195.

Krienitz, M.S., Haase, K.M., Mezger, K., Eckardt, V. & Shaik-Mashail, M.A. (2006). Magma genesis and crustal contamination of continental intraplate lavas in northwestern Syria. *Contributions to Mineralogy and Petrology* **151**, 698-716.

Larsen, L. M. (1977). Aenigmatites from the Ilimaussaq intrusion, south Greenland: chemistry and petrological implications. *Lithos* **10**, 257-270.

Le Bas, M. J. (1971). Peralkaline volcanism, crustal swelling and rifting. *Nature* **230**. 85-86.

Le Pennec, J. –L., Temel, A., Froger, J. –L., Sen, S., Gourgaud, A. & Bourdier, J. –L. (2005). Stratigraphy and age of the Cappadocia ignimbrites, Turkey: reconciling field constraints with paleontologic, radiochronologic, geochemical and paleomagnetic data. *Journal of Volcanology and Geothermal Research* **141**. 45-64.

Leake, B. E.,Woolley, A. R., Arps, C. E. S., Birch, W. D., Gilbert,M. C., Grice, J. D., et al. (1997). Nomenclature of amphiboles: report of the subcommittee on amphiboles of the International Commission on New Minerals and Mineral Names. *Mineralogical Magazine* **61**. 295-321.

LeBas, M. J., LeMaitre, R. W., Streckeisen, A. & Zanettin, B. (1986). A chemical classification of volcanic rocks based on the total alkali-silica diagram. *Journal of Petrology* **27**. 745-750.

Liégeois, J. P. & Black, R. (1987). Alkaline magmatism subsequent to collision in the Pan-African belt of the Adrar des Iforas (Mali). In: Fitton, J. G. & Upton, B. G. J. (eds) *Alkaline Igneous Rocks. Geological Society, London, Special Publications* **30**, 381-401.

Lindsley,D. & Frost, B.R. (1992). Equilibria among Fe–Ti oxides, pyroxenes, olivine, and quartz: Part I. Theory. A*merican Mineralogist* **77**, 987–1003.

Lowenstern, J. B., Mahood, G. A., Herving, R. L. & Sparks, J. (1993). The occurrence and distribution of Mo and molybdenite in unaltered peralkaline rhyolites from Pantelleria, Italy. *Contributions to Mineralogy and Petrology* **114**, 119–129.

Macdonald, R. (1974). Nomenclature and petrochemistry of the peralkaline oversaturated extrusive rocks. In: Bailey, D. K., Barberi, F. & Macdonald, R. (eds) *Oversaturated Extrusive Peralkaline Volcanic Rocks. Bulletin Volcanologique (Special Issue)* **38**, 498–516.

Macdonald, R. (1987). Quaternary peralkaline silicic rocks and caldera volcanoes of Kenya. In: Fitton, J. G. & Upton, B. G. J. (eds) *Alkaline Igneous Rocks. Geological Society, London, Special Publications* **30**, 313-333.

Macdonald, R., Davies, G. R., Bliss, C. M., Leat, P. T., Bailey, D. K. & Smith, R. L. (1987). Geochemistry of high-silica rhyolites, Naivasha, Kenya rift valley. *Journal of Petrology* **28**, 979-1088.

Maggi, A. & Priestley, K. (2005). Surface waveform tomography of the Turkish-Iranian plateau. *Geophysical Journal International* **160**, 1068–1080.

Mahood, G. A. & Baker, D. R. (1986). Experimental constraints on depths of fractionation of mildly alkalic basalts and associated felsic rocks: Pantelleria, Strait of Sicily. *Contributions to Mineralogy and Petrology* **93**, 251–264.

Mahood, G. A. (1981). The chemical evolution of a late Pleistocene rhyolitic centre : The Sierra La Prima vera, Jalisco, Mexico. *Contributions to Mineralogy and Petrology* **77**, 129-49.

Mahood, G. A. (1984). Pyroclastic rocks and calderas associated with strongly peralkaline magmatism. *Journal of Geophysical Research* **89**, 8540–8552.

Markl G. (Ed) (2006). Peralkaline rocks: A special issue dedicated to Henning Sørensen. *Lithos* **91**. ix-xii.

Marks M. & Markl G. (2003). Ilimaussaq "en miniature:" Closed system fractionation in an agpaitic dyke rock from the Gardar province, south Greenland. *Mineralogical Magazine* **67**, 893–919.

Matsuda J.I. (1988). Geochemical study of collision volcanism at the plate boundary in Turkey (comparison with subduction volcanism in Japan). *Initial report of Turkey-Japan Volcanological Project Part* **I**. 31-36.

McBirney, A.R. (1993). Differentiated rocks of the Galapagos hotspot. In: Prichard, H.M., Alabaster, T., Harris, N.B.W., Neary, G.R. (Eds.), *Magmatic Processes and Plate Tectonics. Geological Society of America Special Publication* **76**, 61-69.

McPhie, J., Doyle M. & Allen, R. (1993). Volcanic Textures: a guide to the interpretation of textures in volcanic rocks. *CODES SRC. University of Tasmania*. 198 p.

Mitchell, R.H. (1990). A review of the compositional variation of amphiboles in alkaline plutonic complexes. *Lithos* **26**, 135–156.

Mohr, P. A. (1970). Volcanic composition in relation to tectonics in the Ethiopian rift system: a preliminary investigation. *Bulletin Volcanologique* **34**. 141-157.

Morimoto, M., Fabries, J., Ferguson, A. K., Ginzburg, I. V., Ross, M., Seifert, F. A., Zussman, J., Aoki, K. & Gottardi, G. (1988). Nomenclature of pyroxenes. *Mineralogical Magazine* **52**, 535–550.

Mungall, J., Martin, R.F. (1995). Petrogenesis of basalt–comendite and basalt–pantellerite suites, Terceira, Azores, and some implications for the origin of ocean–island rhyolites. *Contributions to Mineralogy and Petrology* **119**, 43–45.

Mysen, B. (2007). Partitioning of calcium, magnesium, and transition metals between olivine and melt governed by the structure of the silicate melt at ambient pressure. *American Mineralogist* **92**. 844-862.

Nakamura, N. (1974). Determination of REE, Ba, Fe, Mg, Na and K in carbonaceous and ordinary chondrites. *Geochimica et Cosmochimica Acta* **38**, 757-775.

Nekvasil, H., Dondolini, A., Horn, J., Filiberto, J., Long, H. & Lindsley, D. H. (2004). The origin and evolution of silica-saturated alkalic suites: an experimental study. *Journal of Petrology* **45**, 693–721.

Nelson, S.A. & Hegre, J.A. (1990). Volcan Las Navajas, a Pliocene–Pleistocene trachyte/peralkaline rhyolite volcano in the northwestern Mexican volcanic belt. *Bulletin of* Volcanology **52**, 186– 204.

Noble, D. C. (1968). Systematic variation of major elements in comendite and pantellerite glasses. *Earth and Planetary Science Letters* **4**. 167-172.

Notsu, K., Fujitoni, T., Ui, T., Matsuda, J. & Ercan, T. (1995). Geochemical features of collision related volcanic rocks in central and Eastern Anatolia, Turkey. *Journal of Volcanology and Geothermal Research* **64**. 171–192.

O – Ö – P

Okay, A. I., & Tüysüz, O. (1999). Tehtyan sutures of northern Turkey. In B. Durand, L. Jolivet, F. Horvath & M. Seranne (Eds). *The Meditarranean basins: Tertiary extension within the Alpine orogen, Geological Society of London, Special Publication* **156**. 475-515.

Orgulu, G., Aktar, M., Turkelli, N., Sandvol, E. & M. Barazangi (2003). Contribution to the Seismotectonics of the Eastern Anatolian Plateau from Moderate and Small Size Events. *Geophysical Research Letters* **30**(24). doi:10.1029/2003GL018258.

Oswalt, F. (1912). Armenian. *Handbuch der regionalen Geologie* **10**. Heidelberg.

Over, S., Bellier, O., Poisson, A. & Andrieux, J. (1997). Late Cenozoic stress state changes along the central North Anatolian fault zone (Turkey), *Ann Tecton* **XI** (1–2). 75–101.

Özdemir, Y., Karaoglu, Ö., Tolluoglu, A.U. & Gulec, N. (2006). Volcanostratigraphy and petrogenesis of the Nemrut stratovolcano (East Anatolian High Plateau): the most recent post-collisional volcanism in Turkey. *Chemical Geology* **226**, 189–211.

Özdemir, Y., Karaoglu, Ö., Tolluoglu, A.U. & Gulec, N. (2007). Reply to discussion by Evren Çubukçu, Erkan Aydar and Alain Gourgaud of "Volcanostratigraphy and petrogenesis of the Nemrut stratovolcano (East Anatolian High Plateau): The most recent post-collisional volcanism in Turkey" by Y. Özdemir, Ö. Karaoğlu, A.Ü. Tolluoğlu and N. Güleç [Chemical Geology 226 (2006) 189–211], *Chemical Geology* **245**. 130-134.

Özpeker, L. (1973). Nemrut yanardağının volkanolojik incelenmesi: *Tübitak 4.Bilim Kongresi, Yerbilimleri Seksiyonu Tebliğler Kitabı*. 1-17.

Pearce, J.A., Bender, J.F., De Long, S.E., Kidd, W.S.F., Low, P.J., Güner, Y., Şaroğlu, F., Yılmaz, Y., Moorbath, S. & Mitchell, J.J. (1990). Genesis of collision volcanism in eastern Anatolia Turkey. *Journal of Volcanology and Geothermal Research* **44**, 189–229.

Peccerillo, A., Barberio, M. R., Yirgu, G., Ayalew, D., Barbieri, M. & Wu, T. W. (2003). Relationships between mafic and peralkaline silicic magmatism in continental rift setting: a petrological, geochemical and isotopic study of the Gedemsa Volcano, Central Ethiopian Rift. *Journal of Petrology* **44**, 2003–2032.

Powell R. (1984). Inversion of the assimilation and fractional crystallization (AFC) equations; characterization of contaminants from isotope and trace element relationships in volcanic suites. *Journal of the Geological Society London* **141**, 447–452.

Putirka, K. (1997). Magma transport at Hawaii: inferences based on igneous thermobarometry. *Geology* **25**, 69-72.

Putirka, K. D. (2005). Igneous thermometers and barometers based on plagioclase + liquid equilibria: tests of some existing models and new calibrations. *American Mineralogist* **90**, 336–346.

Putirka, K.D., Mikaelian, H., Ryerson, F. & Shaw, H. (2003). New clinopyroxene–liquid thermobarometers for mafic, evolved, and volatile-bearing lava compositions, with applications to lavas from Tibet and the Snake River Plain, Idaho. *American Mineralogist* **88**, 1542-1554.

R – S – Ş

Rasmussen, K. (1995). An overview of database analysis and design for geological systems. *Geological Society Special Publication* **97**, pp. 5-11.

Ren, M., Omenda, P.A., Anthony, E.Y., White, J.C., Macdonald, R. & Bailey, D.K. (2006). Application of the QUILF thermobarometer to the peralkaline trachytes and pantellerites of the Eburru volcanic complex, East African Rift, Kenya *Lithos* **91**, 109-124. doi:10.1016/j.lithos.2006.03.011.

Ricou, L. E. (1994). Tethys reconstructed: plates, continental fragments and their boundaries since 260 Ma from central America to south-eastern Asia. *Geodinamica Acta* **7**. 169-218.

Roeder, P.L. & Emslie, R.F. (1970). Olivine-liquid equilibrium. *Contributions to Mineralogy and Petrology* **29**, 275–289.

Ryabchikov, I. D. & Kogarko, L. N. (2006). Magnetite compositions and oxygen fugacities of the Khibina magmatic system. *Lithos* **91**. 35-45.

Sandvol, E., Tü rkelli, N., Zor, E., Gök, R., Bekler, T., Gürbüz, C., Seber, D. & Barazangi, M. (2003). Shear wave splitting in a young continent–continent collision: an example from Eastern Turkey. *Geophysical Research Letters* **30**. doi:10.1029/2003GL017390.

Scaillet, B. & Macdonald, R. (2001). Phase relations of peralkaline silicic magmas and petrogenetic implications. *Journal of Petrology* **42**. 825–845

Scaillet, B. & Macdonald, R. (2003). Experimental constraints on the relationships between peralkaline rhyolites of the Kenya Rift Valley. *Journal of Petrology* **44**, 1867–1894.

Scaillet, B. & Macdonald, R. (2006). Experimental constraints on pre-eruption conditions of pantelleritic magmas: Evidence from Eburru complex, Kenya Rift. *Lithos* **91**, 95 – 108.

Schönenberger, J., Marks, M., Wagner, T. & Markl, G. (2006). Fluid–rock interaction in autoliths of agpaitic nepheline syenites in the Ilímaussaq intrusion, South Greenland. *Lithos* **91**. 331-351.

Şen, P., Temel, A. & Gourgaud, A. (2004). Petrogenetic modelling of Quaternary post-collisional volcanism: a case study of central and eastern Anatolia. *Geological Magazine* **141**, 81–98.

Şengör, A.M.C. & Kidd, W.S.F. (1979). Post-collisional tectonics of the Turkish–Iranian Plateau and a comparison with Tibet. *Tectonophysics* **55**, 361–376.

Şengör, A.M.C. & Yılmaz, Y. (1981). Tethyan evolution of Turkey: a plate tectonic approach. *Tectonophysics* **75**, 181–241.

Şengör, A.M.C. (1980). Türkiye'nin neotektoniğinin esasları, *Türkiye Jeoloji Kurumu Yayını*, pp 42.

Şengör, A.M.C., Ozeren, S., Genc, T. & Zor, E. (2003). East Anatolian high plateau as a mantle-supported, north–south shortened domal structure. *Geophysical Research Letters* **30** (24), 8045.

Şerefhan (1597). Serefname: Kürt tarihi (translated from arabic to turkish by M. Emin Bozarslan), 4th edn. (1990). *Hasat yayinlari*, 544 pp.

Shand, S. J. (1922). The problem of the alkaline rocks. *Proc. Geol. Soc. S. Afr*. **25**, xix-xxxiii.

Shand, S. J. (1923). The alkaline rocks of the Franspoort libe, Pretoria district, *Trans. Geol. Soc. S. Afr.* **24**. 81-100.

Sisson T. W. & Grove T. L. (1993). Experimental investigations of the role of H2O in calc-alkaline diffrentiation and subduction zone magmatism. *Contributions to Mineralogy and Petrology* **113**. 143-166.

Sørensen, H. (Ed.), 1974. The Alkaline Rocks. *Wiley Interscience,New York.* 622 pp.

Spera, F.J. & Bohrson, W.A. (2001). Energy-constrained open-system magmatic processes: I. General model and energy-constrained assimilation and fractional crystallization (EC-AFC) formulation. *Journal of Petrology* **42**, 999– 1018.

Steiger, R.H. & Jager, E. (1977). Convention on the use of decay constants in geo- and cosmochronology. *Earth and Planetary Science Letters* **36**, 359–362.

Stampfli, G.M. (1996). The Intra-Alpine terrain: A Paleotethyan remnant in the Alpine Variscides. *Eclogae Geol. Helv* **89**, 13-42.

Stormer, J. C. (1983). The effects of recalculation on estimates of temperature and oxygen fugacity from analyses of multicomponent iron–titanium oxides. *American Mineralogist* **66**, 1189–1201.

T – U

Tomiya, A. & Takahashi, E. (2005). Evolution of the magma chamber beneath Usu Volcano since 1663: a natural laboratory for observing changing phenocryst compositions and textures. *Journal of Petrology* **46**. 2395-2426.

Toplis, M.J. & Carroll, M.R. (1995). An experimental study of the influence of oxygen fugacity on Fe–Ti oxide stability, phase relations, and mineral-melt equilibria in ferro-basaltic systems. *Journal of Petrology* **36**, 1137– 1170.

Toplis, M.J. (2005). The thermodynamics of iron and magnesium partitioning between olivine and liquid: criteria for assessing and predicting equilibrium in natural and experimental systems. *Contributions to Mineralogy and Petrology* **149**. 22-39.

Tribuzio R., & Giacomini, F. (2002). Blueschist facies metamorphism of peralkaline rhyolites from the Tenda crystalline massif (northern Corsica): evidence for involvement in the Alpine subduction event?. *Journal of Metamorphic Geology* **20**. 513-526.

Troll, V.R., Sachs, P.M., Schmincke, H.-U. & Sumita, M. (2003). The REE-Ti mineral chevkinite in comenditic magmas from Gran Canaria, Spain: a SYXRF-probe study. *Contributions to Mineralogy and Petrology* **145**, 730–741.

Trua, T., Deniel, C. & Mazzuoli, R. (1998). Crustal control in the genesis of Plio-quaternary bimodal magmatism of the Main Ethiopian Rift (MER): geochemical and isotopic (Sr Nd, Pb) evidence. *Chemical Geology* **155**, 201-231.

Türkecan, A. (1991). Muş yöresindeki Pliyosen yaşlı volkanitlerin petrolojisi. *MTA Dergisi* **112**. 85-101.

Türkelli, N., Sandvol, E., Zor, E., Gok, R., Bekler T., Al-Lazki A., Karabulut H., Kuleli, S., Eken T., Gurbuz C., Bayraktutan S., Seber D. & Barazangi M. (2003). Seismogenic zones in Eastern Turkey. *Geophysical Research Letters* **30** (24). doi:10.1029/2003GL018023

Ulusoy, I., Çubukçu, E., Aydar, A., Labazuy, P., Gourgaud, A. & Vincent P. M. (2004). Volcanic and deformation history of the Bodrum resurgent caldera system (southwestern Turkey). *Journal of Volcanology and Geothermal Research* **136**. 71-96.

Ulusoy, I., Labazuy, P., Aydar, A., Ersoy, O. & Çubukçu, E. (2008). Structure of the Nemrut caldera (Eastern Anatolia, Turkey) and associated hydrothermal fluid circulation. *Journal of Volcanology and Geothermal Research* (in review).

V – W – Y - Z

Vermeesch, P. (2006). Tectonic discrimination of basalts with classification trees. *Geochimica et Cosmochimica Acta* **70**. 1839-1848

Vlach, S. R. F. & Gualda, G. A.. R. (2007), Allanite and chevkinite in A-type granites and syenites of the Graciosa Province, southern Brazil. *Lithos* (in press)

Weaver, S. D., Gibson, I. L., Houghton, B. F. & Wilson, C. J. N., 1990. Mobility of rare earth and other elements during crystallization of peralkaline silicic lavas. *Journal of Volcanology and Geothermal Research* **43**, 57-70.

Wedepohl, K. H. (1995). The composition of the continental crust. *Geochimica et Cosmochimica Acta* **59**, 1217–1232.

White J. C., Benker, S. C., Ren, M., Urbanczyk, K. M. & Corrick.(2006). Petrogenesis and tectonic setting of the peralkaline Pine Canyon caldera, Trans-Pecos Texas, USA. *Lithos* **91**. 74-94.

White, J. C., Ren, M. & Parker, D. F. (2005). Variation in mineralogy, temperature, and oxygen fugacity in a suite of strongly peralkaline lavas and tuffs, Pantelleria, Italy. *Canadian Mineralogist* **43**, 1331–1347.

White, J.C., Holt, G.S., Parker, D.F. & Ren, M. (2003). Trace-element partitioning between alkali feldspar and peralkalic quartz trachyte to rhyolite magma. Part I: Systematics of trace-element partitioning. *American Mineralogist* **88**, 316–329.

Wilson, M. (1989). Igneous petrogenesis: A global tectonic approach: *Unwin Hyman, Boston*, 466p.

Yılmaz, Y. (1993). New evidence and model for the evolution of the southeast Anatolian orogen. *Geological Society of American Bulletin* **105**. 251–271.

Yılmaz, Y., Guner, Y. & Şaroğlu, F. (1998). Geology of the Quaternary volcanic centres of the east Anatolia. *Journal of Volcanology and Geothermal Research* **85**. 173–210.

Zor, E., Gurbuz, C., Turkelli, N., Sandvol, E., Seber, D. & Barazangi, M. (2003). The crustal structure of the East Anatolian Plateau from receiver functions. *Geophysical Research Letters* **30**, 8044.